



**US Army Corps  
of Engineers®**  
Engineer Research and  
Development Center

*Laboratory Discretionary Research and Development Program*

# **Investigation of Bond Slip Between Concrete and Steel Reinforcement Under Dynamic Loading Conditions**

John H. Weathersby

August 2003

# Investigation of Bond Slip Between Concrete and Steel Reinforcement Under Dynamic Loading Conditions

John H. Weathersby

*Geotechnical and Structures Laboratory  
U.S. Army Engineer Research and Development Center  
3909 Halls Ferry Road  
Vicksburg, MS 39180-6199*

Final report

Approved for public release; distribution is unlimited

**ABSTRACT:** Structural failures during recent earthquakes and terrorist attacks have demonstrated shortcomings in the design procedures for reinforced concrete structures. Earlier research has demonstrated that a major limitation of the Finite Element (FE) modeling of the response of reinforced concrete is the accurate modeling of the interaction of the concrete with the steel reinforcement. Presently, there are insufficient data on the dynamic nonlinear interaction between the concrete material and the steel reinforcement to develop a numerical model of this interaction.

The primary objective of this study was to experimentally investigate the dynamic interaction (bond slip) of reinforcement with concrete and gain a better understanding of the parameters that control this interaction. Specifically, the effects of concrete confinement, bar deformation and bar diameter on the bond slip, and the influence of loading rates - static to impact – on these effects were investigated. Additionally, the variation of the strain along the length of the steel bar and strain transfer to the concrete were investigated. Finite Element analyses were performed using the experimental parameters to determine the value of the chemical adhesion and to compare the experimental results with the analytical values.

To accomplish the research objectives, 33 pullout tests were performed. The test specimens were subjected to quasi-static, dynamic, and impact loadings to investigate the influence of rebar size and shape, confinement and loading rate on pullout resistance, and failure mode.

The results of the study have shown that, for the concrete and steel used in this investigation, the stress resulting from static friction and chemical adhesion is 960 psi for quasi-static loading, 2,600 psi for dynamic loading, and 3,200 psi for impact loading. The steel bar deformations accounted for 70 to 77 percent of the total resistance to pullout regardless of loading rate. Impact loaded specimens had nearly twice the pullout resistance of the quasi-statically loaded specimens, and the development length decreased as the loading rate or confinement increased. Bond stresses obtained for both smooth and deformed bars were in good agreement with results obtained in earlier studies involving quasi-static tests.

**DISCLAIMER:** The contents of this report are not to be used for advertising, publication, or promotional purposes. Citation of trade names does not constitute an official endorsement or approval of the use of such commercial products. All product names and trademarks cited are the property of their respective owners. The findings of this report are not to be construed as an official Department of the Army position unless so designated by other authorized documents.

## **ACKNOWLEDGEMENTS**

I wish to thank Dr. Vijay Gopu, Professor Emeritus, Louisiana State University, for his patient guidance and meticulous review of my work. This task would have been insurmountable without his hard work, knowledge, and editing skills. I gratefully acknowledge all who served on my committee: Dr. Roger Seals, Dr. Richard Avent, Dr. Mark Levitan, and Dr. Richard Haymaker.

This research was funded by Headquarters, U.S. Army Corps of Engineers, under the Discretionary Research Program. Technical supervision was provided by Dr. Reed Mosher, Technical Director for Survivability and Protective Structures, Geotechnical and Structures Laboratory (GSL), U.S. Army Engineer Research and Development Center (ERDC), Vicksburg, MS, and Dr. Stanley Woodson, GSL, ERDC. A special thanks to Ms. Pamela Kinnebrew, Chief, Survivability Engineering Branch, GSL ERDC, for her support and encouragement throughout this endeavor. Thanks to Messrs. Donald Nelson and Tommy Bevins and Dr. Jim O'Daniel, GSL, for their assistance in the finite element analysis.



# TABLE OF CONTENTS

ACKNOWLEDGEMENTS .....	iii
TABLE OF CONTENTS.....	iv
LIST OF TABLES .....	viii
LIST OF FIGURES .....	x
PREFACE .....	xvii
CONVERSION FACTORS, NON-SI TO SI UNITS OF MEASUREMENT .....	xviii
CHAPTER 1 INTRODUCTION.....	1
1.1 Background.....	1
1.2 Objective.....	2
1.3 Methodology.....	2
1.4 Scope .....	3
CHAPTER 2 LITERATURE REVIEW.....	5
2.1 Static and Dynamic Bond-Slip Experiments.....	5
2.2 Strain Rate Effects on Concrete.....	9
2.3 Cracking of Concrete Around Deformed Bars .....	10
2.4 Finite-Element Analysis of Bond Slip.....	15
CHAPTER 3 EXPERIMENTAL PROCEDURES .....	19
3.1 Material Properties .....	19
3.1.1 Concrete Properties.....	19
3.1.2 Steel Properties .....	20
3.2 Test Specimens.....	21
3.2.1 Sample Dimensions .....	21
3.2.2 Strain Measurements in Steel.....	22
3.2.3 Strain Measurements in Concrete .....	22
3.2.4 Final Specimen Preparation .....	29
3.3 Testing Equipment and Data Acquisition.....	38
3.3.1 200 Kip Dynamic Loader.....	38
3.3.2 Data Recording .....	43
3.3.3 Still Photography .....	43
3.4 Testing Program .....	44
3.4.1 Test Matrix.....	44
3.4.2 Test Procedure .....	46
3.4.3 Results of Typical Test .....	48

CHAPTER 4	EXPERIMENTAL RESULTS	57
4.1	Quasi-Static Loading of a #8 Deformed Bar Embedded in a 10-inch Diameter Concrete Cylinder	57
4.1.1	Test 1	58
4.1.2	Test 2	58
4.1.3	Test 3	60
4.1.4	Evaluation of Results of Tests 1, 2 and 3	62
4.2	Impact Loading of a #8 Deformed Bar Embedded in a 10-inch Diameter Concrete Cylinder	66
4.2.1	Test 4	67
4.2.2	Test 5	68
4.2.3	Test 6	68
4.2.4	Evaluation of Results of Tests 4, 5, and 6	69
4.3	Dynamic Loading of a #8 Deformed Bar Embedded in a 10-inch Diameter Concrete Cylinder	70
4.3.1	Test 7	72
4.3.2	Test 8	72
4.3.3	Test 9	73
4.3.4	Evaluation of Results of Tests 7, 8, and 9	73
4.4	Impact Loading of a #8 Deformed Bar Embedded in a 20-inch Diameter Concrete Cylinder	75
4.4.1	Test 10	76
4.4.2	Test 11	77
4.4.3	Test 12	77
4.4.4	Evaluation of Results of Tests 10, 11 and 12	78
4.5	Dynamic Loading of a #8 Deformed Bar Embedded in a 20-inch Diameter Concrete Cylinder	81
4.5.1	Test 13	81
4.5.2	Test 14	82
4.5.3	Test 15	82
4.5.4	Evaluation of Results of Tests 13, 14 and 15	83
4.6	Quasi-Static Loading of a #8 Deformed Bar Embedded in a 20-inch Diameter Concrete Cylinder	83
4.6.1	Test 16	85
4.6.2	Test 17	86
4.6.3	Test 18	86
4.6.4	Evaluation of Results of Tests 16, 17 and 18	87
4.7	Impact Loading of a 1-inch Smooth Bar Embedded in a 20-inch Diameter Concrete Cylinder	90
4.7.1	Test 19	90
4.7.2	Test 20	90
4.7.3	Evaluation of Results of Tests 19 and 20	90
4.8	Dynamic Loading of a 1-inch Smooth Bar Embedded in a 20-inch Concrete Cylinder	92
4.8.1	Test 21	93
4.8.2	Test 22	93

4.8.3	Evaluation of Results of Tests 21 and 22.....	94
4.9	Quasi-Static Loading of a 1-inch Smooth Bar Embedded in a 20-inch Concrete Cylinder.....	96
4.9.1	Test 23.....	96
4.9.2	Test 24.....	97
4.9.3	Evaluation of Results of Tests 23 and 24.....	97
4.10	Impact Loading of a #10 Deformed Bar Embedded in a 20-inch Diameter Concrete Cylinder.....	100
4.10.1	Test 25.....	100
4.10.2	Test 26.....	101
4.10.3	Test 27.....	101
4.10.4	Evaluation of Results of Tests 25, 26 and 27.....	102
4.11	Dynamic Loading of a #10 Deformed Bar Embedded in a 20-inch Diameter Concrete Cylinder.....	105
4.11.1	Test 28.....	105
4.11.2	Test 29.....	106
4.11.3	Test 30.....	107
4.11.4	Evaluation of Results of Tests 28, 29, and 30.....	107
4.12	Quasi-Static Loading of a #10 Deformed Bar Embedded in a 20-inch Diameter Concrete Cylinder.....	110
4.12.1	Test 31.....	110
4.12.2	Test 32.....	110
4.12.3	Test 33.....	111
4.12.4	Evaluation of Results of Tests 31, 32 and 33.....	111
CHAPTER 5	EMPIRICAL ANALYSIS OF TEST DATA.....	115
5.1	Effects of Loading Rate.....	115
5.1.1	Effects of Loading Rate on Failure Mode.....	115
5.1.2	Effects of Loading Rate on Failure Loads .....	116
5.1.3	Effects of Loading Rate on Steel Strains .....	117
5.1.4	Effects of Loading Rate on Concrete Strains.....	118
5.1.5	Effects of Loading Rate on Development Length .....	119
5.2	Effects of Specimen Diameter.....	120
5.2.1	Effects of Specimen Diameter on Failure Mode.....	120
5.2.2	Effects of Specimen Diameter on Failure Loads .....	120
5.2.3	Effects of Specimen Diameter on Steel Strains .....	121
5.2.4	Effects of Specimen Diameter on Concrete Strains.....	122
5.2.5	Effects of Specimen Diameter on Development Length .....	122
5.3	Effects of Bar Diameter.....	123
5.3.1	Effects of Bar Diameter on Failure Mode.....	123
5.3.2	Effects of Bar Diameter on Failure Loads .....	124
5.3.3	Effects of Bar Diameter on Steel Strains .....	124
5.3.4	Effects of Bar Diameter on Concrete Strains.....	125
5.3.5	Effects of Bar Diameter on Development Length .....	126
5.4	Effects of Bar Deformation .....	126
5.4.1	Effects of Bar Deformation on Failure Mode.....	126

5.4.2	Effects of Bar Deformation on Failure Loads.....	127
5.4.3	Effects of Bar Deformation on Steel Strains.....	128
5.4.4	Effects of Bar Deformation on Concrete Strains .....	128
5.4.5	Effects of Bar Deformation on Development Length.....	129
CHAPTER 6 NUMERICAL ANALYSIS OF SPECIMENS .....		131
6.1	Mesh Generation.....	133
6.1.1	Smooth Bar .....	133
6.1.2	Dynamic and Impact Loaded Deformed Bars .....	136
6.1.3	Quasi-Static Loaded Deformed Bars .....	137
6.2	1- Inch Diameter Smooth Bar Embedded in a 20-inch Diameter Concrete Cylinder .....	139
6.2.1	Quasi-Static Loading .....	139
6.2.2	Dynamic Loading.....	140
6.2.3	Impact Loading .....	144
6.3	Analysis of a Number 8 Deformed Bar Embedded in a 20-inch Diameter Concrete Cylinder.....	147
6.3.1	Quasi-Static Loading .....	147
6.3.2	Dynamic Loading.....	150
6.3.3	Impact Loading .....	154
6.4	Analysis of a Number 8 Deformed Bar embedded in a 10-inch Diameter Concrete Cylinder.....	155
6.4.1	Quasi-Static Loading .....	155
6.4.2	Dynamic Loading.....	159
6.4.3	Impact Loading .....	162
CHAPTER 7 SUMMARY, CONCLUSIONS AND RECOMMENDATIONS.....		165
7.1	Summary.....	165
7.2	Conclusions .....	169
7.3	Recommendations .....	170
BIBLIOGRAPHY .....		171
APPENDIX A: STRESS-STRAIN CURVES FOR STEEL AND CONCRETE .....		174
APPENDIX B: SUMMARY OF TEST DATA.....		180
VITA.....		263

## LIST OF TABLES

Table 3.1	CSPC mix design.....	20
Table 3.2	Physical dimensions of test specimens .....	36
Table 3.3	Complete test matrix.....	45
Table 3.4	Calculation of engineering strain for fiber optic gage 8 test 18.....	53
Table 4.1	Complete Test Matrix .....	114
Table 5.1	Failure Mode.....	116
Table 5.2	Average Failure Loads.....	116
Table 5.3	Average Steel Strains at Failure.....	117
Table 5.4	Average Concrete Strains at Failure .....	118
Table 5.5	Development Length.....	119
Table 5.6	Failure Mode.....	120
Table 5.7	Average Failure Loads.....	121
Table 5.8	Average Steel Strains at Failure.....	121
Table 5.9	Average Concrete Strains at Failure .....	122
Table 5.10	Development Length.....	123
Table 5.11	Failure Mode.....	123
Table 5.12	Average Failure Loads.....	124
Table 5.13	Average Steel Strains at Failure.....	125
Table 5.14	Average Concrete Strains at Failure .....	125
Table 5.15	Development Length.....	126
Table 5.16	Failure Mode.....	127
Table 5.17	Average Failure Loads.....	127

Table 5.18 Average Steel Strains at Failure.....	128
Table 5.19 Average Concrete Strains at Failure .....	128
Table 5.20 Development Length and Bond Strength.....	129

## LIST OF FIGURES

Figure 3-1 Micro-Measurements foil strain gage .....	23
Figure 3-2 Steel bar prior to placement of strain gages .....	23
Figure 3-3 Test specimen and strain gage locations .....	24
Figure 3-4 Attaching instrumentation cables to the ends of the strain gage lead wires...	24
Figure 3-5 Fiber-Optic Strain gage .....	26
Figure 3-6 Drawing of the silica capillary tube containing the input/output and reflector fibers .....	26
Figure 3-7 Attenuated FOSS I output .....	27
Figure 3-8 Equations for calculating partial fringes .....	28
Figure 3-9 A typical change in strain direction .....	29
Figure 3-10 Long grout tubes damaged after testing .....	31
Figure 3-11 Placing the fiber-optic gage inside the grout tube form .....	31
Figure 3-12 placing grout in the tubes .....	32
Figure 3-13 Grout tubes containing fiber-optic strain gages curing in racks .....	32
Figure 3-14 Bottom of plywood form cut in half to facilitate form removal .....	33
Figure 3-15 First plywood donut and spacer blocks in place .....	34
Figure 3-16 Split plywood donut and steel bar in place .....	34
Figure 3-17 Sono tub placed over plywood donuts .....	35
Figure 3-18 Grout tubes placed in wire ladder .....	36
Figure 3-19 Grout tubes placed inside concrete form.....	37
Figure 3-20 Placing the concrete .....	37
Figure 3-21 Characteristics of 200-Kip Loader .....	38
Figure 3-22 Loading modes for 200-Kip Loader.....	39
Figure 3-23 Old superstructure designed to hold long bar samples.....	41

Figure 3-24 New superstructure designed to hold concrete sample. ....	41
Figure 3-25 Rupture disk assembly .....	42
Figure 3-26 Fast opening valve.....	43
Figure 3-27 Spreading Sikadu on the plastic sheet.....	46
Figure 3-28 Failure due to pullout of the smooth steel bar.....	48
Figure 3-29 Failure due to the yielding of the steel bar .....	49
Figure 3-30 Failure due to radial cracking of the concrete .....	49
Figure 3-31 Load vs. Time for test 18 .....	50
Figure 3-32 Steel strain vs. Time for SS-03, test 18 .....	51
Figure 3-33 Raw fiber-optic output from the FOSS I for FO-02, test 18 .....	52
Figure 3-34 Normalized FOSS I output for FO-02, test 18 .....	53
Figure 3-35 Reduced fiber-optic data showing strain vs. time for FO-02, test 18 .....	54
Figure 3-36 Average concrete strains from test 18.....	55
Figure 3-37 Steel strains for tests 16, 17 and 18 showing linear regression of the data..	55
Figure 3-38 Concrete strain for tests 16, 17 and 18 showing no regression of data.....	56
Figure 4-1 Specimen 1 post test.....	59
Figure 4-2 Adjusted steel strains test 1 .....	59
Figure 4-3 Adjusted concrete strains, test 1 .....	60
Figure 4-4 Steel strains, test 2.....	61
Figure 4-5 Adjusted concrete strains, test 2.....	61
Figure 4-6 Test specimen 3 post-test .....	62
Figure 4-7 Crushing of concrete on the leading edges of the steel deformations.....	63
Figure 4-8 Deformed steel bar post-test.....	63
Figure 4-9 Adjusted steel strains, test 3 .....	64
Figure 4-10 Adjusted concrete strains, test 3 .....	64



Figure 4-11 Adjusted steel strains, quasi-static loading, 10-inch diameter samples, #8 deformed bars.....	65
Figure 4-12 Adjusted concrete strains, quasi-static loading, 10-inch diameter samples, #8 deformed bars.....	67
Figure 4-13 Test specimen 6 post-test .....	70
Figure 4-14 Adjusted steel strains, impact loading, 10-inch diameter sample, #8 deformed bar .....	71
Figure 4-15 Adjusted concrete strains, impact loading, 10-inch diameter sample, #8 deformed bar .....	71
Figure 4-16 Test specimen 8 post-test .....	74
Figure 4-17 Adjusted steel strains, dynamic loading, 10-inch diameter sample, #8 deformed bar .....	75
Figure 4-18 Adjusted concrete strains, dynamic loading, 10-inch diameter sample, #8 deformed bar .....	76
Figure 4-19 Test specimen 10 post-test .....	79
Figure 4-20 Adjusted steel strains, impact loading, 20-inch diameter sample, #8 deformed bar .....	80
Figure 4-21 Adjusted concrete strains, impact loading, 20-inch diameter sample, #8 deformed bar .....	80
Figure 4-22 Test specimen 13 post-test .....	84
Figure 4-23 Adjusted steel strains, dynamic loading, 20-inch diameter sample, #8 deformed bar .....	84
Figure 4-24 Adjusted concrete strains, dynamic loading, 20-inch diameter sample, #8 deformed bar .....	85
Figure 4-25 Test specimen 17 post-test .....	88
Figure 4-26 Adjusted steel strains, quasi-static loading, 20-inch diameter sample, #8 deformed bar .....	89
Figure 4-27 Adjusted concrete strains, quasi-static loading, 20-inch diameter sample, #8 deformed bar .....	89
Figure 4-28 Test specimen 20 post-test .....	91

Figure 4-29 Adjusted steel strains, impact loading, 20-inch diameter sample, 1-inch smooth bar .....	92
Figure 4-30 Adjusted concrete strains, impact loading, 20-inch diameter sample, 1-inch smooth bar .....	93
Figure 4-31 Test specimen 22 post-test .....	95
Figure 4-32 Adjusted steel strains, dynamic loading, 20-inch diameter sample, 1-inch smooth bar .....	95
Figure 4-33 Adjusted concrete strains, dynamic loading, 20-inch diameter sample, 1-inch smooth bar .....	96
Figure 4-34 Test specimen 23 post-test .....	98
Figure 4-35 Test specimen 23 post-test .....	98
Figure 4-36 Adjusted steel strains, quasi-static loading, 20-inch diameter sample, 1-inch smooth bar .....	99
Figure 4-37 Adjusted concrete strains, quasi-static loading, 20-inch diameter sample, 1-inch smooth bar .....	100
Figure 4-38 Test specimen 25 post-test .....	103
Figure 4-39 Test specimen 25 post-test. Note crushing of concrete on leading edges of the steel deformations .....	103
Figure 4-40 Adjusted steel strains, impact loading, 20-inch diameter sample, #10 deformed bar .....	104
Figure 4-41 Adjusted concrete strains, impact loading, 20-inch diameter sample, #10 deformed bar .....	105
Figure 4-42 Test specimen 29 post-test .....	108
Figure 4-43 Adjusted steel strains, dynamic loading, 20-inch diameter sample, #10 deformed bar .....	109
Figure 4-44 Adjusted concrete strains, dynamic loading, 20-inch diameter sample, #10 deformed bar .....	109
Figure 4-45 Test specimen 31 post-test .....	112
Figure 4-46 Adjusted steel strains, quasi-static loading, 20-inch diameter sample, #10 deformed bar .....	113

Figure 4-47 Adjusted concrete strains, quasi-static loading, 20-inch diameter sample, #10 deformed bar .....	113
Figure 6-1 Smooth bar showing Cartesian coordinates with projected outer surface to form the cylinder.....	133
Figure 6-2 Complete finite element model for smooth bar runs.....	134
Figure 6-3 Loads applied to the 133 nodes on the bottom of the steel bar .....	135
Figure 6-4 Nodes on the bottom of the concrete restrained in the Z direction .....	135
Figure 6.5 Deformed bar showing deformations deleted to model the strain gage groove .....	137
Figure 6-6 Larger mesh size used in the NIKE3D runs.....	138
Figure 6-7 Simplified deformation pattern used on the NIKE3D runs.....	138
Figure 6-8 Composite steel strains, 1-inch smooth bar, 20-inch diameter sample, dynamic loading.....	141
Figure 6-9 Composite concrete strains, 1-inch smooth bar, 20-inch diameter sample, dynamic loading.....	142
Figure 6-10 Comparison of empirical and numerical steel strains, 1-inch smooth bar, 20-inch diameter sample, dynamic loading .....	143
Figure 6-11 Comparison of empirical and numerical concrete strains, 1-inch smooth bar, 20-inch diameter sample, dynamic loading .....	143
Figure 6-12 Composite steel strains, 1-inch smooth bar, 20-inch diameter sample, impact loading.....	144
Figure 6-13 Composite concrete strains, 1-inch smooth bar, 20-inch diameter sample, impact loading .....	145
Figure 6-14 Comparison of empirical and numerical steel strains, 1-inch smooth bar, 20-inch diameter sample, impact loading .....	146
Figure 6-15 Comparison of empirical and numerical concrete strains, 1-inch smooth bar, 20-inch diameter sample, impact loading.....	146
Figure 6-16 Composite steel strains, #8 deformed bar, 20-inch diameter sample, quasi-static loading .....	148
Figure 6-17 Composite concrete strains, #8 deformed bar, 20-inch diameter sample, quasi-static loading .....	149

Figure 6-18 Failure due to excessive deformation of the concrete elements.....	149
Figure 6-19 Comparison of empirical and numerical steel strains, #8 deformed bar, 20-inch diameter sample, quasi-static loading.....	150
Figure 6-20 Comparison of empirical and numerical concrete strains, #8 deformed bar, 20-inch diameter sample, quasi-static loading.....	150
Figure 6-21 Composite steel strains, #8 deformed bar, 20-inch diameter sample, dynamic loading.....	151
Figure 6-22 Composite concrete strains, #8 deformed bar, 20-inch diameter sample, dynamic loading.....	152
Figure 6-23 Comparison of empirical and numerical steel strains, #8 deformed bar, 20-inch diameter sample, dynamic loading .....	153
Figure 6-24 Comparison of empirical and numerical concrete strains, #8 deformed bar, 20-inch diameter sample, dynamic loading .....	153
Figure 6-25 Composite steel strains, #8 deformed bar, 20-inch diameter sample, impact loading.....	154
Figure 6-26 Composite concrete strains, #8 deformed bar, 20-inch diameter sample, impact loading.....	155
Figure 6-27 Comparison of empirical and numerical steel strains, #8 deformed bar, 20-inch diameter sample, impact loading .....	156
Figure 6-28 Comparison of empirical and numerical concrete strains, #8 deformed bar, 20-inch diameter sample, impact loading.....	156
Figure 6-29 Composite steel strains, #8 deformed bar, 10-inch diameter sample, quasi-static loading .....	157
Figure 6-30 Composite concrete strains, #8 deformed bar, 10-inch diameter sample, quasi-static loading .....	158
Figure 6-31 Failure due to excessive deformation of the concrete elements.....	158
Figure 6-32 Comparison of empirical and numerical steel strains, #8 deformed bar, 10-inch diameter sample, quasi-static loading.....	159
Figure 6-33 Comparison of empirical and numerical concrete strains, #8 deformed bar, 10-inch diameter sample, quasi-static loading.....	159
Figure 6-34 Composite steel strains, #8 deformed bar, 10-inch diameter sample, dynamic loading.....	160

Figure 6-35 Composite concrete strains, #8 deformed bar, 10-inch diameter sample, dynamic loading.....	161
Figure 6-36 Comparison of empirical and numerical steel strains, #8 deformed bar, 10-inch diameter sample, dynamic loading .....	161
Figure 6-37 Comparison of empirical and numerical steel concrete, #8 deformed bar, 10-inch diameter sample, dynamic loading .....	162
Figure 6-38 Composite steel strains, #8 deformed bar, 10-inch diameter sample, impact loading.....	163
Figure 6-39 Composite concrete strains, #8 deformed bar, 10-inch diameter sample, impact loading.....	163
Figure 6-40 Comparison of empirical and numerical steel strains, #8 deformed bar, 10-inch diameter sample, impact loading .....	164
Figure 6-41 Comparison of empirical and numerical concrete strains, #8 deformed bar, 10-inch diameter sample, impact loading .....	164

## **PREFACE**

The U.S. Army Engineer Research and Development Center (ERDC), Geotechnical and Structures Laboratory (GSL), Vicksburg, MS, conducted this research project during 1997 through 2003. This final report details the results of that effort.

The research was conducted by Dr. John H. Weathersby, Survivability Engineering Branch, Geosciences and Structures Division, ERDC, under the general supervision of Dr. Reed Mosher, Technical Director; Ms. Pamela G. Kinnebrew, Chief, Survivability Engineering Branch; Dr. Robert L. Hall, Chief, Geosciences and Structures Division; and Dr. David W. Pittman, Acting Director, GSL. The POC at ERDC for this study was Dr. Weathersby, (601) 634-3228. The research was funded by the Laboratory Discretionary Research and Development Program, ERDC. This work was completed as a dissertation in partial fulfillment to satisfy requirements for the degree of Doctor of Philosophy from Louisiana State University, Baton Rouge.

At the time of publication of this report, Commander and Executive Director of ERDC was COL James R. Rowan, EN, and Dr. James R. Houston was Director.

## CONVERSION FACTORS, NON-SI TO SI UNITS OF MEASUREMENT

<b>Multiply</b>	<b>By</b>	<b>To Obtain</b>
degrees	0.01745329	radians
feet	0.3048	metres
gallon	3.79	liters
inches	25.4	millimetres
pounds (force)	4.448222	newtons
pounds (force) per square in.	0.006894757	megapascals
pounds (mass) per cubic foot	16.01846	kilograms per cubic metre

# CHAPTER 1 INTRODUCTION

## 1.1 Background

Structural failures during recent earthquakes and terrorist attacks have demonstrated shortcomings in the design procedures for reinforced concrete structures. Detailed first-principle analyses requiring High-Performance Computing (HPC) resources are capable of modeling the basic phenomenology that occurs during the events and has directed researchers to an understanding of the critical parameters controlling the nonlinear dynamic structural response of these structures.

The development of numerical procedures is needed to accurately predict the response of reinforced concrete structures subjected to earthquake and shock loadings. Research has been conducted to develop constitutive models for predicting the nonlinear response of concrete (Papados 1997; Prinaris and Papados 1996; and Malvar and Simons 1996). These concrete constitutive models have been validated with 1:6, 1:3, and full-scale experiments (Papados et al. 1995). These experiments have also demonstrated that one major limitation of the Finite Element (FE) modeling of the nonlinear response of reinforced concrete is the accurate modeling of the interaction of the concrete with the steel reinforcement (Prinaris et al. 1994 and Prinaris and Papados 1996).

Presently, there are insufficient data on the dynamic nonlinear interaction between the concrete material and the steel reinforcement to develop a numerical model of this interaction.



## 1.2 Objective

The primary objective of this study was to experimentally investigate the dynamic interaction (bond slip) of reinforcement with concrete to determine for static and dynamic loading conditions; a) the chemical adhesion between the smooth steel bars and concrete, b) the increase in pullout resistance of smooth and deformed bars and c) the influence of concrete confinement and bar diameter on pullout resistance. Additionally, the variation of tensile strain along the length of the steel bar, and the strain in the concrete surrounding the rebar will be investigated. A finite element analysis will be performed using the experimental parameters to determine the value of the chemical adhesion and the analytical results will be compared with the experimental values.

## 1.3 Methodology

A series of static and dynamic pullout tests was conducted. A single steel bar was cast in the center of a concrete matrix. The concrete specimens were sized so that three different failure modes could be investigated. These were radial cracking of the concrete, yielding of the deformed steel bar and pullout of the smooth steel bar. The steel reinforcing bar had two grooves 0.06-inches wide by 0.08-inches<sup>1</sup> deep machined along its sides. The grooves were 180° apart and ran the entire length of the bar. Micro-measurement EA-06-125BZ-350 with option W strain gages were mounted in the grooves at various locations along the length of the bar to measure the strain distribution along the bar. F & S, Inc., embeddable Extrinsic Fabry-Perot Interferometer (EFPI) fiber-optic strain gages were used to determine the normal component of the strain

---

<sup>1</sup> A table for converting non-SI units of measurement to SI units is presented on page xviii.

distribution in the concrete. These strain gages were embedded in a specially designed grout tubes that were placed in the concrete form prior to the placement of the concrete. The grout was designed to match the modulus of elasticity and the compressive strength of the concrete. The fiber optical signal was analyzed using an F & S FOSS I EFPI measurement system. The concrete used in this investigation was a 5,000-psi Conventional Strength Portland Cement (CSPC). This Waterways Experiment Station, (WES), designed mix has been extensively tested, and its static and dynamic properties are well documented. Both static and dynamic loads were generated using the WES 200-kip dynamic loader. This machine is capable of generating loads of up to 200,000 lb with rise times varying from 1 msec. to static loadings.

#### **1.4 Scope**

Thirty-three pullout tests were performed. The loading rates varied from static loadings to dynamic loadings, with rise times of approximately 5 msec in order to include the full spectrum of strain rates. Deformed #8 and #10 reinforcing bars and 1-inch smooth steel bars were tested. The smooth bars were used as a benchmark to determine the values of the adhesive and frictional forces. The #8 and #10 deformed bars were used to determine the effects of bar diameter on the failure mode. Concrete cylinder diameters of 10-inches and 20-inches were used to determine the effects of increased concrete confinement on these failures. A depth of embedment of 10-inches for all steel bars was maintained in all the tests.

A detailed Finite Element (FE) analysis of the dynamic interaction of the /concrete and steel reinforcement was conducted using the program DYNA3D. This analysis was conducted in two stages. First an analysis of the 1-inch smooth bars was conducted to

determine the values of the chemical adhesion between the cement and the steel bar under both dynamic and static loadings. Once these values were determined, a detailed fine grid analysis, which included modeling the individual deformations on the steel bar, was conducted. Using the information gained on the first part of the FE analysis, the effects of confinement and loading rates were investigated for the deformed bars.

## **CHAPTER 2 LITERATURE REVIEW**

Although extensive research has been directed towards static bond slip, with literally thousands of pullout tests performed on both smooth and deformed bars, relatively little work has been performed in the dynamic arena. Most of the static work was performed with the goal of determining the optimum deformation patterns and to quantitatively determine the embedment length required to develop the full strength of the bar.

### **2.1 Static and Dynamic Bond-Slip Experiments**

Menzel, 1939, conducted a series of tests to investigate the effects of surface condition on smooth and deformed bar pull out. He also investigated the effects of cement ratio, embedment length and position of the bar relative to placement direction of the concrete. He found that the surface condition of the smooth bars had a very marked effect on the pull out resistance. A polished bar had only about  $\frac{1}{4}$  the pull out resistance of a hot rolled smooth bar. A 1-inch diameter hot rolled bar with an embedment length of 30-inches produced a pull out resistance of 41,000 psi (based on the diameter of the bar). This yielded an average bond stress of 342 psi. A 1-inch diameter deformed bar with an embedment length of 20-inches produced a pull out resistance of 67,000 psi (based on the diameter of the bar). This yielded an average bond stress of 840 psi. Menzel also concluded that increased cement ratio or increased embedment resulted in increased pull out resistance.

Furguson and Thompson, 1962, conducted a set of experiments to determine the development length of high strength reinforcement in beam elements. Variables included bar size (#3, #7 and #11) with and without stirrups, and with varying beam dimensions.

It was determined that bond was a function of development length, and not bar size. Ultimate bond stress varied as  $\sqrt{f_c}$ . Bar cover and beam width were also important factors.

Ferguson and Thompson, 1965, carried out a study on the development length of large (#11 and #18) deformed bars. In the investigation, bar cover, beam width, stirrup ratio, development length and depth of concrete cast below the bar were the primary variables. They found that as in the previous work, increased embedment length lead to decreased bond stresses. Also crack growth in the concrete tended to be more severe for the larger bars than it was for the smaller bars. Finally, increased cover increased the bond resistance, but was not helpful in reducing surface crack width.

McDermott, 1969, prepared a report for ACI Committee 439 that investigated the effect of steel strength and of reinforcement ratio on the mode of failure and the strain energy capacity of reinforced concrete beams. The committee concluded that within the ductile range, the yield strength of the steel bars had no effect on the strain energy of beams of equal static bending strength that were subjected to moderate strain rates. Therefore the resistance to blast or other dynamic loads of beams reinforced with 60,000 psi or 70,000 psi bars would be as ductile as those containing 40,000 psi bars.

ACI Committee 408 investigated the effects that cyclic loading had on the concrete-steel bond. In their report (Mitchell, et al., 1992), they stated that the average bond stress for deformed bars ranged from 1500 psi to 3000 psi but that design requirements and development length requirements usually limited this to 350 psi. They also stated that bond forces were a combination of three components. These were the chemical adhesion between the cement and the steel, which was a function of the shear strength of the

concrete, the mechanical interlocking of the steel deformations and the concrete, and the friction between the concrete and the steel.

An in-depth study of bond slip under impact loading for plain, polypropylene fiber reinforced and steel reinforced concrete was performed (Yan 1992). Dynamic loads were generated using a 345-kg mass drop weight impact machine. The experiments consisted of both pullout and push-in tests. For both types of tests, the experimental work was carried out for three different types of loading: static, dynamic, and impact loading, which covered a stress rate ranging from  $0.5 \times 10^{-8}$  to  $0.5 \times 10^{-2}$  Mpa/s. The other important variables considered in the experimental study were: two different types of reinforcing bars (smooth and deformed), two different concrete compressive strengths (normal and high), two different fibers (polypropylene and steel), different fiber contents (0.1 %, 0.5 %, and 1.0 % by volume), and surface conditions (epoxy coated and uncoated). The load applied to the rebar and the strains along the rebar were measured directly. The axial force in the concrete was determined from the difference between two consecutive strain readings in the steel bar, and the normal force in the concrete was calculated based on a static equilibrium analysis.

It was found that for smooth rebar, there existed a linear bond-slip relationship under both static and high-rate loading. Different loading rates, compressive strengths, types of fibers, and fiber contents were found to have no significant effect on the bond-slip relationship.

For deformed bars, the shear mechanism due to the ribs bearing on the concrete was found to play a major role in the bond resistance. The bond stress-slip relationship under a dynamic loading changes with time and is different at different points along the

reinforcing bar. In terms of the average bond stress-slip relationship over the time period and the embedment length, different loading rates, compressive strengths, types of fibers, and fiber contents were found to have a great influence on this relationship. Higher loading rates, higher compressive strengths, and steel fibers at a sufficient content significantly increased the bond-resistance capacity and the fracture energy in bond failure. All of these factors had a great influence on the stress distributions in the concrete, the slips at the interface between the rebar and the concrete, and the crack development. It was also found that there is always higher bond resistance for push-in loading than for pullout loading.

In the analytical study, FE analysis with fracture mechanics was carried out to investigate the bond phenomenon under high rate loading. The analytical model took into account the chemical adhesion, the frictional resistance, and the rib-bearing mechanism. In the analysis, solid isoperimetric elements with 20 nodes and 60 degrees of freedom were employed for the rebar and concrete before cracking. After cracking, the concrete elements were replaced by quadratic singularity elements, which were quarter-point elements able to model curved crack fronts. A special interface element, the “bond-link element,” was adopted to model the connection between the reinforcing bar and concrete. It connected two nodes and had no physical thickness, therefore it could be thought of conceptually as consisting of two orthogonal springs, which simulated the mechanical properties in the connection, i.e. they transmitted the shear and normal forces between two nodes

A set of dynamic experiments with the goal of quantitatively defining the bond-stress relationship for inclusion in FE analyses was performed (Vos 1983). Vos used a Split

Hopkinson Bar test device to load his samples. In this work, only one bar diameter (10 mm) and one embedment length ( $3d = 30$  mm) were used. Three different concrete strengths (22, 45, and  $55 \text{ N/mm}^2$ ) were tested. Additionally, three types of steel reinforcement (plain, deformed, and strands) were used. Vos reached conclusions similar to those reached by Yan; namely, that the bond resistance of plain bars is independent of loading rate and concrete strength. The deformed bar on the other hand showed a marked increase in bond resistance with an increase in either loading rate or concrete strength.

## **2.2 Strain Rate Effects on Concrete**

Bentur et al. 1986 and Banthia et al. 1988 conducted a series of experiments to investigate the behavior of concrete under impact loading. Their work involved the testing and analysis of both plain and conventionally reinforced beams subjected to impact loads. The test specimens had a length by width by depth of 1,400 by 100 by 125 mm and a span length of 960 mm. The dynamic loads were generated by a drop weight machine, which had the capability of dropping a 345-kg mass from a height of 3 m. From these tests, it was determined that concrete can withstand a higher peak bending load under impact than under static conditions. They concluded that concrete is a significantly stress-rate dependent material that is stronger and more energy absorbing under impact than static loading. Moreover, in the beams made with deformed bars, the reinforcing bars frequently failed in a ductile mode of failure at the point of impact. This, they concluded, was due to the fact that under impact loading, with the maximum load being reached in less than 1 msec, there was not enough time for extensive bond slip to occur along the length of the bar. Instead, the steel deformation was confined primarily to the region, only a few centimeters long, beneath the point of impact, exceeding the



strain capability of the steel in this region. This was clearly related to strain rate; under quasi-static loading, beams deflected to the same degree showed no evidence of steel failure; instead, there were signs of cracking and de-bonding along a significant length of the reinforcing bar.

### **2.3 Cracking of Concrete Around Deformed Bars**

A set of experiments was performed to study the formation of cracks in concrete surrounding a deformed reinforcing bar (Goto 1971). In these tests, a single deformed reinforcing bar was encased in a long concrete prism, and an axial tension load was applied to the exposed end of the bar. Ink was injected into the concrete to mark the cracks, and the specimens were split longitudinally along the bar. The crack patterns were then analyzed and recorded. Goto reported three different types of cracks: lateral, internal and longitudinal. Lateral cracks are visible at the concrete surface and are at right angles to the bar axis. Internal cracks form around the deformed bars shortly after the formation of the lateral cracks. These small cracks do not appear at the concrete surface. Longitudinal cracks are formed at high steel-stress levels. In this case, the concrete adjacent to existing lateral cracks also cracks in the direction of the bar axis.

A series of pullout tests were performed to determine the effect the depth of cover had on the bond stress and to determine the bond stress at different levels of concrete cracking (Tepfers 1979). In these tests, a single reinforcing bar was cast eccentrically in a concrete prism. The specimens were 200 mm by 150 mm with a depth of 3.13 bar diameters. The bars were placed at distances varying from 16 mm to over 90 mm from the edge of the sample. Equations were developed expressing the bond stress at three different stages based on the crack condition of the concrete cover. These were the

un-cracked elastic stage, the plastic stage, and the partly cracked elastic stage. In the un-cracked elastic stage, the bond force or stresses can be divided into radial and tangential components. If the tangential bond stress is considered for an element,  $dx$ , of the reinforcing bar, the tangential bond stress can be expressed as the change in stress in the reinforcement over the length,  $dx$  (equation 2.1),

$$\tau = \frac{A_s}{\pi d} \frac{d\sigma_s}{dx} = \frac{d}{4} \frac{d\sigma_s}{dx} \quad (2.1)$$

Where:

$\tau$  = bond stress

$A_s$  = area of reinforcement

$D$  = diameter of reinforcing bar

$\sigma_s$  = stress in reinforcement

$\alpha$  = angle between the principle compressive bond stress and the axis of the reinforcing bar.

When the load is first applied, the properties of concrete in tension and compression are equal, and the angle,  $\alpha$ , is therefore  $45^\circ$ . The magnitudes of the principal stresses are the same. This will remain so until the principal tensile stress,  $\alpha_t$ , reaches the ultimate tensile strength for the concrete,  $f_{ct}$ , and then becomes zero. At this moment, the angle,  $\alpha$ , may change, and the radial stress,  $\sigma_r$ , develop. The radial bond component  $\sigma_r$  is (equation 2.2)

$$\sigma_r = -\sigma_2 \sin^2 \alpha = \tau \tan \alpha \quad (2.2)$$

Where:

$\sigma_2$  = principle compressive bond stress.

$\sigma_r$  = radial bond stress

The radial stress,  $\sigma_r$ , due to bond action on the concrete can be regarded as a hydraulic pressure acting on a thick-walled concrete ring. The concrete ring approximates the effect of the surrounding concrete. Timosenko, (Popov 1976) gives a solution for the stresses in a thick-walled cylinder that is subject to internal pressure. For a cylinder subjected to internal pressure, the tangential stress, equation 2.3 is

$$\sigma_t = \frac{(d/2)^2 \tau \tan \alpha}{(c_y + d/2)^2 - (d/2)^2} \left[ 1 + \frac{(c_y + d/2)^2}{r^2} \right] \quad (2.3)$$

Where:

$r$  = radius

$\sigma_t$  = tangential ring stress

$c_y$  = thickness of vertical concrete cover.

The stress,  $\sigma_t$ , equations 2.4 and 2.5, is always tensile and has a maximum at the inner surface of the cylinder

$$(\sigma_t)_{\max} = \tau \tan \alpha \frac{(c_y + d/2)^2 + (d/2)^2}{(c_y + d/2)^2 - (d/2)^2} \quad (2.4)$$

$$f_{cbc} = f_{ct} \frac{(c_y + d/2)^2 - (d/2)^2}{(c_y d/2)^2 + (d/2)^2} \quad (2.5)$$

Where

$f_{cbc}$  = bond stress when the concrete cover cracks

$f_{ct}$  = tensile strength of the concrete.

This equation shows that  $(\sigma_t)_{max}$  is always numerically greater than the internal pressure, and approaches this quantity as the concrete cover,  $c_y$ , increases. Failure occurs when  $(\tau_t)_{max} = f_{ct}$ .

If the concrete behaves in a perfectly elastic manner, the ultimate load for the initiation of longitudinal cracks occurs when the maximum tensile stress in the concrete cover,  $(\sigma_t)_{max}$ , exceeds the ultimate tensile strength of the concrete,  $f_{ct}$ .

The bond action in the plastic stage is analyzed on the same concrete ring model as in the elastic stage. The plastic stage represents the highest possible bond resistance for the model at the instant the longitudinal cover crack appears. The radial bond-stress component,  $\sigma_r$ , can be regarded as a hydraulic pressure on the inner surface of a thick-walled concrete cylinder surrounding the steel bar. The concrete is assumed to act plastically; that is, the cylinder will not break until the stress in the tangential direction at every part of the cylinder has reached the ultimate tensile concrete strength,  $f_{ct}$ . The tangential stress in the cylinder can be expressed by equation 2.6.

$$\sigma_t = \frac{d}{2c_y} \tau \tan \alpha \quad (2.6)$$

The concrete cylinder breaks and the longitudinal crack appears when  $\sigma_t$  exceeds the ultimate tensile strength for the concrete,  $f_{ct}$ . If we set  $\alpha = 45^\circ$ , we get the bond stress, equation 2.7, when the cover cracks as

$$f_{cbc} = f_{ct} \frac{2c_y}{d} \quad (2.7)$$

In the elastic stage, the ultimate load on the concrete ring around the reinforcing bar is reached very quickly because of the high tensile-stress peak in the concrete near the bar. If the plastic behavior of the concrete is disregarded and it is assumed that the concrete is

a completely elastic material, an internal crack will start when the peak tensile stress exceeds the ultimate tensile stress of the concrete. The longitudinal crack starting at this point will not penetrate through the concrete cover if the load-carrying capacity of the concrete ring has not yet been reached at that moment.

Consider a concrete ring loaded internally and radially by the radial bond-stress components from a reinforcing bar. The ring has internal cracks where the circumferential stresses have reached the ultimate tensile concrete stress. The bond force is now transferred through the concrete teeth between the internal cracks to the un-cracked part of the ring. The inner area of this ring is larger than that of the ring without internal cracks. The pressure from the reinforcing bar on the inner area of the internally cracked ring must be reduced in comparison with the pressure on the inner surface of the un-cracked ring. The change in inner pressure is (equations 2.8 and 2.9)

$$p_1 \pi d = p_2 \pi 2e \quad (2.8)$$

with  $p_1 = \sigma_r = \tau \alpha$  introduced

$$p_2 = (d / 2e) \tau \tan \alpha \quad (2.9)$$

Where:

$p_1$  = internal pressure in the ring of radial component of the bond force

$p_2$  = internal pressure on the ring perimeter corresponding to the depth of internal cracks

$e$  = radius of the perimeter corresponding to the depth of internal crack.

The circumferential stress distribution in the un-cracked part of the concrete ring of inner radius,  $e$ , can be written as shown in equation 2.10.

$$\sigma_t = \frac{e^2(d/2e)\tau \tan \alpha}{(c_y + d/2)^2 - e^2} \left[ 1 + \frac{(c_y + d/2)^2}{r^2} \right] \quad (2.10)$$

and the maximum stress at the inner surface of the untracked part of the cylinder of radius,  $e$ , is given by equation 2.11.

$$(\sigma_t)_{\max} = \frac{d}{2e} \tau \tan \alpha \frac{(c_y + d/2)^2 + e^2}{(c_y + d/2)^2 - e^2} \quad (2.11)$$

## 2.4 Finite-Element Analysis of Bond Slip

Numerous attempts have been made to model the steel concrete interface using FE's; in fact, several of the large FE codes have routines that were written to specifically handle this problem. For instance, DYNA-3D has a one-dimensional slide line, which was intended for use in modeling bond slip. In this model, the slave node of a string of beam elements, modeling the rebar, is forced to slide along a master line of nodes embedded in the solid mesh which models the concrete matrix. This kinematic constraint is applied using a penalty function approach; fictitious springs are inserted between slave nodes and their projections over the master lines. These springs produce internal forces normal to the rebar and proportional to the distance between slave nodes and master lines.

Axial bond forces, which develop when the rebar is pulled from the concrete, depend on the relative axial displacements (slippage) between rebar nodes and corresponding locations along the concrete master line. Two models are available to calculate bond forces from relative displacements.

In the first model, the shear force,  $F$ , varies linearly with the relative displacement,  $d$ , up to a maximum value,  $F_{max}$ , and remains constant thereafter, except for elastic unloading.  $F_{max}$  is evaluated by equation 2.12.

$$F_{max} = K u_{max}, \quad (2.12)$$

Where:

$K = 2\pi R_e G_s$  is the elastic stiffness of the bond per unit length of rebar

$R_e$  = radius of the rebar

$G_s$  = bond shear modulus

$u_{max}$  = maximum elastic slippage

This perfectly elasto-plastic relationship can be expressed by equation 2.13.

$$F_{n+1} = F_n + K \Delta d, \quad F_{n+1} = \min (F_{n+1}, F_{max}), \quad F_{n+1} = \max (F_{n+1}, -F_{max}) \quad (2.13)$$

Where:

$F_{n+1}$  is the bond force at the end of the step

$\Delta d$  = slippage increment during the step

This equation implies that the bond can maintain its maximum strength regardless of how much slippage takes place. However, previous test data show that the bond strength decreases due to cracking in the concrete surrounding the rebar. This effect can be taken into account by redefining the maximum bond force as a function of a suitable damage parameter. The following expression, equation 2.14, for  $F_{max}$  was adopted:

$$F_{max} = K u_{max} (\xi + (1 - \xi) e^{-HD}) \quad (2.14)$$

where the damage parameter,  $D$ , is defined as the sum of the absolute values of the plastic displacement increments,  $\Delta d_p$  equation 2.15.

$$D_{n+1} = D_n + |\Delta d_p| \quad (2.15)$$

and  $H$  is a decay parameter obtained from test datum, and  $\xi$  is the fraction of residual strength after the bond is completely degraded.

The second model type was introduced to eliminate the corner that appears at the largest value of  $F$ . Experimental pullout curves show a smooth transition from the hardening part to the softening part as shown below. This was achieved by redefining the end of step bond force as given by equation 2.16:

$$F_{n+1} = F_n (F_{max} - F_n) e^{-\Delta d / u_{max}} \quad (2.16)$$

Here too,  $F_{max}$  can be calculated as a function of the damage parameter,  $D$ .

Vervuurt, et al., 1993 and Vervuurt and Van Mier, 1995, devised a lattice approach for analyzing the steel-concrete bond-slip layer. In this approach, the steel-concrete interface fracture was modeled at the meso level. Vervuurt proposed that at this level, a simple linear-elastic fracture law seems to be sufficient to explain global fracture mechanisms of composite materials. Interfaces between the concrete matrix and the reinforcing bars were simulated using a lattice model. In this model, the material is discretized as a lattice of brittle breaking beam elements. Disorder of the material was implemented by assigning different strength and stiffness properties to the beam elements. Cracking was simulated by removing, in each time step, the element with the greatest stress-over-strength ratio. Vervuurt reported that comparisons between the simulations presented in his paper and experimental data show that the bond-displacement behavior was still too brittle.

Filippou and Taucer, 1996, developed a fibre beam-column element for the non-linear static and dynamic analysis of reinforced concrete frames. This model looked at reinforced concrete at the macro level. The algorithm proved accurate and stable even in



the presence of strength loss, thereby making it capable of modeling the highly non-linear behavior of reinforced concrete members under dynamic loading.

## **CHAPTER 3 EXPERIMENTAL PROCEDURES**

A series of thirty-three dynamic and quasi-static experiments were conducted to experimentally evaluate the effects that confinement, bar diameter, bar deformation and loading rate had on the interaction of steel reinforcement and a concrete matrix.

### **3.1 Material Properties**

The static and dynamic properties of the concrete and steel bars used in this investigation were determined in order to provide material properties for the finite element analysis.

#### **3.1.1 Concrete Properties**

The concrete selected for the experiment was a WES developed mix referred to as Conventional Strength Portland Cement (CSPC). This mix was selected because its static and dynamic properties are well documented and it is representative of the types of concrete used in conventional construction. CSPC has a design compressive strength of 5,600 psi, direct tensile strength of 520 psi and a modulus of elasticity in compression ( $E_c$ ) of  $6.1 \times 10^6$  psi. The mix design is shown in Table 3.1. The static and dynamic properties of CSPC and its development are documented (Nealy, 1991).

Quality control specimens taken from the batches used in casting the test specimens indicated that the actual compressive strength of the concrete was greater than the design strength. The static compressive strength was 7,650 psi with a modulus of elasticity of  $6.45 \times 10^6$  psi. The compressive strength decreased to 7,250 psi but the modulus of elasticity increased to  $6.95 \times 10^6$  psi as the loading rate was increased to 200 msec.

When the loading rate was further increased to 5 msec, the compressive strength returned

**Table 3.1 CSPC mix design**

Item	Mixture Proportions Saturated Surface-Dry lb/yd <sup>3</sup>
Type II portland cement	553
3/8-in limestone coarse aggregate	1,743
Limestone fine aggregate	1359
Water	315
WRA	44
Air-entraining agent	0.55
w/c	0.57

to near the static value at 7,633 psi, but the modulus of elasticity was half way between the static value and the 200 msec value at  $6.73 \times 10^6$  psi. The stress-strain curves and the concrete cylinder test data are shown in Appendix A.

### 3.1.2 Steel Properties

The steel used in the experiment was a grade 60 #8 or #10 concrete reinforcing bar, for the deformed bars, and 1-inch diameter hot rolled, grade 60 for the smooth bars. The #8 bars had static yield strength of 65,950 psi with a corresponding modulus of elasticity (E) in tension of  $3.1 \times 10^6$ . The yield strength increased to 74,700 psi when the specimen was loaded in 500 msec. The modulus of elasticity, which is not rate dependent for steel, remained constant. The #10 bars had a static yield strength of 71,100 psi with a corresponding modulus of elasticity (E) in tension of  $3.0 \times 10^6$ . The yield strength increased to 73,550 psi when the specimen was loaded in 500 msec. The smooth bars had a static yield strength of 91,200 psi and (E) of  $30.2 \times 10^6$  psi. The yield strength decreased to 85,050 psi when the specimen was loaded in 500 msec. For the yield strength to decrease with increased strain rate is very unusual. Since there was only one

statically loaded specimen, it is difficult to determine if this is an actual phenomena, or experimental error. However, since the smooth bars fail at a stress well below the yield stress, it is not important for this investigation Both the static and dynamic stress strain curves for the steel bars is shown in Appendix A.

### **3.2 Test Specimens**

Thirty-three test specimens were prepared and tested. These specimens were dimensioned so that several failure modes would be bracketed during the investigation. The specimens were instrumented with a combination of fiber optical and conventional foil strain gages. The strain gages were used to determine the distribution of strain along the length of the steel bars, and the strain in the concrete normal to the axis of the steel bars.

#### **3.2.1 Sample Dimensions**

A series of pullout tests were conducted to determine the most practical physical dimensions to be used in the experiment. It was desired to have as large of strains in the concrete as possible and to have the predominant failure mechanism being radial cracking of the concrete, and not yielding of the steel bar. The ACI code required a development length of 28-inches for a #8 bar. Since the codes are conservative, and previous research has indicated that full development might be obtained in only half this length, an embedment lengths of 10-inches and 14-were used. Concrete confinements of 5-inches, 10-inches and 15-inches were tested. The specimens with 5-inches and 10-inches of confinement and 10-inches embedment length failed due to radial cracking of the concrete while the specimen containing the 15-inches of confinement or embedment

lengths of 14-inches failed due to yielding of the steel bar. Since it was desirable to investigate the interaction bond slip through a wide range of concrete and steel strains, various failure modes, an embedment length of 10-inches was selected for use in all tests. Depths of cover of 4-1/2-inches and 9-1/2 inches were chosen. “Sono-tubes” of 10 and 20-inch diameters were used as forms for casting the samples with the reinforcing bar placed in the center and parallel with the axis of the tube.

### 3.2.2 Strain Measurements in Steel

The strain measurements in the steel were made with Micro-Measurements (MM) EA-06-125BZ-350 with option W foil strain gages, Figure 3-1. These gages are 0.04-inches wide and 0.06-inches long. They were mounted in a groove 0.06-inches wide and approximately 0.04-inches deep machined along the longitudinal rib on both sides of the reinforcing bar (Figure 3-2). The gages were located on the  $0^0$  and  $180^0$  azimuths beginning 1-inch from the bottom of the specimen and located every 2-inches thereafter. The gages were labeled SS-## where SS stood for steel strain and ## was a number from 01 to 10 beginning at the bottom and numbered consecutively to the top with the odd numbers on the  $0^0$  azimuth and the even numbers on the  $180^0$  azimuth (Figure 3-3). After epoxying the gages to the bottom of this groove, the lead wires were placed in the groove and both the lead wire and gage were covered with MM Gage Coat 5 protective coating. The lead wires were run out the top of the sample (Figure 3-4).

### 3.2.3 Strain Measurements in Concrete

One of the major problems encountered during this investigation, was how to make accurate, location specific strain measurements in concrete. There are several

commercially available concrete strain gages on the market; however, none were suitable for this investigation. These gages ranged in size from 4 to 9 inches in length and were designed to measure the average strain over that length. Since the concrete strain that

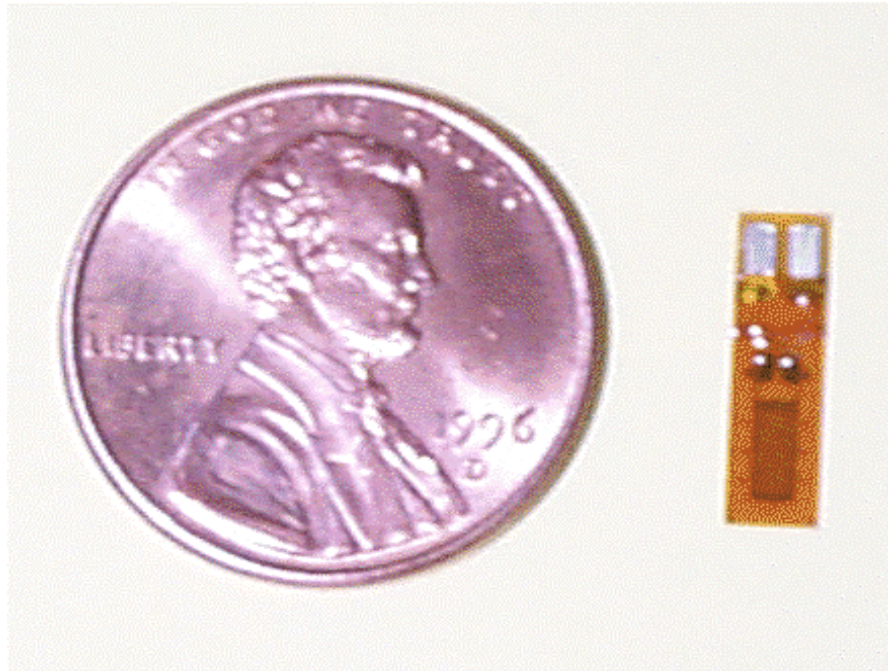


**Figure 3-1 Micro-Measurements foil strain gage**



**Figure 3-2 Steel bar prior to placement of strain gages**



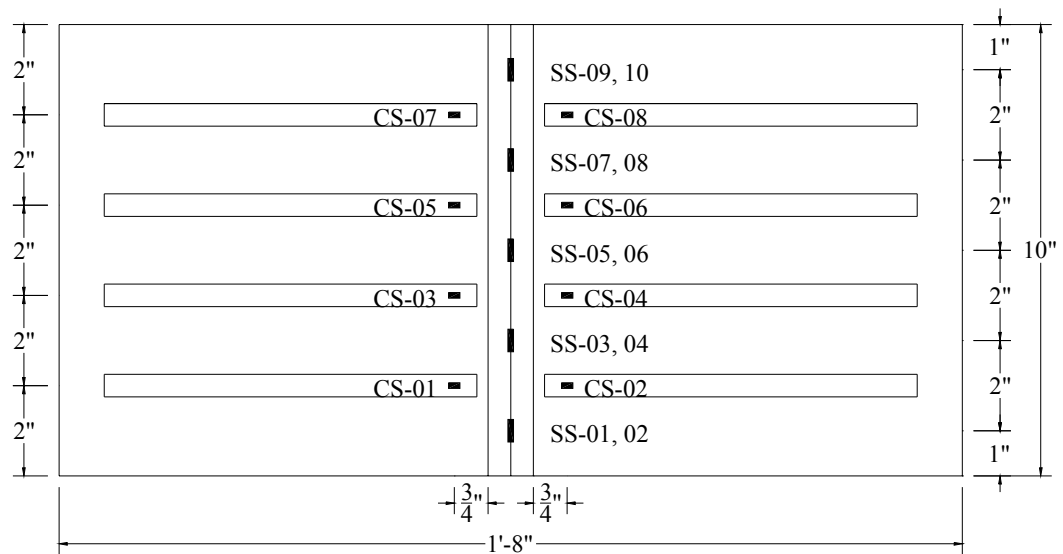


**Figure 3-3 Test specimen and strain gage locations**



**Figure 3-4 Attaching instrumentation cables to the ends of the strain gage lead wires**

was of the most interest was the strain normal to the rebar, and this strain varies according to the distance from the rebar, a gage that measured a direction specific strain over a very short distance was required. A search of the different technologies available indicated that the new fiber-optic strain gages showed the most promise. Of these gages, the extrinsic Fabry-Perot interferometric (EFPI) fiber optic strain gage made by Fiber and Sensor Technologies (F&S), Inc. was selected for this work. The EFPI strain gage (Figure 3-5) is fabricated by inserting two optical fibers into a silica capillary tube. The EFPI is a reflective-type fiber optic sensor meaning that the same optical fiber serves as both input and output to the strain gage element. During fabrication, the input/output and reflector optical fibers are fused to the inside of the silica capillary tube. The distance between the input/output and reflector attachment points in the silica Capillary tube is the gage length or gage factor (Figure 3-6).

The standard EFPI strain gage is covered by a thin polyimide coating similar to the coatings used in foil strain gages. The polyimide increases the strength of the gage and provides a very good stress/strain transfer interface between the silica of the sensor and the host material.

Operation of the EFPI revolves around the air gap, which is the distance between the input/output optical fiber and the reflector. The EFPI is operated by the Fiber Optic Support System FOSS I which provides a voltage signal proportional to the “raw” interferometric optical signal returned from the EFPI strain sensor. The output of the FOSS I is a periodic (sinusoidal) function of changes in the distance between the two optical fibers in the EFPI (air gap or sensor gap). The period of this function is  $\frac{1}{2}$  of the





**Figure 3-5 Fiber-Optic Strain gage**

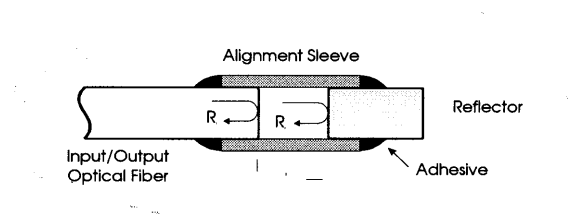


**Figure 3-6 Drawing of the silica capillary tube containing the input/output and reflector fibers**

source wavelength of 1310 nanometers, or 655 nanometers. The FOSSI is a differential strain measurement system, and only measures changes in the gap separation of the EFPI. Consequently, if the FOSSI is connected to an EFPI strain sensor that is not being dynamically strained, a flat line will be outputted from the FOSSI. When the EFPI strain sensor is strained, each time the gap displacement changes by 650 nanometers, an entire

fringe will be outputted. Relative strain is then calculated by dividing the changes in gap distance by the gage factor, or gage length, of the EFPI sensor.

To convert the FOSS I output into strain, the number of fringes and the gage length (gage factor) are used. Each period of a fringe (one total period of the sinusoidal output) indicates that the sensor gap (air gap) displacement has changed length corresponding to  $\frac{1}{2}$  the wavelength of the laser in the FOSS I, which is 1310 nm. As a result, each fringe means that the gap has changed 655 nm. To calculate strain, the change in sensor gap displacement must be divided by the gage length of the sensor as shown in equation 3.1.

$$strain(\text{microstrain}) = \frac{\#ofFringes * .655(\text{micrometers})}{gageFactor(\text{mil lim eters})} * 1000 \quad (3.1)$$

Due to the physical properties of the FOSS I sensing system, the fringe contrast of the sensor output is a dynamic quantity. Fringe contrast is the amplitude of the sinusoidal varying output from the FOSS I system. As the distance between the fiber ends in the sensor increase, the amplitude of the sinusoidal output signal is attenuated. This consideration is important when counting partial fringes, due to the non-linearity of the sensor output vs. strain relationship. Figure 3-7 shows an attenuated FOSS I output. Equation 3.2 provides the needed relationship for the re-normalization of  $x_0$  between the values of  $-1$  and  $+1$ .

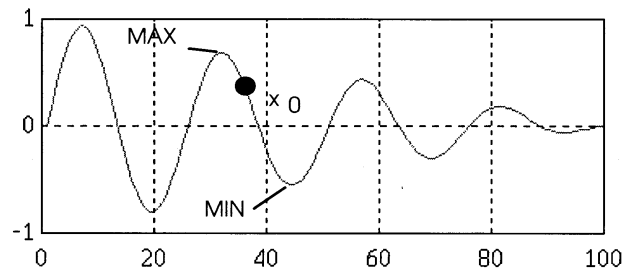


**Figure 3-7 Attenuated FOSS I output**

$$x'_0 = 2 * \frac{x_0 - MIN}{MAX - MIN} - 1 \quad (3.2)$$

In the normalized format, -1 corresponds to the bottom of a fringe and +1 corresponds to the top of a fringe. To calculate partial fringes equation 3.3 and equation 3.4 can be used with the data point  $x_0$  as shown Figure 3-8. If the value of the data point is negative, the absolute value of the number is used.  $\Delta F$  is the partial fringe.  $\Delta F = 1$  corresponds to a full period of the fringe.

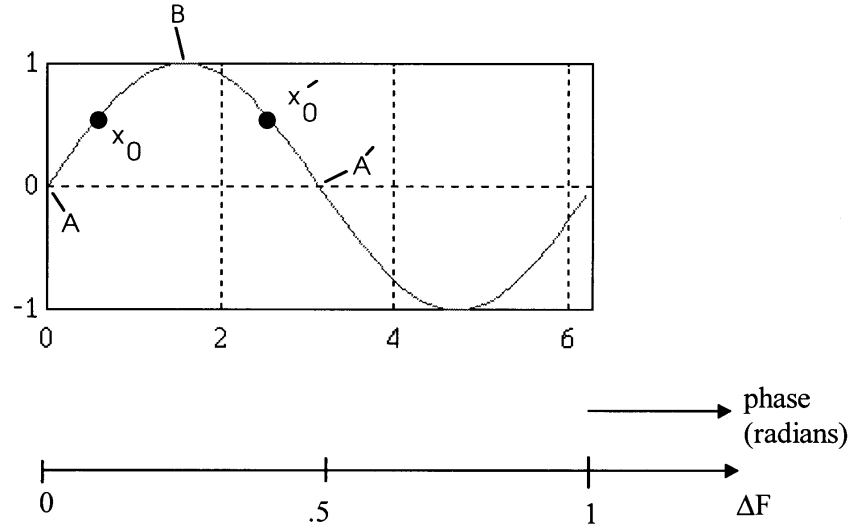


**Figure 3-8 Equations for calculating partial fringes**

$$\Delta F(x_0 \rightarrow B) = \Delta F(B \rightarrow x'_0) = \frac{\frac{\pi}{2} - \sin^{-1}(x_0)}{2\pi} \quad (3.3)$$

$$\Delta F(a \rightarrow x_0) = \Delta F(x'_0 \rightarrow A) = \frac{\sin^{-1}(x_0)}{2\pi} \quad (3.4)$$

Very important in reducing the output from the FOSS I is the detection of changes in strain direction (compressive to tension and vice versa). A typical change in strain direction is shown in Figure 3-9.

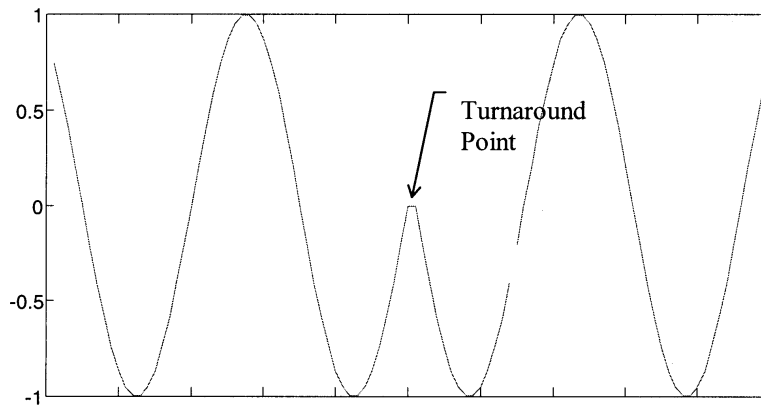


**Figure 3-9 A typical change in strain direction**

As a backup to the experimental fiber optic strain gages, conventional foil strain gages were also used to measure concrete strains. These gages were attached to the outside of the grout tubes containing the fiber optic gages.

The concrete strains were labeled either FO-## or CS-##, where FO stood for Fiber Optic concrete strain and CS for Concrete Strain and ## was a number from 01 to 08. The gages were located on the  $90^{\circ}$   $270^{\circ}$  azimuth and began 2-inches from the bottom of the sample and were located every 2-inches there after. The odd numbers were located on the  $90^{\circ}$  azimuth and the even numbers were located on the  $270^{\circ}$  azimuth (Figure 3-3)

#### 3.2.4 Final Specimen Preparation

The test specimens were prepared in the following manner: First, the steel bar was cut to length 16- inches, two grooves were machined along the side as described in section 3.2.1, and a threaded connector was welded to the end of the rebar with fillet welds above and below the connector. This connector was a metal pipe 1-1/2-inches long with an outside diameter of 2-inches and an inside diameter equal to the diameter of the steel bar.

Next grout tubes containing the fiber optic gages were built. These tubes consisted of a form made out of  $\frac{3}{4}$  inch PVC pipe. The pipe was cut to a length of 10-inches for test 1, 14-inches for test 2, and 6-inches for all remaining tests. The tubes were shortened because the protruding grout tubes were difficult to install in the formwork and were easily damaged (Figure 3-10). Once the tubes were cut to length, they were split longitudinally with a band saw. A small groove was then cut about 0.04-inches from the end and a piece of monofilament fishing line stretched across the tube and taped down using Polyken<sup>®</sup> fabric tape. Thin pieces of this same tape were then placed in the middle of the tube and then at the other end of the tube. The EFPI gage had a fiber that was approximately 1-1/2-inches long, and attached to the far end of the silica capillary tube. This fiber was shortened to approximately 0.04-inches and the EFPI was then placed in the PVC pipe. The fiber extension was then attached to the monofilament line using Micro Measurements M-Bond 200<sup>®</sup> Adhesive, and the gage cable was taped in place in two locations along the length of the tube, Figure 3-11. The two halves of the PVC pipe were then reassembled, and taped together. Tape was also used to seal the end of the tube and the two seams. The tube was then placed in a rack and the rack placed on a shaker table and a specially prepared grout poured into the tubes (Figure 3-12). Once the tubes were filled, and as much air removed as possible, the exterior of the tubes were washed off, and the tubes were allowed to cure for four days (Figure 3-13). At this time, the tape was removed from the tubes, and the two halves of the PVC pipe were separated and the grout tube containing the EFPI gage was removed.



**Figure 3-10 Long grout tubes damaged after testing**

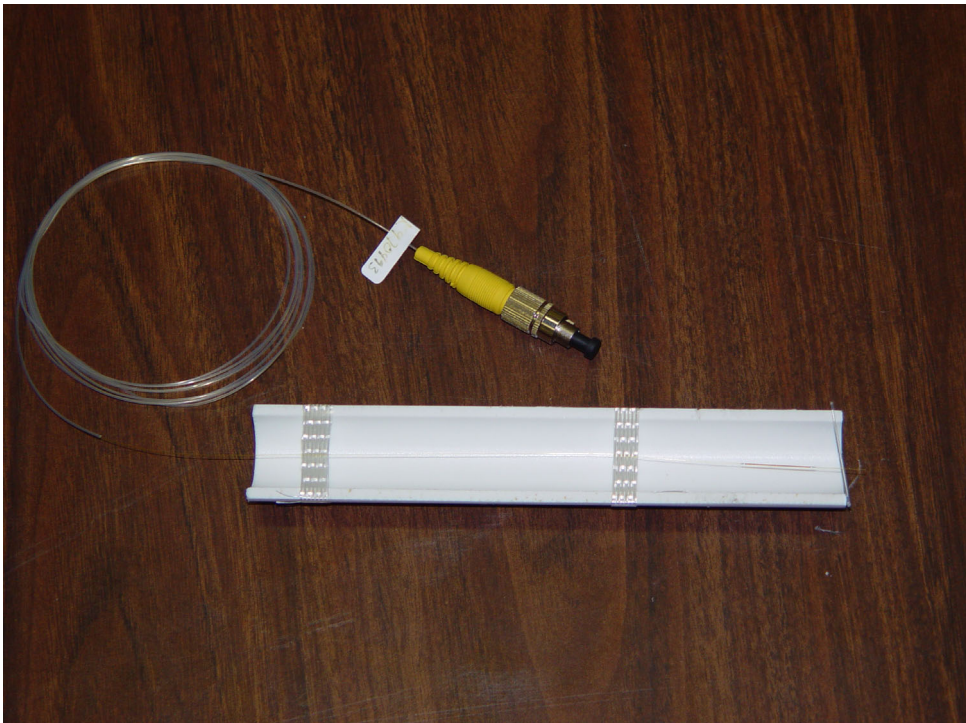


**Figure 3-11 Placing the fiber-optic gage inside the grout tube form**





**Figure 3-12 placing grout in the tubes**



**Figure 3-13 Grout tubes containing fiber-optic strain gages curing in racks**

To build the concrete forms, sono tubes were cut to a length of 15-1/4-inches and two donuts were cut from 3/4-inch plywood. The outside of the donuts was the inside diameter of the *sono-tube*. The inside diameter of one of the donuts was 2-inches (the diameter of the threaded connectors) and the inside diameter of the other was the diameter of the rebar. The latter was cut in half, and then refastened using two cleats to facilitate form removal prior to testing (Figure 3-14). Spacer blocks that were 3-3/4-inches thick separated the two donuts (Figure 3-15). The rebar was placed in the center of the two donuts and the donuts placed inside the sono tube (Figure 3-16 and Figure 3-17).

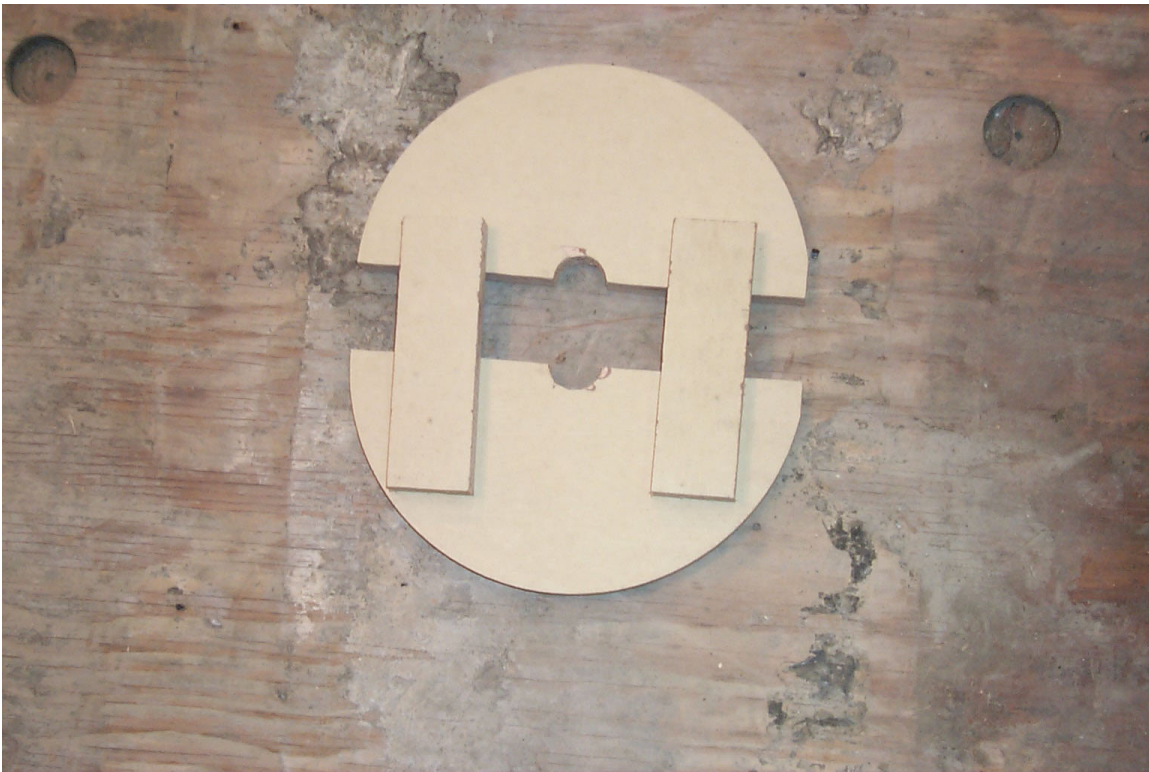


**Figure 3-14 Bottom of plywood form cut in half to facilitate form removal**



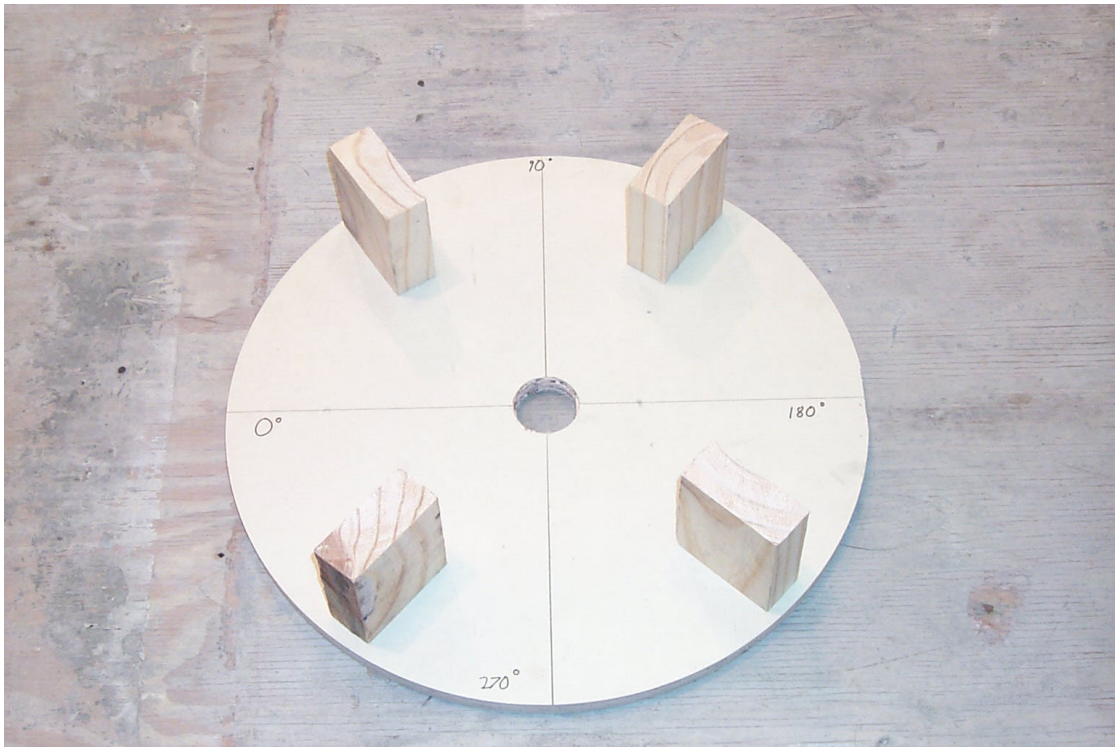


**Figure 3-15 First plywood donut and spacer blocks in place**

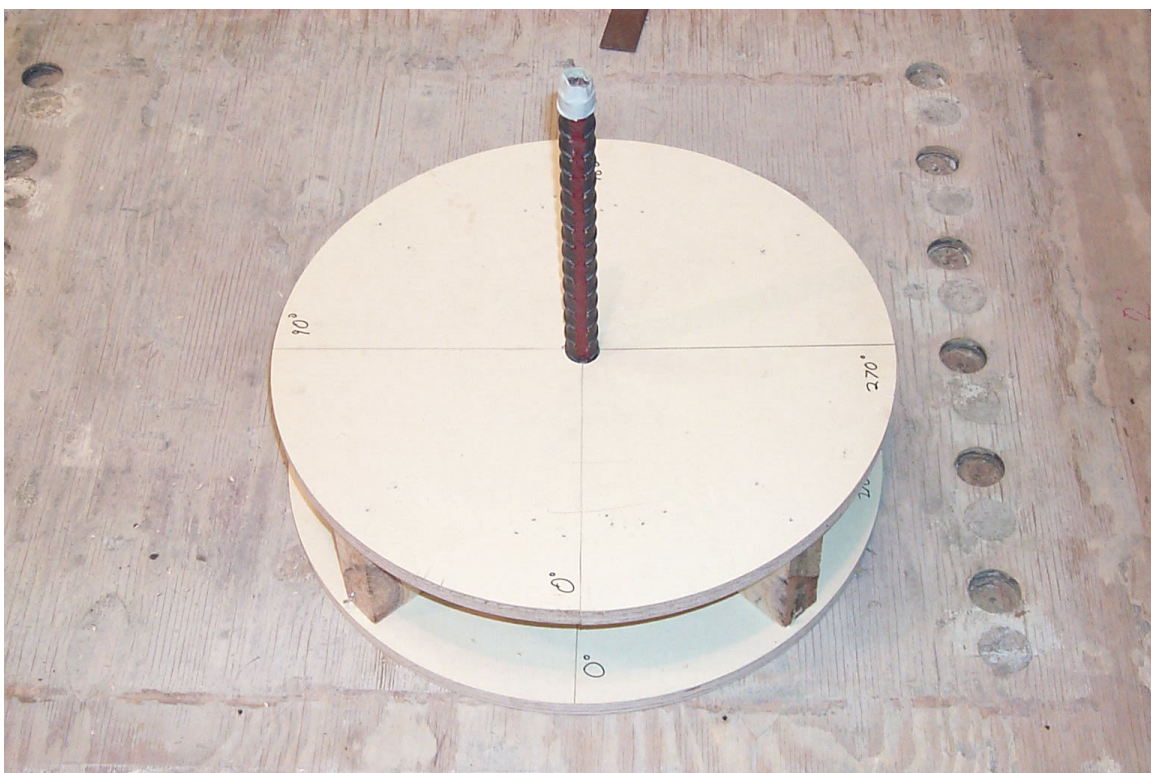


**Figure 3-16 Split plywood donut and steel bar in place**

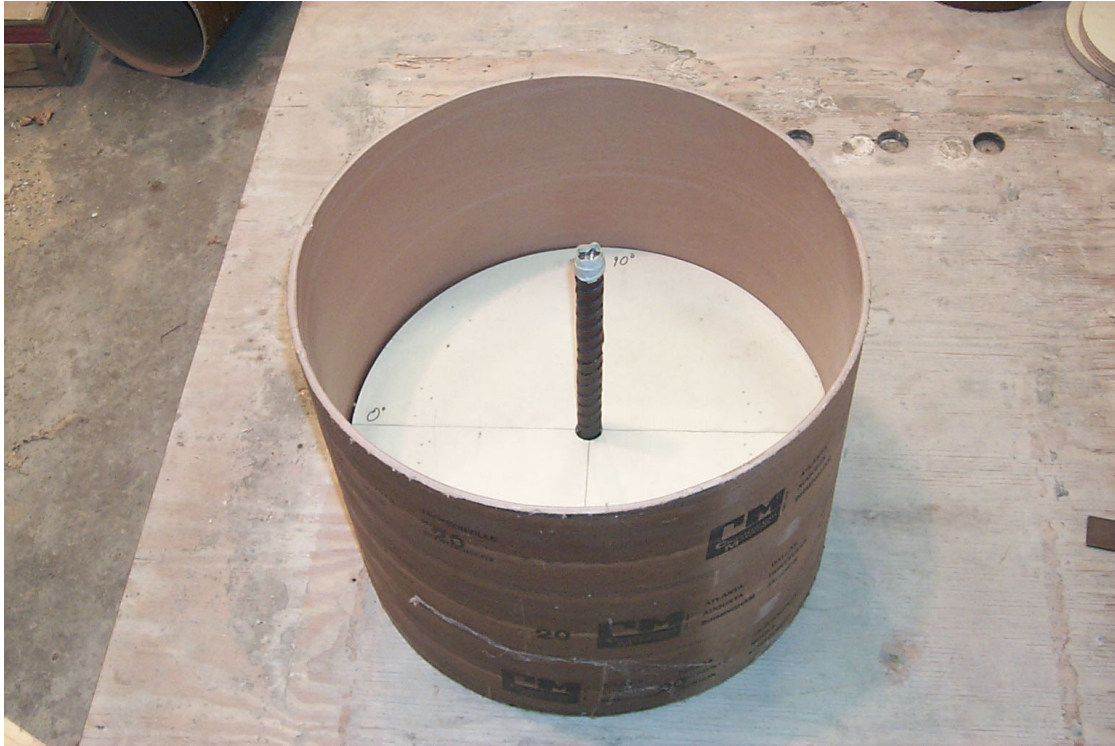


**Figure 3-17 Sono tub placed over plywood donuts**

On tests 1 through 9 (all 10-inch diameter specimens), a series of holes were drilled in the side of the sono-tubes at  $90^0$  and  $270^0$  to accommodate the grout tubes. On all other tests, the grout tubes were completely contained inside the concrete form, and all wires run out of two small holes, also at  $90^0$  and  $270^0$ . On test 1 the free end of the grout tubes was positioned 1/2-inch from the edge of the rebar and held in place by a vertical D-3 bar to which each grout tube was wired. On shot two, a small “ladder” was made from the D-3 bars, and the free end of the grout tubes was placed in this ladder. On all other tests, two ladders 3-inches apart were constructed and the grout tubes placed in this ladder and epoxyed in place (Figure 3-18). The ladder was then placed inside the form so that the gage elements would be located 3/4-inch from the edge of the rebar, and the gage ladder was epoxyed in place to prevent movement during concrete placement (Figure 3-19). Once the forms were completed, concrete was placed in the forms on the  $0^0$  and  $180^0$



azimuths using a scoop and vibrated into place using a  $\frac{3}{4}$ -inch pencil vibrator to prevent damage to the grout tubes (Figure 3-20). The test specimens were cured for a minimum of 28 days before the forms were stripped off and the specimens tested. A total of 33 test specimens were prepared. Nine specimens were 10-inch in diameter, and 24 had an outside diameter of 20-inches. Six specimens contained 1-inch smooth bars, 9 specimens contained #10 deformed bars, and the remaining 18 specimens contained #8 deformed bars. The specimen types are summarized in Table 3.2.

**Table 3.2 Physical dimensions of test specimens**

Number of Test Specimens	Specimen Diameter (inches)	Specimen Height (inches)	Bar Diameter	Deformations
9	10	10	#8	Yes
9	20	10	#8	Yes
6	20	10	1-inch	No
9	20	10	#10	Yes

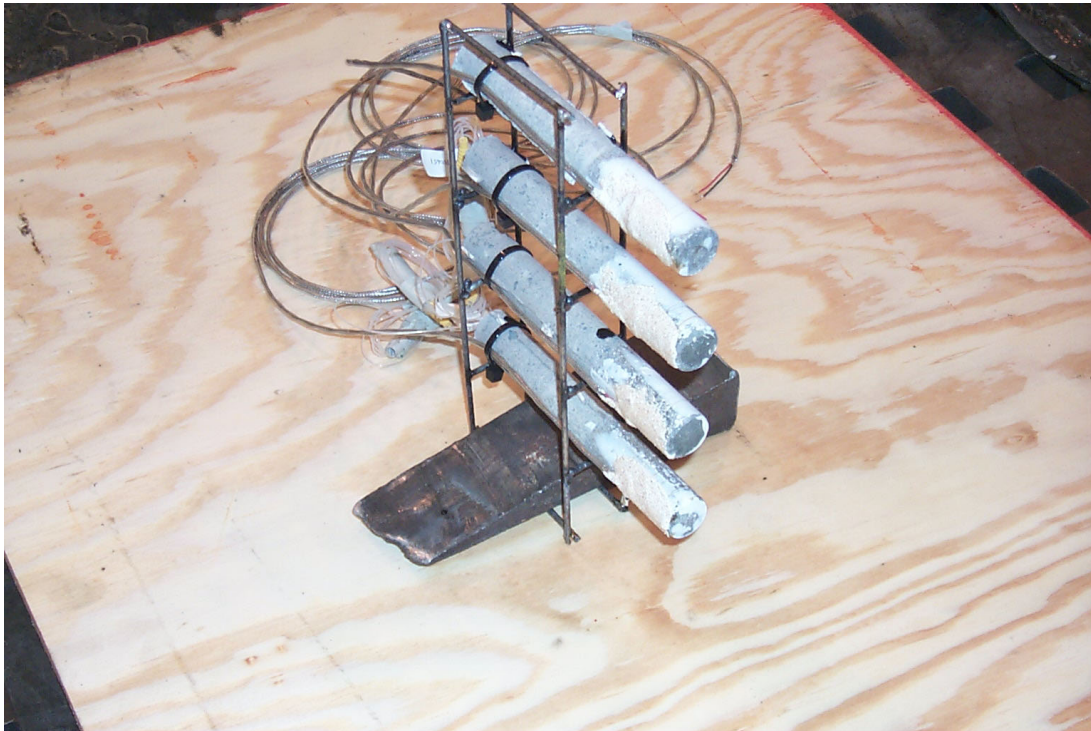


**Figure 3-18 Grout tubes placed in wire ladder**

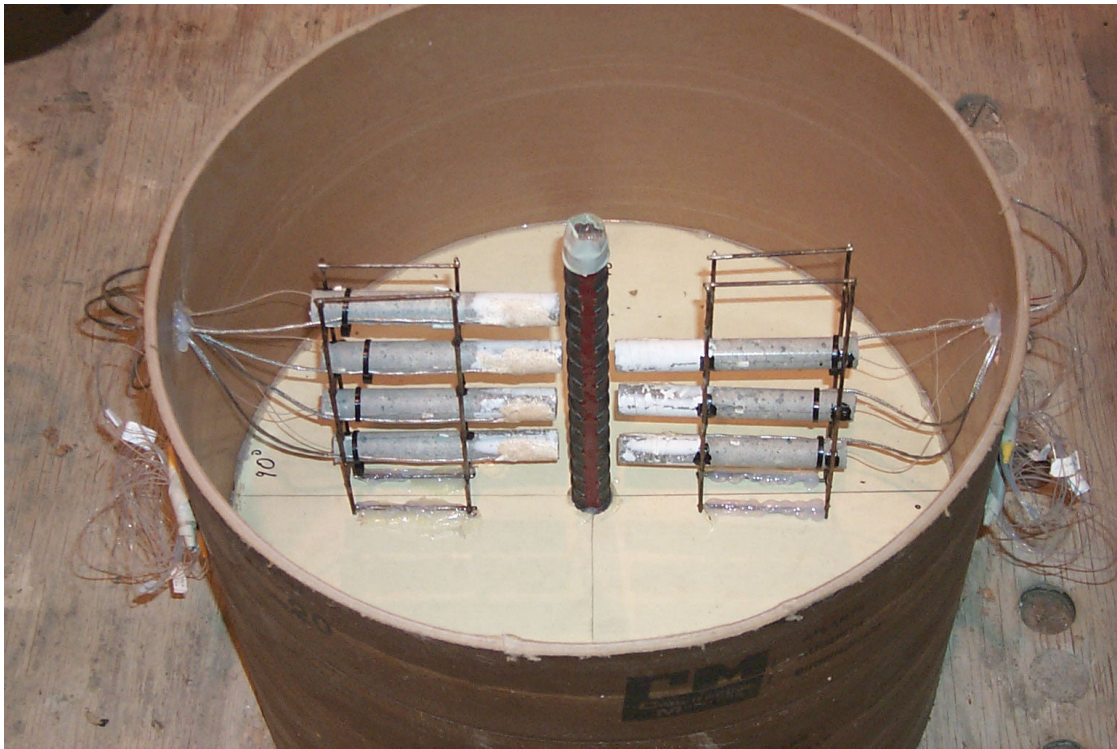


**Figure 3-19 Grout tubes placed inside concrete form**



**Figure 3-20 Placing the concrete**

### 3.3 Testing Equipment and Data Acquisition

Both static and dynamic loads were generated using the 200 Kip Dynamic Loader. The electronic gages were recorded using Pacific Instruments digital recorders, and all experiments were documented with digital photographs.

#### 3.3.1 200 Kip Dynamic Loader

The 200-Kip Loader (Figure 3-21 and Figure 3-22) is a device capable of applying a concentrated load in short times over a maximum stroke of 6 inches. The machine is capable of loading rates varying from slow static loading to ones in which the maximum load is reached in a very few milliseconds.

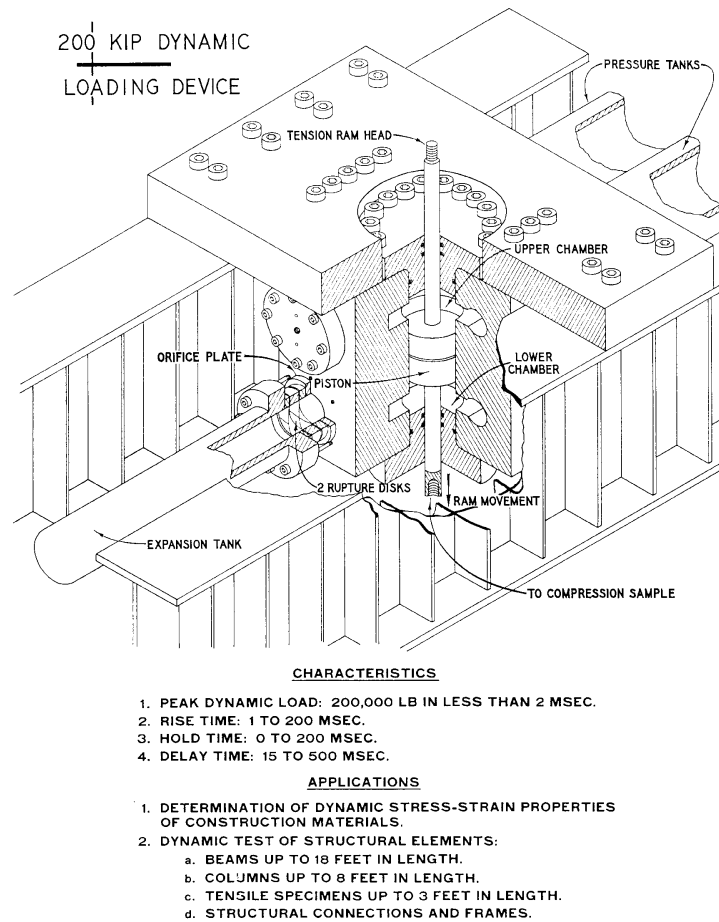
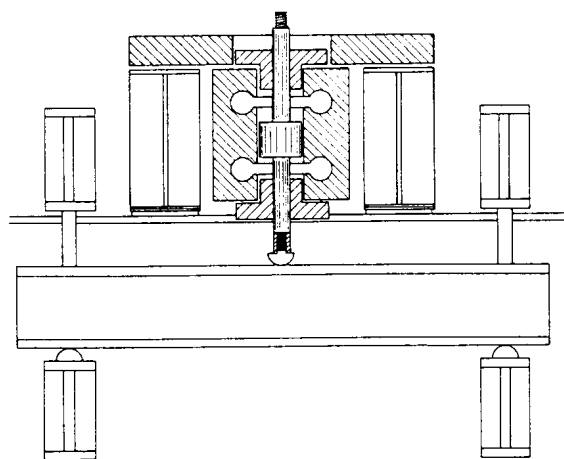
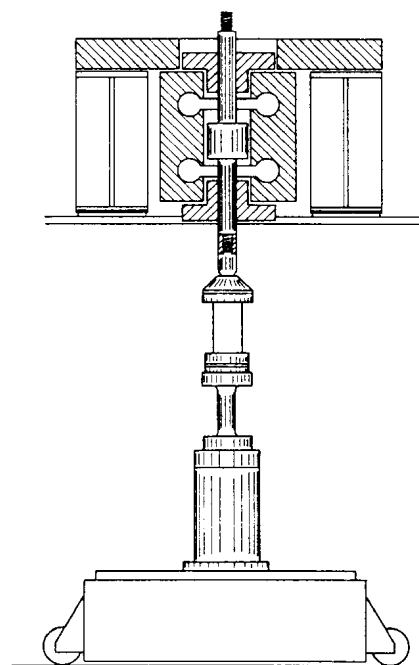


**Figure 3-21 Characteristics of 200-Kip Loader**

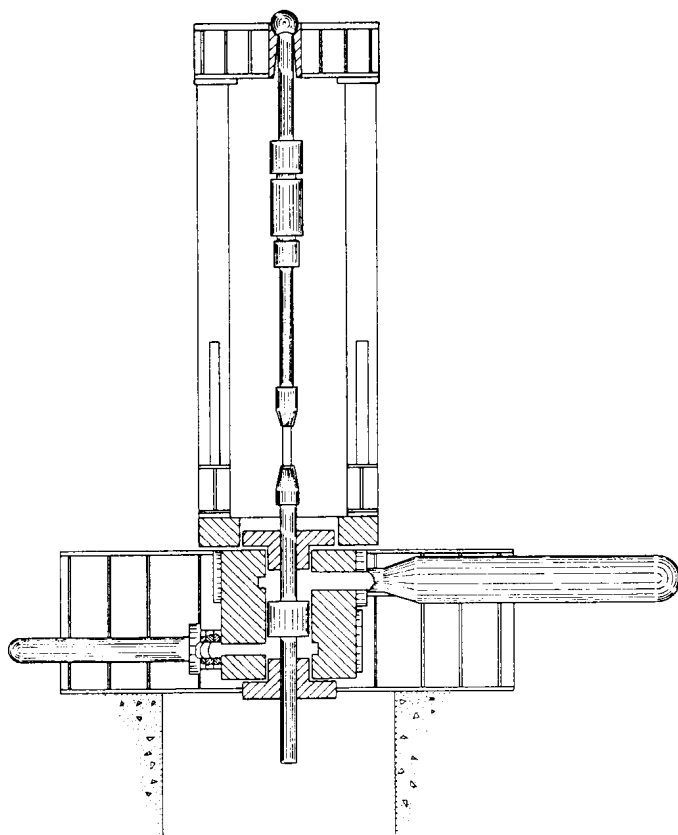


FLEXURE

200 KIP DYNAMIC  
LOADING DEVICE



COMPRESSION



TENSION

Figure 3-22 Loading modes for 200-Kip Loader



The loader was designed to apply forces varying from 10,000 to 200,000 lb. in either tension or compression. The design of the device is such that loads as high as 400,000 lb. may be possible; however, the maximum load capability of the device is dependent on the use to which it is subjected.

The types and sizes of specimens that can be tested include beams up to 24 in. deep, 18 in. wide, and 144 in. long; columns with a maximum height of 6 ft and cross-section diameter of 18 in.; circular specimens having a specimen diameter at the grips of 2-1/2 in. and length of approximately 36 in. under tensile loading; and members requiring 2-point loading with up to a maximum of 4 ft between points of load application. To produce a static tensile load with this machine, the valve to the lower chamber is opened, and the oil removed. Oil is then slowly pumped into the upper chamber until the desired load is obtained. To produce dynamic tensile loads, both the upper and lower chambers, and the area between the two-rupture disks are filled with oil. Oil is then pumped into both chambers and the area between the two rupture disks maintaining a ratio of 91.5% of the lower chamber pressure in the upper chamber and  $\frac{1}{2}$  of the lower chamber pressure between the two-rupture disks. The pressure between the two rupture disks is then released, causing failure of first the up-stream rupture disk followed by the failure of the down stream disk. This quickly causes the loss of pressure below the piston, thereby producing the tensile load. The rise time for the load can be controlled to some extent by the size of the orifice plate placed just upstream of the first opening valve.

In order to perform the proposed pull-out test, it was necessary to redesign the superstructure. The existing superstructure (Figure 3-23), which was designed to hold a

10-ft-long reinforcing bar was removed and replaced with one design to hold the concrete samples for this test. The new superstructure is shown in Figure 3-24.

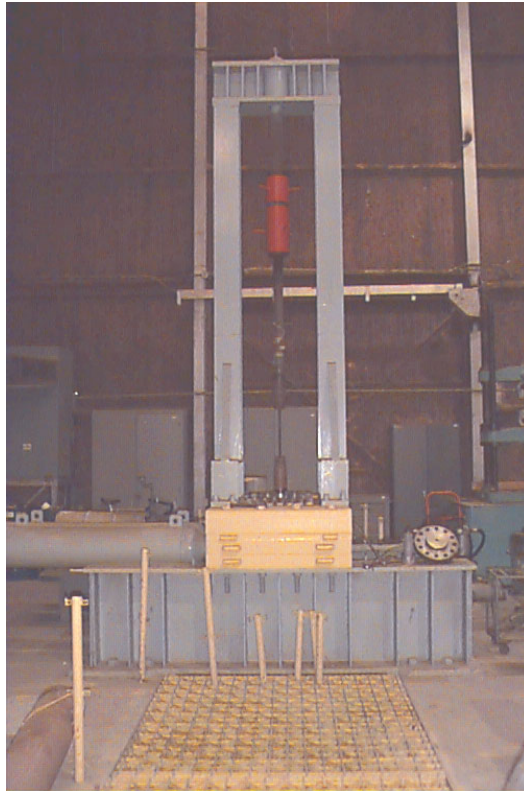


**Figure 3-23 Old superstructure designed to hold long bar samples**

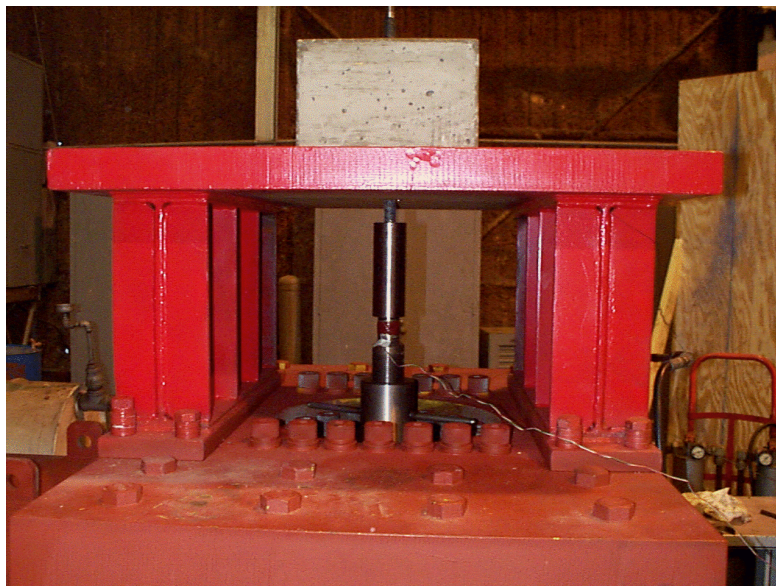


**Figure 3-24 New superstructure designed to hold concrete sample**



In order to gain better control over the loading function, and to reduce the set-up time required for each test, the rupture disc assembly (Figure 3-25) was replaced with a fast opening valve. Manifolds were constructed which attached the fast-opening valve to the loader (Figure 3-26). The new valve, which merely replaced the rupture disc assembly, was attached to the loader between the orifice plate expansion chamber. This cut the set-up time for each experiment from 4 hours to 15 minutes. The manifolds were designed in such a way that no permanent modifications were made to the loader in case it was desired to return to the rupture disc assembly at a later time.

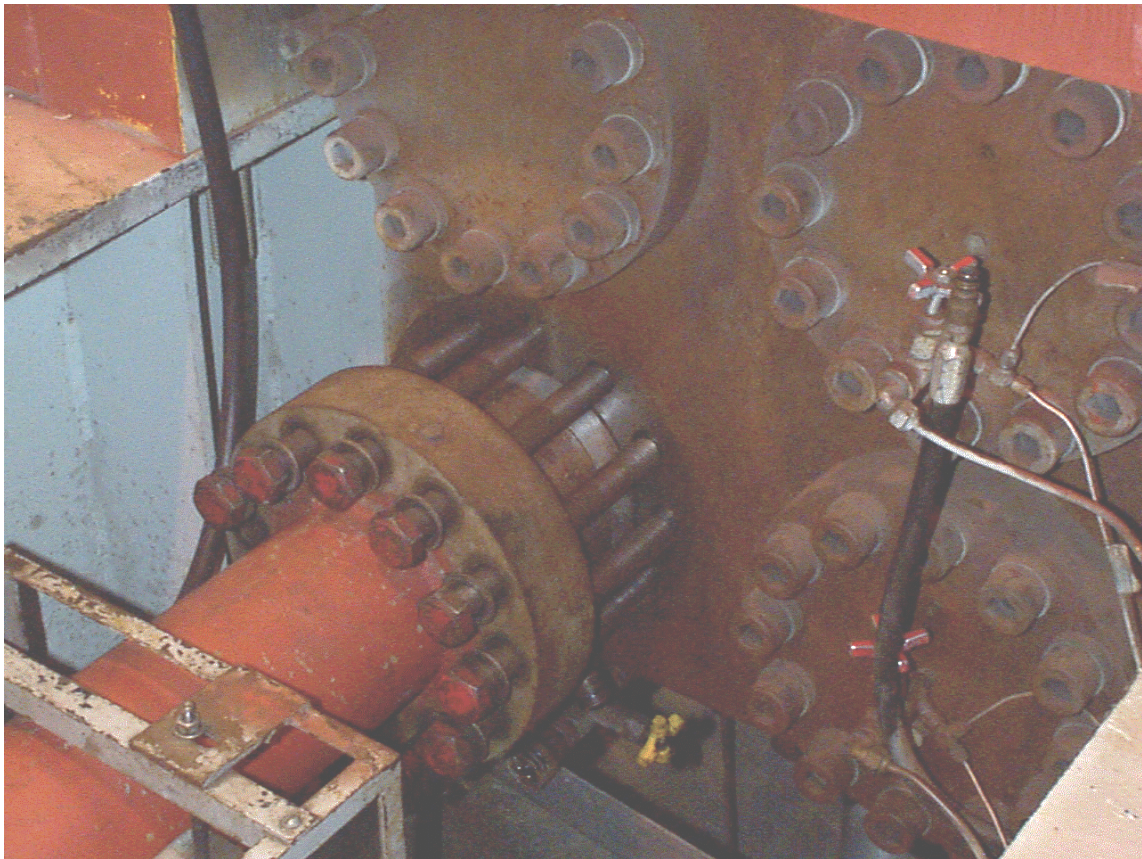


**Figure 3-25 Rupture disc assembly**

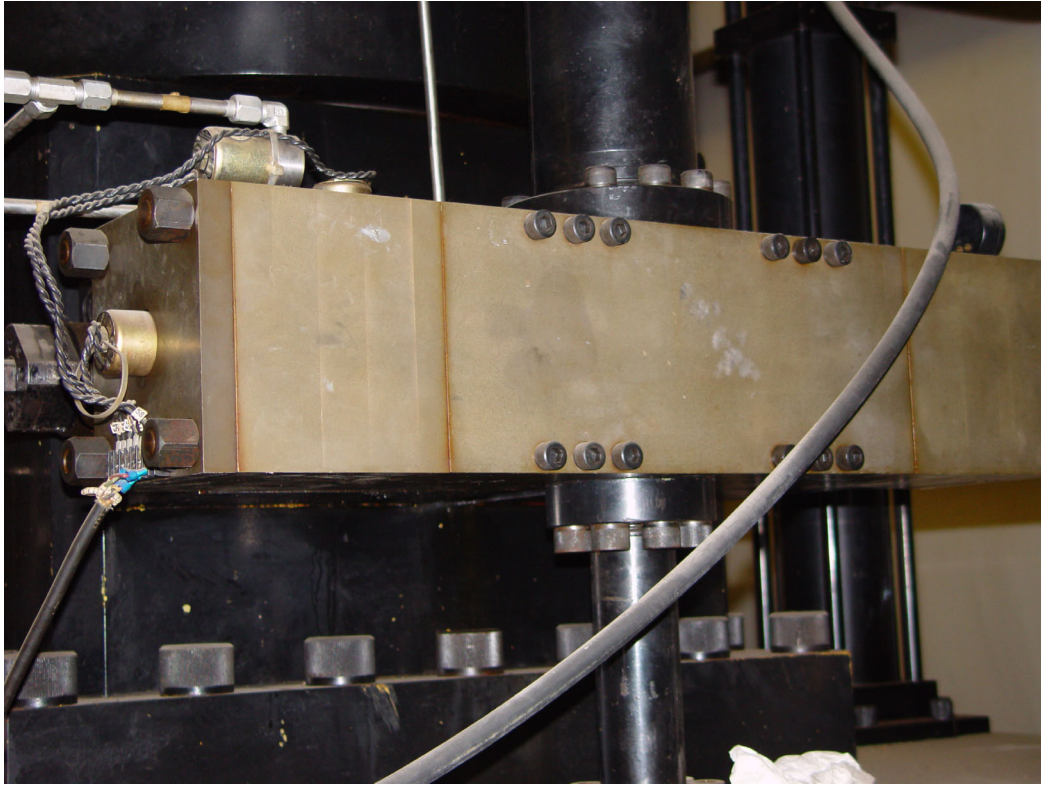


**Figure 3-26 Fast opening valve**

### 3.3.2 Data Recording

Data were recorded using a Pacific Instruments 12 bit vertical resolution TDRs with a recording frequency of 122.1 Hz for the static tests, 250.0 kHz for the 200 msec loadings, and 500 kHz for the 5 msec loadings. The fiber-optic strain gage signals were pre-processed using a FOSS I to convert the light input to a voltage output. The data were analyzed and plotted using DPLOT.

### 3.3.3 Still Photography

All still photography was taken with a Kodak DC120 Zoom digital camera. All images were taken at a resolution of 1280 x 960, true color in the Kodak native format. The

images were then converted to tiff format, 256 colors, using Adobe PhotoShop, so the images could be manipulated using MS word and MS Power Point software.

### **3.4 Testing Program**

The testing program was designed to quantitatively investigate the phenomenon associated with the interaction of reinforcement and concrete when subjected to a variety of loading rates, and determine the effects that several parameters had on this interaction. This would then be followed by a finite element analysis to gain a better understanding of the physics behind this relationship.

#### **3.4.1 Test Matrix**

A total of thirty-three specimens were prepared. The baseline specimens consisted of a #8 deformed bar cast in the center of a 20-inch diameter concrete cylinder. Nine of these specimens were fabricated and tested. Three were loaded statically, three were loaded in 200 msec, and three were loaded to failure in approximately 5 msec. Three other variables were investigated. These included: effects of concrete confinement, (i.e., 20-inch diameter samples vs. 10-inch diameter samples); effects of bar diameter, (i.e., #8 deformed bar vs. #10 deformed bar); and the effects of bar deformation, (i.e., #8 deformed bar vs. 1-inch smooth bar). In each case multiple samples were loaded to failure statically, in 200 msec and in 5 msec. For each variable and loading rate combination, three samples were tested, except for the smooth bars where only two were tested for each loading rate. This was done in order to determine the repeatability of the experiments, and to obtain a better statistical basis for the data. The complete test matrix is shown in Table 3.3

**Table 3.3 Complete test matrix**

<b>Test Number</b>	<b>Load Rate</b>	<b>Bar Diameter</b>	<b>Specimen Diameter</b>	<b>Deformation Pattern</b>
1	Quasi-Static	#8	10"	Deformed
2	Quasi-Static	#8	10"	Deformed
3	Quasi-Static	#8	10"	Deformed
4	Impact	#8	10"	Deformed
5	Impact	#8	10"	Deformed
6	Impact	#8	10"	Deformed
7	Dynamic	#8	10"	Deformed
8	Dynamic	#8	10"	Deformed
9	Dynamic	#8	10"	Deformed
10	Impact	#8	20"	Deformed
11	Impact	#8	20"	Deformed
12	Impact	#8	20"	Deformed
13	Dynamic	#8	20"	Deformed
14	Dynamic	#8	20"	Deformed
15	Dynamic	#8	20"	Deformed
16	Quasi-Static	#8	20"	Deformed
17	Quasi-Static	#8	20"	Deformed
18	Quasi-Static	#8	20"	Deformed
19	Impact	#8	20"	Smooth
20	Impact	#8	20"	Smooth
21	Dynamic	#8	20"	Smooth
22	Dynamic	#8	20"	Smooth
23	Quasi-Static	#8	20"	Smooth
24	Quasi-Static	#8	20"	Smooth
25	Impact	#10	20"	Deformed
26	Impact	#10	20"	Deformed
27	Impact	#10	20"	Deformed
28	Dynamic	#10	20"	Deformed
29	Dynamic	#10	20"	Deformed
30	Dynamic	#10	20"	Deformed
31	Quasi-Static	#10	20"	Deformed
32	Quasi-Static	#10	20"	Deformed
33	Quasi-Static	#10	20"	Deformed



### 3.4.2 Test Procedure

The Standard Operating Procedure (SOP) for conducting the dynamic experiments was as follows. First a sheet of 4-mil polyurethane plastic was placed on top of the reaction frame. Sikadur<sup>R</sup> was then mixed and a thin layer spread over the plastic sheet (Figure 3-27) and covered with another sheet of plastic. An “X” was cut in the center of the plastic sheets. The test specimen was then lowered into place with the protruding steel bar and connector passing through the cut in the plastic sheets. The specimen was then connected to the load cell, and the loader’s piston lowered to set the concrete specimen firmly in the Sikadur<sup>R</sup>. The Sikadur<sup>R</sup> was then allowed to cure for approximately 20 hours. The Sikadur<sup>R</sup> ensured that the specimen had an even base and would be loaded uniformly, while the plastic sheets prevented adhesion of the sample to the reaction structure, thereby allowing expansion in the radial direction. While the Sikadur<sup>R</sup> was curing, the instrumentation cables were connected to the Pacific Instruments recording equipment and the gages checked and balanced.



**Figure 3-27 Spreading Sikadur on the plastic sheet**

When the Sikadur<sup>R</sup> was completely cured, the fast opening valve was tested to ensure proper function, and the upper and lower cylinders of the loader were bled to remove and entrapped air bubbles. The piston control valve was then cycled to ensure that no loads were being applied to the specimen. The load cell output was then set to zero and the low-pressure valves on the loader closed. The high-pressure hydraulic pump was then started, and the valve to the upper cylinder opened. The valve to the lower cylinder was then opened and closed as necessary to maintain zero load on the test specimen.

When the prescribed hydraulic pressure had been obtained, 2250 psi for 200 msec loadings and 3000 psi for 5 msec loadings, all valves closed, and the pump shut off. When the instrumentation personnel indicated that they were ready, a 5-second count down commenced. The fast opening valve was armed at T-4 seconds, the instrumentation system was armed at T-3 seconds and the fast opening valve was fired at T=0.

Immediately following the test, the data records were transferred from the system's RAM to the hard drive. Once this critical stage had been completed, the test specimen was photographed and removed, the expansion chamber drained, and the loader prepared for the next experiment.

The SOP for the static tests was identical to the dynamic test except for the loading stage. Once the system had been bled and the lower pressure valves closed, the fast opening valve was opened. Oil was then pumped into the upper cylinder while zero pressure was maintained in the lower cylinder. The loading was continued until the specimen failed. The remainder of the procedure was the same.

### 3.4.3 Results of Typical Test

The data acquisition for a typical test consisted of a physical description of the failure mode, the load cell time history, the steel strain records, concrete foil strain gage records and, on some tests, the concrete fiber-optic strain gage records. All test records were analyzed and plotted using a WES developed data analysis program called DPLOT. The fiber optic strain records were reduced in accordance with the procedures outlined in Section 3.2.3. All specimens in the test series failed in one of three failure modes; pull out of the steel bar (Figure 3-28), yielding of the steel bar (Figure 3-29) or radial cracking of the concrete cylinder (Figure 3-30).

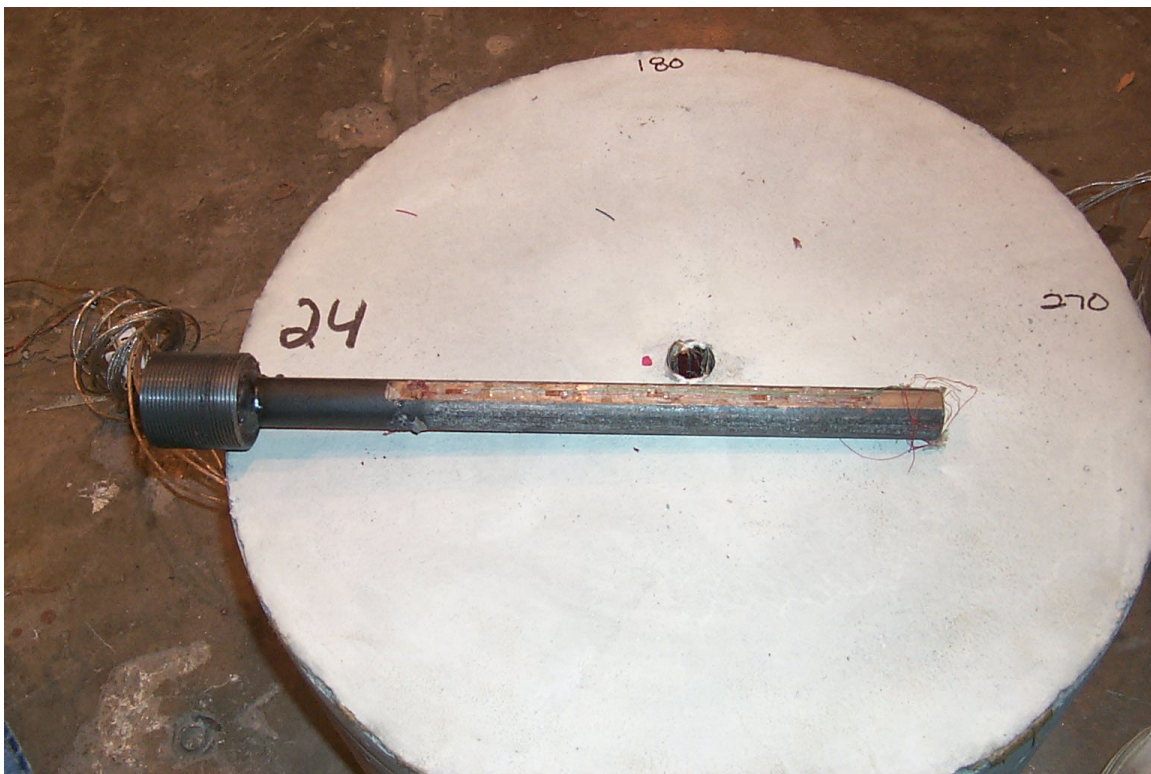


**Figure 3-28 Failure due to pullout of the smooth steel bar**





**Figure 3-29 Failure due to the yielding of the steel bar**

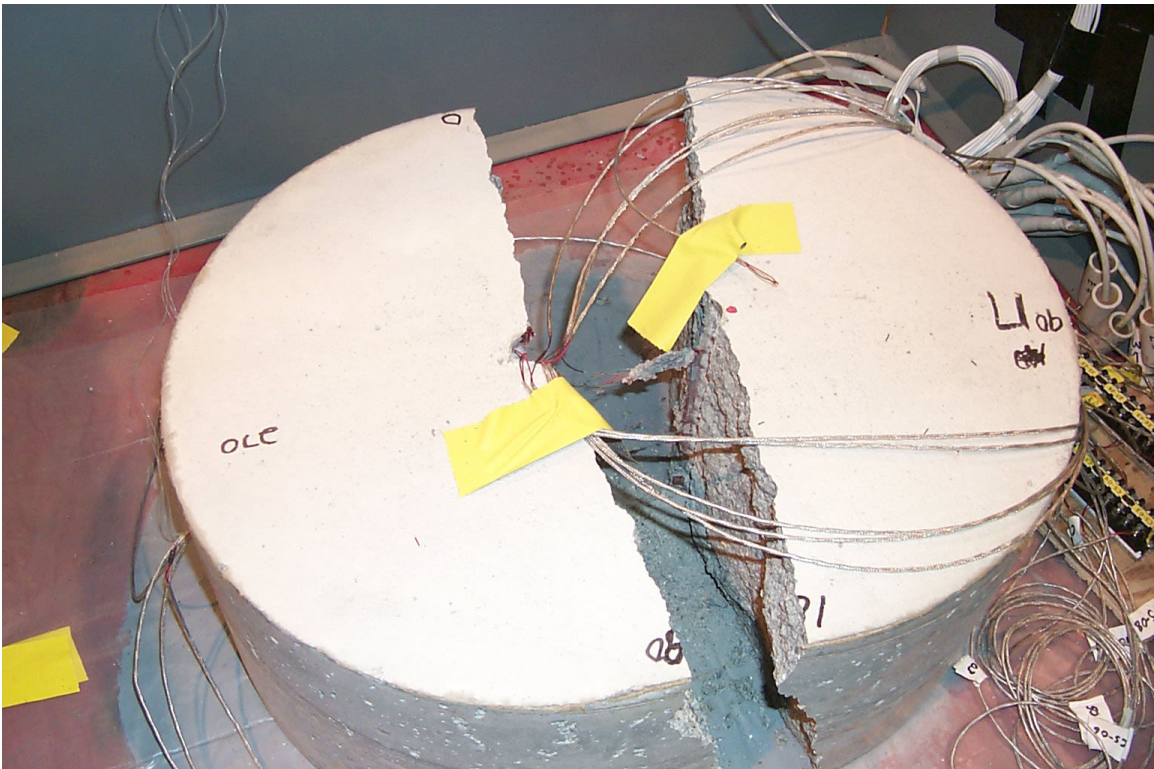


**Figure 3-30 Failure due to radial cracking of the concrete**



A typical load cell record for a specimen that failed due to radial cracking of the concrete is shown in Figure 3-31. The load cell provided not only the maximum load applied to the sample, but also the time the load was applied, loading rate and the time of failure. Most load cell records have a short non-linear loading rate at the beginning, which is due to slight differential movement between the mechanical connectors, and seating of the specimen on the reaction base. This is followed by a linear loading rate for most of the record, followed by a short non-linear loading just prior to failure of the system.

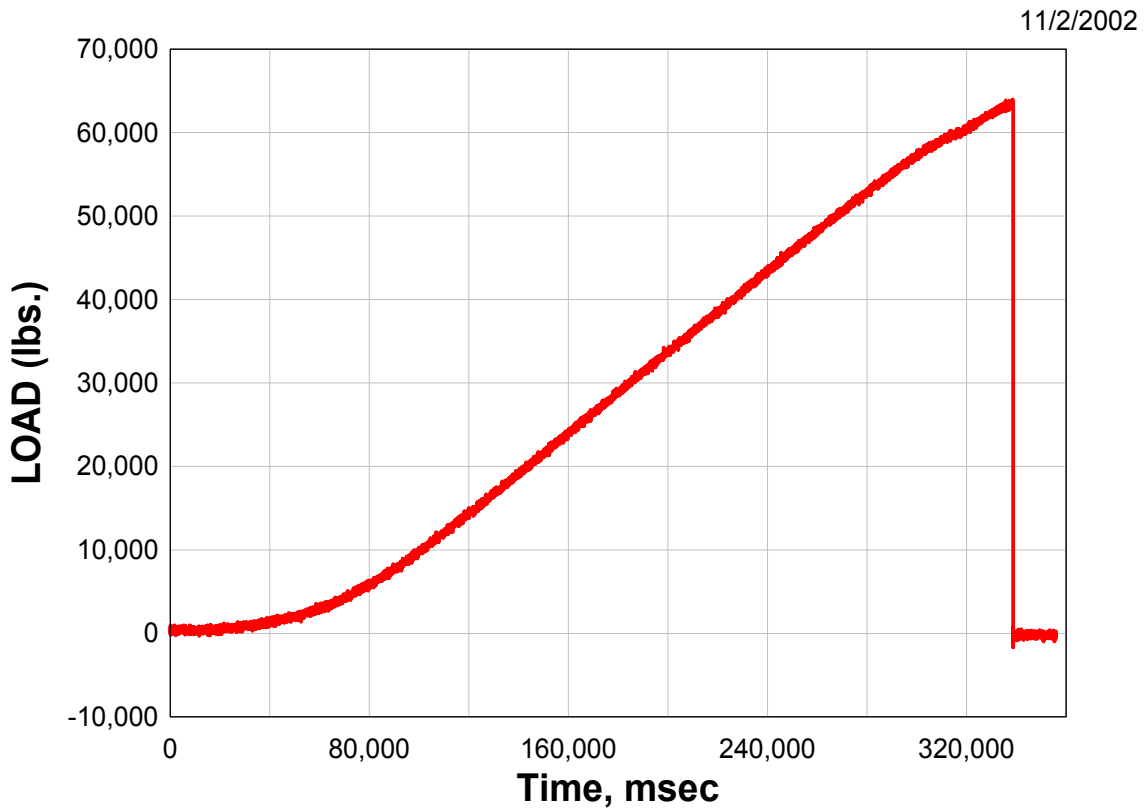


**Figure 3-31 Load vs. Time for test 18**

The vast majority of the steel strains remained in the elastic range. Since the steel did not go plastic, the steel strain records were similar to that of the load cell, with the

maximum value occurring at the same time as the maximum load (Figure 3-32). The maximum steel strains occurred at the bottom of the bar, where the load was applied, and decreased linearly to 0 at the top of the bar.

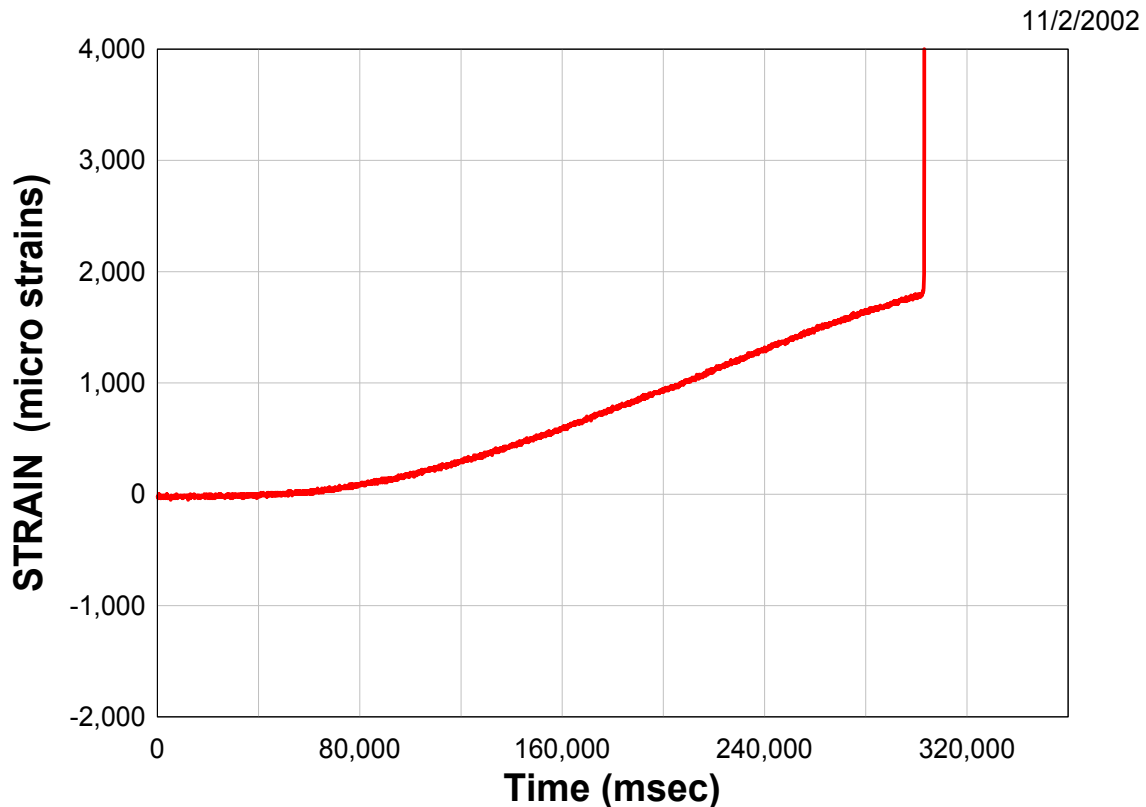


**Figure 3-32 Steel strain vs. Time for SS-03, test 18**

The concrete foil strain gage records tended to show large variation in strains. This can be contributed to several factors. Concrete is a non-homogeneous, non-isotropic material, it is therefore reasonable to expect larger variations than one would expect in a homogeneous material such as steel. Also, on dynamic test, complex shock waves were running through the concrete in both the vertical and radial directions. The shockwaves originated along the steel bar and reaction base. They then propagate outward and upward as compression waves. Once they reach the free surface, they reflect as a tension

wave. The interaction of these shock waves can cause large and some times apparently random variations in the strain data. All this aside, the radial concrete strains measured in this test indicated radial compression of the concrete without significant variation from top to bottom of the specimen.

To convert the sinusoidal output of the fiber-optic gages, Figure 3-33, to engineering strain, it was first necessary to normalize the data so that the top and bottom of a typical sine wave corresponded to +1 and -1 respectively. Once this was done, it was necessary to count the number of sign waves and partial sign waves. These points are shown as \* in Figure 3-34. By counting the number of complete and partial waves, and properly applying equations 3.1 through 3.4, the engineering strain was calculated (Table 3.4). This data was then used in DPLOTT to obtain a plot of engineering strain vs. time (Figure 3-35). The fiber-optic strain data was in good agreement with that obtained using the foil strain gages.

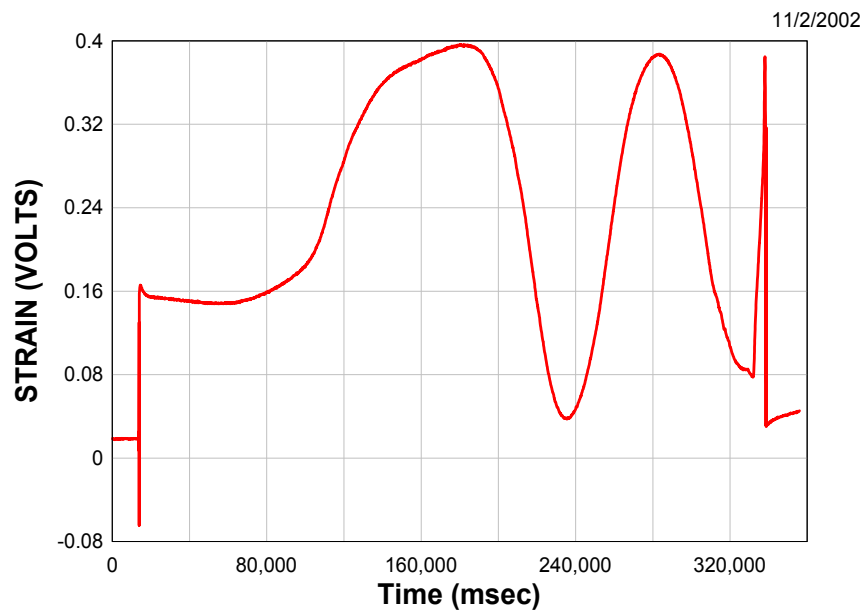


**Figure 3-33 Raw fiber-optic output from the FOSS I for FO-02, test 18**

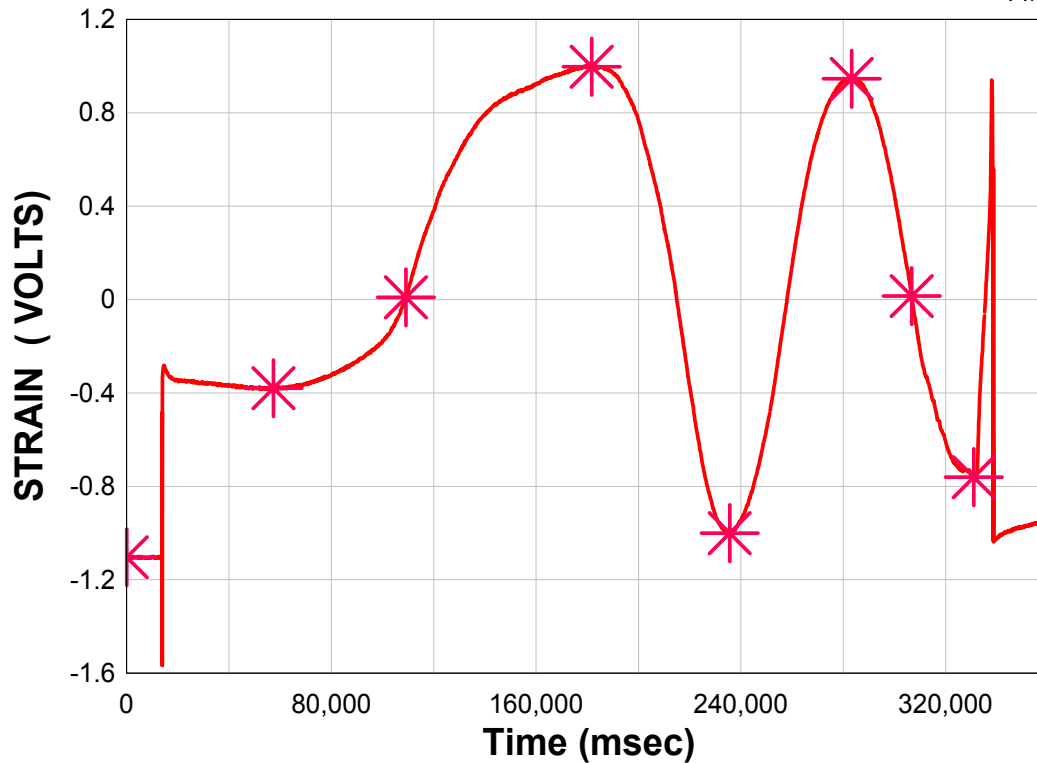


**Figure 3-34 Normalized FOSS I output for FO-02, test 18**

**Table 3.4 Calculation of engineering strain for fiber optic gage 8 test 18**

Fiber Optic Gage 8, Test 18						
Gage Factor= 4.04						
Data Point	Time (msec)	Y Value	Delta F	Sum Delta F	Time (msec)	Strain (micro strains)
1	14.97461	-1.04681	0	0	14.97461	0
2	96680.59	0.895969	0	0	96680.59	0
3	158939.8	0.006502	-0.17676	-0.17676	158939.8	-28.6577
4	209730.2	-1	-0.25	-0.42676	209730.2	-69.1899
5	293288.6	0.953186	-0.5	-0.92676	293288.6	-150.254
6	330644.2	0.011703	-0.25	-1.17676	330644.2	-190.786

A statistical analysis was performed on all data. For each test, like measurements i.e., fiber-optic and foil concrete strains, 2-inches from the bottom on  $90^0$  and  $270^0$  (four total measurements) were averaged and plotted as shown in Figure 3-36. The data from

repeated tests such as all 20-inch diameter samples containing #8 deformed bars loaded statically (tests 16, 17 and 18) were analyzed. The average load applied to cause failure

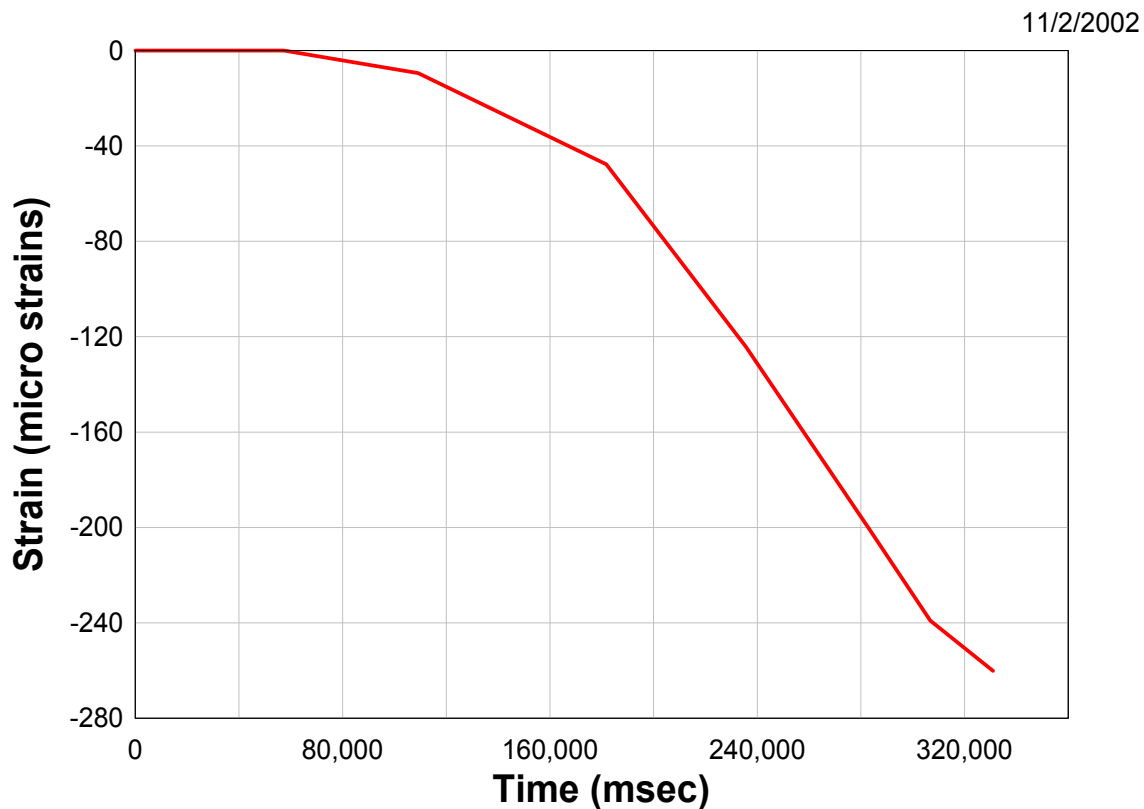


**Figure 3-35 Reduced fiber-optic data showing strain vs. time for FO-02, test 18**

was determined. Each specimen failed at a slightly different load, which would have caused different strains in the steel and concrete. Since we wished to compare strains under similar conditions, the smallest load, which caused failure of the group of specimens, was chosen. The time that this load occurred in the other two specimens was determined, and the steel and concrete strains at that time used for the statistical comparison. These strains are referred to as adjusted strains. For the steel strain data, the values at each location were averaged, and a linear regression fit to the data to show the variation of strain along the length of the bar, Figure 3-37. For the concrete data, the

values at each location were averaged. Since there did not appear to be any ordered regression of the data, (Figure 3-38) the overall average concrete strain was calculated.

The complete statistical analysis of the data is shown in Appendix B.

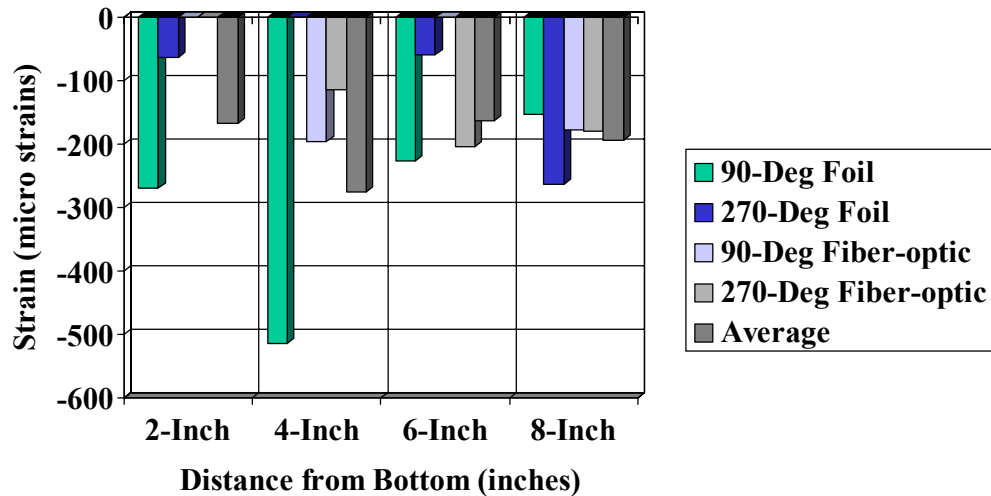


Figure 3-36 Average concrete strains from test 18

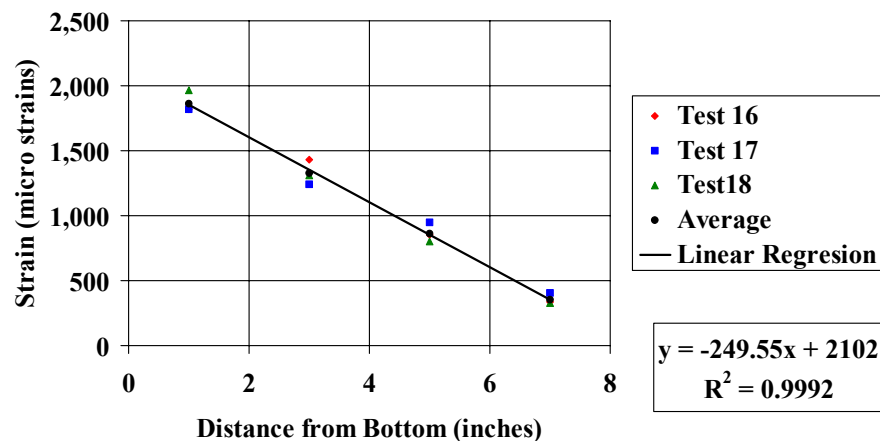


Figure 3-37 Steel strains for tests 16, 17 and 18 showing linear regression of the data

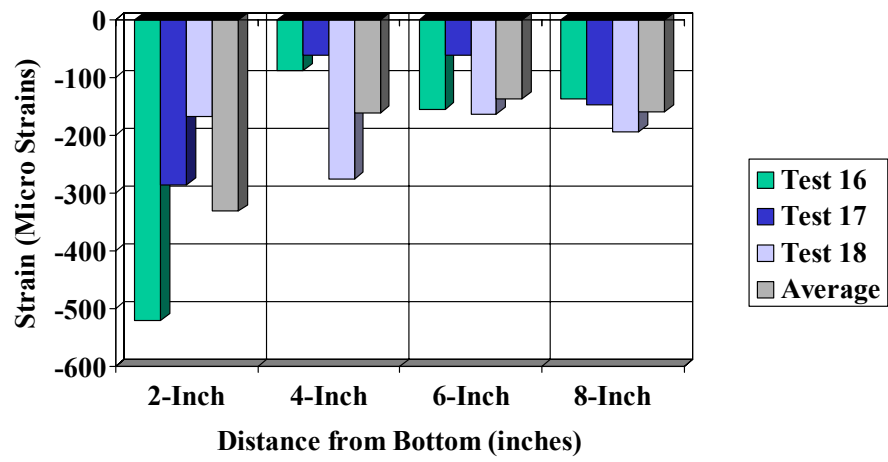


Figure 3-38 Concrete strain for tests 16, 17 and 18 showing no regression of data

## **CHAPTER 4 EXPERIMENTAL RESULTS**

This chapter presents the actual test data obtained from each test. A series of three similar tests were conducted for each variable. Since failure for each specimen occurred at slightly different loads, the smallest load that caused failure in the group was used as the maximum load. The time that this load occurred in the other two tests was determined, and the strain values at that time used in the comparisons. A complete summary including post test pictures of the specimens, Summary graphs of the steel strains and concrete strains for each test, and a statistical analysis of the data can be found in Appendix B.

### **4.1 Quasi-Static Loading of a #8 Deformed Bar Embedded in a 10-inch Diameter Concrete Cylinder**

Tests 1, 2 and 3 consisted of a 10-inch diameter cylinder with a #8 deformed bar loaded quasi-statically. Oil was pumped into the upper cylinder of the machine to create the loads applied to the specimens. The rate at which the loads were applied was a function of the rate that the oil was pumped. This could be affected by many variables such as the manifold pressure or the temperature of the oil. The loads applied to each specimen were slowly increased until failure occurred. The maximum loads applied to the three test specimens before failure were 41,000 lbs. at time  $t = 417$  sec. For test 1, 40,300 lbs. at  $t = 240$  sec. for test 2 and 42,580 lbs. at  $t = 713$  sec. Since these were all quasi-static tests, the differences in time had no effect on the results. In order to compare all data under comparable loading conditions, a maximum load of 40,300 lbs. will be used for these three tests.



#### 4.1.1 Test 1

On test 1, a total of 27 channels of active instrumentation were used. Of these, twenty-one returned useful data for a total data return of 77.8%. These consisted of one (1) load-cell, successful, ten steel strains, all ten of which were successful, eight foil concrete strains, seven of which were successful, and eight fiber-optic concrete strains, three of which were successful. The adjusted maximum load of 40,300 lbs. was reached at  $t = 412$  sec, for a loading rate of 210 lbs/sec. The two flat portions of the loading curve were caused by ice forming in the main pump control valve. The sample, Figure 4-1, failed due to radial cracking of the concrete, and broke into three pieces.

The steel strains varied from 1980 micro strains for SS-01 down to 270 micro strains for SS-10. Figure 4-2 shows the individual and average values of strain at each of the five positions. The foil concrete strains varied from  $-177$  micro strains for CS-05 down to  $-64$  micro strains for CS-07. The three fiber-optic gages, which survived the test, returned values ranging from  $-129$  micro strains for FO-03 down to  $-97.8$  micro strains for FO-07. The individual and average concrete strains for each of the four positions are shown graphically in Figure 4-3.

#### 4.1.2 Test 2

On test 2, a total of 19 channels of active instrumentation were run, of which all 19 (100%) returned usable data. These consisted of one load-cell, ten steel strains and 8 foil concrete strains. No fiber-optic gages were run on this test. The maximum load of 40,300 lbs. occurred at  $t = 240$  sec. The nonlinear portion of the load-cell record,  $t = 0$  to 60 sec. is due to slack in the system and the compression of tiny air bubbles in the

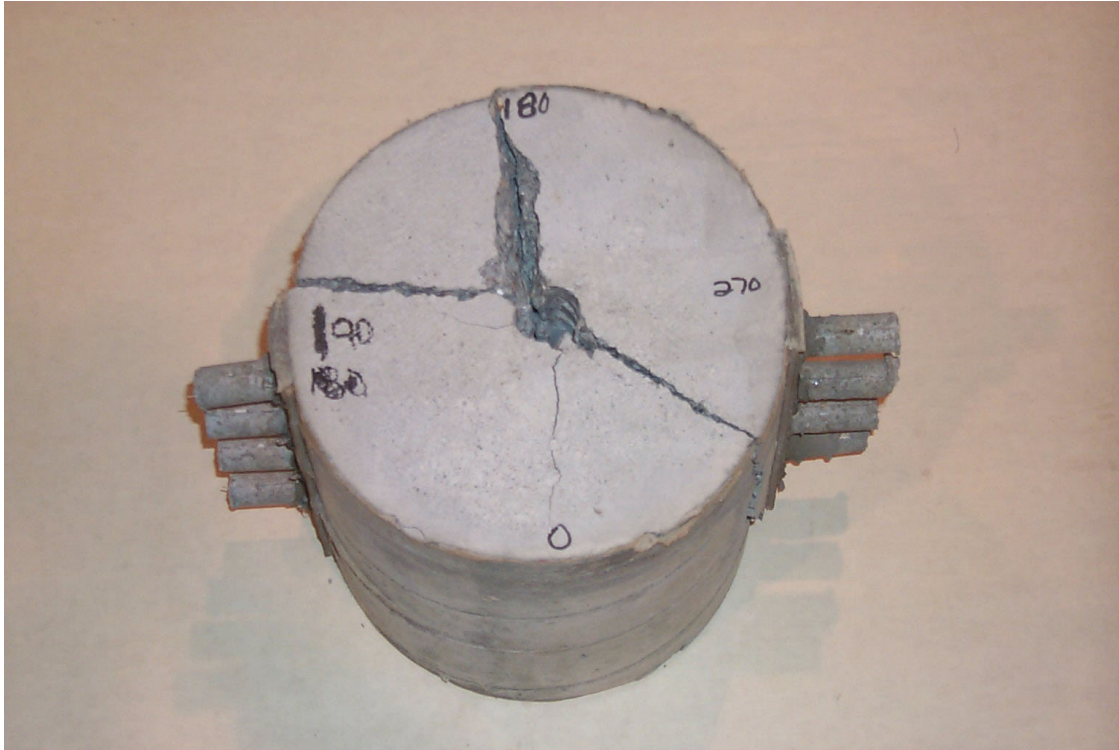


Figure 4-1 Specimen 1 post test

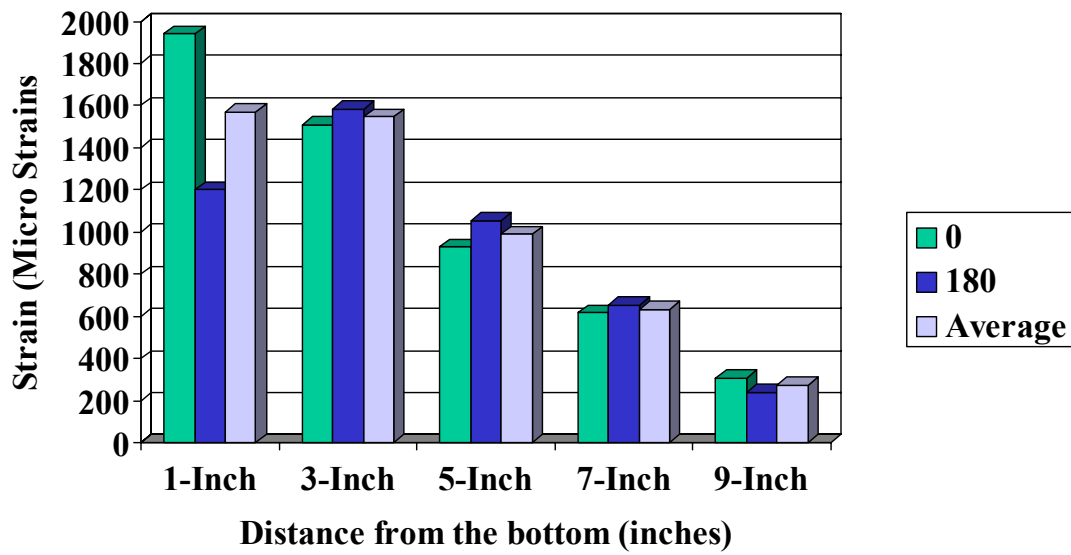
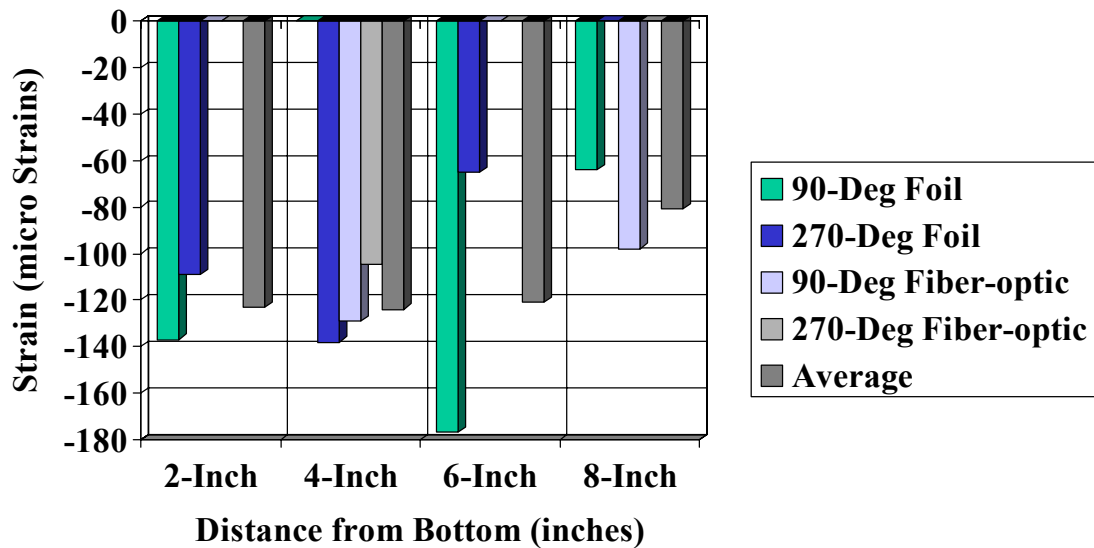


Figure 4-2 Adjusted steel strains test 1



**Figure 4-3 Adjusted concrete strains, test 1**

hydraulic oil. The remainder of the record shows a liner-loading rate of 200 lbs/sec. The loading remains linear until brittle failure occurred at  $t=240$  sec. As in test 1, the sample failed due to radial cracking of the concrete and broke into three pieces.

The steel strains varied from 1960 micro strains for SS-01 to 425 micro strains for SS-10. Figure 4-4 shows the individual and average steel strains for each of the five positions. As shown in Figure 4-5 foil concrete strains varied from  $-260$  micro strains at CS-04 down to  $-20$  micro strains at CS-08.

#### 4.1.3 Test 3

Test 3 contained 19 channels of active instrumentation with 17 returning usable data for a data return of 89.5%. These consisted of one load-cell (successful), ten steel strains (ten successful) and eight foil concrete strains (six successful). No fiber-optic gages were included in this test. The adjusted maximum load of 40,300 lbs. occurred at  $t = 698$  sec,

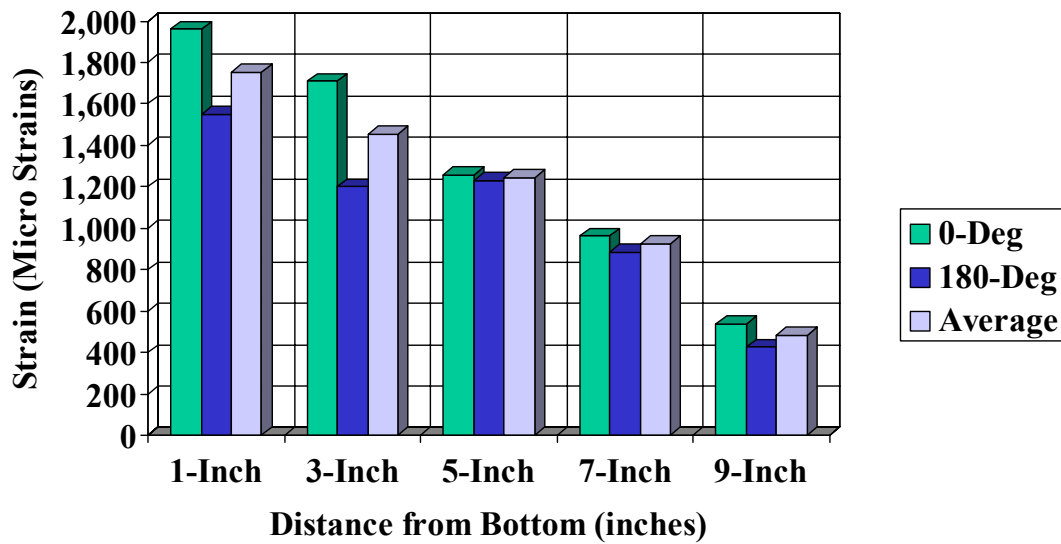


Figure 4-4 Steel strains, test 2

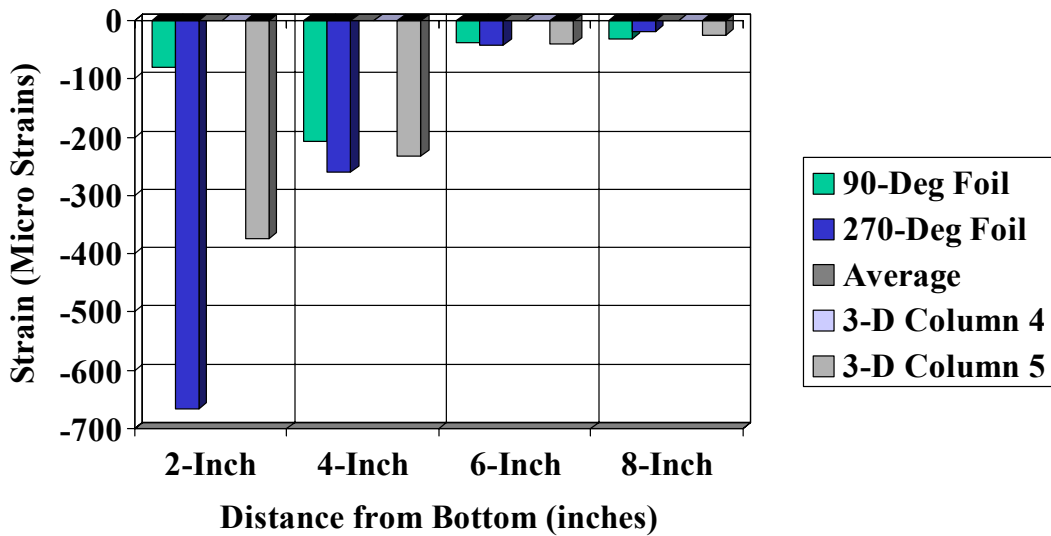
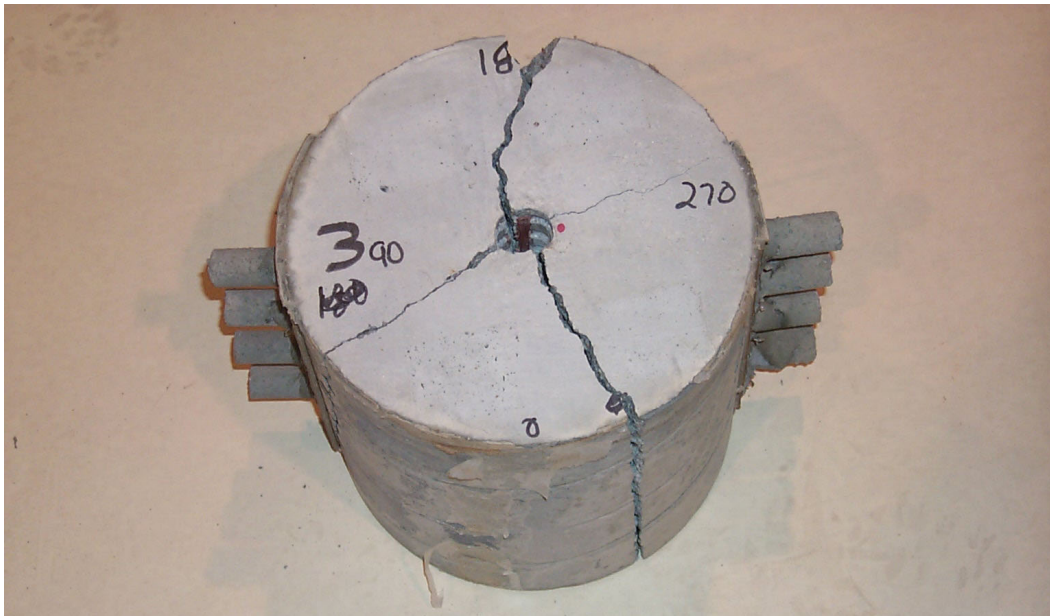


Figure 4-5 Adjusted concrete strains, test 2

for a loading rate of 160 lbs/sec. The load-cell record is similar to the record obtained from shot 1 including two breaks in the loading. Once again, this was caused by ice formation in the main pump control valve. A line heater was installed after this test to prevent further occurrences of this problem. The sample (Figure 4-6), failed due to radial

cracking of the concrete, and broke into three separate pieces. There was the typical crushing of the concrete on the leading edges of the steel bar deformations, then clean separation of the remainder of the concrete-steel interface (Figure 4-7 and Figure 4-8).

The steel strains varied from a maximum of 1,980 micro strains for SS-01 to a minimum of 486 micro strains for SS-09. Figure 4-9 graphically shows the individual and average steel strains. The foil concrete strains Figure 4-10 varied from –333 micro strains at CS-02 to –42 micro strains at CS-05. There were no fiber-optic gages in this test.



**Figure 4-6 Test specimen 3 post-test**

#### 4.1.4 Evaluation of Results of Tests 1, 2 and 3

The average load applied to the three samples before failure was 41,300 lbs. All three samples failed due to radial cracking of the concrete and broke into three separate pieces. There was crushing of the concrete on the leading edge of the deformations on the steel



bar. This caused a wedging action, thereby inducing compressive stress in the concrete normal to the axis of the steel bar (radial strain). This caused circumferential tensile



**Figure 4-7 Crushing of concrete on the leading edges of the steel deformations**



**Figure 4-8 Deformed steel bar post-test**

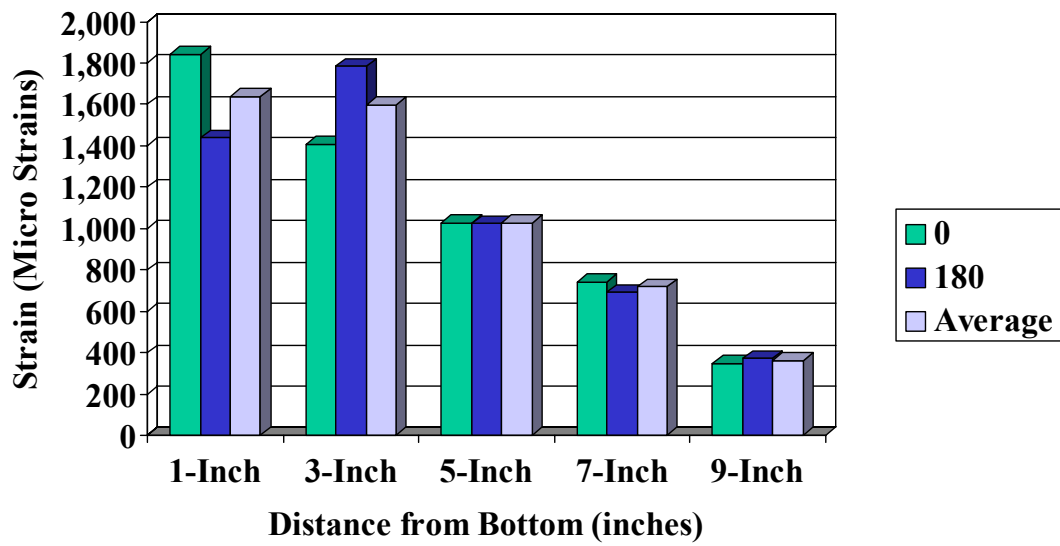


Figure 4-9 Adjusted steel strains, test 3

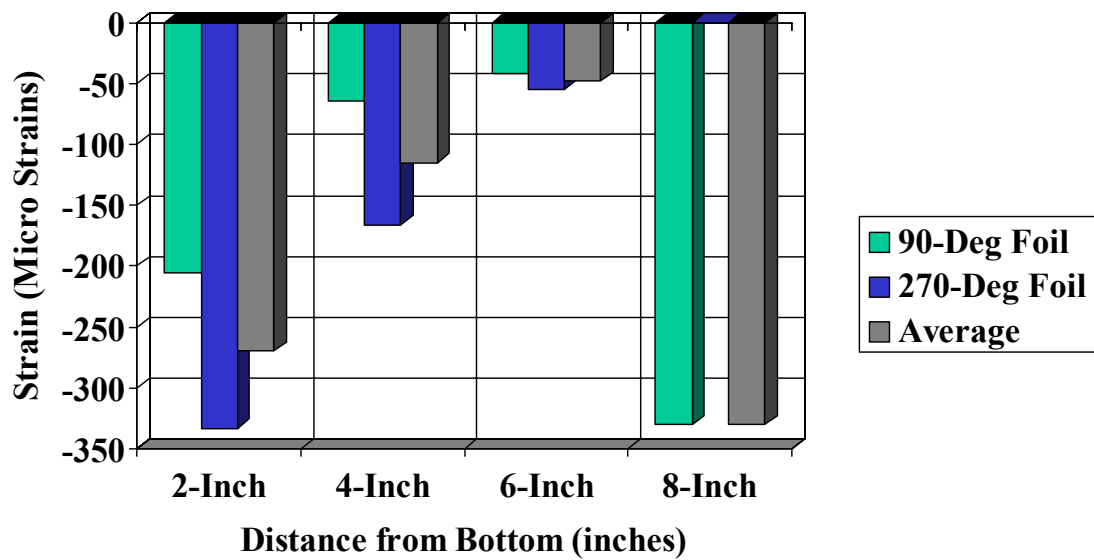
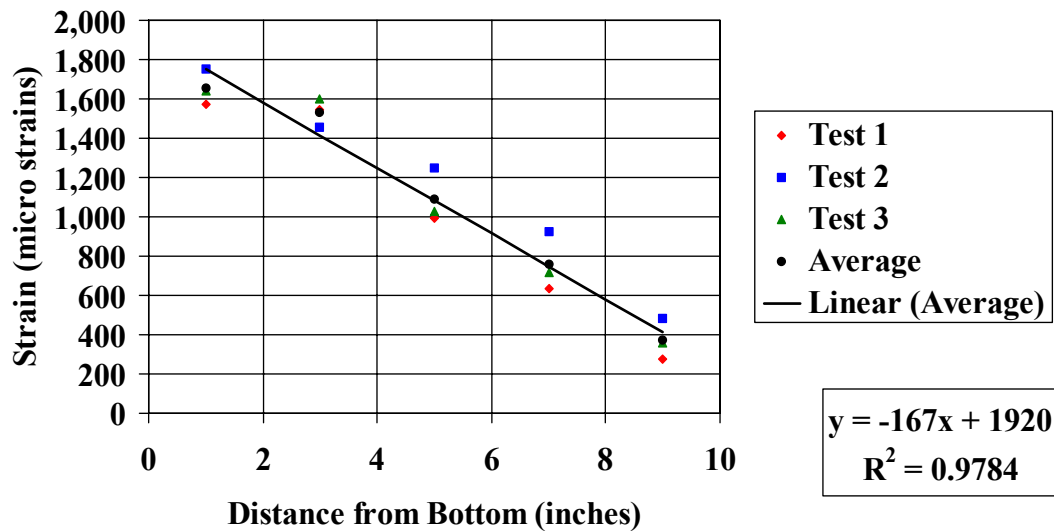


Figure 4-10 Adjusted concrete strains, test 3

stress in the concrete. When this stress reached the tensile strength of the concrete, radial cracks formed, breaking the sample into three pieces, and the steel bar was released.

The average steel strains as we begin at the bottom of the sample were, 1,655 micro strains a 1-inch, 1,533 micro strains at 3-inches, 1,088 micro strains at 5-inches, 758 micro strains at 7-inches and 372 micro strains at 9-inches. The average coefficient of variation for this data was 18.2. If we plot the data (Figure 4-11) we find a linear relationship as expressed by equation 4.1:



**Figure 4-11 Adjusted steel strains, quasi-static loading, 10-inch diameter samples, #8 deformed bars**

$$Y = -167X + 1920 \quad (4.1)$$

with an  $R^2 = 0.9784$ . By setting equation 4.1 equal to the yield stress of 2,000 micro strains, we can calculate the embedment length required to develop the full yield strength of the steel bar for this loading, bar and confinement combination. For a #8 deformed



bar, embedded in a 10-inch diameter cylinder loaded quasi-statically, the required embedment length is 10-1/2-inches.

Since only three of the fiber optic gages returned useful data, it is difficult to make any definitive statements regarding the comparison of concrete strain measured with the fiber optic gages vs. that measured with the foil gages, see. However, as shown in Appendix B, there appears to be no significant variations between the two different types of gages. The average concrete strains beginning at the bottom were -255.3 micro strains at 2-inches, -152.7 micro strains at 4-inches, -69.8 micro strains at 6-inches, and -108.8 micro strains at 8-inches, Figure 4-12. On this set of specimens, and as will be seen on the remaining tests, there appears to be no relationship between strain and location. In fact, there is more variation between strains at the same location and test i.e. test 2 CS-01 (-80 micro strains) and CS-02 (-667 micro strains) than there is between the average strains at different locations i.e. -255.3 micro strains at 2-inches and -69.8 micro strains at 6-inches. Although there is a very high variation in concrete strain, this is not unusual, when you consider the non-homogenous nature of concrete, especially on the micro level. This is caused by not only the variations in strength of the different basic materials, i.e., large aggregate vs. small aggregate vs. cement, but also on controllable variations in the production process, i.e. entrapped air, aggregate separation, moisture evaporation rates, etc. The average concrete strain was -147 micro strains.

#### **4.2 Impact Loading of a #8 Deformed Bar Embedded in a 10-inch Diameter Concrete Cylinder**

Tests 4, 5, and 6 consisted of a 10 in. diameter cylinder with a number eight deformed bar subjected to an impact loading. The maximum loads applied to the three specimens

before failure were 71,300 lbs. at time  $t=4.06$  msec for test 4, 64,215 lbs. at time  $t=4.5$  msec, and 77,980 lbs. at time  $t=3.92$  msec. In order to compare all data under

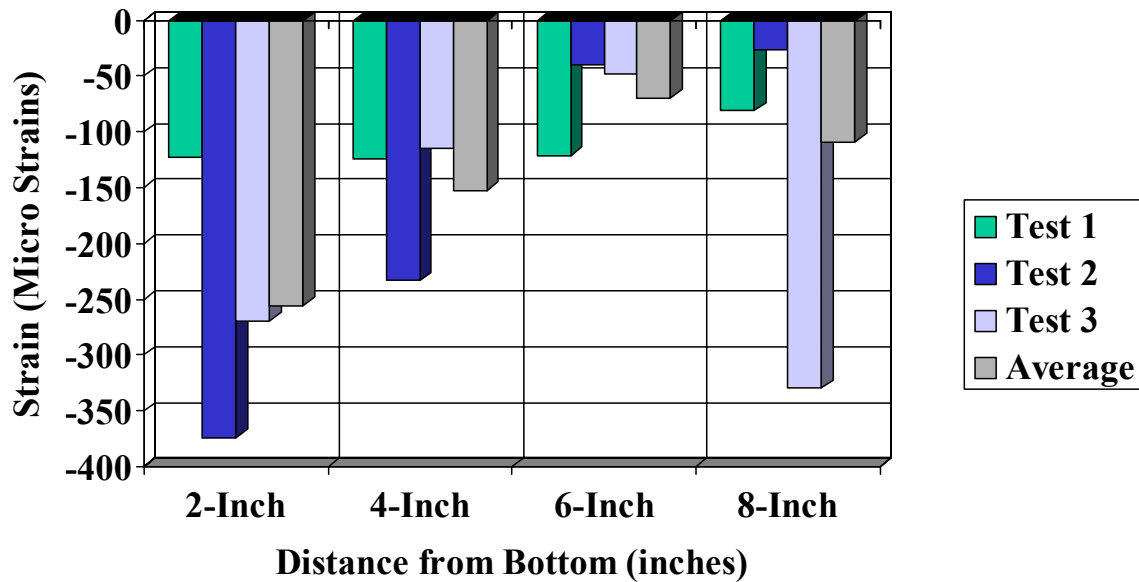


**Figure 4-12 Adjusted concrete strains, quasi-static loading, 10-inch diameter samples, #8 deformed bars**

comparable loading conditions, a maximum load all of 64,215lbs. will be used for these three tests.

#### 4.2.1 Test 4

On test 4, a total of 27 channels of active instrumentation were run, of these, 21 returned useful data for a total data return of 77.8%. These consisted of one load-cell, successful, ten steel strains, nine of which were successful, eight concrete strains, seven of which were successful, and eight fiber optic concrete strains, four of which were successful. The maximum load of 64,215 lbs. was reached at  $t=3.72$  msec for a loading

rate of 32,000 lbs/msec. The sample failed due to radial cracking of the concrete and broke into three pieces.

The steel strains varied from 2,919 micro strains for SS-01 down to 299 micro strains for SS-09. The individual and average values of strain at each of the five positions can be found in Appendix B. The foil concrete strains varied from -233 for CS-03 down to -21 for CS-07. The fiber optic gauges returned values ranging from -106 micro strains for FO-0 1 down to -2 micro strains for FO-0 5.

#### 4.2.2 Test 5

On test 5 a total of 19 channels of active instrumentation were run, of these, 11 returned useful data for a data return of 57.9%. These consisted of one load sale, successful, ten steel strains, all ten of which were successful, and eight fiber optic gages, none of which were successful. The maximum load of 64,215 pounds was obtained in 2.77 msec. The linear portion of the loading rate was 19,600 lbs./msec. The specimen failed due to radial cracking of the concrete.

The steel strains varied from 2,930 micro strains for SS-02 down to 273 micro strains for SS-10. There were no successful concrete strain records for this test.

#### 4.2.3 Test 6

Test 6 contains 19 channels of active instrumentation with 15 returning usable data for a data returned all 78.9%. These consisted of one load sale, successful, ten steel strains, eight successful, and eight foil concrete strains of which six were successful. No fiber optic gauges were included in this test. The maximum load of 64,215 pounds was obtained in 2.77 msec, the linear portion of the record yielded a loading rate of

31,000 lbs./msec. The sample failed due to radial cracking of the concrete, and broke into four separate pieces. There was the typical crushing of the concrete on the leading edges of the steel bar deformations, then clean separation of the remainder of the concrete-steel interface.

The steel strains varied from 1,647 micro strains for SS-03 down to 283 micro strains for SS-10. The foil concrete strains varied from -94 micro strains for CS-01 down to -3 micro strains for CS-08. There were no fiber optic gages in this test.

#### 4.2.4 Evaluation of Results of Tests 4, 5, and 6

The average load applied to the three samples before failure was 71,165 lbs. All three samples failed due to radial cracking of the concrete and broke into three or four separate pieces, Figure 4-13. There was the usual crushing of the concrete on the leading edge of the deformations on the steel bar.

The average steel strains beginning at the bottom of the sample were, 2,886 micro strains at 1-inch, 1,928 micro strains at 3-inches, 1,350 micro strains at 5-inches, 734 micro strains at 7-inches and 307 micro strains at 9-inches. The average coefficient of variation for this data was 8.1. The data (Figure 4-14) has a linear relationship expressed by equation 4.2:

$$Y = -318X + 3030 \quad (4.2)$$

with an  $R^2 = 0.9945$ . Once again, if we set equation 4.2 equal to the yield stress of 2,000 micro strains, we can calculate the required embedment length as 6.75-inches.

Although, as in the earlier test, there was significant variation between the individual concrete strains, there was no clear difference between the F.O. data and the foil gage data. Also, there was no pattern to the average concrete strains at different locations

(Figure 4-15). The average concrete strains beginning at the bottom were  $-94.6$  micro strains at 2-inches,  $-118.6$  micro strains at 4-inches,  $-33$  micro strains at 6-inches, and  $-20$  micro strains at 8-inches. The average concrete strain was  $-61$  micro strains.

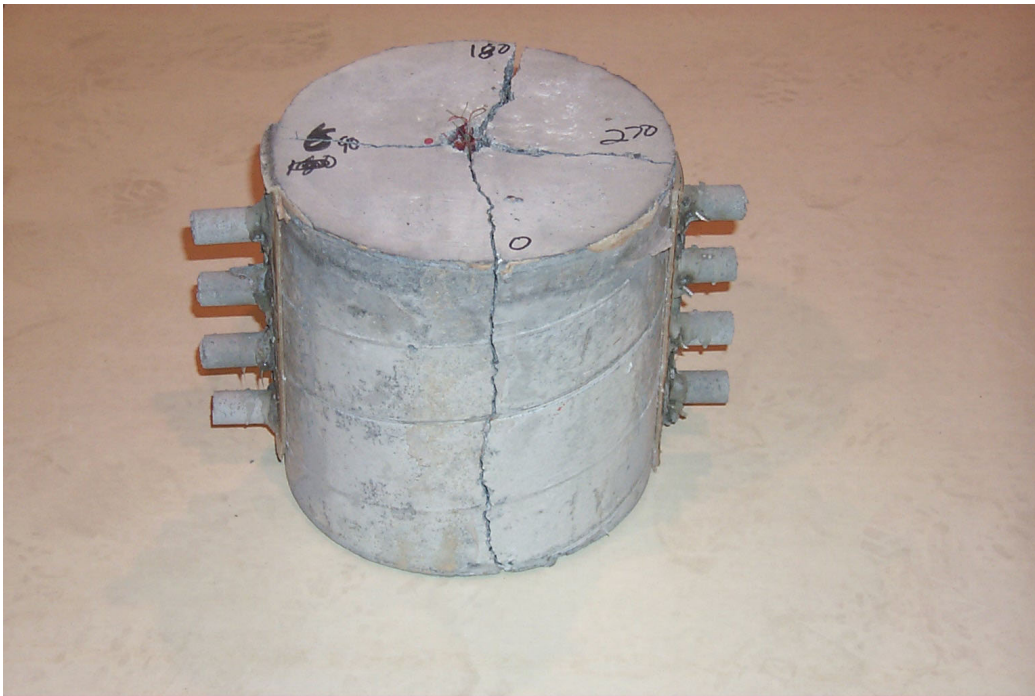


**Figure 4-13 Test specimen 6 post-test**

#### **4.3 Dynamic Loading of a #8 Deformed Bar Embedded in a 10-inch Diameter Concrete Cylinder**

Tests 7, 8, and 9 consisted of a 10 in. diameter cylinder with a #8 deformed bar loaded dynamically. The maximum load applied to the three specimens before failure were 70,300 lbs. at time  $t = 117$  msec for test 7, 69,050 lbs. time  $t = 132$  msec for test 8 and 66,350 lbs. at time  $t = 93$  msec for test 9. In order to compare all data under comparable loading conditions a maximum load of 66,350 lbs. will be used for these three tests.

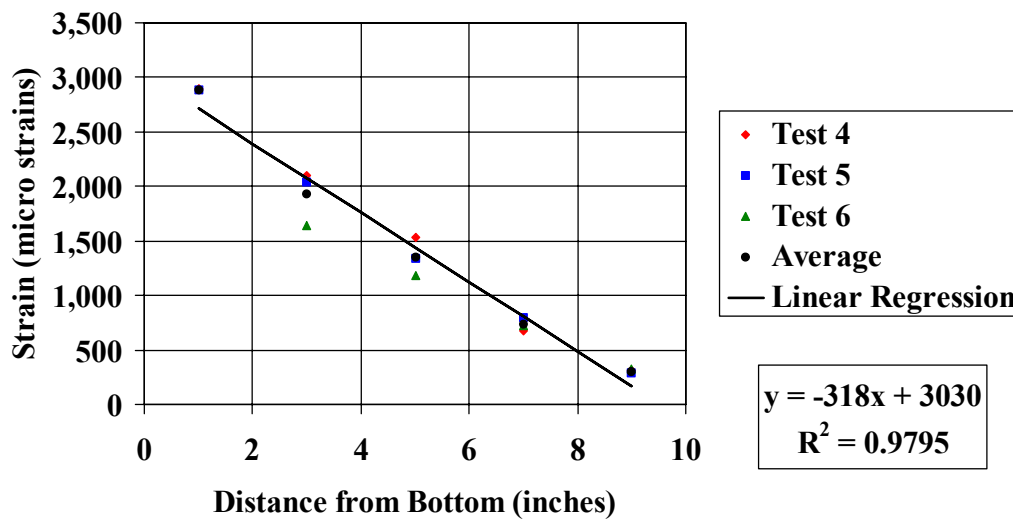


Figure 4-14 Adjusted steel strains, impact loading, 10-inch diameter sample, #8 deformed bar

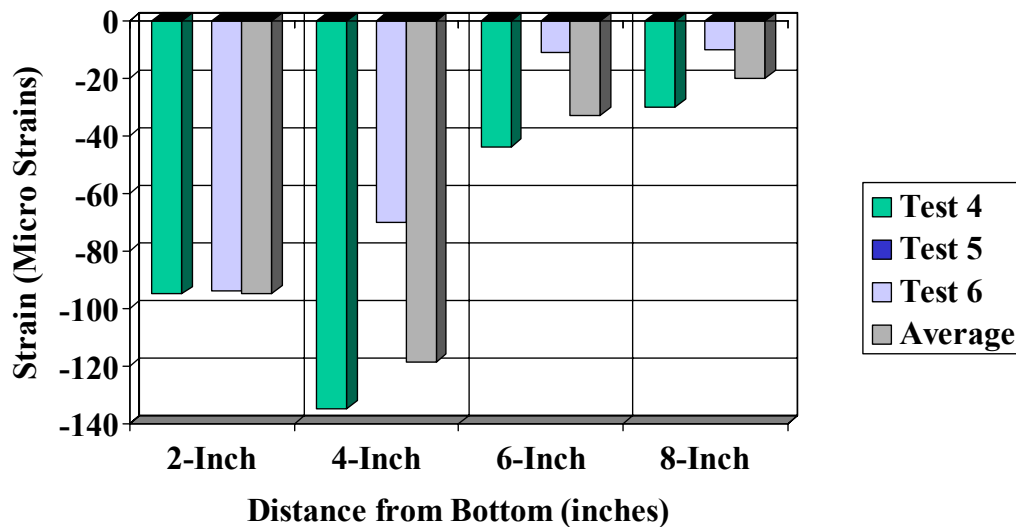


Figure 4-15 Adjusted concrete strains, impact loading, 10-inch diameter sample, #8 deformed bar

#### 4.3.1 Test 7

On test 7 a total of 27 channels of active instrumentation were run, of these, 24 returned useful data for a total data return of 88.9%. These consisted of one load-cell, successful, ten steel strains, eight of which were successful, eight foil concrete strains, all eight of which were successful, and eight fiber optic concrete strains, seven of which were successful. The adjusted maximum load of 66,350 lbs. occurred at  $t = 93$  msec. The loading rate was linear from time  $t = 0$  until  $t = 80$  msec, with a loading rate of 790. lbs./msec. From time  $T$ . equals 80 msec until failure at  $t = 117$  msec, the loading time was non-linear. The sample failed due to radial cracking of the concrete, and broke into three separate pieces.

The steel strains varied from 2,386 micro strains for S. S. for down to 367 micro strains for SS-10. The foil concrete strains varied from -425 for CS-03 down to -5 micro strains for CS-04. The fiber optic strains recorded values ranging from -317 micro strains for FO-02 down to -90 micro strains for FO-05.

#### 4.3.2 Test 8

On test 8 a total of 19 channels of active instrumentation were run, of these 16 returned useful data for a data returned of 84.2%. These consisted of one load cell, successful, ten steel strains seven of which were successful, eight foil concrete strains, all eight of which were successful. There were no fiber-optic gages in this test. The maximum load of 66,350 lbs. was obtained at 118 msec. The load cell record is very similar to the one obtained on test 7. A linear loading rate of 740 lbs./msec was obtained from  $t = 0$  msec until  $t = 80$  msec. The loading rate was nonlinear from  $t = 80$  msec until failure at  $t = 132$  msec. The sample failed due to radial cracking and broke into three pieces.

The steel strains varied from a high value of 2,763 micro strains for SS-04 to a low value of 386 micro strains for SS-10. The foil concrete strains varied from -167 micro strains for CS-02 down to -6 micro strains for CS-07.

#### 4.3.3 Test 9

On test nine a total of 19 channels of active instrumentation were run, of these, 16 returned useful data for a data return of 84.2%. These consisted of one load cell, successful, ten concrete strains seven of which were successful, and eight foil concrete strains, all eight of which were successful. The maximum load of 66,350 lbs. was obtained in 92 msec. The loading rate of 825 lbs./msec remained linear until  $t = 80$  msec. The sample failed due to radial cracking and broke into three pieces. The loading rate was then nonlinear until failure at  $t = 92$  msec.

The steel strains varied from 2,280 micro strains for SS-03 down to 545 micro strains for SS-10. The foil concrete strains varied from a high value of -669 micro strains for CS-04 to less than one micro strain for CS-07.

#### 4.3.4 Evaluation of Results of Tests 7, 8, and 9

The average load applied to the three samples before failure was 68,566 lbs. All three samples failed due to radial cracking of the concrete and broke into three separate pieces, Figure 4-16. There was crushing of the concrete on the leading edge of the deformations on the steel bar.



The average steel strains beginning at the bottom of the sample were: 2,384 micro strains at 3-inches, 1,645 micro strains at 5-inches, 966 micro strains at 7-inches and 566 micro strains at 9-inches. All gages at the 1-inch positioned failed. The average coefficient of variation for this data was 21. The data (Figure 4-17) had a linear relationship as expressed by equation 4.3:

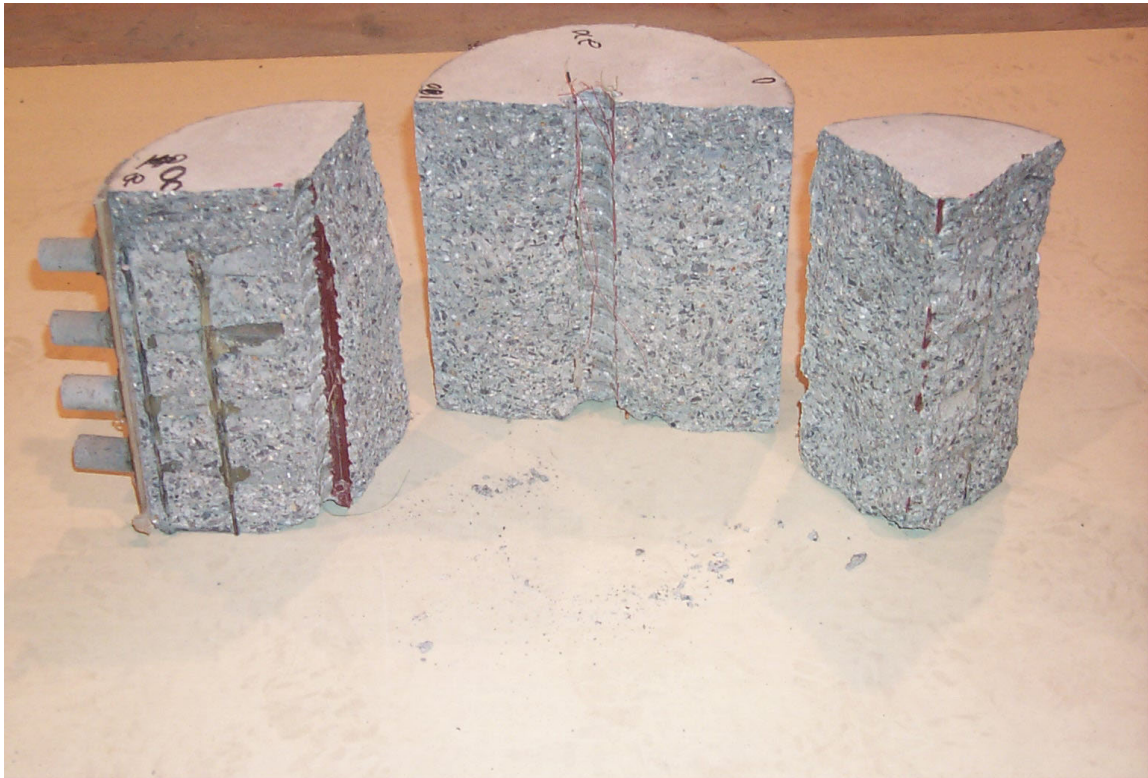


**Figure 4-16 Test specimen 8 post-test**

$$Y = -307X + 3230 \quad (4.3)$$

with an  $R^2 = 0.9837$ . Using equation 4.3, the required embedment length is 6-inches.

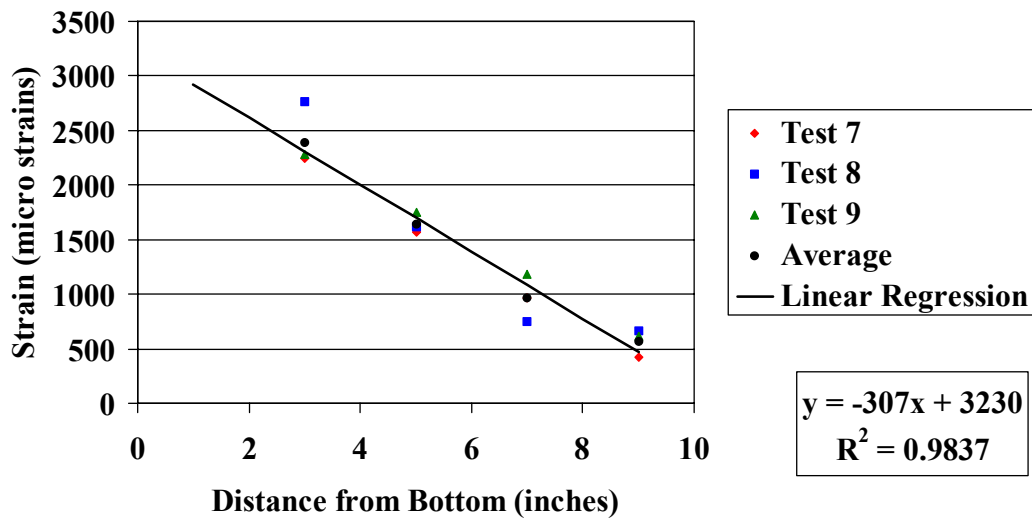


**Figure 4-17 Adjusted steel strains, dynamic loading, 10-inch diameter sample, #8 deformed bar**

Once again, there was larger variation between strains at the same location than there were between the strains measured with the two different types of gages or the strains at various locations. The average strains (Figure 4-18) beginning at the bottom were -123.3 micro strains at 2-inches, -227 micro strains at 4-inches, -51.5 micro strains at 6-inches, and -57.6 micro strains at 8-inches. The average strain was -114.6 micro strains.

#### **4.4 Impact Loading of a #8 Deformed Bar Embedded in a 20-inch Diameter Concrete Cylinder**

Tests 10, 11, and 12 consisted of a 20 in. diameter cylinder with a number eight deformed bar subjected to an impact loading. The maximum loads applied to the three test specimens before failure were 77,490 lbs. at  $t = 3.8$  msec for test 10, 93,550 lbs. at  $t = 6.5$  msec for test 11 and 87,240 lbs. at  $t = 7.4$  msec. In order to compare all data under

comparable loading conditions the maximum load of 77,490 lbs., which was obtained on test number 10, will be used.

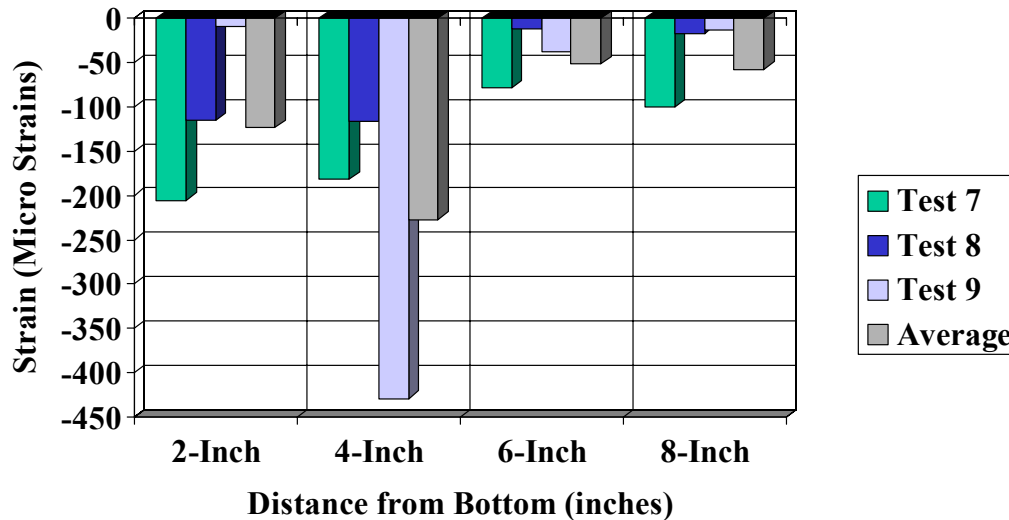


**Figure 4-18 Adjusted concrete strains, dynamic loading, 10-inch diameter sample, #8 deformed bar**

#### 4.4.1 Test 10

On test 10, twenty-one channels of active instrumentation were run, of these, 17 returned good data for a data return of 81%. These consisted of one load cell, successful, ten steel strains, eight of which were successful, eight foil concrete strains, seven of which were successful, and two fiber-optic strains, one of which was successful. The maximum load of 77,490 lbs. was obtained and 3.8 msec. The test specimen failed when the weld on the connection block broke. The data record indicates that the loading rate was non-linear for approximately the first 1.5 msec, from 1.5 until 3.8 msec the loading rate was linear with a loading of 32,700 lbs./msec.

The steel strains varied from a maximum of 2,390 micro strains for SS-04 down to a minimum of 390 micro strains for SS-10. The foil concrete strains varied from a maximum of -435 micro strains for CS-05 down to a minimum of -82 micro strains for CS-01. The one successful fiber-optic record was FO-01, which returned a peak value of -138 micro strains.

#### 4.4.2 Test 11

On test 11, 27 channels of active instrumentation were run with 17 returning good data for a data return of 63%. This consisted of one load cell, which was successful, ten steel strains, two of which were successful, eight foil concrete strains, all eight of which were successful, and eight fiber-optic gages, six of which were successful. The adjusted maximum load of 77,490 lbs. was obtained in 4.79 msec. The data record shows the customary two msec nonlinear beginning followed by a linear loading of 33,400 lbs./msec until  $t = 3.3$  msec. There is then a change in slope to 8,600 lbs./msec until ultimate failure at  $t = 6.49$  msec. The sample failed due to yielding of the weld joints on the connection block.

The maximum steel strains recorded on this test was 754 micro strains for SS-09 and the minimum was 487 micro strains for SS-10. The concrete foil gages recorded a maximum strain of -479 micro strains for CS-01 to a minimum of -16 micro strains for CS-04. The fiber-optic strains varied from a maximum of -429 micro strains for FO-07 to a minimum of -85 micro strains for FO-01.

#### 4.4.3 Test 12

On test 12, a total of twenty-seven channels of active instrumentation were run with 20 channels returning usable data. This gave a data return of 74.1%. These consisted of one load cell, which was successful, ten steel strains, five of which were successful, eight foil

concrete strains, seven of which were successful and eight fiber-optic strains, seven of which were also successful. The adjusted maximum load of 77,490 lbs. was obtained in 5.4 msec. The loading rate was nonlinear on both ends with a linear loading rate of 33,300 lbs./msec between  $t = 2$  msec and  $t = 4$  msec. The load then drops drastically to around 12 msec, at which time it begins to rebound back to around 90,000 lbs. This second loading is not real but most likely caused by the loader abruptly reaching the limits of its stroke. The sample had an identical failure to the samples in test 10 and 11.

The maximum steel strain recorded was 1,790 micro strains for SS-06 and the minimum was 282 micro strains for SS-09. The foil concrete strains varied from a maximum of -517 micro strains for CS-01, down to a minimum of -20 micro strains for CS-05. The fiber optic strains varied from a maximum of -267 micro strains for FO-03, to a minimum of -13.6 micro strains for FO-02.

#### 4.4.4 Evaluation of Results of Tests 10, 11 and 12

The average load applied to the three samples before failure was 86,100 lbs. All three samples failed due to failure of the welds between the connecting block and the #8 reinforcing bar, Figure 4-19.

The average steel strains beginning at the bottom of the sample were 2,345 micro strains at 3-inches, 1,655 micro strains at 5-inches, 1,020 micro strains at 7-inches and 478 micro strains at 9-inches. All gages at the 1-inch positioned failed. The average coefficient of variation for this data was 22. The data (Figure 4-20) had a linear relationship as expressed by equation 4.4:

$$Y = -312X + 3250 \quad (4.4)$$

with an  $R^2=0.9972$ . Setting  $Y=2,000$  micro strains, the embedment length required to reach the yield limit of the steel is 6-inches.



**Figure 4-19 Test specimen 10 post-test**

The concrete strains showed the same large variations seen in the previous tests. The average concrete strains beginning at the bottom were -192.3 micro strains at 2-inches, -177.6 micro strains at 4-inches, -230.9 micro strains at 6-inches, and -220.6 micro strains at 8-inches. These strains are summarized in Figure 4-21. The average concrete strain was -208.4 micro strains.

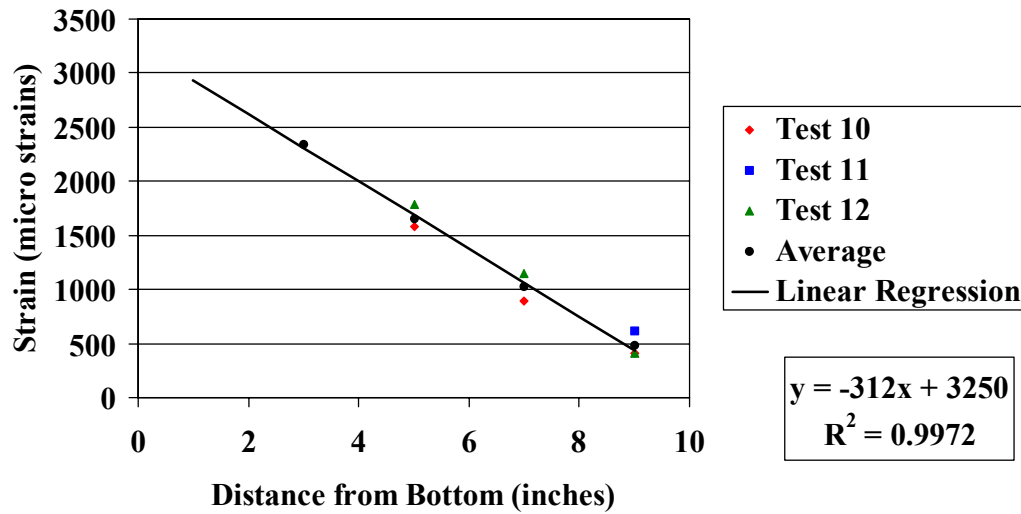


Figure 4-20 Adjusted steel strains, impact loading, 20-inch diameter sample, #8 deformed bar

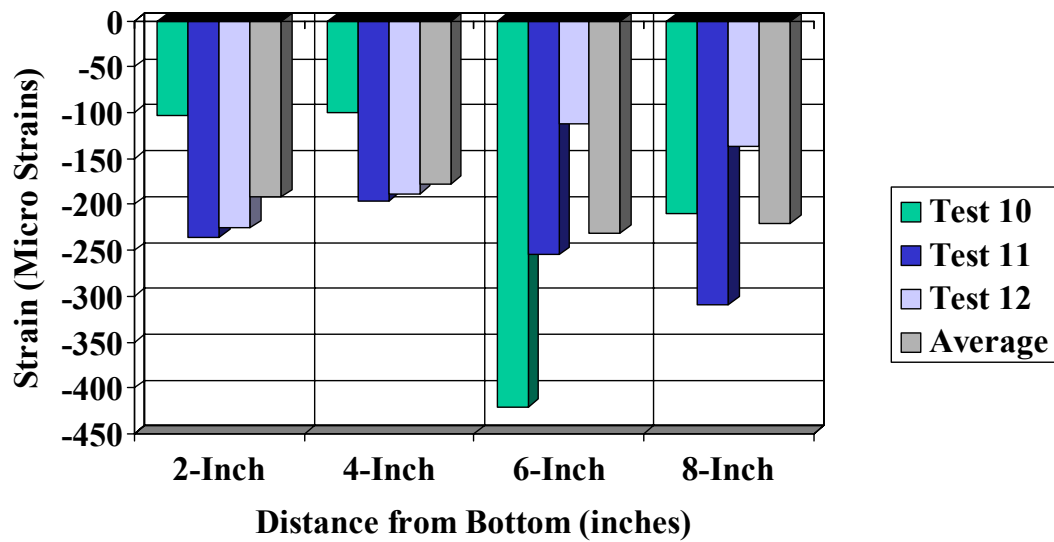


Figure 4-21 Adjusted concrete strains, impact loading, 20-inch diameter sample, #8 deformed bar

#### **4.5 Dynamic Loading of a #8 Deformed Bar Embedded in a 20-inch Diameter Concrete Cylinder**

Tests 13, 14 and 15 consisted of a 20 in. diameter cylinder with main #8 deformed bar loaded dynamically. The maximum loads applied to the three test specimens before failure were 86,770 lbs. at  $t = 200$  msec for test 13; 72,750 lbs. at  $t = 121$  msec for test 14; and 85,130 lbs. at  $t = 194$  msec for test 15. The lower value of 72,750 obtained on test 14 will be used for these three tests.

##### **4.5.1 Test 13**

On test 13, 27 channels of active instrumentation were run with 18 channels returning usable data for a return of 66.7%. These consisted of one load cell, successful, ten steel strains, all of which were successful, eight foil concrete strains, all eight of which were successful, and eight fiber-optic strains, five of which were successful. The adjusted maximum load of 72,750 lbs. was obtained and 115 msec. The loading remains linear at 800 lbs./msec until  $t = 90$  msec, at which time there is a change in slope until failure at  $t = 200$  msec. The specimens failed by yielding of the steel bar. It is the yielding of the steel bar which caused the change in slope at  $t = 90$  msec.

The steel strains varied from a maximum 1,682 micro strains for SS-05 down to 282 micro strains for SS-09 the concrete foil strain gages varied from a maximum of -294 for CS-01 down to a minimum of -48 for CS-04. The fiber optic strains varied from -280 for FO-08 down to -88 for FO-05.



#### 4.5.2 Test 14

On test 14, a total of 27 channels were run with 20 returning good data for a total return 74.1%. These consisted of one load cell, ten concrete strains, five of which were successful, eight foil concrete strains, all eight of which were successful, and eight fiber optic strains, six of which were successful. The maximum load of 72,750 lbs. was obtained in 121 msec. The loading rate remained linear at 780 lbs./msec until  $t = 85$  msec, at which time there is a change in slope until failure at 121 msec. The sample failed due to yielding of the steel bar; it is this yielding which caused the change in slope.

The steel strains varied from 2,690 micro strains for SS-04 down to 420 micro strains for SS-10. The foil concrete strains varied from a maximum of -331 micro strains for CS-06 down to five micro strains for CS-07. The fiber optic strains varied from -328 mica strains for FO-05 down to -158 micro strains for FO-06.

#### 4.5.3 Test 15

On test 15, a total of 27 channels of instrumentation were run, and 22 returned usable data for a return of 81.5%. These consisted of one load cell, ten steel strains, eight of which were successful, eight concrete strains, seven of which were successful, and eight fiber optics strain gages, six of which were successful. The adjusted maximum load of 72,750 lbs. was obtained in 126 msec. The load cell data plot shows the customary linear loading rate of 780 lbs./msec until  $t = 90$  msec and then the reduction in slope until the failure at  $t = 194$  msec. Once again this change in slope is due to the yielding of the steel bar.

The steel strains varied from a maximum of 3,600 into micro strains for SS-03 down to 270 mica strains for SS-09. The foil concrete strains varied from a maximum of -279

more strains for CS-05 to -29 micro strains for CS-04 the fiber optic readings varied from a maximum of -384 micro strains for FO-01 to -87 micro strains for FO-04.

#### 4.5.4 Evaluation of Results of Tests 13, 14 and 15

The average load applied to the three samples before failure was 81,550 lbs. Samples 13 and 14 failed due to yielding of the steel bar above the connection block as shown in Figure 4-22. Sample 15 failed due to the welds on the connection block breaking.

The average steel strains beginning at the bottom of the sample were, 3,074 micro strains at 3-inches, 1,798 micro strains at 5-inches, 1066 micro strains at 7-inches and 434 micro strains at 9-inches. All gages at the 1-inch positioned failed. The average coefficient of variation for this data was 15.3. The data (Figure 4-23) had a linear relationship as expressed by equation 4.5:

$$Y = -433X + 4190 \quad (4.5)$$

with an  $R^2 = 0.9706$ . Setting  $Y = 2,000$  micro strains, we calculate the embedment length required to reach the yield strength of the steel as 5-inches.

The average concrete strains beginning at the bottom were -184.6 micro strains at 2-inches, -162.7 micro strains at 4-inches, -176.7 micro strains at 6-inches, and -167.4 micro strains at 8-inches (Figure 4-24). The average concrete strain was -171.9 micro strains.

#### 4.6 Quasi-Static Loading of a #8 Deformed Bar Embedded in a 20-inch Diameter Concrete Cylinder

Test 16, 17 and 18 consisted of a 20 in. diameter cylinder with a number eight deformed bar loaded statically. The maximum loads applied to the three test specimens before failure were 71,770 lbs. at  $t = 578$  seconds for test 16, 60,600 lbs. at  $t = 288$  seconds, for test 17, and 63,480 lbs. at  $t = 337$  sec., for test 18. In order to compare all

data under comparable loading conditions a maximum load of 60,600 lbs. will be used for these three tests.



Figure 4-22 Test specimen 13 post-test

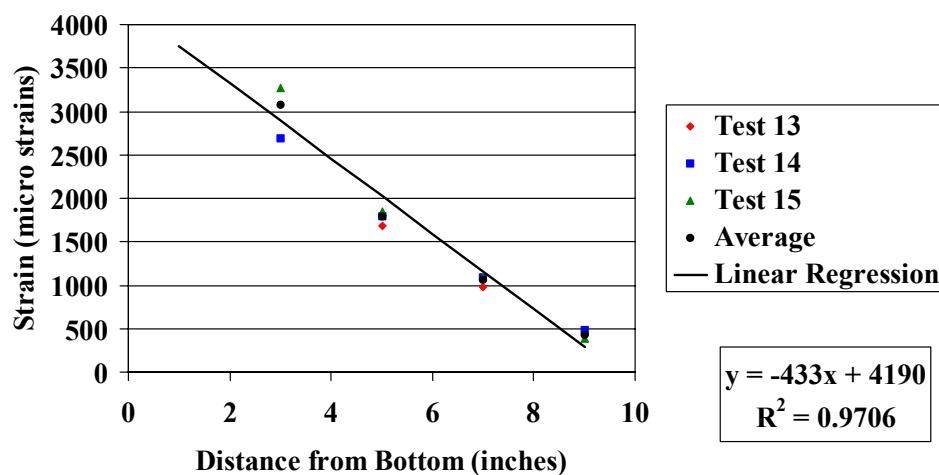
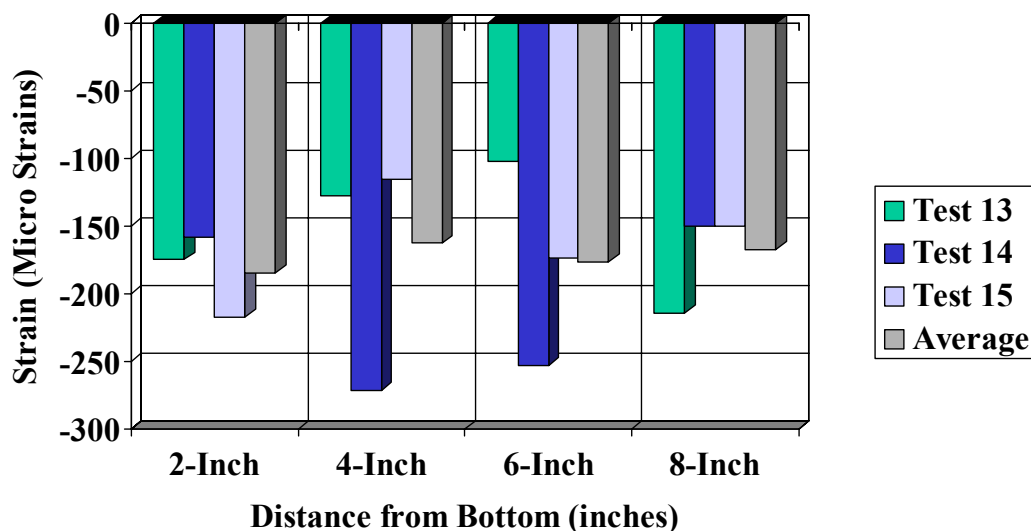


Figure 4-23 Adjusted steel strains, dynamic loading, 20-inch diameter sample, #8 deformed bar



**Figure 4-24 Adjusted concrete strains, dynamic loading, 20-inch diameter sample, #8 deformed bar**

#### 4.6.1 Test 16

On test 16, a total of 27 channels of active instrumentation were run, of these 22 channels returned usable data for a data return of 81.5%. These consisted of one load cell, successful, ten steel strains, nine of which were successful, eight foil concrete strains, all eight of which were successful, and eight fiber optic concrete strains, four of which were successful. The adjusted maximum load of 60,600 lbs. was obtained in 491 seconds. The load cell indicated a linear loading rate of 210 lbs./seconds until  $t = 480$  at which time there is a slight reduction in the loading rate until failure occurred at  $t = 578$  seconds. The sample failed due to two radial cracks along the  $0^{\circ} - 180^{\circ}$  azimuth. The concrete showed the typical crushing on the leading edges of the steel deformations.

The steel strains varied from a maximum of 7,500 micro strains for SS-01 to a minimum of 268 micro strains for SS-09. The foil concrete strains varied from a maximum of -744 for CS-01 to a minimum of -6 micro strains for CS-03. The fiber optic concrete strains varied from a maximum of -193 for FO-05, to a minimum of -152 micro strains for FO-08.

#### 4.6.2 Test 17

On test 17, a total of 27 channels of active instrumentation were run. Of these, 20 returned good data for a total data return of 74%. These consisted of one load cell, successful, ten steel strains, all ten of which were successful, eight foil concrete strains, seven of which were successful, and eight fiber-optic concrete strains, two of which were successful. The maximum load of 60,600 lbs. was obtained in 288 seconds. The load cell showed a linear loading rate of 240 lbs./seconds until failure at  $t = 288$  seconds. The failure mode for this test was identical to test 16 with radial cracks forming along the  $0^0 - 180^0$  degree azimuth.

The steel strains varied from a maximum of 8,000 micro strains for SS-02 to a minimum of 388 micro strains for SS-09. The foil concrete strains varied from a maximum of -286 micro strains for CS-01 to a minimum of -26 micro strains for CS-06. The two successful fiber optic strains were -144 micro strains for FO-07 and -178 micro strains for FO-08.

#### 4.6.3 Test 18

On test 18, a total of 27 channels of active instrumentation were run with 23 returning good data for a data return of 85.2%. These consisted of one load cell, successful, ten

steel strains, all ten of which were successful, eight foil concrete strains, seven of which were successful, and eight fiber optic concrete strains, five of which were successful. The adjusted maximum load of 60,600 lbs. was obtained in 321 seconds. The load cell showed a linear loading rate of 240 lbs./seconds until  $t = 320$  seconds at which time there is a reduction in loading rate until failure at  $t = 337$  seconds. The sample failed due to radial cracking along the  $0^0 - 180^0$  azimuth.

The steel strains varied from a maximum of 13,340 micro strains for SS-02, to a minimum of 275 micro strains for SS-10. The foil concrete strains varied from a maximum of -515 micro strains for CS-03 to a minimum of -59 micro strains for CS-06. The fiber optic concrete strains varied from a -203 for FO-06 down to -115 micro strains for FO-04.

#### 4.6.4 Evaluation of Results of Tests 16, 17 and 18

The average load applied to the three samples before failure was 65,300 lbs. All three samples failed due to radial cracking of the concrete and broke into two separate pieces, with the crack forming along the  $0^0 - 180^0$  azimuth, Figure 4-25. There was crushing of the concrete on the leading edge of the deformations on the steel bar.

The average steel strains beginning at the bottom of the sample were, 9,022 micro strains at 1-inch, 1866 micro strains at 3-inches, 1,327 micro strains at 5-inches, 866 micro strains at 7-inches and 356 micro strains at 9-inches. If we disregard the strain data from the 1-inch position, which was clearly in the plastic range, we get an average coefficient of variation for this data of 12 and a linear relationship (Figure 4-26) expressed by equation 4.6:

$$Y = -250X + 2600 \quad (4.6)$$

with an  $R^2=0.9992$ . The required development length required to reach the yield strength of the bar is 7.6-inches.

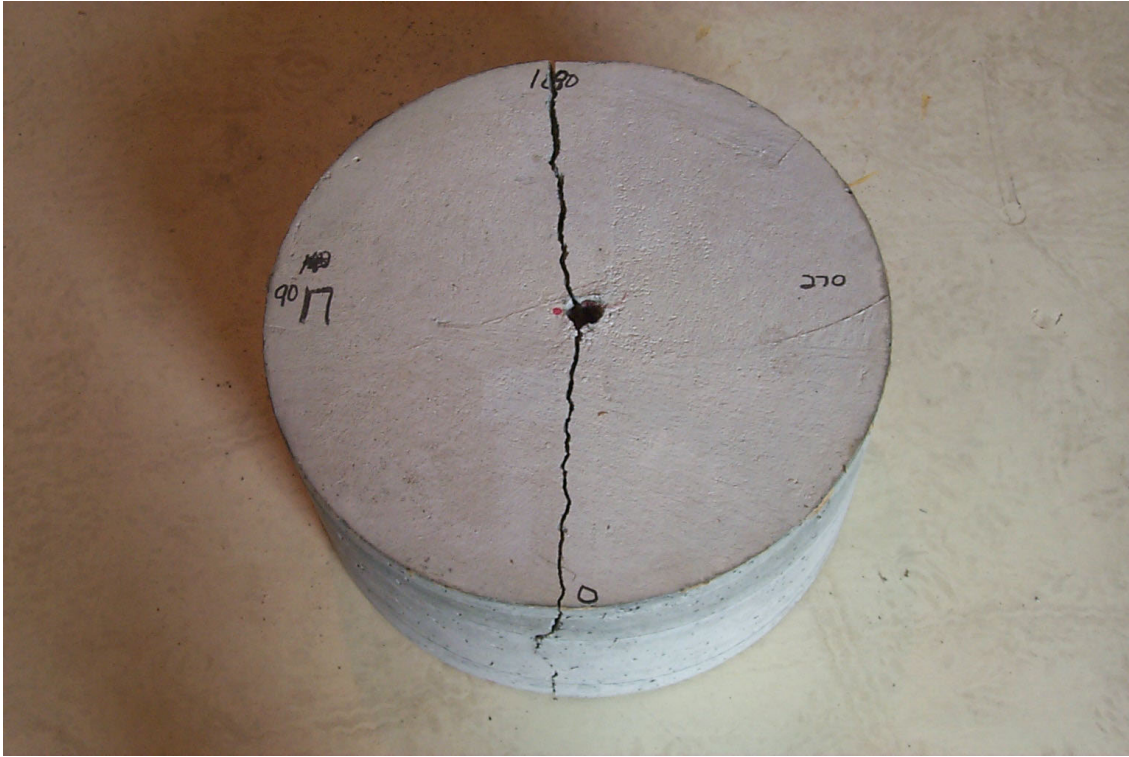


**Figure 4-25 Test specimen 17 post-test**

The average concrete strains beginning at the bottom were  $-331.8$  micro strains at 2-inches,  $-160.7$  micro strains at 4-inches,  $-136.9$  micro strains at 6-inches, and  $-159.5$  micro strains at 8-inches (Figure 4-27). The average strain was  $-180$  micro strains. Except for the 2-inch position on this group of tests, the concrete strains in the 20-inch diameter samples were much more consistent than they were in the 10-inch diameter samples.

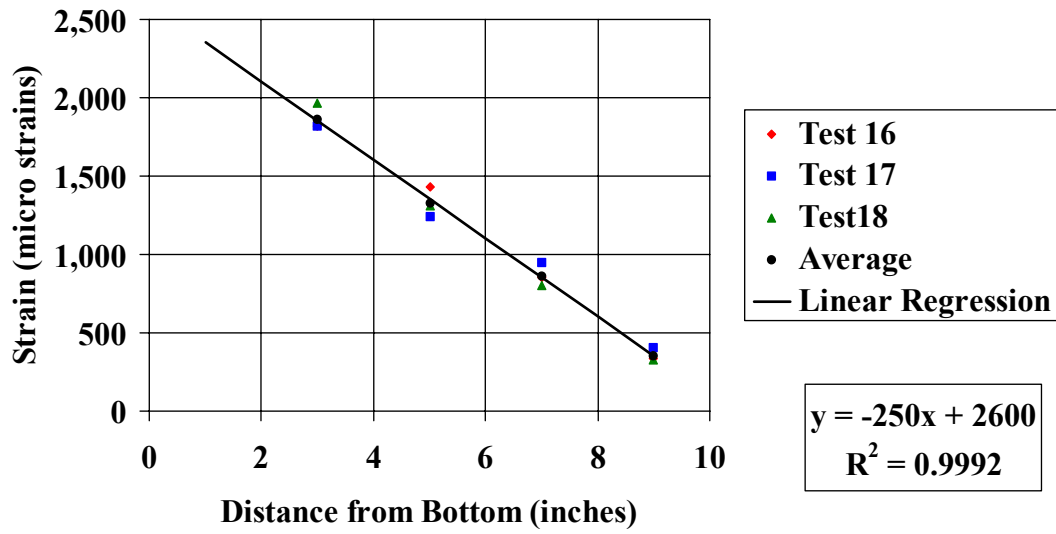


Figure 4-26 Adjusted steel strains, quasi-static loading, 20-inch diameter sample, #8 deformed bar

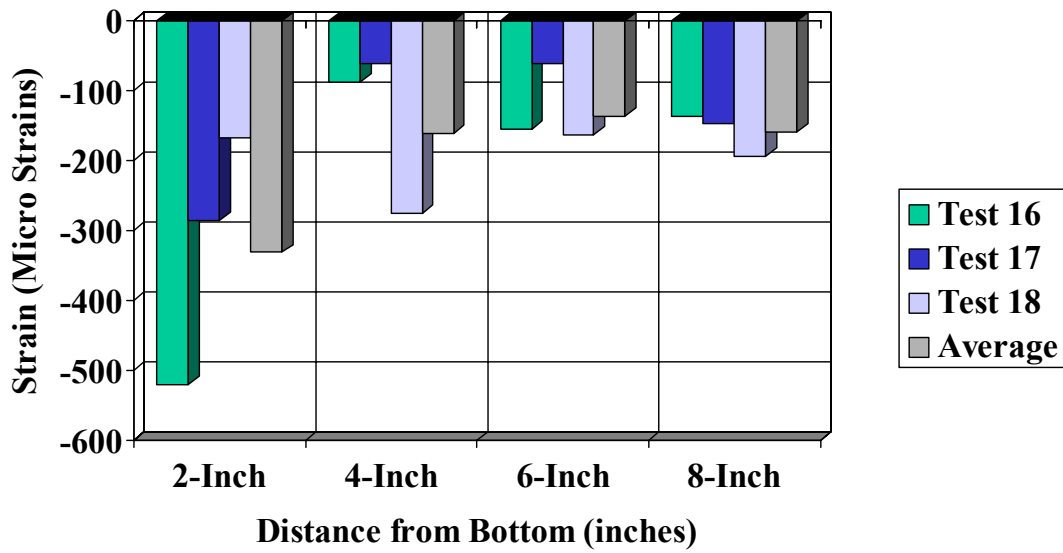


Figure 4-27 Adjusted concrete strains, quasi-static loading, 20-inch diameter sample, #8 deformed bar



#### **4.7 Impact Loading of a 1-inch Smooth Bar Embedded in a 20-inch Diameter Concrete Cylinder**

Tests 19 and 20 consisted of a 20-in.-diameter cylinder with a 1-in.-diameter smooth steel bar subjected to an impact loading. The maximum load obtained on these two tests was 25,908 lbs. at  $t = 2.5$  msec.

##### **4.7.1 Test 19**

On test 19 the triggering device failed resulting in no data being recorded for this test.

##### **4.7.2 Test 20**

On test 20, 19 channels of active instrumentation were run, and 17 of these returned good data for a data return of 89.5%. These consisted of one load cell, successful, ten steel strains, all ten of which were successful, and eight foil concrete strains, six of which were successful. There were no fiber optic gages on this test. The maximum load of 25,908 lbs. was obtained in 2.5 msec, the load decayed to 0 by  $t = 8.4$  msec. The loading was fairly uniform with a loading rate of 19,400 lbs./msec. The sample failed due to the smooth bar pulling out of the concrete.

The maximum steel strain was 1,000 micro strains for SS-02, and the minimum was 165 micro strains for SS-09. The concrete foil strain gages varied from -210 for CS-08 down to -39 for CS-01.

##### **4.7.3 Evaluation of Results of Tests 19 and 20**

Both samples failed due to the smooth steel bar pulling out of the concrete matrix, Figure 4-28. The maximum resisting force developed was 25,908 lbs.



**Figure 4-28 Test specimen 20 post-test**

The average steel strains beginning at the bottom of the sample were 885 micro strains at 1-inch, 731 micro strains at 3-inches, 570 micro strains at 5-inches, 356 micro strains at 7-inches, and 173 micro strains at 9-inches. Due to the limited number of data points, no reference can be made to the coefficient of variation, however, the available data does show a linear relationship (Figure 4-29) expressed by equation 4.7

$$Y = -90X + 993 \quad (4.7)$$

with an  $R^2 = 0.9961$ . For the smooth bar to be able to develop its full yield strength, an embedment length of 21-inches would be required.

There is very little data on the concrete strains for this set up since only two tests were planned, and one of those failed. Therefore there are only six concrete strain readings available. These tend to indicate a linear relationship to the data with the average strain beginning at the bottom being -39 micro strains at 2-inches, -90 micro strains at 4-inches,

-135 micro strains at 6-inches, and -210 micro strains at 8-inches (Figure 4-30).

However, due to the small number of samples, and the fact that none of the other concrete data showed this relationship is probable due to variation in the small sample population and would not be present in a larger population. The average concrete strain was -116.5 micro strains.

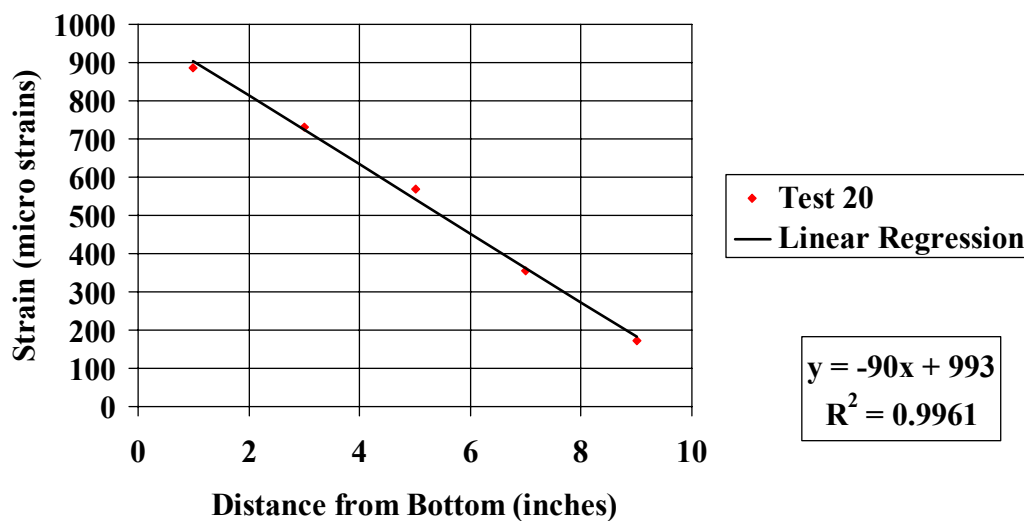


**Figure 4-29 Adjusted steel strains, impact loading, 20-inch diameter sample, 1-inch smooth bar**

#### **4.8 Dynamic Loading of a 1-inch Smooth Bar Embedded in a 20-inch Concrete Cylinder**

Tests 21 and 22 consisted of a 20 in. diameter cylinder with a 1 in. diameter smooth steel bar loaded dynamically. The maximum load obtained on these two tests was 24,670 lbs. at  $t = 30.8$  msec.

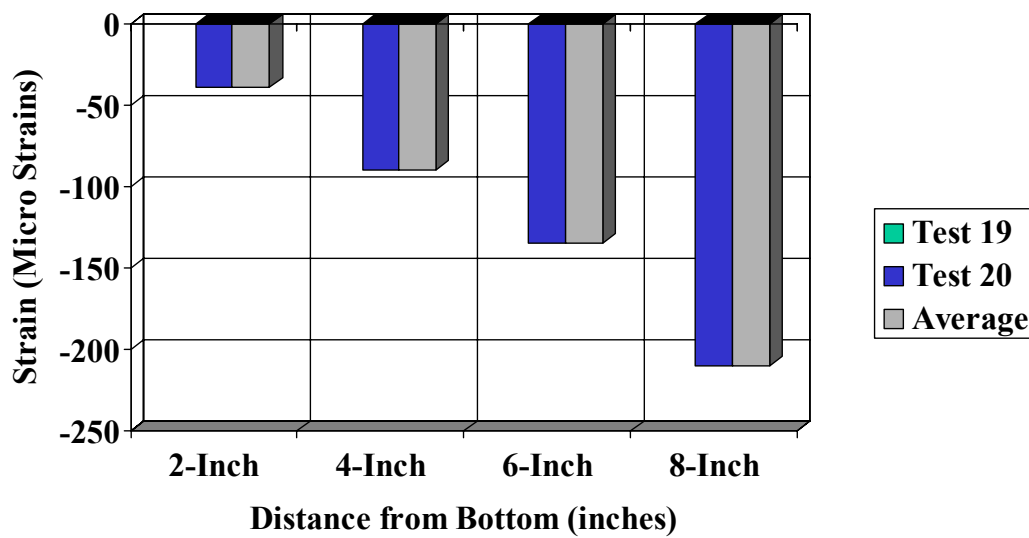


**Figure 4-30 Adjusted concrete strains, impact loading, 20-inch diameter sample, 1-inch smooth bar**

#### 4.8.1 Test 21

On test 21 the concrete-steel bond was accidentally broken during the installation of the test specimens. Therefore no useful data was obtained on this test.

#### 4.8.2 Test 22

On test 22, a total of 19 channels of active instrumentation were run with 18 channels returning useful data for a data return of 94.7%. The maximum load of 24,670 lbs. was obtained in 30.8 msec. The loading rate was 840 lbs./msec. The load cell also indicated a nonlinear decay of the load, however, the data recording ended before the load returned to 0. The sample failed due to the smooth steel bar pulling out of the concrete.

The steel strains varied from a maximum of 1,126 micro strains for SS-01 to a minimum of 89 micro strains for SS-10. The concrete foil strains varied from -131 micro strains for CS-03 to -20 micro strains for CS-01.

#### 4.8.3 Evaluation of Results of Tests 21 and 22

Both samples failed due to the smooth steel bar pulling out of the concrete matrix, Figure 4-31. There was no indication of any cracking of the concrete. The maximum resisting force developed was 24,670 lbs.

The average steel strains beginning at the bottom of the sample were 980 micro strains at 1-inch, 715 micro strains at 3-inches, 391 micro strains at 5-inches, 259 micro strains at 7-inches and 96 micro strains at 9-inches. Due to the limited number of data points, no reference can be made to the coefficient of variation, however, the available data do show a linear relationship (Figure 4-32) expressed by equation 4.8:

$$Y = -111X + 1040 \quad (4.8)$$

with an  $R^2 = 0.9715$ . This yields a required embedment length of 18.6-inches.

Once again there is very little concrete strain data available due to the limited number of tests planned and the failure of one of these tests. However, from the data available (seven records), there appears to be no relationship of strain to location. The average strains beginning at the bottom are -24 micro strains at 2-inches, -131 micro strains at 4-inches, -53 micro strains at 6-inches, and -47.5 micro strains at 8-inches (Figure 4-33). The average concrete strain was -54.3 micro strains.



**Figure 4-31 Test specimen 22 post-test**

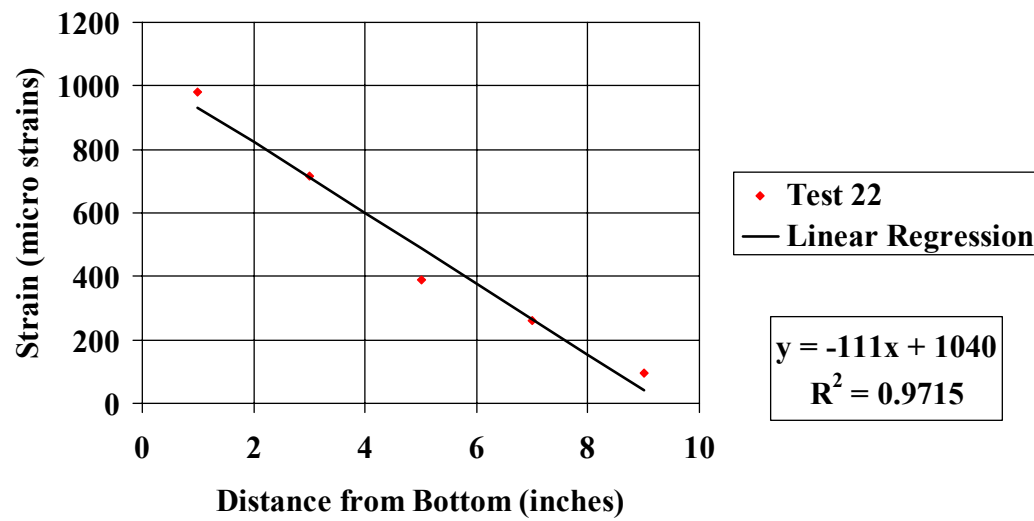


**Figure 4-32 Adjusted steel strains, dynamic loading, 20-inch diameter sample, 1-inch smooth bar**

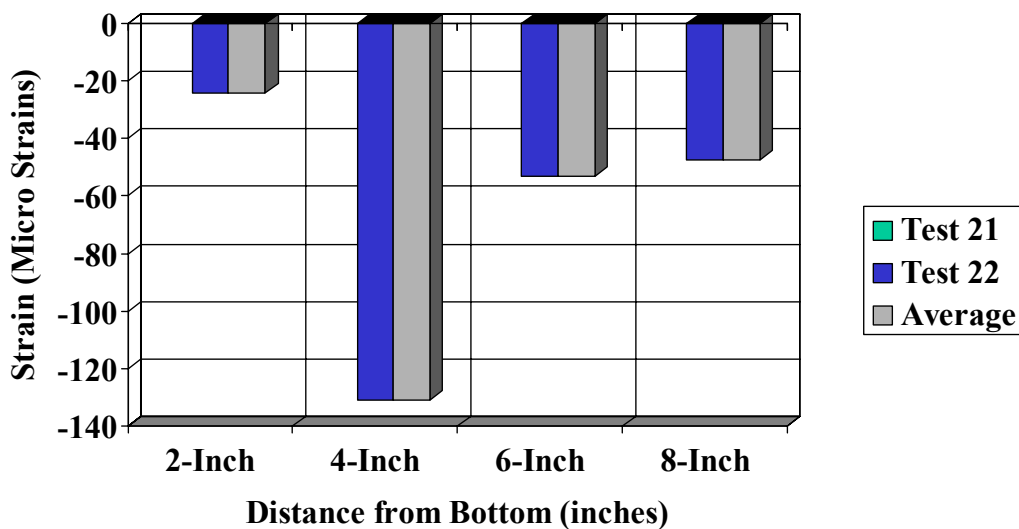


**Figure 4-33 Adjusted concrete strains, dynamic loading, 20-inch diameter sample, 1-inch smooth bar**

#### **4.9 Quasi-Static Loading of a 1-inch Smooth Bar Embedded in a 20-inch Concrete Cylinder**

Tests 23 and 24 consisted of a 20 in. diameter cylinder with a 1 in. diameter smooth steel bar loaded statically. The maximum loads applied to the two specimens before failure were 14,100 lbs. at  $t = 87$  seconds for test 23, and 16,000 lbs. at  $t = 152$  seconds for test 24. The maximum adjusted load of 14,100 lbs. will be used for these two tests.

##### **4.9.1 Test 23**

On test 23, a total of 19 channels of active instrumentation were run. All 19 channels were successful for a data return of 100%. These consisted of one load cell, ten steel strains and eight foil concrete strains. The maximum load of 14,100 lbs. was obtained in 87 seconds. The load cell indicated a linear loading rate of 230 lbs./sec until failure. The

load decay was nonlinear with the data record ending before the load returned to 0. The specimen failed due to the steel bar pulling out of the concrete.

The maximum steel strain was 681 micro strains for SS-01, and minimum was 60 micro strains for SS-09. The concrete foil strains varied from a maximum of -77 micro strains for CS-04, to a minimum of -15 micro strains for CS-02. There were no fiber-optic gages in this test.

#### 4.9.2 Test 24

On test 24, a total of 19 active channels of instrumentation were run with 18 channels returning good data for a data return of 94.7%. These consisted of one load cell, ten steel strains, and eight foil concrete strains. The CS-04 was the only gage, which did not return good data. The adjusted maximum load of 14,100 lbs. was obtained in 143 seconds. The load cell indicated a linear loading rate of 200 lbs./seconds. The load decay was nonlinear with a discontinuity occurring at approximately  $t = 340$  seconds. The cause of this discontinuity is not clear. The sample failed due to pull out of the smooth steel bar.

SS-02 recorded the maximum steel strains with 608 micro strains, the minimum occurred at SS-09 with 25 micro strains. The foil concrete strains varied from a maximum of -53 micro strains for CS-01 to a minimum of -11 micro strains for CS-03.

#### 4.9.3 Evaluation of Results of Tests 23 and 24

Both samples failed due to the smooth steel bar pulling out of the concrete matrix, Figure 4-34 and Figure 4-35. There was no indication of any cracking of the concrete. The average maximum resisting force developed was 15,050 lbs.





**Figure 4-34 Test specimen 23 post-test**



**Figure 4-35 Test specimen 23 post-test**

The average steel strains beginning at the bottom of the sample were 558 micro strains at 1-inch, 381 micro strains at 3-inches, 284 micro strains at 5-inches, 187 micro strains at 7-inches, and 69 micro strains at 9-inches. The average coefficient of variation for this data was 30.5. The data has a linear relationship (Figure 4-36) expressed by equation 4.9

$$Y = -58.6X + 589 \quad (4.9)$$

with an  $R^2 = 0.9852$ . This yields a required embedment length of 34-inches.

On this set up, there was slightly more concrete strain data available with 15 recorded strain readings from two tests. The strains appear to be relatively constant with an average reading of -32.5 micro strains at 2-inches, -41.3 micro strains at 4-inches, -41.8 micro strains at 6-inches, and -25.3 micro strains at 8-inches (Figure 4-37). The average strain was -34.8 micro strains.

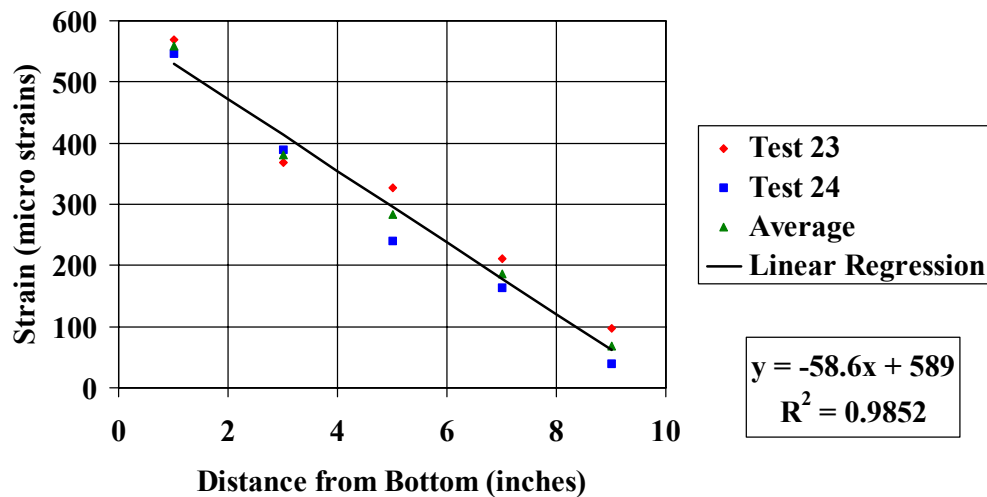


**Figure 4-36 Adjusted steel strains, quasi-static loading, 20-inch diameter sample, 1-inch smooth bar**

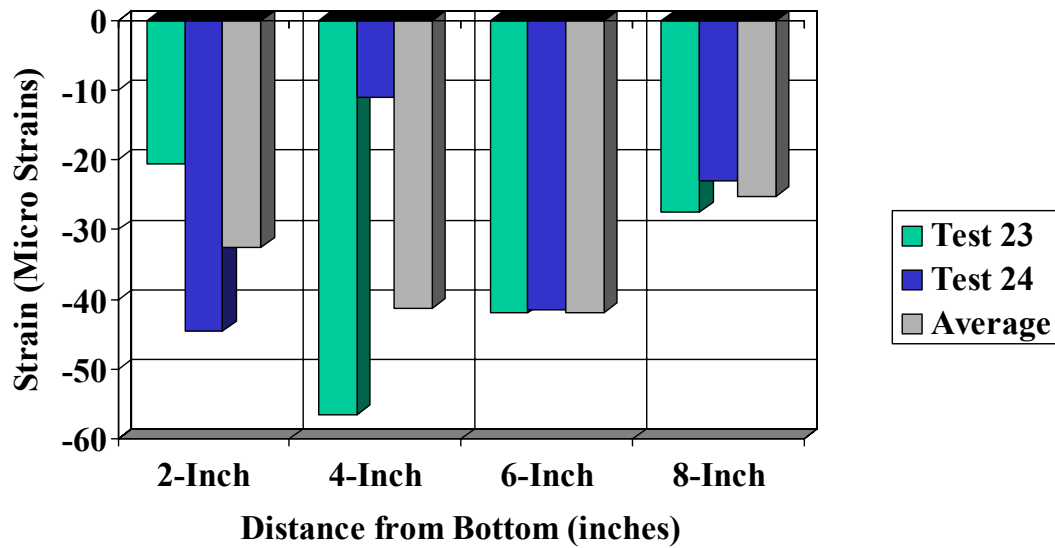


**Figure 4-37 Adjusted concrete strains, quasi-static loading, 20-inch diameter sample, 1-inch smooth bar**

#### **4.10 Impact Loading of a #10 Deformed Bar Embedded in a 20-inch Diameter Concrete Cylinder**

Tests 25, 26, and 27 consisted of a 20-inch diameter cylinder with a number ten deformed bar subjected to an impact loading. The maximum loads applied to the test specimens before failure were 111,340 lbs. at  $t = 5$  msec for test 25 and 120,260 lbs. at  $t = 4.04$  msec test 27. No data was obtained on test 26. The fast-opening valve failed causing failure of the specimen before the data recorder was armed. In order to compare the data from the two remaining tests, a maximum load of 111,340 lbs. will be used for these tests.

##### **4.10.1 Test 25**

On test 25 a total of 27 channels of active instrumentation were run of these 24 returned good data for a data return of 88.9%. These included one load cell, successful, ten steel

strains, all ten of which were successful, eight foil concrete strains, seven of which successful, and eight fiber optic concrete strains, six of which were successful. The maximum load of 111,340 lbs. was obtained in 5 msec. The linear portion of the loading rate was 34,900 lbs./msec, until failure occurred at  $t = 5$  msec. The sample failed due to radial cracking along the  $0^0 - 180^0$  azimuth.

The concrete shows the typical crushing on the leading edges of the deformations.

The steel strains varied from a maximum of 6010 micro strains for SS-01 to 505 micro strains for SS-09. The foil concrete strains varied from a maximum of -624 micro strains for CS-for to a minimum of -38 micro strains for CS-03. The fiber optic strains varied from a maximum of -305 micro strains for FO-02 to -119 micro strains for FO-03.

#### 4.10.2 Test 26

No data were obtained on test 26. The sample prematurely failed due to a failure of the fast opening valve. Test failure occurred before the data recorder was armed, resulting in a loss of all data. The sample itself failed similar to test 25.

#### 4.10.3 Test 27

On test 27 a total of 19 channels of active instrumentation were run of these, 17 return useful data for a data return of 89.5%. These consisted of one load cell, successful, ten steel strains, nine of which were successful, and eight foil concrete strains, seven of which were successful. There were no fiber optic gages on this test. The adjusted maximum load 111,340 lbs. was obtained in 4 msec. The linear loading rate was 40,800 lbs./msec until brittle failure occurred at  $t = 4.04$  msec. The sample broke into three

pieces, with the typical crushing of the concrete on the leading edges of the steel deformations.

The steel strains varied from a maximum of all 3,151 micro strains for SS-01 to 475 micro strains for SS-10. The concrete strains varied from a maximum all -405 micro strains for CS-06 to a minimum of -125 micro strains for CS-05. There were no fiber optic gages in this test.

#### 4.10.4 Evaluation of Results of Tests 25, 26 and 27

The average load applied to the two samples before failure was 115,800 lbs. All three samples failed due to radial cracking of the concrete and broke apart. Samples 25 and 26 broke into two separate pieces, with the crack forming along the  $0^{\circ} - 180^{\circ}$  azimuth, Figure 4-38. Sample 27 broke into three separate pieces, with one crack forming along the  $180^{\circ}$  azimuth, and the other two cracks spaced evenly on either side of the  $0^{\circ}$  azimuth. There was crushing of the concrete on the leading edge of the deformations on the steel bar, Figure 4-39.



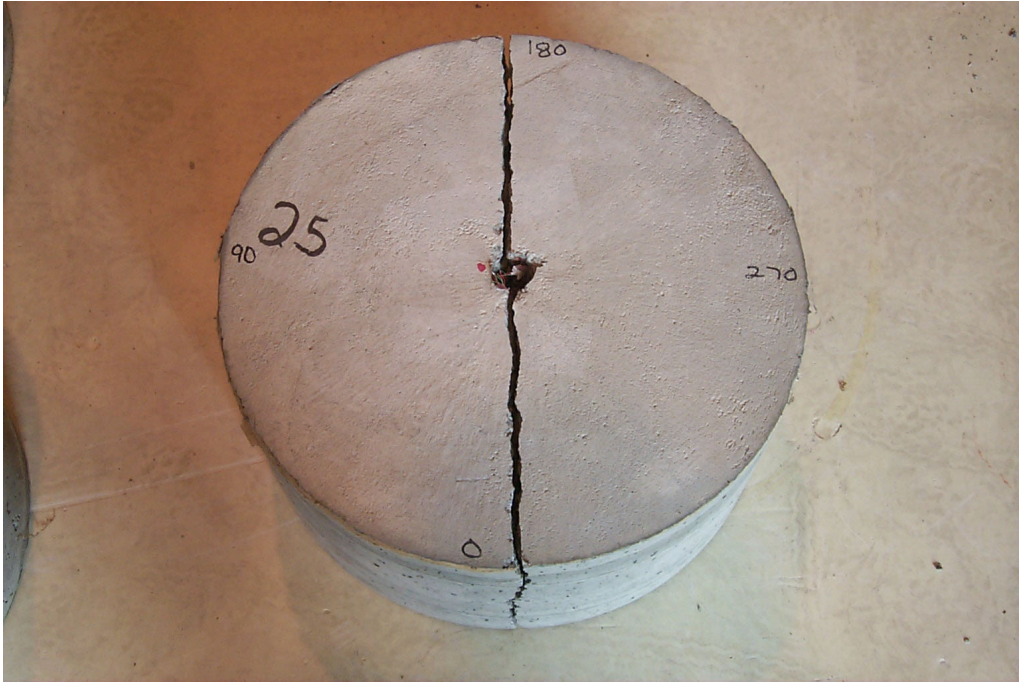


**Figure 4-38 Test specimen 25 post-test**



**Figure 4-39 Test specimen 25 post-test. Note crushing of concrete on leading edges of the steel deformations**

The average steel strains beginning at the bottom of the sample were 3,592 micro strains at 1-inch, 2,403 micro strains at 3-inches, 1,719 micro strains at 5-inches, 1,157 micro strains at 7-inches and 498 micro strains at 9-inches. If we disregard the strain data from the 1-inch position, where some strains were clearly in the plastic range, we get an average coefficient of variation for this data of 7.7 and a linear relationship (Figure 4-40) expressed by equation 4.10:

$$Y = -314X + 3330 \quad (4.10)$$

with an  $R^2 = 0.9987$ . To develop the full yield strength of the #10 bar, an embedment length of 5.8-inches would be required.

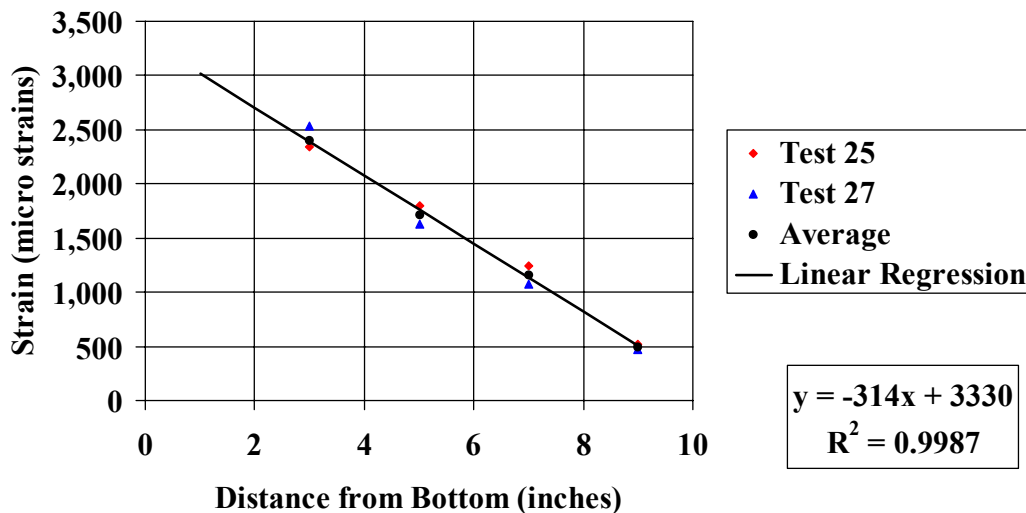


**Figure 4-40 Adjusted steel strains, impact loading, 20-inch diameter sample, #10 deformed bar**

The average concrete strains beginning at the bottom were -168.9 micro strains at 2-inches, -233.6 micro strains at 4-inches, -268.6 micro strains at 6-inches, and -199 micro strains at 8-inches (Figure 4-41). The average concrete strain was -215.8 micro strains.

#### 4.11 Dynamic Loading of a #10 Deformed Bar Embedded in a 20-inch Diameter Concrete Cylinder

Tests 28, 29, and 30 consisted of a 20- inch diameter concrete cylinder with a #10 deformed steel bar loaded dynamically. The maximum loads applied to the three test specimens before failure were 105,000 at  $t = 157$  msec for test 28, 82,990 lbs. at  $t = 109$  msec for test 29, and 76,788 lbs. at  $t = 100$  msec for test 30. A maximum adjusted load of 76,788 lbs. will be used for these three tests.

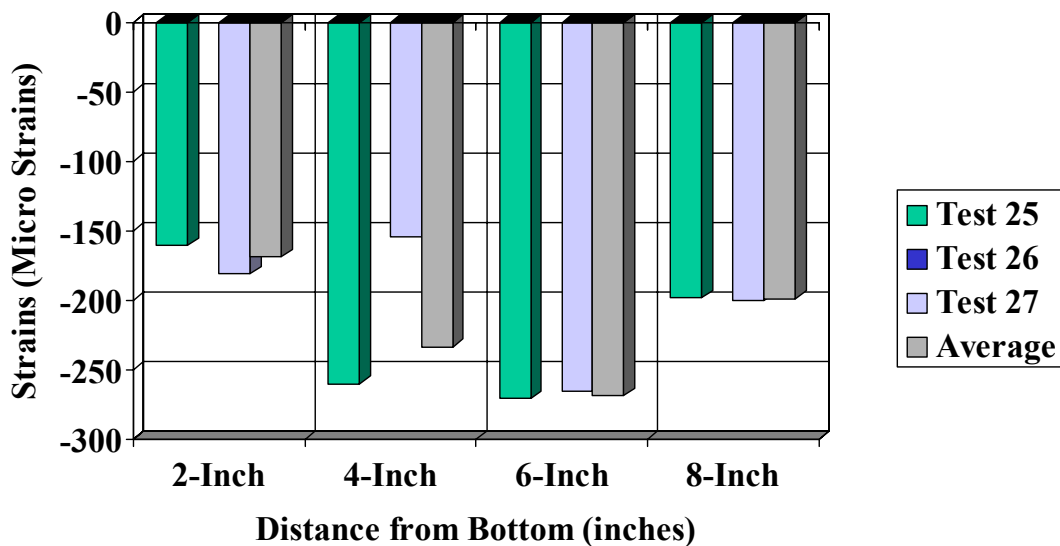


Figure 4-41 Adjusted concrete strains, impact loading, 20-inch diameter sample, #10 deformed bar

##### 4.11.1 Test 28

On test 28, a total of 27 channels of active instrumentation were fielded. Of these, 23 channels returned useful data for a data return of 85.2%. These consisted of one load cell, successful, ten steel strains, all ten of which were successful, eight foil concrete



strains, seven of which were successful, and eight fiber optic concrete strains, five of which were successful. The load cell indicated a slight non-linearity to the loading rate, however, the average loading rate was 690 lbs./msec. The sample failed due to radial cracking and broke into three separate pieces. There was the usual crushing of the concrete on the leading edges of the deformations.

The steel strains varied from a maximum of 2,590 micro strains for SS-03 to a minimum of 278 micro strains for SS-10. The foil concrete strains varied from a maximum of -161 micro strains for CS-08 to a minimum of -32 micro strains for CS-04. The fiber optic concrete strains varied from a maximum of -295 micro strains for FO-07 to a minimum all of -86 micro strains for FO-06.

#### 4.11.2 Test 29

On test 29, a total of 19 channels of active instrumentation were run, of these 15 returned good data for a data return of 78.9%. These consisted of one load cell, successful, ten steel strains, seven of which were successful, and eight foil concrete strains, seven of which were successful. There were no fiber-optic gages on this test. The adjusted maximum load of 76,788 lbs. was obtained in 96 msec. The load cell showed the same nonlinear loading as observed on test 28. The average loading rate was approximately 770 lbs./msec. The sample failed in a brittle manner due to radial cracking and broke into two separate pieces with the crack forming on the  $0^0$  -  $180^0$  azimuth. Once again, the concrete was crushed on the leading edges of the steel deformations.

The steel strains varied from a maximum of 1,307 micro strains for SS-03 to a minimum of 177 micro strains for SS-09. The concrete strains varied from a maximum

of -163 micro strains for CS-08 to a minimum of -21 micro strains for CS-04. There were no fiber optic gages on this test.

#### 4.11.3 Test 30

On test 30 a total of 19 channels were run with 18 returning usable data for a return of 94.7%. These consisted of one load cell, successful, ten steel strains, nine of which were successful, and eight foil concrete strains all eight of which were successful. There were no fiber optic gages on this test. The maximum load of 76,788 lbs. was obtained in 100 msec and the loading rate was nonlinear, as was same on test 28 and test 29. The average loading rate was 790 lbs./msec. The sample had a brittle failure due to radial cracking and broke into two separate pieces. There was crushed concrete on the leading edges of the steel deformations.

The steel strains varied from a maximum of 2,550 micro strains for SS-01, down to 443 micro strains for SS-09. The foil concrete strains varied from a maximum of -528 micro strains for CS-02 to a minimum of -69 micro strains for CS-04.

#### 4.11.4 Evaluation of Results of Tests 28, 29, and 30

The average load applied to the three samples before failure was 88,260 lbs. All three samples failed due to radial cracking of the concrete. On test 28, the sample broke into three pieces. On tests 29 and 30, the samples broke into two separate pieces, with the crack forming along the  $0^{\circ} - 180^{\circ}$  azimuth, Figure 4-42. There was crushing of the concrete on the leading edge of the deformations on the steel bar.

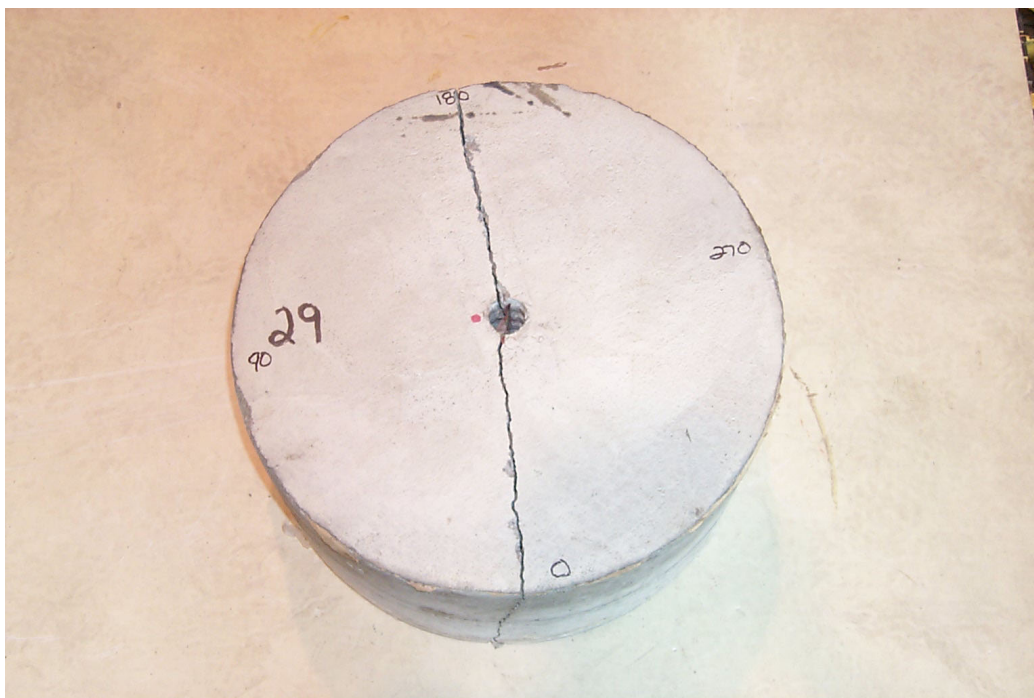


**Figure 4-42 Test specimen 29 post-test**

The average steel strains beginning at the bottom of the sample were 2,178 micro strains at 1-inch, 1,667 micro strains at 3-inches, 1,059 micro strains at 5-inches, 683 micro strains at 7-inches, and 285 micro strains at 9-inches. The average coefficient of variation for this data was 27.1. A plot of the data produced a straight line (Figure 4-43) expressed by equation 4.11:

$$Y = -239X + 2370 \quad (4.11)$$

with an  $R^2 = 0.9911$ . This yields a required embedment length of 8.5-inches.

The average concrete strain beginning at the bottom was -206.3 micro strains at 2-inches, -127.2 micro strains at 4-inches, -93 micro strains at 6-inches, and -170.2 micro strains at 8-inches (Figure 4-44). The average concrete strain was -145.8 micro strains.

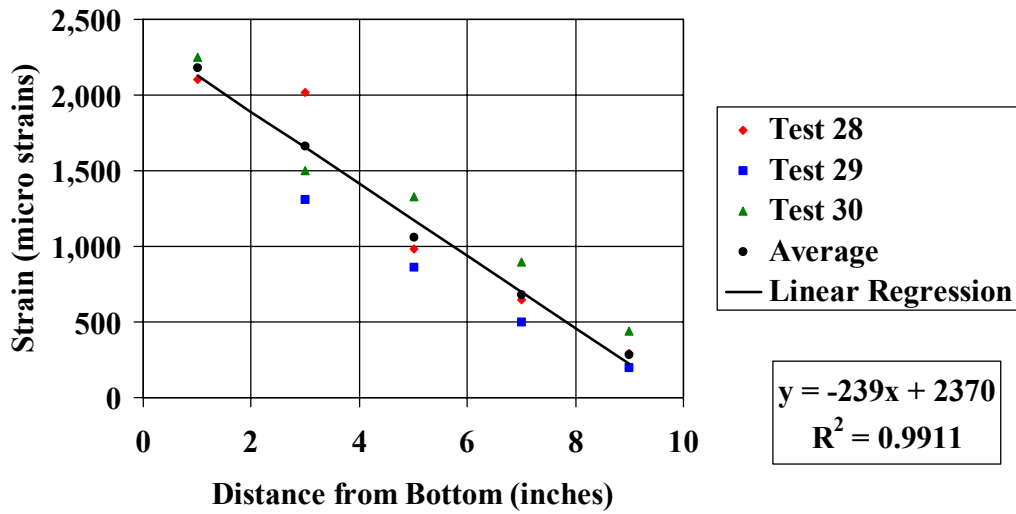


Figure 4-43 Adjusted steel strains, dynamic loading, 20-inch diameter sample, #10 deformed bar

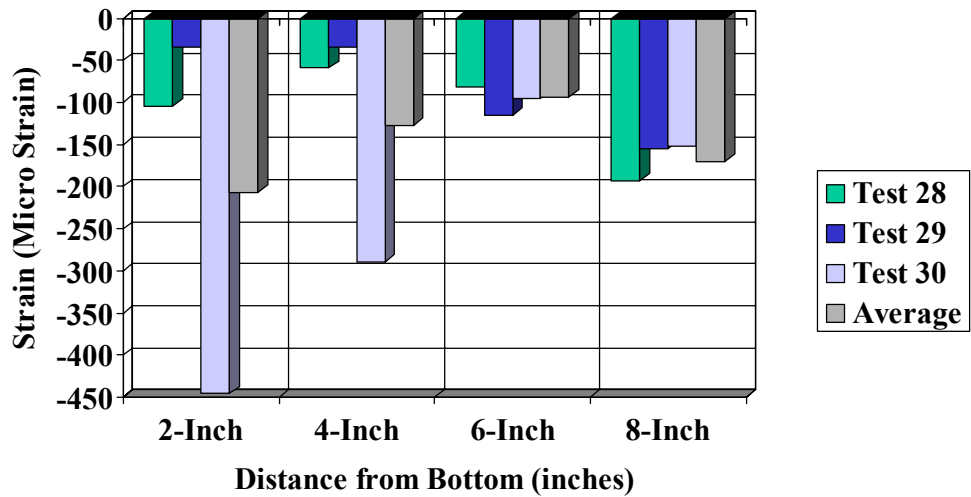


Figure 4-44 Adjusted concrete strains, dynamic loading, 20-inch diameter sample, #10 deformed bar

#### **4.12 Quasi-Static Loading of a #10 Deformed Bar Embedded in a 20-inch Diameter Concrete Cylinder**

Tests 31, 32, and 33 consisted of a 20- inch diameter cylinder with a #10 deformed steel bar loaded statically. The maximum loads applied to the three test specimens before failure were 57,320 lbs. at  $t = 254$  sec. for test 31, 62,780 lbs. at  $t = 201$  sec. for test 32, and 51,000 lbs. at  $t = 267$  sec. for test 33. The adjusted maximum load for these three tests was 51,000 lbs.

##### **4.12.1 Test 31**

On test 31, a total of 27 channels of instrumentation were run with 22 channels returning usable data for a return of 81.5%. These consisted of one load cell, successful, ten steel strains, all ten of which were successful, eight failed concrete strains, all eight of which were successful, and eight fiber optic concrete strains, three of which were successful. The load cell indicated a linear loading rate of 240 lbs./msec until failure. The specimens failed due to radial cracking along the  $0^{\circ} - 180^{\circ}$  azimuth. The steel bar indicated the common crushing of the concrete on the leading edges of the deformations.

The steel strains varied from a maximum of 4,248 micro strains for SS-01 to a minimum of 171 micro strains for SS-10. The foil concrete strains varied from a maximum of -183 micro strains for CS-02 to a minimum of -24 micro strains for CS-05. The fiber-optic concrete strains varied from a maximum all of -129 micro strains for FO-03 to a minimum of -98 micro strains for FO-07.

##### **4.12.2 Test 32**

On test 32, a total of 19 channels of instrumentation were run with 18 channels returning usable data for a data return of 94.7%. These consisted of one load cell,

successful, ten steel strains, all ten of which were successful, and eight foil concrete strains, seven of which were successful. There were no fiber optic gages on this test. The adjusted maximum load of 51,000 lbs. was obtained in 150 sec. The load cell indicated a linear loading rate of 250 lbs./msec. The failure of test specimen 32 was similar to that of test 31 with the common radial cracking occurring along the  $0^{\circ}$  -  $180^{\circ}$  azimuth and crushing of the concrete on the leading edges of the steel deformations.

The steel strains varied from a maximum of 1,164 micro strains for SS-01 to a minimum of 128 micro strains for SS-09. The concrete strains varied from a maximum of -145 micro strains for CS-04 to a minimum of -49 micro strains for CS-07.

#### 4.12.3 Test 33

On test 33, 19 channels of active instrumentation were run with 17 channels returning usable data for a return of 89.5%. These consisted of one load cell, successful, ten steel strains, eight of which were successful, and eight foil concrete strains, all eight of which were successful. There were no fiber optic gages on this test. The maximum load of 51,000 lbs. was obtained in 267 sec. The load cell indicated a linear loading of 250 lbs./msec. The specimens failed in the same manner as on tests 31 and 32.

The steel strains varied from a maximum of 3,400 micro strains for SS-01 to a minimum all of 175 micro strains for SS-09. The Foil concrete strains varied from a maximum of -150 micro strains for CS-05 to a minimum of -15 micro strains for CS-04.

#### 4.12.4 Evaluation of Results of Tests 31, 32 and 33

The average load applied to the three samples before failure was 57,000 lbs. All three samples failed due to radial cracking of the concrete and broke into two separate pieces,

with the crack forming roughly along the  $0^{\circ} - 180^{\circ}$  azimuth, Figure 4-45. There was crushing of the concrete on the leading edge of the deformations on the steel bar.

The average steel strains beginning at the bottom of the sample were 2,233 micro strains at 1-inch, 1,014 micro strains at 3-inches, 703 micro strains at 5-inches, 412 micro strains at 7-inches and 191 micro strains at 9-inches. If we disregard the strain data from the 1-inch position, where some strain readings were clearly in the plastic range, we get an average coefficient of variation for this data of 17.9 and a linear relationship (Figure 4-46) expressed by equation 4.12

$$Y = -138X + 1410 \quad (4.12)$$

with an  $R^2 = 0.9944$ . To develop the full yield strength of the #10 bar, a development length of 14.25-inches would be required.

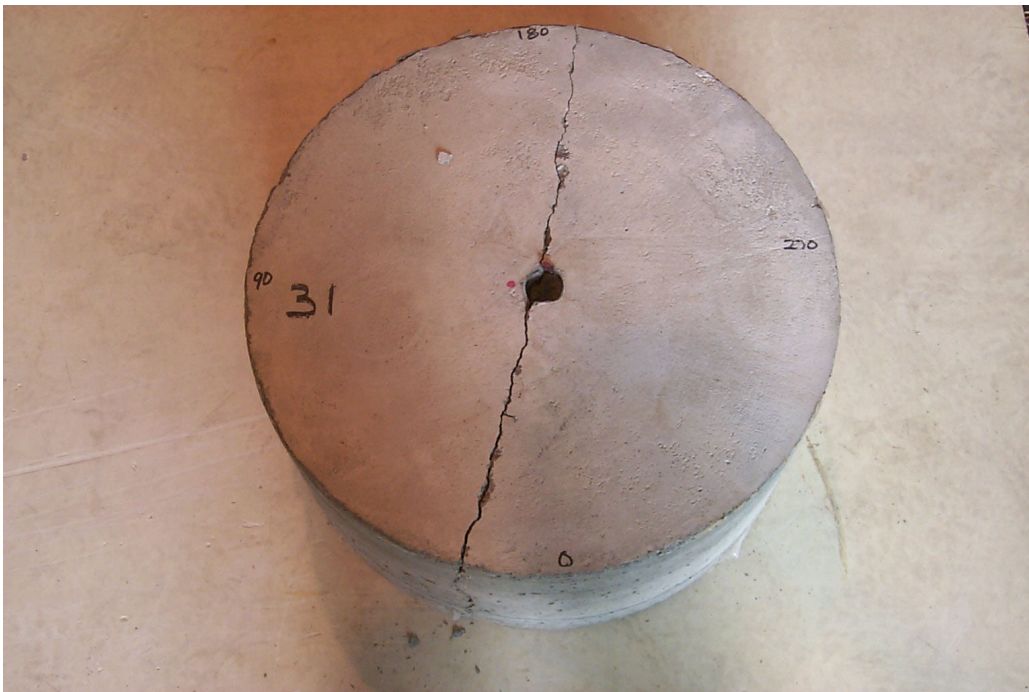


**Figure 4-45 Test specimen 31 post-test**

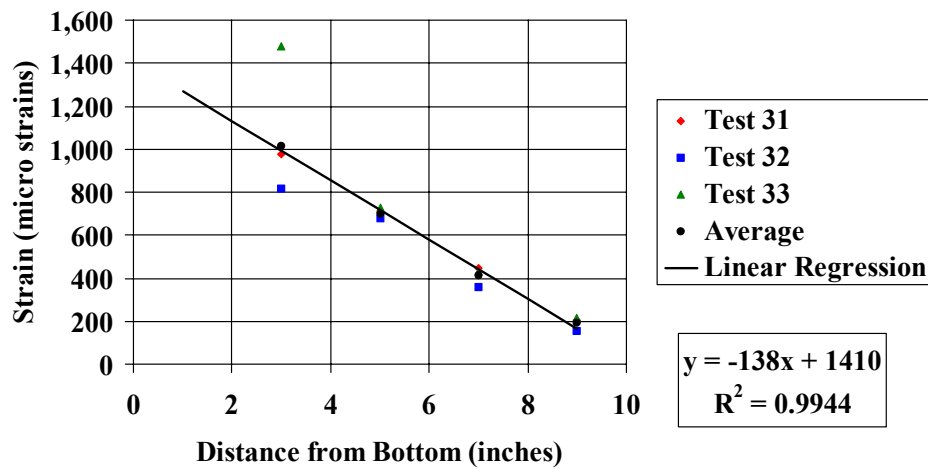


**Figure 4-46 Adjusted steel strains, quasi-static loading, 20-inch diameter sample, #10 deformed bar**

The average concrete strain beginning at the bottom was -119.6 micro strains at 2-inches, -78.1 micro strains at 4-inches, -74.3 micro strains at 6-inches, -73.7 micro strains at 8-inches (Figure 4-47). The average concrete strain was -84 micro strains.

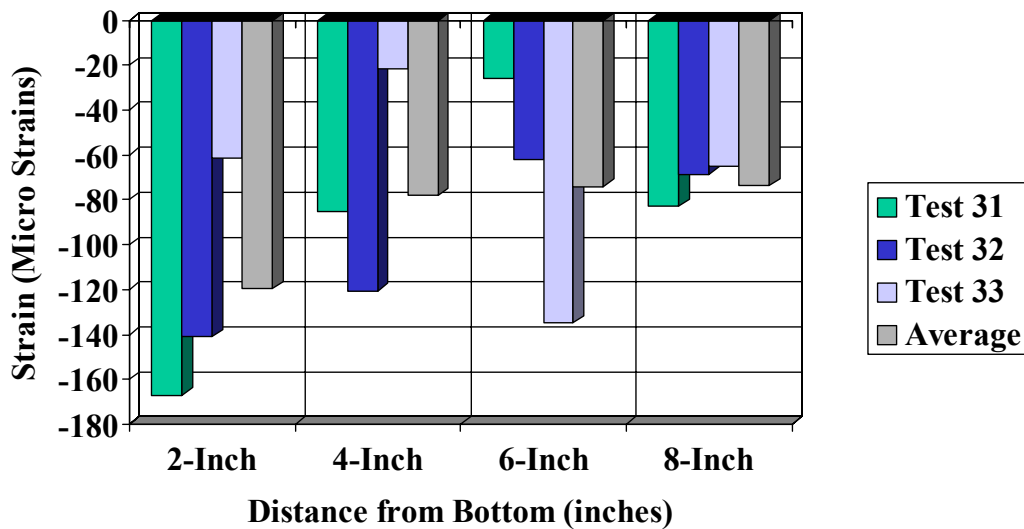


**Figure 4-47 Adjusted concrete strains, quasi-static loading, 20-inch diameter sample, #10 deformed bar**



**Table 4.1 Complete Test Matrix**

<b>Test Number</b>	<b>Load Rate</b>	<b>Bar Diameter and Type</b>	<b>Specimen Diameter</b>	<b>Failure Load (lbs)</b>	<b>Failure Mode</b>
1, 2 and 3	Quasi-Static	#8 Deformed	10"	41,300	Radial Cracking Of Concrete
4, 5 and 6	Impact	#8 Deformed	10"	71,200	Radial Cracking Of Concrete
7, 8 and 9	Dynamic	#8 Deformed	10"	68,600	Radial Cracking Of Concrete
10, 11 and 12	Impact	#8 Deformed	20"	86,100	Yielding of Steel Bar
13, 14 and 15	Dynamic	#8 Deformed	20"	81,600	Yielding of Steel Bar
16, 17 and 18	Quasi-Static	#8 Deformed	20"	65,300	Radial Cracking Of Concrete
19 and 20	Impact	#8 Smooth	20"	26,000	Bar Pull Out
21 and 22	Dynamic	#8 Smooth	20"	24,700	Bar Pull Out
23 and 24	Quasi-Static	#8 Smooth	20"	15,100	Bar Pull Out
25, 26 and 27	Impact	#10 Deformed	20"	116,000	Radial Cracking Of Concrete
28, 29 and 30	Dynamic	#10 Deformed	20"	88,200	Radial Cracking Of Concrete
31, 32 and 33	Quasi-Static	#10 Deformed	20"	57,000	Radial Cracking Of Concrete

## **CHAPTER 5 EMPIRICAL ANALYSIS OF TEST DATA**

An empirical analysis of the test data was performed. The effects that the loading rate, specimen diameter, bar diameter and bar deformations had on the failure mode, the failure load, the average steel strain, the average concrete strains and the development length was addressed for static, dynamic and impact loadings. Static loadings were actually quasi-static loadings, which brought the system to failure in 87 to 713 seconds. Dynamic loadings induced failure in 30.8 msec to 200 msec, and impact loadings caused failure in 3.92 msec to 7.4 msec.

In this chapter, the test data are evaluated on an empirical basis. Unusual variations in the data that can be attributed to the testing procedure or the physical response of the specimens are discussed in this chapter. Other effects are dealt within the next chapter.

### **5.1 Effects of Loading Rate**

#### **5.1.1 Effects of Loading Rate on Failure Mode**

The loading rate had no effect on the failure mode of the 10-inch diameter test specimens and the 20-inch diameter specimens with the #10 deformed bars. All of these specimens failed due to radial cracking of the concrete and split into two or three pieces. Likewise, the loading rate had no effect on the failure mode of the specimens with 1-inch smooth bars; all of which failed due to bar pullout. However, the loading rate did have an effect on the failure mode of the 20-inch diameter specimens with #8 deformed bars. For the static and dynamic loadings, the steel bar failed due to yielding of the bar or failure of the welds in the vicinity of the connection block. For the impact loading, the

specimens failed due to radial cracking of the concrete. The failure modes for the test specimens are summarized in Table 5.1.

**Table 5.1 Failure Mode**

	10" Dia. Specimens with #8 Bars	20" Dia. Specimens with #8 Bars	20" Dia. Specimens with 1" Smooth Bars	20" Dia. Specimens with #10 Bars
Static Loading	Radial Cracking of Concrete	Radial Cracking of Concrete	Bar Pull-out	Radial Cracking of Concrete
Dynamic Loading	Radial Cracking of Concrete	Yielding of Steel Connector	Bar Pull-out	Radial Cracking of Concrete
Impact Loading	Radial Cracking of Concrete	Yielding of Steel Connector	Bar Pull-out	Radial Cracking of Concrete

#### 5.1.2 Effects of Loading Rate on Failure Loads

The failure loads applied to the specimens increased as the loading rate increased for all specimens. This is summarized in Table 5.2.

**Table 5.2 Average Failure Loads**

	10" Dia. Specimen with #8 Bars	20" Dia. Specimens with #8 Bars	20" Dia. Specimens with 1" Smooth Bars	20" Dia. Specimens with #10 Bars
Static Loading	41,300	65,300	15,100	57,000
Dynamic Loading	68,600	81,600	24,700	88,200
Impact Loading	71,200	86,100	25,900	116,000

For the 10-inch diameter specimens, the maximum applied load increased by 66% when loading types changed from quasi-static to dynamic, and another 4% when going from dynamic to impact. For the 20-inch diameter specimens containing the #8 deformed bars, the increase was 25%, as the loading rate went from quasi-static to dynamic, and a further 6% as the loading rate was increased to impact. For the smooth bars, the failure

load increased 64% from quasi-static to dynamic, and 5% for dynamic to impact. For the 20-inch diameter specimens containing the #10 deformed bars, the failure load increased by 55% when the loading rate was increased from quasi-static to dynamic and by another 31% as the loading rate was increased to impact loading. This data indicates that the majority of the rate effects occurred between the quasi-static and dynamic loadings.

### 5.1.3 Effects of Loading Rate on Steel Strains

As the loading rate increased from quasi-static to dynamic, the steel strains increased for all of the specimens. However, as the loading rate was further increased to impact, the steel strains decreased for all of the specimens except those containing the #10 deformed bars. This is slightly misleading. Due to the very fast loading rates, the strains do not have sufficient time to distribute themselves along the length of the bar. This would cause larger strains at the bottom of the bar (6-inches from the first strain gage), which would induce failure before the larger strain readings were seen farther up the bar. The equations defining the linear regression of strain along the length of the steel bars are shown in Table 5.3. In these equations  $x$  represents the location along the steel bar, in inches, with  $x=0$  being the bottom of the steel bar and  $x=10$  being the top of the bar;  $y$  represents the strain in micro strains at location  $x$ .

**Table 5.3 Average Steel Strains at Failure**

	10" Dia. Specimen with #8 Bars	20" Dia. Specimens with #8 Bars	20" Dia. Specimens with 1" Smooth Bars	20" Dia. Specimens with #10 Bars
Static Loading	$y = -167x + 1920$ $R^2 = .9784$	$y = -250x + 2600$ $R^2 = .9992$	$y = -58.6x + 589$ $R^2 = .9852$	$y = -138x + 1410$ $R^2 = .9944$
Dynamic Loading	$y = -307x + 3230$ $R^2 = .9837$	$y = -433x + 4190$ $R^2 = .9706$	$y = -111x + 1040$ $R^2 = .9715$	$y = -239x + 2370$ $R^2 = .9911$
Impact Loading	$y = -274x + 2720$ $R^2 = .9945$	$y = -312x + 3250$ $R^2 = .9972$	$y = -90x + 993$ $R^2 = .9961$	$y = -314x + 3330$ $R^2 = .9987$

Since all of the steel strains were linear with respect to the length of the bar, and were 0 at the top of the test specimen ( $x=10$ -inches), direct comparisons can be made with respect to the maximum strain ( $y$  when  $x=0$ -inches). For the 10-inch diameter specimens, the maximum strain increased 69%, as the loading rate increased from quasi-static to dynamic. As the loading rate was further increased to impact, the maximum strain decreased by 16%. For the 20-inch diameter specimens containing the #8 deformed bars, the maximum strain increased 61% as the loading rate went from quasi-static to dynamic. The impact loading yielded a maximum strain decrease of 23%. Likewise for the smooth bars, the maximum strains increased 77% as the loading rate went from quasi-static to dynamic. The maximum strain for the impact loading decreased by 5%. For the #10 bars, the maximum strain increased 68% and then increased another 41% as the loading rates were increased from quasi-static to dynamic to impact.

#### 5.1.4 Effects of Loading Rate on Concrete Strains

Since there is large variation in the concrete data, it is very difficult to draw definitive conclusions. However, overall, the strain in the concrete tended to increase with an increase in loading rates except for the 10-inch diameter specimens, Table 5.4.

**Table 5.4 Average Concrete Strains at Failure**

	10" Dia. Specimen with #8 Bars	20" Dia. Specimens with #8 Bars	20" Dia. Specimens with 1" Smooth Bars	20" Dia. Specimens with #10 Bars
Static Loading	-147	-180	-35	-84
Dynamic Loading	-115	-172	-54	-146
Impact Loading	-61	-208	-116	-216

For the #8 deformed bars in 10-inch diameter specimens, the concrete strains decreased 22% as the loading rate went from static to dynamic, and by another 47% as the loading rate went from static to impact. For the #8 deformed bars in 20-inch diameter specimens, the concrete strains decreased by 4% as the loading rate went from static to dynamic then increased by 21% as the loading rate was increased to impact loading. The concrete strains in the 20-inch diameter specimens containing the 1-inch smooth bars increased by 54% as the loading rate went from static to dynamic and increased another 115% as we went from dynamic loading to impact loadings. Finally, for the #10 bars in 20-inch diameter specimens, the concrete strains increased by 74% and 48% as the loading rates went from static to dynamic to impact, respectively.

#### 5.1.5 Effects of Loading Rate on Development Length

As the loading rate increased, from quasi-static to dynamic loading, the embedment length required to develop the full yield strength of the steel bars, i.e. the development length, decreased. However, as the loading rate was farther increased to impact loading, the development length increased for all samples except for the specimens containing the #10 deformed bars. This is the same phenomena that was seen in the steel strains, and is a function of the test setup. The development lengths are summarized in Table 5.5

**Table 5.5 Development Length**

	10" Dia. Specimen with #8 Bars (in)	20" Dia. Specimens with #8 Bars (in)	20" Dia. Specimens with 1" Smooth Bars (in)	20" Dia. Specimens with #10 Bars (in)
Static Loading	10.5	7.6	34	14.25
Dynamic Loading	6	5.0	18.6	8.5
Impact Loading	6.75	6.0	21	5.8

## 5.2 Effects of Specimen Diameter

To determine the effects that the diameter of the concrete cylinder had, and therefore the effects of increased confinement on the system, we will compare the 10-inch diameter specimens containing the #8 deformed bars with the 20-inch diameter specimens containing the #8 deformed bars.

### 5.2.1 Effects of Specimen Diameter on Failure Mode

The specimen diameter affected the failure mode for the dynamic and impact loadings, but had no effect on the failure mode for the static loadings. The 10-inch diameter specimens all failed due to radial cracking of the concrete, as did the 20-inch diameter specimens loaded statically. However, the 20-inch diameter specimens that were loaded in dynamic and impact loading, all failed due to yielding of the steel bar or failure of the steel bar connection device. This is summarized in Table 5.6.

**Table 5.6 Failure Mode**

	10" Dia. Specimens with #8 Bars	20" Dia. Specimens with #8 Bars
Static Loading	Radial Cracking of Concrete	Radial Cracking of Concrete
Dynamic Loading	Radial Cracking of Concrete	Yielding of Steel Connector
Impact Loading	Radial Cracking of Concrete	Yielding of Steel Connector

### 5.2.2 Effects of Specimen Diameter on Failure Loads

The failure loads applied to the specimens increased as the specimen diameter increased for all loading conditions. For the quasi-static loadings, the failure loads increased 58% from the 10-inch diameter specimens to the 20-inch diameter specimens. For the dynamic loading rate, the failure loads increased 19% from the 10-inch diameter specimens to the 20-inch diameter

specimens. For the impact loading rates, the failure loads increased 21% from the 10-inch diameter specimens to the 20-inch diameter specimens. These results are summarized in Table 5.7. This shows that regardless of the loading rate, increased confinement does increase the strength of the concrete. This increase appears to be less pronounced at higher loading rates, but this is most likely due to the shift in failure modes.

**Table 5.7 Average Failure Loads**

	10" Dia. Specimens with #8 Bars	20" Dia. Specimens with #8 Bars	Percent Change
Static Loading	41,300	65,300	58%
Dynamic Loading	68,600	81,600	19%
Impact Loading	71,200	86,100	21%

### 5.2.3 Effects of Specimen Diameter on Steel Strains

The steel strains showed the same relationship as the failure loads, with the maximum steel strains increasing as the specimen diameter increased for all loading rates, Table 5.8.

**Table 5.8 Average Steel Strains at Failure**

	10" Dia. Specimens with #8 Bars	20" Dia. Specimens with #8 Bars	Percent Change
Static Loading	$y = -167x + 1920$ $R^2 = .9784$	$y = -250x + 2600$ $R^2 = .9992$	36%
Dynamic Loading	$y = -307x + 3230$ $R^2 = .9837$	$y = -433x + 4190$ $R^2 = .9706$	30%
Impact Loading	$y = -274x + 2720$ $R^2 = .9945$	$y = -312x + 3250$ $R^2 = .9972$	19%

For the static loading, the maximum steel strain increased 36% as the specimen diameter increased from 10-inches to 20-inches. Likewise, for the dynamic loading rate, the maximum steel strain increased 30%. Finally, for the impact loading, the maximum steel strain increased 19%. These results are summarized as was seen with the failure loads applied to the specimens, increased confinement did increase the amount of strain



in the steel bars regardless of loading rate. This effect became less noticeable as the loading rate increased.

#### 5.2.4 Effects of Specimen Diameter on Concrete Strains

The concrete strains increased from the 10-inch diameter specimens to the 20-inch diameter specimens for all three loading rates. This is shown in Table 5.9.

**Table 5.9 Average Concrete Strains at Failure**

	10" Dia. Specimens with #8 Bars	20" Dia. Specimens with #8 Bars	Percent Change
Static Loading	-147	-180	22%
Dynamic Loading	-115	-172	50%
Impact Loading	-61	-208	240%

For the static loadings, the concrete strains increased 22% from the 10-inch diameter specimens to the 20-inch diameter specimens. For the dynamic loading, the concrete strains increased 50% as the specimen diameter increased from 10-inches to 20-inches. Finally, for the impact loading, the strains increased 240% from the 10-inch diameter specimens to the 20-inch diameter specimens. As was stated earlier, due to the large variation in the concrete strain data, care should be exercised in drawing any conclusive thoughts on the concrete strains. However, the data does show that the concrete strains increased with increased confinement, and that this effect became more pronounced with increasingly faster loading rates.

#### 5.2.5 Effects of Specimen Diameter on Development Length

Increased confinement resulted in decreased development lengths for all three loading conditions. The reductions were 28% for the quasi-static loading, 17% for the dynamic loading and 11% for the impact loading. This is summarized in Table 5.10

**Table 5.10 Development Length**

	10" Dia. Specimens with #8 Bars (in)	20" Dia. Specimens with #8 Bars (in)	Percent Change
Static Loading	10.5	7.6	28%
Dynamic Loading	6	5	17%
Impact Loading	6.75	6	11%

### 5.3 Effects of Bar Diameter

To determine the effects that the bar diameter had on the tests, we will compare the 20-inch diameter specimens containing the #8 deformed bars with the 20-inch diameter specimens containing the #10 deformed bars.

#### 5.3.1 Effects of Bar Diameter on Failure Mode

The bar diameter effected the failure mode for the dynamic and impact loadings, but had no effect on the failure mode for the static loadings. All of the specimens containing the #10 deformed bars failed due to radial cracking of the concrete as did the specimens containing the #8 deformed bars loaded statically. The remaining specimens containing the #8 deformed bars that were loaded dynamically or in impact all failed due to yielding of the steel bars or failure of the welds on the connection blocks. These results are summarized in Table 5.11.

**Table 5.11 Failure Mode**

	20" Dia. Specimens with #8 Bars	20" Dia. Specimens with #10 Bars
Static Loading	Radial Cracking of Concrete	Radial Cracking of Concrete
Dynamic Loading	Yielding of Steel Connector	Radial Cracking of Concrete
Impact Loading	Yielding of Steel Connector	Radial Cracking of Concrete

### 5.3.2 Effects of Bar Diameter on Failure Loads

The failure loads increased as the bar diameter increased for the dynamic and impact loadings but decreased for the static loading. For the static loading, the failure loads decreased by 13%. For the dynamic and impact loadings, the load increased by 8% and by 35% respectively. These results are summarized in Table 5.12. The load decreased for the static loading because both specimens failed due to radial cracking of the concrete, and the specimen containing the #10 bar had less concrete cover due to the larger bar diameter. Larger dynamic and impact loads were applied to the specimens containing the #10 bar because of the increased cross-sectional area of the #10 bar. This additional strength was sufficient to force the change in failure modes.

**Table 5.12 Average Failure Loads**

	20" Dia. Specimens with #8 Bars	20" Dia. Specimens with #10 Bars	Percent Change
Static Loading	65,300	57,000	-13%
Dynamic Loading	81,600	88,200	8%
Impact Loading	86,100	116,000	35%

### 5.3.3 Effects of Bar Diameter on Steel Strains

The steel strains were smaller in the #10 bars than they were in the #8 bars with the exception of the impact loadings, which showed a very small increase for the #10 bars. For the static loading, the maximum steel strains decreased by 46% from the #8 bars to the #10 bars. This is slightly less than the ratios of the two cross-sectional areas and reflects the slight decrease in confinement mentioned earlier. For the dynamic loading, the maximum steel strains decreased by 43% from the #8 bars to the #10 bars. For the

impact loading, the maximum steel strains increased by 3% from the #8 bars to the #10 bars. This small of an increase is not statistically significant. These results are summarized in Table 5.13.

**Table 5.13 Average Steel Strains at Failure**

	20" Dia. Specimens with #8 Bars	20" Dia. Specimens with #10 Bars	Percent Change
Static Loading	$y = -250x + 2600$ $R^2 = .9992$	$y = -138x + 1400$ $R^2 = .9944$	-46%
Dynamic Loading	$y = -433x + 4190$ $R^2 = .9706$	$y = -239x + 2370$ $R^2 = .9911$	-43%
Impact Loading	$y = -312x + 3250$ $R^2 = .9972$	$y = -314x + 3330$ $R^2 = .9987$	3%

#### 5.3.4 Effects of Bar Diameter on Concrete Strains

The concrete strains increased slightly for the impact loading, but decreased for the dynamic and static loading as the bar diameter increased from #8 to #10, Table 5.14.

**Table 5.14 Average Concrete Strains at Failure**

	20" Dia. Specimens with #8 Bars	20" Dia. Specimens with #10 Bars	Percent Change
Static Loading	-180	-84	-53%
Dynamic Loading	-172	-146	-15%
Impact Loading	-208	-216	4%

For the static loading, the concrete strains decreased by 53% from the #8 bars to the #10 bars. For the dynamic loading rate, they decreased by 15% as the bar diameter increased from #8 to #10. For the impact loading, the concrete strains increased 4% from the #8 bars to the #10 bars.

### 5.3.5 Effects of Bar Diameter on Development Length

As the bar diameter increased, the development length increased for the quasi-static loading (88%) and dynamic loading (70%). The development length decreased slightly (3%) for the dynamic loading. Since the failure mode changed for the dynamic and impact loadings, the percent change can be misleading. These values are summarized in Table 5.15

**Table 5.15 Development Length**

	20" Dia. Specimens with #8 Bars (in)	20" Dia. Specimens with #10 Bars (in)	Percent Change
Static Loading	7.6	14.25	88%
Dynamic Loading	5.0	8.5	70%
Impact Loading	6.0	5.8	-3%

## 5.4 Effects of Bar Deformation

To determine the effects that the bar deformation had on the test, we will compare the 20-inch diameter specimens containing the #8 deformed bars with the 20-inch diameter specimens containing the 1-inch diameter smooth bars.

### 5.4.1 Effects of Bar Deformation on Failure Mode

The bar deformations effected the failure mode for all loading rates. As has been stated earlier, the specimens containing the #8 deformed bars failed due to either the yielding of the steel bars or connection device for the dynamic and impact loading rates or radial cracking of the concrete for the static loading rates. However, all of the specimens containing the smooth bars failed, as would be expected, due to pull out of the steel bar, regardless of the loading rate. These results are summarized in Table 5.16.

**Table 5.16 Failure Mode**

	20" Dia. Specimens with #8 Bars	20" Dia. Specimens with 1" Smooth Bars
Static Loading	Radial Cracking of Concrete	Bar Pull-out
Dynamic Loading	Yielding of Steel Connector	Bar Pull-out
Impact Loading	Yielding of Steel Connector	Bar Pull-out

#### 5.4.2 Effects of Bar Deformation on Failure Loads

The failure loads were always lower for the smooth bars than they were for the deformed bars, for all three loading rates. For the static loading, the failure load decreased by 77%. For the dynamic loading, the load decreased by 70%. Finally, for the impact loading, the failure load decreased by 70%. This indicates that the chemical adhesion accounts for only 23% to 30% of the total bar resistance to pullout while the mechanical interlocking of the steel deformations with the concrete account for 70% to 77% of the resistance. Additionally, this ratio does not appear to have a strong rate dependency. These results are summarized in Table 5.17.

**Table 5.17 Average Failure Loads**

	20" Dia. Specimens with #8 Bars	20" Dia. Specimens with 1" Smooth Bars	Percent Change
Static Loading	65,300	15,100	77%
Dynamic Loading	81,600	24,700	70%
Impact Loading	86,100	25,900	70%

#### 5.4.3 Effects of Bar Deformation on Steel Strains

The steel strains were always lower in the smooth bars than they were in the deformed bars for all loading rates. For the static loading the maximum steel strains decreased by 77%. As the loading rate was increased to a dynamic loading, the maximum steel strains decreased by 75%. As the loading rate was further increased to impact, the maximum steel strains decreased by 70%. This is summarized in Table 5.18.

**Table 5.18 Average Steel Strains at Failure**

	20" Dia. Specimens with #8 Bars	20" Dia. Specimens with 1" Smooth Bars	Percent Change
Static Loading	$y = -250x + 2600$ $R^2 = .9992$	$y = -58.6x + 589$ $R^2 = .9852$	77%
Dynamic Loading	$y = -433x + 4190$ $R^2 = .9706$	$y = -111x + 1040$ $R^2 = .9715$	75%
Impact Loading	$y = -312x + 3250$ $R^2 = .9972$	$y = -90x + 993$ $R^2 = .9961$	70%

#### 5.4.4 Effects of Bar Deformation on Concrete Strains

The concrete strains were also always lower in the specimens containing the smooth bars than they were in the specimens containing the deformed bars. This is shown in Table 5.19.

**Table 5.19 Average Concrete Strains at Failure**

	20" Dia. Specimens with #8 Bars	20" Dia. Specimens with 1" Smooth Bars	Percent Change
Static Loading	-180	-35	80%
Dynamic Loading	-172	-54	69%
Impact Loading	-208	-116	44%

For the static loading, the concrete strains decreased by 80%. For the dynamic loading rates, the reduction was 69%. Finally, for the impact loading, the concrete strains

decreased by 44%. The large reduction in concrete strains induced by the static loadings is due to the fact that there is no means to transfer radial strains from the smooth steel bar to the concrete as there are with the steel lugs on the deformed bars. The small radial strains that were seen were probable due to Poisson's effects. This became less obvious for the dynamic and impact loadings since they induced shockwaves in the concrete that could cause small radial strains.

#### 5.4.5 Effects of Bar Deformation on Development Length

Bar deformations greatly reduced the development length required. Compared to the smooth bars, the deformations reduced the required development lengths by 78% for the quasi-static loading, 73% for the dynamic loading and 71% for the impact loading. This is summarized in Table 5.20.

**Table 5.20 Development Length and Bond Strength**

Loading Rate	20" Dia. Specimens with 1" Smooth Bars		20" Dia. Specimens with #8 Bars (in)		Percent Reduction / Increase	
	Development Length (in)	Bond Strength (psi)	Development Length (in)	Bond Strength (psi)	Development Length (in)	Bond Strength (psi)
Static	34	480	7.6	2080	78%	433%
Dynamic	18.6	786	5.0	2600	73%	331%
Impact	21	824	6.0	2740	71%	333%

This work was in good agreement with previously conducted work. Menzel found that for 3,000 psi concrete, the average bond strength for a 1-inch diameter smooth bar subjected to static loading was 342 psi and for a 1-inch diameter deformed bar was 838 psi. Menzel also stated that the bond stress was dependent on  $\sqrt{f'_c}$ . If we adjust Menzel's values for the increased concrete strength used in this investigation, we get a bond stress



of 483 psi for the smooth bar and 1,200 psi for the deformed bar. This compares well with 480 psi for the smooth bar and 1,310 psi for the deformed bar obtained for static loading in this investigation and presented in Table 5.20.

## CHAPTER 6 NUMERICAL ANALYSIS OF SPECIMENS

Since the quasi-static loading of the smooth bars could be considered to be in static equilibrium, a closed form solution was obtained for this configuration. However, since the dynamic loadings and the quasi-static loadings of the deformed bars were much more complex, and no closed form solution was available, a finite element analysis of the dynamic loadings and quasi-static loadings of the deformed bars was conducted.

DYNA3D (Lin 1999) was chosen as the finite element code to be used in the dynamic analysis. DYNA3D is a nonlinear, explicit, three-dimensional finite element code used for solid and structural mechanics. Dr. John O. Halquist of Lawrence Livermore National Laboratories (LLNL) originated DYNA3D. Dr. Jerry L. Lin is now maintaining the program.

The elements available within the program include one-dimensional truss and beam elements, two-dimensional quadrilateral and triangular shell elements, and three-dimensional continuum elements. Also, a wide variety of material models are available including elastic, plastic, elastic-plastic, composite thermal effects, explosive detonations, and rate dependence. Additionally, a variety of contact surfaces including frictional sliding, tied, tied with breaking, and single surface contact are available.

NIKE3D (Puso 2001) was chosen for the quasi-static analysis. This program is a general purpose, three-dimensional, non-linear finite element code designed for solving problems in solid and structural mechanics. This program was also developed at LLNL. It utilizes implicit time integration, making it most effective for static and low rate dynamic problems. Unlike DYNA3D, NIKE3D utilizes a relatively small set of elements and low order interpolation, requiring no mid-side node definitions. This approach

appears to be robust enough for non-linear quasi-static loadings while greatly reducing the computing resources required for the analysis.

The elements available within NIKE3D include solid, beam and shell. The program includes 22 material models including elastic, elastic-plastic, thermo elastic-plastic, and thermo elastic creep. As with the element selection, the slide lines available in NIKE3D are more limited than those in DYNA3D. These include tied, sliding only, sliding with gaps and friction, single surface and auto contact.

The program INGRID (Christon 1992) that was also developed at LLNL was used as the pre-processor for DYNA3D and NIKE3D. INGRID is a generalized 3-D finite element mesh generator used for modeling non-linear systems. It provides the capability to generate complex geometric models using beam, shell, and hexahedral elements. Additionally, boundary conditions, initial conditions, material properties and contact surfaces can be specified.

Finally, post-processing was accomplished using the LLNL program GRIZ (Speck 1996). GRIZ is a general purpose, post-processor application supporting interactive visualization of finite element analysis results on unstructured grids. In addition to basic state variable display, GRIZ provides 3-D visualization techniques such as isocontours, isosurfaces, cutting planes, vector field display and partial tracing.

All four of these programs are part of a set of public domain codes developed in the Methods Development Group at LLNL.

## 6.1 Mesh Generation

INGRID was used to generate the finite element mesh. Different INGRID models were developed for the smooth bars, the dynamically loaded deformed bars and the quasi-statically loaded deformed bars.

### 6.1.1 Smooth Bar

If cylindrical coordinates were used throughout the grid, multiple elements would have one single node in the center. This would cause DYNA3D to go unstable. Therefore Cartesian coordinates were used to model the steel bar. The four corners of the grid were deleted, and the remaining elements projected onto a surface with a radius of 0.5-inches. The result is shown in Figure 6.1. The remainder of the model was developed in cylindrical coordinates. The concrete cylinder was modeled as three concentric rings that were attached to each other using a tied slide line. The complete model is shown in Figure 6.2.

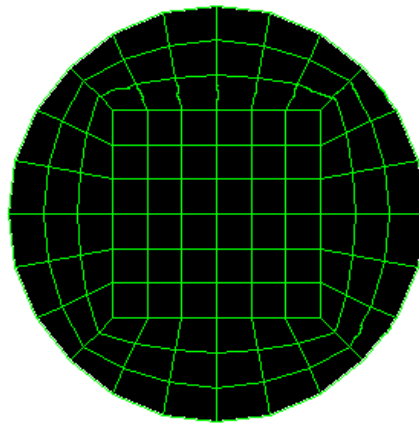


**Figure 6.1 Smooth bar showing Cartesian coordinates with projected outer surface to form the cylinder**

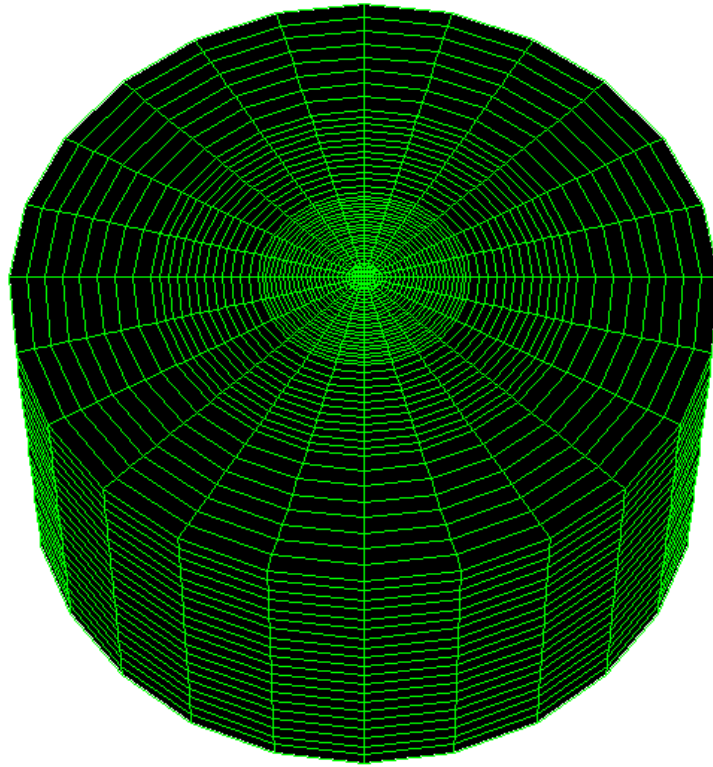


**Figure 6.2 Complete finite element model for smooth bar runs**

The load functions were obtained from the load cell records from the experimental work. The loads were applied to the 133 nodes on the bottom of the steel bar (Figure 6.3). The nodes on the bottom of the concrete cylinder were restrained in the Z direction from a radius of 1.5-inches to the outside of the concrete cylinder (Figure 6.4).

The concrete was attached to the steel bar using a break slide line. This allowed a sheering force,  $\sigma_s$  to be transferred across the slide line. Once  $\sigma_s$  reached  $\sigma_{ST}$  the slide line broke, and the steel bar was free to move. Solid element time history blocks were inserted into the mesh to obtain strain vs. time plots at locations in the model corresponding to the strain measurements made in the experimental portion of this

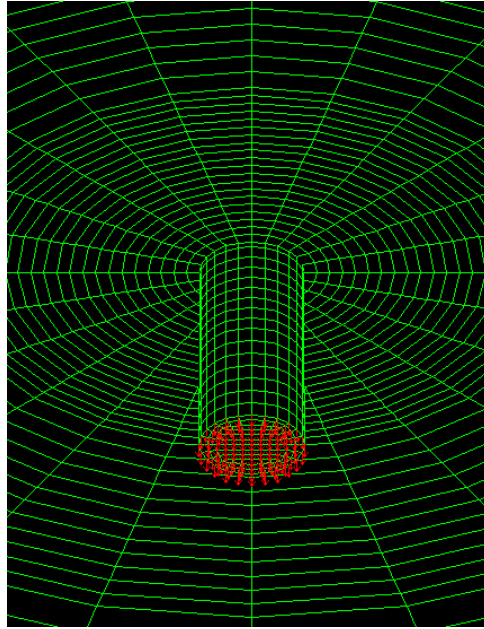


**Figure 6.3 Loads applied to the 133 nodes on the bottom of the steel bar**

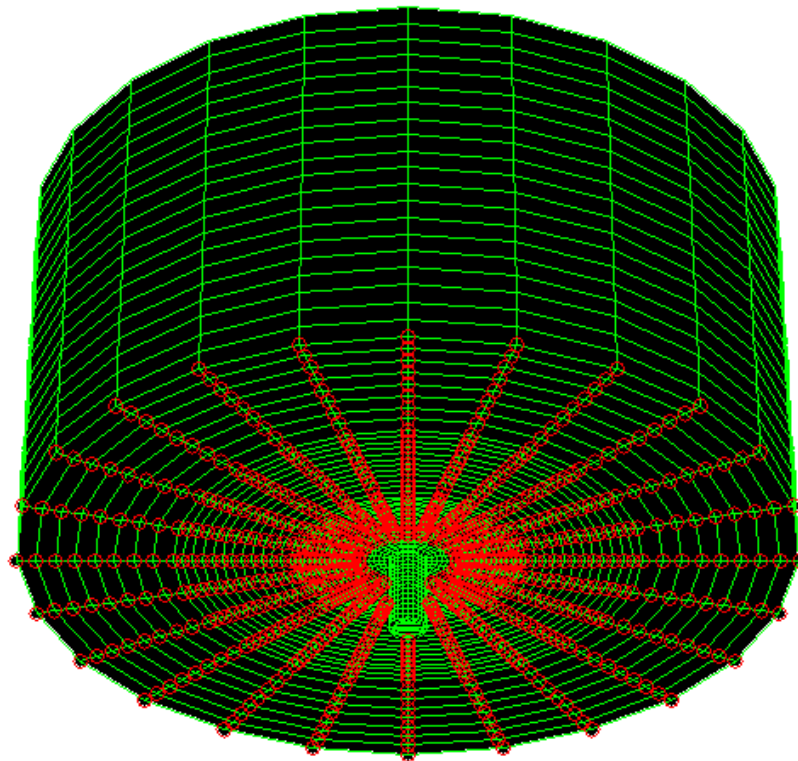


**Figure 6.4 Nodes on the bottom of the concrete restrained in the Z direction**

investigation. For the steel bar these were elements 1081, 1225, 1369, 1513 and 1657, which corresponded to 1-inch, 3-inch, 5-inch, 7-inch and 9-inch from the bottom of the sample respectively. In the concrete, they were elements 31297, 33985, 36673 and 39361, which corresponded to 2-inch, 4-inch, 6-inch and 8-inch from the bottom of the sample respectively.

#### 6.1.2 Dynamic and Impact Loaded Deformed Bars

The mesh for the dynamic and impact loaded deformed bars was generated similar to the smooth bars except the individual deformations on the bar were also modeled. The center of the steel bar was generated the same as the smooth bar except the radius was 0.25-inches. Another ring of steel was placed around the center ring and attached using a tied slide line. The steel between the deformations was then deleted, and the nodes on the remaining steel moved up or down to produce the sloped faces of the deformations. The deformations were also deleted between  $340^{\circ}$  and  $20^{\circ}$  and between  $160^{\circ}$  and  $200^{\circ}$ , Figure 6.5. This represented the strain gage grooves that were machined on the steel bars. The concrete was generated in three concentric rings as before except that parts of the inside of the inner ring were deleted and the remaining nodes moved up or down to produce voids for the steel deformations to fit into. The interface between the steel and concrete was handled using the same tied slide line used in the smooth bar model. Solid element time-history blocks were inserted in elements 10827, 10927, 11107, 11247 and 11587 for the steel bar and elements 92675, 94733, 96693 and 98751 for the concrete.



**Figure 6.5 Deformed bar showing deformations deleted to model the strain gage groove**

#### 6.1.3 Quasi-Static Loaded Deformed Bars

Since NIKE3D cannot handle as large of a problem as DYNA3D, the mesh size was increased to reduce the number of nodes and elements (Figure 6.6). Since this is a quasi-static analysis, the larger elements would not adversely affect the results. Additionally, NIKE3D cannot handle the breaking slide line used in the previous analysis. Therefore, this slid line was changed to a tied slide line, and the strain gage grooves were not modeled (Figure 6.7). This greatly simplified the steel concrete interface. Solid element time history blocks were inserted in elements 6641, 6653, 6665, 6677 and 6685 for the steel and 14002, 14506, 15073 and 15640 for the concrete.



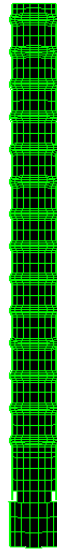


**Figure 6.6 Larger mesh size used in the NIKE3D runs**



**Figure 6.7 Simplified deformation pattern used on the NIKE3D runs**

## 6.2 1- Inch Diameter Smooth Bar Embedded in a 20-inch Diameter Concrete Cylinder

A set of calculations was performed to determine the value of the chemical adhesion of the cement to the steel bar, and how this value varied with strain rate. A closed form solution was obtained for the quasi-static loading, and a finite element analysis was performed for the dynamic and impact loading.

### 6.2.1 Quasi-Static Loading

Since the load was applied to the steel bar, while the concrete cylinder was restrained, and the system was in static equilibrium, a force equal to the static loading force was transferred from the steel bar to the concrete. The only mechanism for this force transfer was the sheering resistance of the chemical adhesion of the cement paste to the steel bar. Knowing the total force applied and the diameter and embedment length of the steel bar, the average sheering force  $\sigma_{SA}$  can be calculated as (Equation 6.1).

$$\sigma_{SA} = \frac{f}{A} \quad (6.1)$$

Using a total force of  $f=15,050$  lbs (average quasi-static load applied to the smooth bars before failure) and a diameter and length of 1-inch and 10-inches respectively, and applying equation 6.1, we obtain

$$\sigma_{SA} = \frac{15,050 \text{ lbs}}{\pi(1 \text{ inch}) \times (10 \text{ inches})} = 479.1 \text{ psi} \approx 480 \text{ psi}$$

Since the strain decays linearly along the length of the steel bar, with its maximum value at the bottom of the sample and 0 at the top of the sample, the shear transferred from the steel to the concrete will have the same relationship. Therefore, the maximum shear

stress  $\sigma_{ST}$  will occur at the bottom of the sample just prior to the bond failure, and will decay linearly to 0 at the top of the sample. This leads to Equation 6.2.

$$\sigma_{ST} = 2\sigma_{SA} \quad (6.2)$$

Or for test 23 we obtain:

$$\sigma_{ST} = 2 \times 480 \text{ psi} = 960 \text{ psi}$$

Since there are no means of transferring radial forces from the smooth steel bar to the concrete, the radial strains will be very low. The small strains that were seen in the experimental work (34.8 micro strains) were probably due to Poison's effects

#### 6.2.2 Dynamic Loading

A triangular loading function with a maximum value of 24,670 lbs and duration of 32 msec was used to simulate the average dynamic load applied to the smooth bars. An initial estimate of  $\sigma_{ST}$  was made, and the input deck for DYNA3D generated. DYNA3D was then run on a Silicon Graphics workstation. Iterative runs were made until calculated steel strains were in close agreement with those obtained from equation 4.8.

For these runs,  $\sigma_{ST}$  was determined to be 2,600 psi. As the run progressed, the strains in the steel bar increased until  $t=27$  msec., at which time the slide line broke, and the steel bar was released. The maximum steel strain at each of the element dumps is shown in Figure 6.8.

The concrete strains, although very small as would be expected, show a very unusual response. The concrete first went into radial tension, and then into compression, then back into tension before the slide line broke. The readings closest to the bottom of the

model showed the largest tensile strain while the readings at the top of the model showed the largest compressive readings. This phenomenon is likely due to the boundary

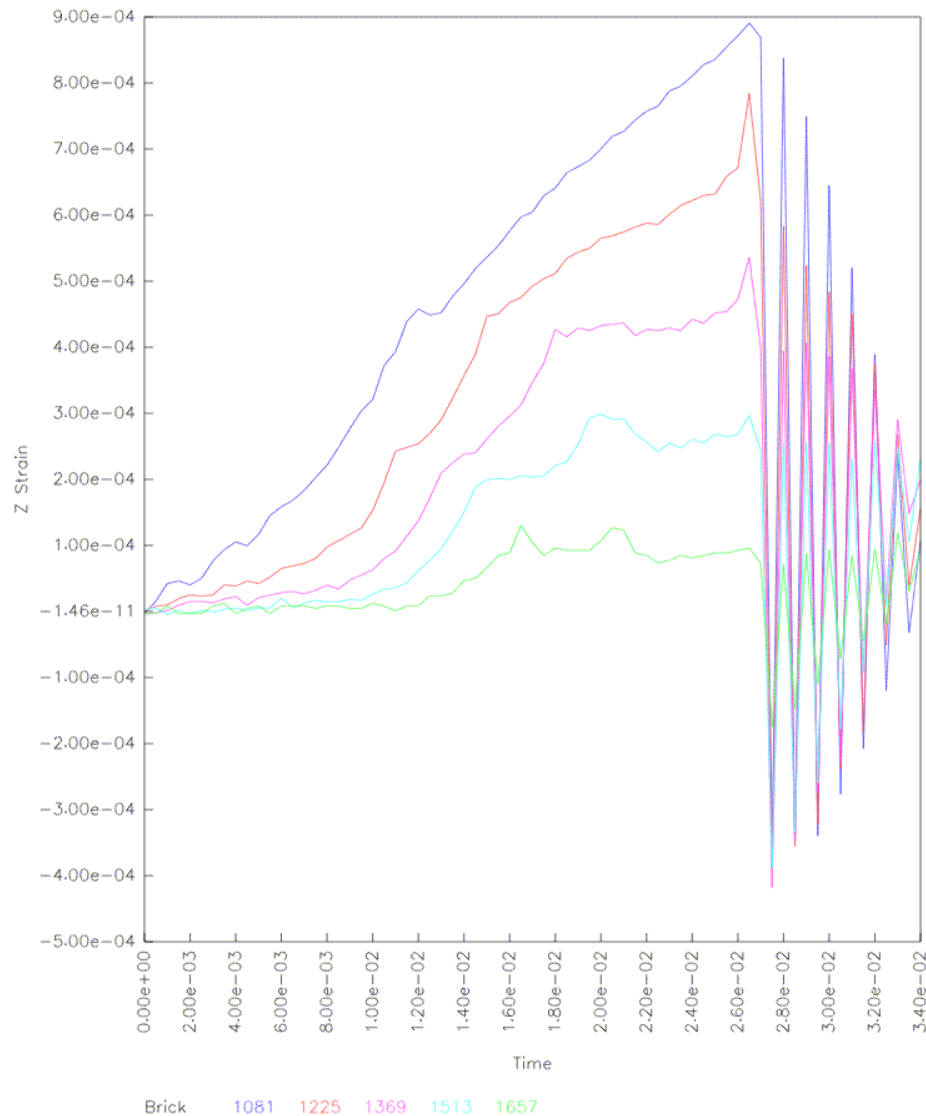


**Figure 6.8 Composite steel strains, 1-inch smooth bar, 20-inch diameter sample, dynamic loading**

conditions and the dynamic behavior of the concrete and steel materials themselves.

Remember that there are no radial forces being applied to the concrete, therefore the radial strains are very small. The shock waves that are running through the system could easily be numerically larger than any strains caused by Poisson's effects. Also there is a

very complex boundary condition at the bottom of the concrete cylinder, where part of the concrete in the vicinity of the first gage is not supported in the Z direction. The concrete strains are shown in Figure 6.9.

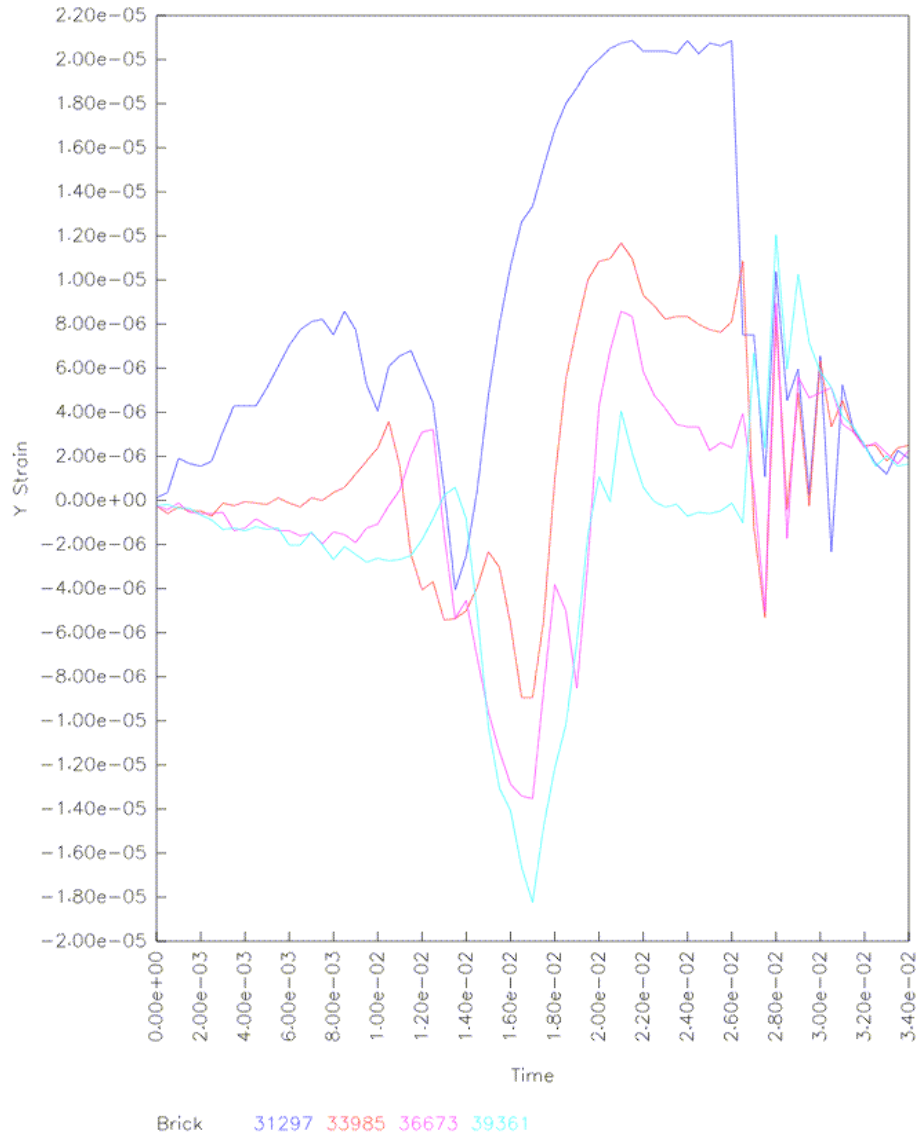


**Figure 6.9 Composite concrete strains, 1-inch smooth bar, 20-inch diameter sample, dynamic loading**

When we compare the empirical and numerical steel strains, Figure 6.10, we see that there is very close agreement in the data. Figure 6.11 shows the comparison between the empirical and numerical concrete strains and the 95% confidence interval for the

empirical data. The calculated strains fall slightly above the upper limits of the confidence interval.

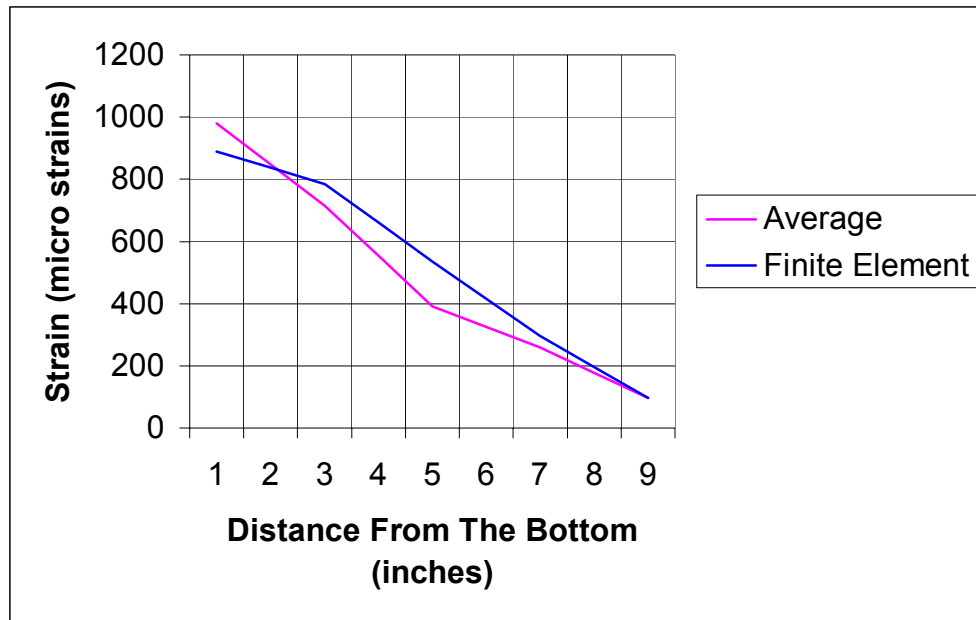


**Figure 6.10 Comparison of empirical and numerical steel strains, 1-inch smooth bar, 20-inch diameter sample, dynamic loading**

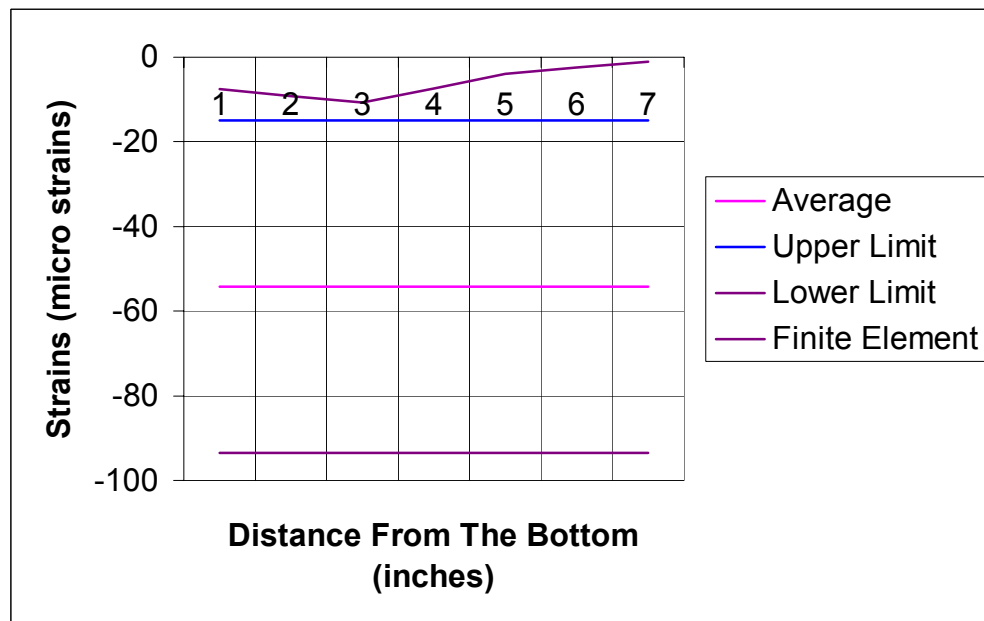


**Figure 6.11 Comparison of empirical and numerical concrete strains, 1-inch smooth bar, 20-inch diameter sample, dynamic loading**

### 6.2.3 Impact Loading

The input file used in the dynamic loading was modified by changing the triangular loading function to a peak value of 25,908 lbs and duration of 3.2 msec. Iterative runs were then made varying the value of  $\sigma_{ST}$  until the strains in the steel bar were in good agreement with the experimental data. This yielded a value of  $\sigma_{ST} = 3,200$  psi. As in the dynamic run, the tensile strains increased until  $\sigma_S = \sigma_{ST}$  at which time ( $t = 1.8$  msec) the slide line broke and released the steel bar. The maximum steel strains are shown in Figure 6.12.

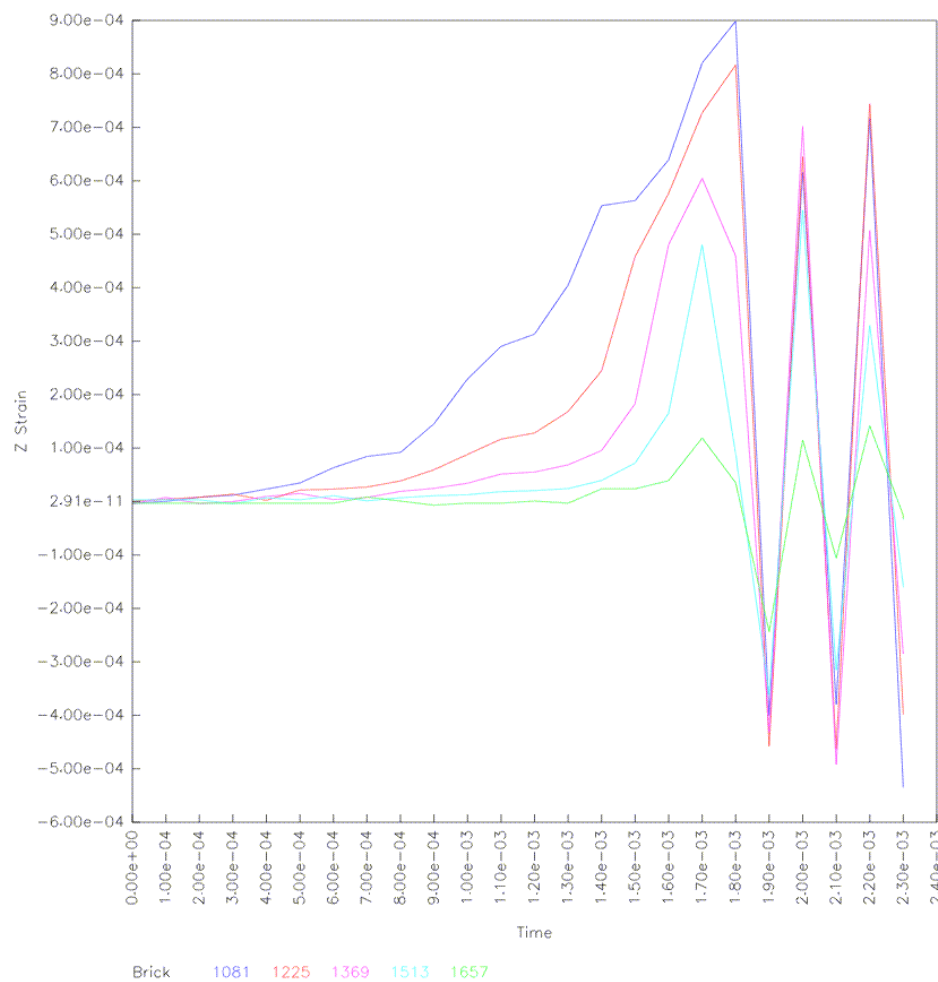


**Figure 6.12 Composite steel strains, 1-inch smooth bar, 20-inch diameter sample, impact loading**

The concrete strains showed the same apparent variability that was seen in the dynamic run. The lowest gage went from tension (2.0 micro strains at  $t=1.8$  msec ) to compression (-8.8 micro strains at  $t=1.8$  msec) back to tension (5.1 micro strains at  $t=1.9$  msec). The second gage location only went into tension (8.1 micro strains at  $t=1.5$  msec). The third gage location, 6-inches from the bottom, went into compression (-3.4 micro strains at  $t=1.4$  msec then into tension (6.9 micro strains at  $t=1.6$  msec). The last location, 8-inches from the bottom, went into compression -6.4 micro strains at  $t=1.5$  msec then rebounded slightly to a compressive strain of -2.5 micro strains at  $t=1.66$  msec. The average compressive strain measured in the experimental work under these loading conditions was -54.3 micro strains, Figure 6.13 shows the concrete strain plots from the numerical analysis.

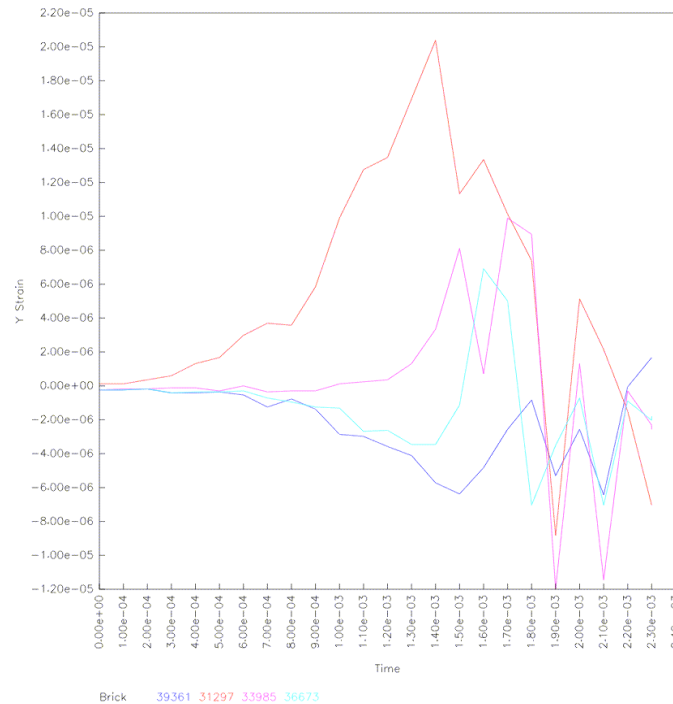


**Figure 6.13 Composite concrete strains, 1-inch smooth bar, 20-inch diameter sample, impact loading**



The repeat reversal of strain along with the very small values clearly indicate that at these loading rates, the concrete strains are dominated by shock waves traveling through the concrete, reflecting off of the surface and returning back through the concrete.

When we compare the numerical and empirical work, we find the same relationship we saw in the dynamic loading. The steel strains, Figure 6.14, are in very close agreement, but the numerical concrete strains are slightly above the upper limits of the 95% confidence interval for the empirical data, Figure 6.15

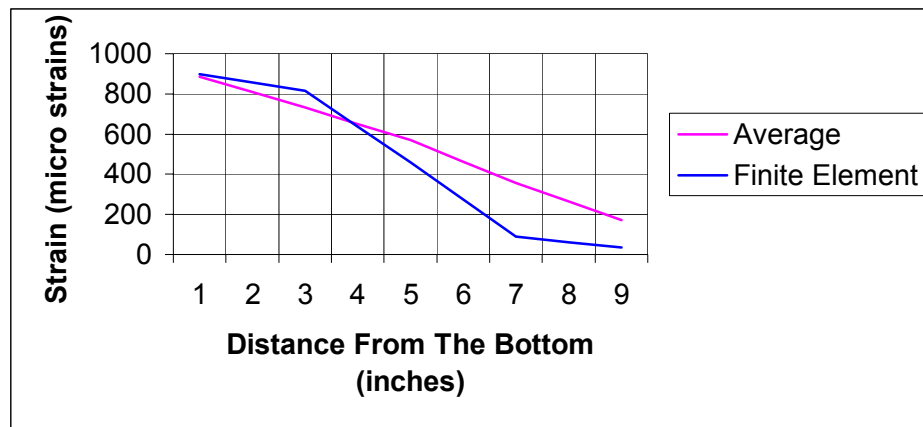


**Figure 6.14 Comparison of empirical and numerical steel strains, 1-inch smooth bar, 20-inch diameter sample, impact loading**

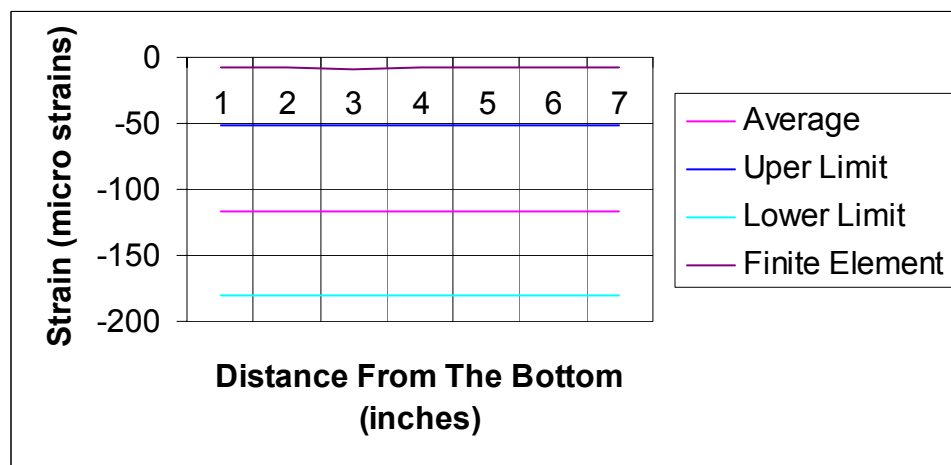


**Figure 6.15 Comparison of empirical and numerical concrete strains, 1-inch smooth bar, 20-inch diameter sample, impact loading**

### **6.3 Analysis of a Number 8 Deformed Bar Embedded in a 20-inch Diameter Concrete Cylinder**

NIKE3D was used to model the quasi-static loading while DYNA3D was used to determine the strains present in the steel and concrete when it was subjected to a dynamic or impact loading.

#### **6.3.1 Quasi-Static Loading**

A modified triangular loading function with a peak value of 65,283 lbs in 288 seconds was added to the Ingrid mesh file, and the input file for NIKE3D generated. Since this program could not handle break slide lines, a tied slide line was used between the steel and the concrete. As the load increased, the strains in the steel increased to a maximum of 489 micro strains, which was obviously well within the elastic limits, Figure 6.16. The concrete strains all went into compression until  $t=60$  sec when the strains in element 14,002 changed direction and finally went into tension around  $t=120$  sec. The rest of the strains remained in compression, and increased until failure, Figure 6.17. In this model, failure was caused by excessive deformation of the concrete elements in the vicinity of the first steel deformation, Figure 6.18. As was mentioned earlier, the material used to model the concrete was elastic-plastic. While this did a very good job of modeling the elastic loading of the concrete, it did a very poor job of modeling the failure of the concrete. While concrete has a very brittle failure mode, this material model had a very ductile failure mode. This ductile failure caused the excessive deformations of the concrete elements in the vicinity of the first steel deformation. The importance of the model is that the concrete reached its plastic range, which would have represented the beginning of cracking in the real concrete, long before the steel reached its elastic limit.

This would indicate that the model would fail due to radial cracking of the concrete before yielding of the steel, which is what was observed in the physical experiments for this loading.

When we compare the numerical data with the empirical data, we see that NIKE3D greatly underestimated the strains in both the steel, Figure 6.19 and the concrete, Figure 6.20

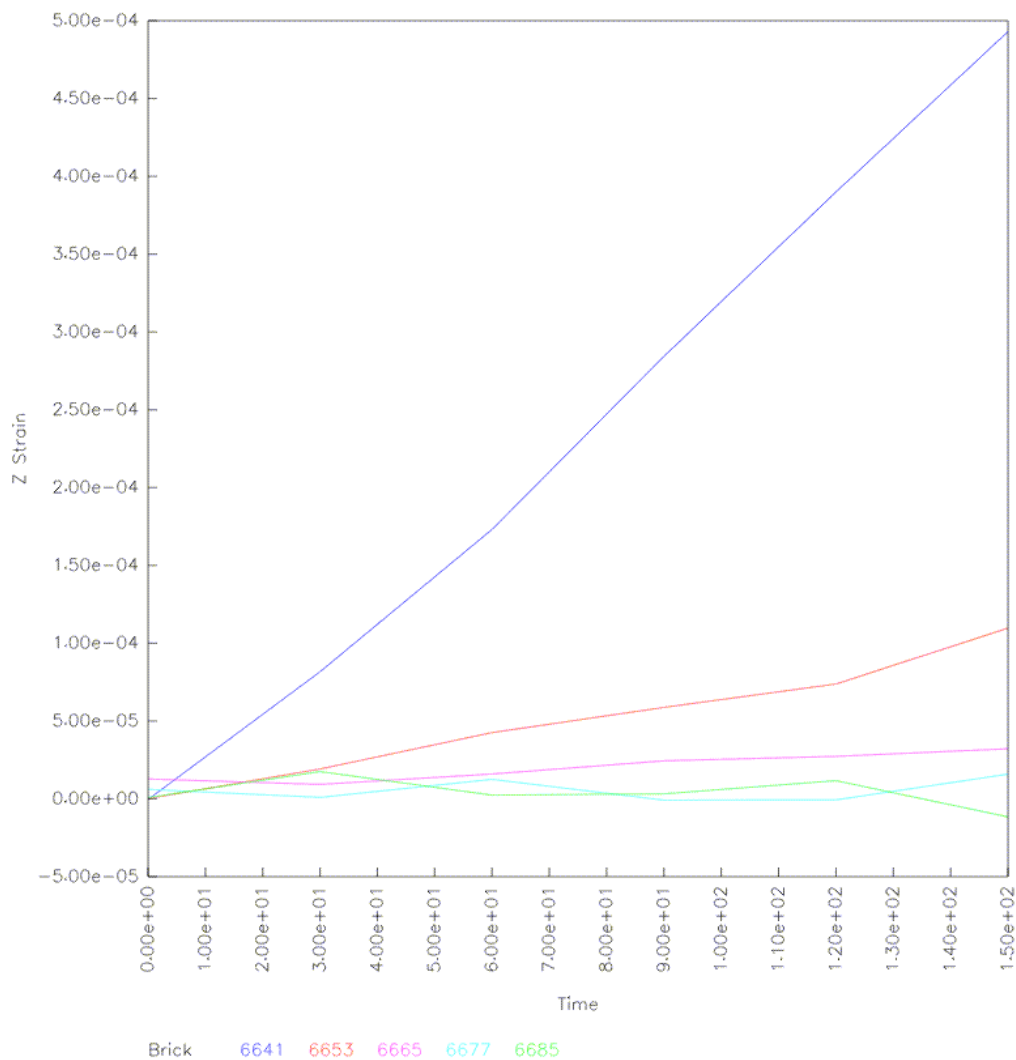


**Figure 6.16 Composite steel strains, #8 deformed bar, 20-inch diameter sample, quasi-static loading**

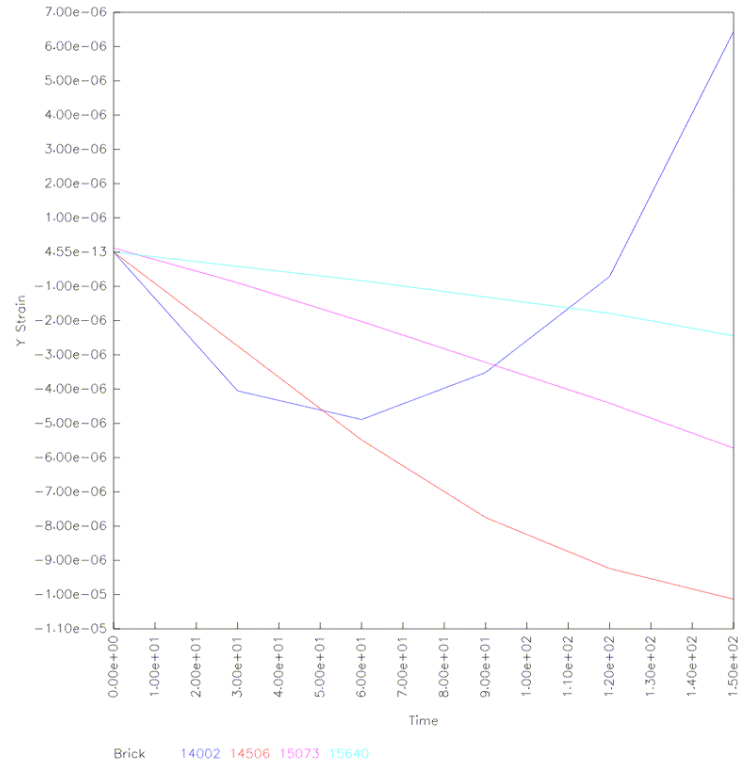


**Figure 6.17 Composite concrete strains, #8 deformed bar, 20-inch diameter sample, quasi-static loading**

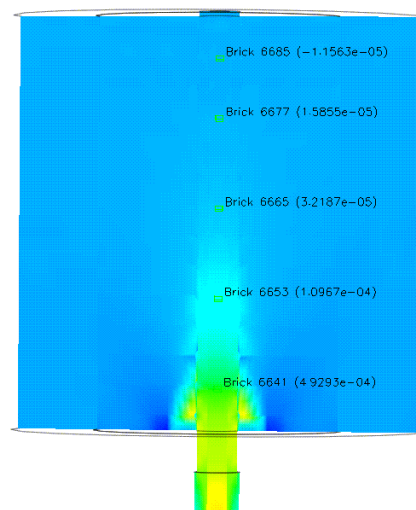


**Figure 6.18 Failure due to excessive deformation of the concrete elements**

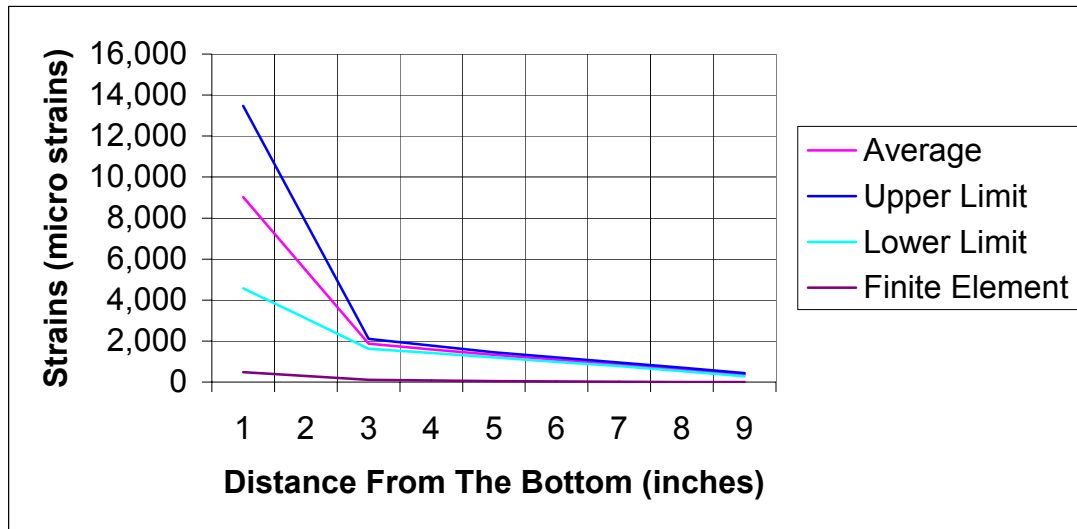


**Figure 6.19 Comparison of empirical and numerical steel strains, #8 deformed bar, 20-inch diameter sample, quasi-static loading**

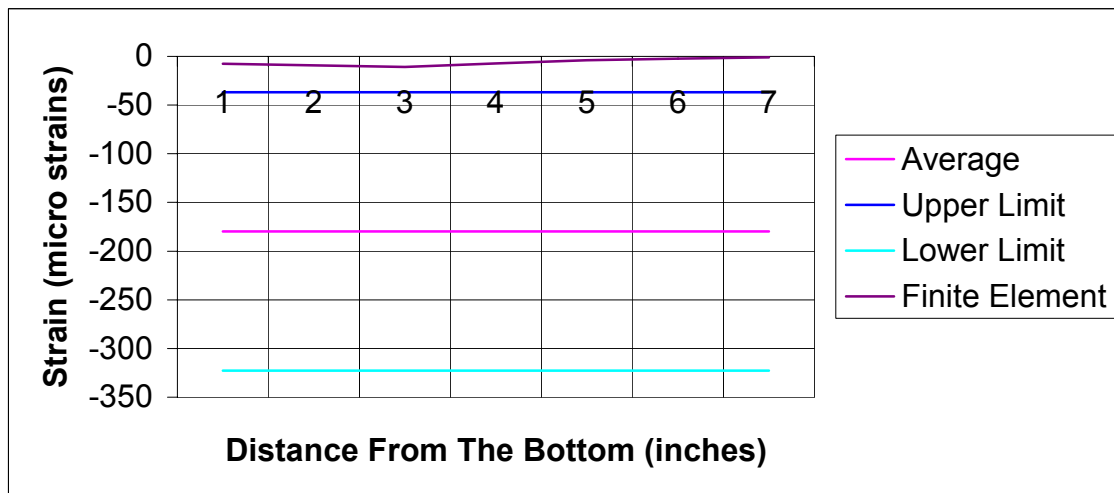


**Figure 6.20 Comparison of empirical and numerical concrete strains, #8 deformed bar, 20-inch diameter sample, quasi-static loading**

### 6.3.2 Dynamic Loading

A modified triangular loading function with a maximum value of 81,550 lbs and duration of 122 msec was added to the Ingrid mesh file, and the input file for DYNA3D generated. Since DYNA3D could handle breaking slide lines the value of  $\sigma_{ST} = 2600$  psi obtained from the smooth bar runs was used to model the chemical adhesion between the

steel and the concrete. As the load was applied, the strain in the steel increased until around 50 msec. From 50 msec to 60 msec the strains in the steel continued to increase for the 1-inch, 3-inch and 5-inch positions while decreasing for the 7-inch and 9-inch positions. At this time the steel strains were 3,170 micro strains at 1-inch, 2,600 micro strains at 3-inches, 1,010 micro strains at 5-inches, 1,120 micro strains at 7-inches and 720 micro strains at 9-inches, Figure 6.21. The run terminated normally at the end of the load function.

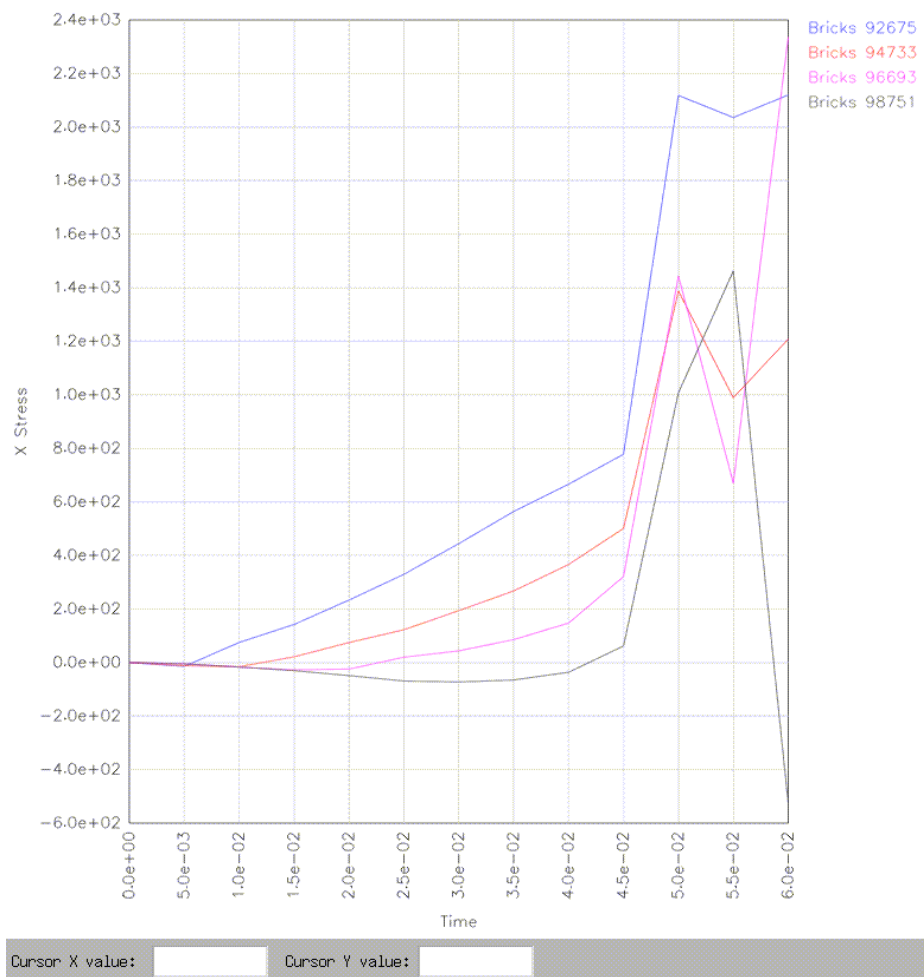


**Figure 6.21 Composite steel strains, #8 deformed bar, 20-inch diameter sample, dynamic loading**

The concrete strains all went into compression and continued to increase in the elastic range until time  $t=50$  msec. At this time, the concrete strains reached the elastic limit and became plastic, Figure 6.22. The fact that both the steel and concrete strains went plastic at the same time indicates that this combination of specimen and loading was on the edge of the failure envelope for yielding the steel bar before the concrete broke.

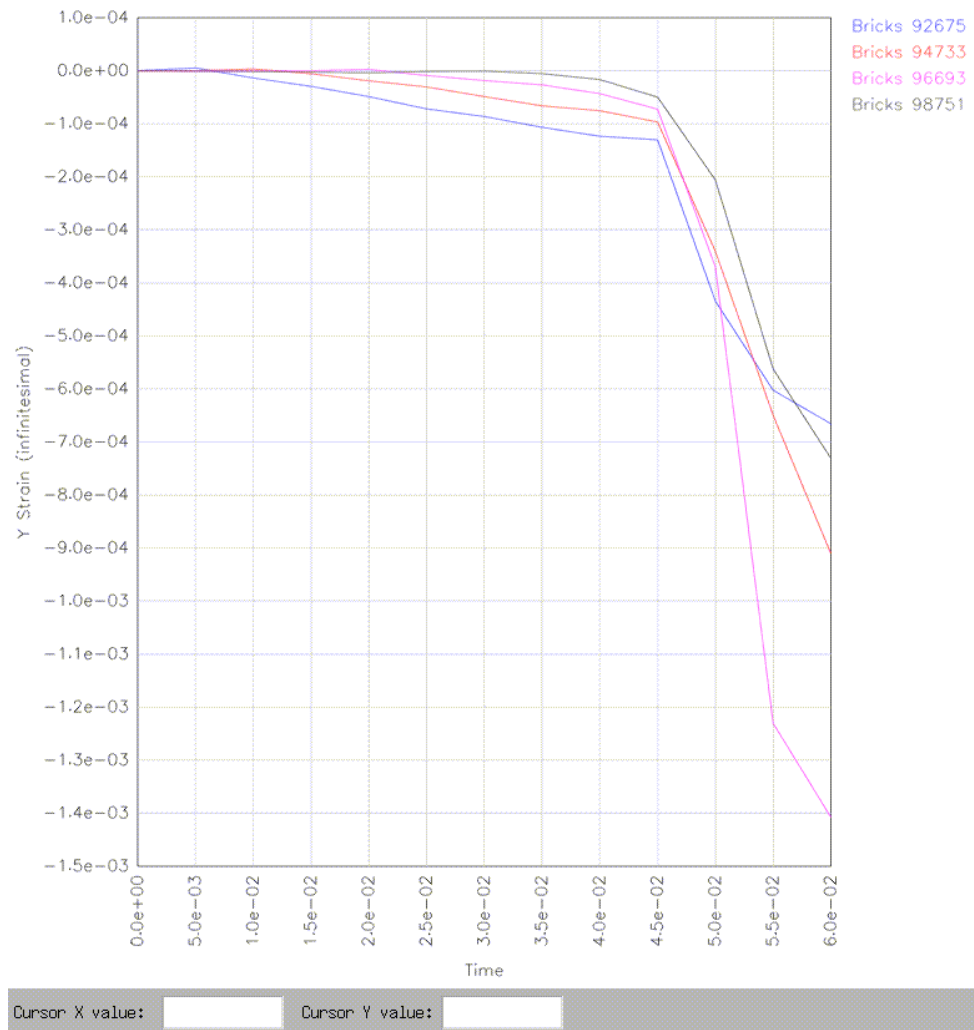


**Figure 6.22 Composite concrete strains, #8 deformed bar, 20-inch diameter sample, dynamic loading**

From Figure 6.23 we see that there is very good agreement between the empirical and numerical steel strains, but the numerical concrete strains, Figure 6.24, were much larger than the empirical data.

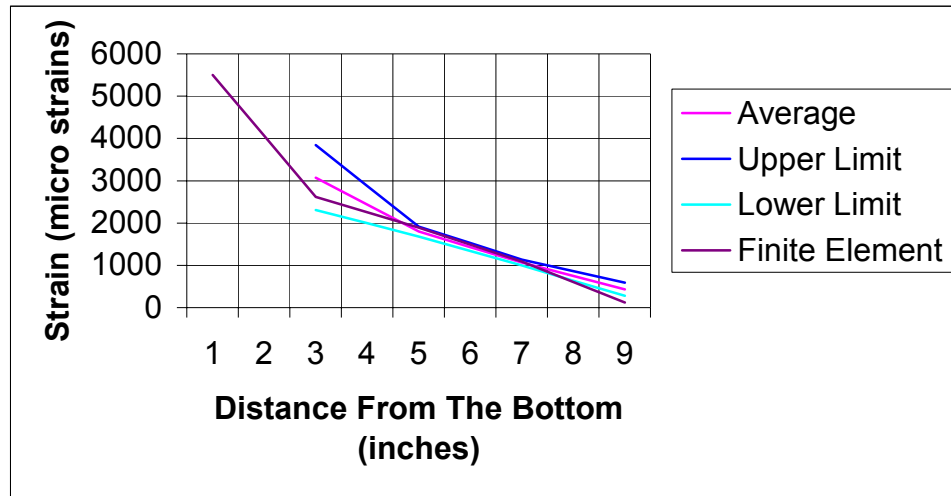


**Figure 6.23 Comparison of empirical and numerical steel strains, #8 deformed bar, 20-inch diameter sample, dynamic loading**

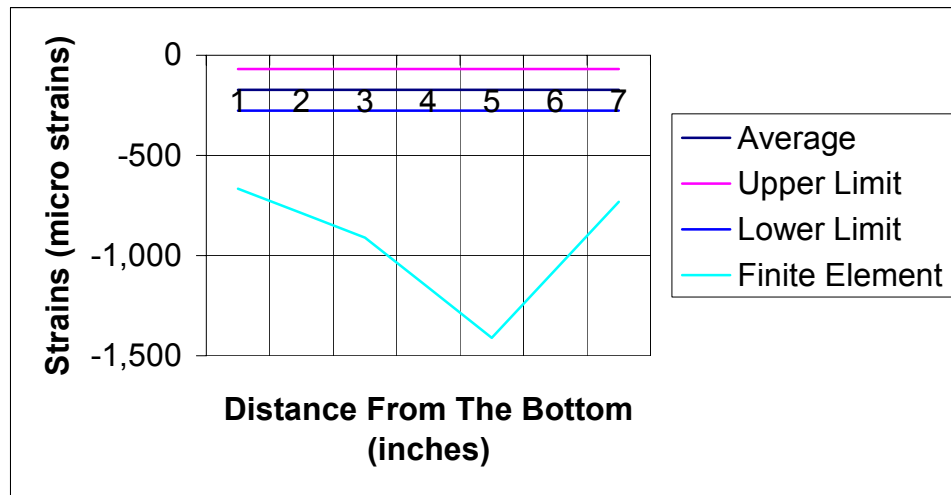


**Figure 6.24 Comparison of empirical and numerical concrete strains, #8 deformed bar, 20-inch diameter sample, dynamic loading**



### 6.3.3 Impact Loading

The same input file used in the dynamic loading was used in the impact loading with the exception of  $\sigma_{ST} = 3,200$  psi (impact loading smooth bar) and the load function was changed to have a peak value of 86,093 lbs and duration of 3.9 msec. The steel strains increased in the elastic range until time  $t=3.3$  msec, at which time the strains in the lower part of the steel bar went plastic. The maximum strain in the steel at failure was 16,865 micro strains at 1-inch from the bottom of the bar, Figure 6.25. This is well in excess of the plastic limit. The concrete strains showed a definite pattern with the largest strain (-319 micro strains) occurring 2-inches from the bottom and decreasing to -82 micro strains, 8-inches from the bottom, Figure 6.26. The concrete strains all remained in the elastic range while the steel strains exceeded the plastic limit, indicating failure due to yielding of the steel bar.

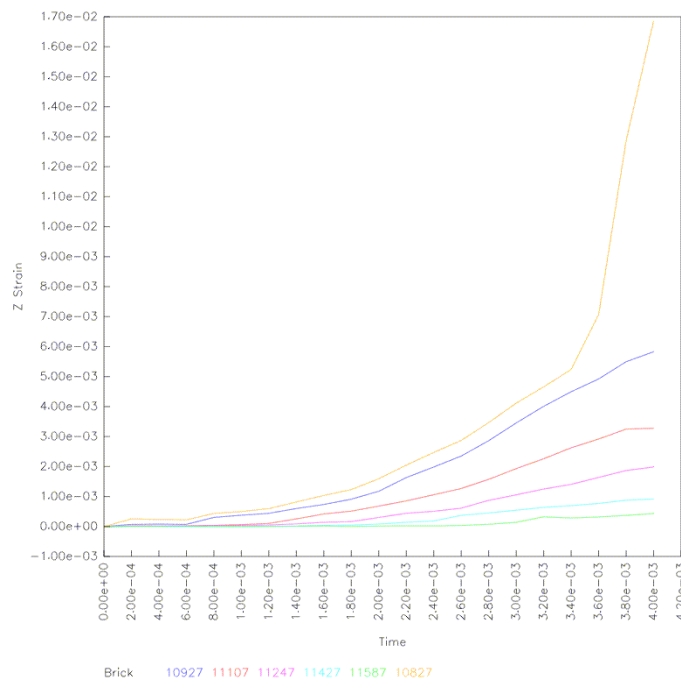


**Figure 6.25 Composite steel strains, #8 deformed bar, 20-inch diameter sample, impact loading**

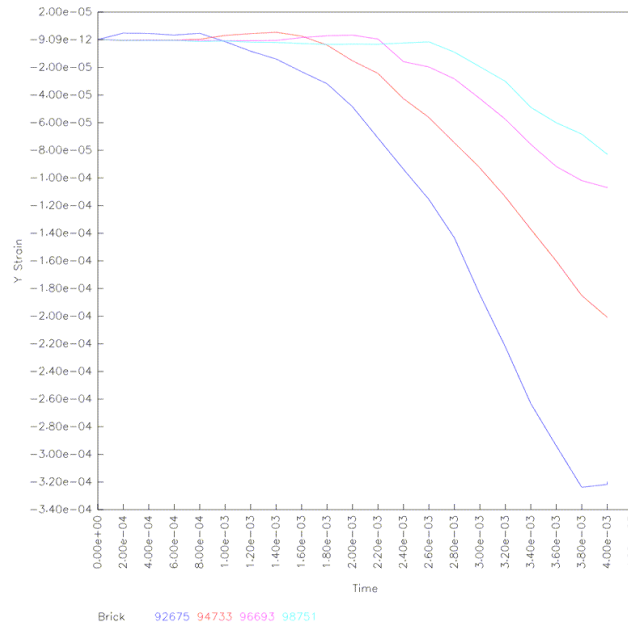


**Figure 6.26 Composite concrete strains, #8 deformed bar, 20-inch diameter sample, impact loading**

Once again, the numerical and empirical steel strains were in good agreement, with the numerical values falling within the bounds of the 95% confidence interval, Figure 6.27.

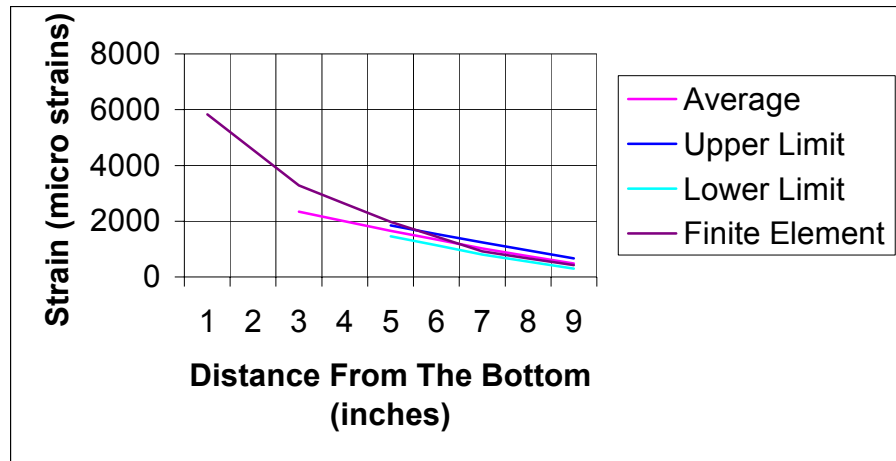
This time, the numerical and empirical concrete strains were also in good agreement, with the calculated values falling between the bounds of the 95% confidence interval,

Figure 6.28

## 6.4 Analysis of a Number 8 Deformed Bar embedded in a 10-inch Diameter Concrete Cylinder

### 6.4.1 Quasi-Static Loading

The input file for this run was identical to the one in section 6.3.1 except the outer ring of concrete was deleted to yield a 10-inch diameter specimen. As the load was applied, the strain in the steel increased to a maximum of 492 micro strains 1-inch from the



**Figure 6.27 Comparison of empirical and numerical steel strains, #8 deformed bar, 20-inch diameter sample, impact loading**

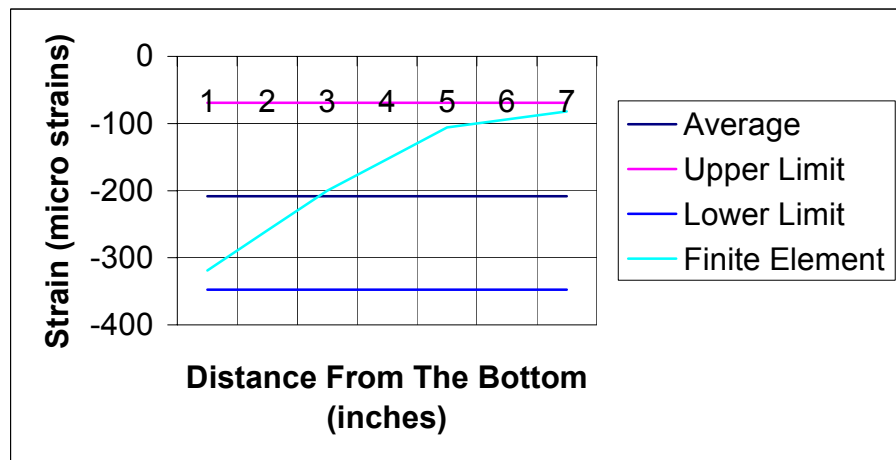


**Figure 6.28 Comparison of empirical and numerical concrete strains, #8 deformed bar, 20-inch diameter sample, impact loading**

bottom to  $-11$  micro strains 1-inch from the top as shown in Figure 6.29. All are obviously well within the elastic limit of the steel. The concrete strains showed the same behavior that was seen with the 20-inch diameter sample, in that all concrete strains were initially in compression, but the strains 2-inches from the bottom changed direction and finally became tensile, Figure 6.30. The run finally failed due to excessive deformation of the concrete elements in the vicinity of the steel deformations as shown in Figure 6.31.

As was stated in section 6.3.1, this indicated that the concrete reached its plastic limit and failed due to radial cracking of the concrete before yielding of the steel bar.

As with the quasi-static loading of the 20-inch diameter sample, NIKE3D underestimated both the steel stresses (Figure 6.32) and the concrete stresses (Figure 6.33).

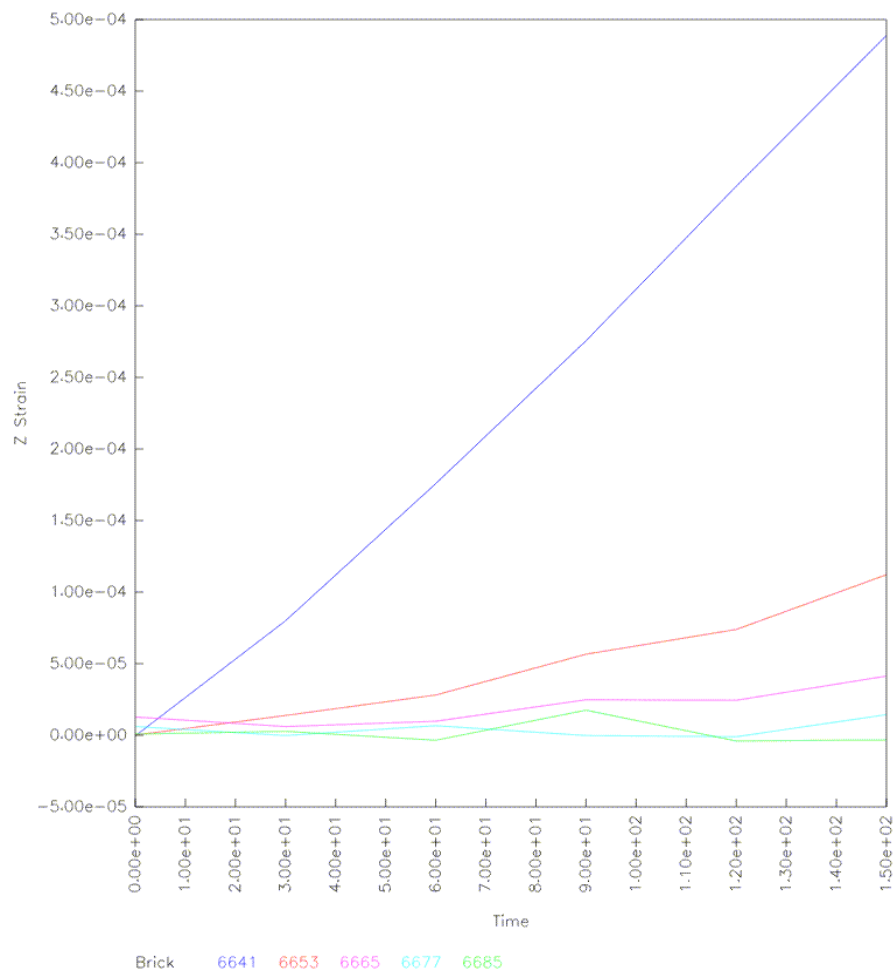


**Figure 6.29 Composite steel strains, #8 deformed bar, 10-inch diameter sample, quasi-static loading**

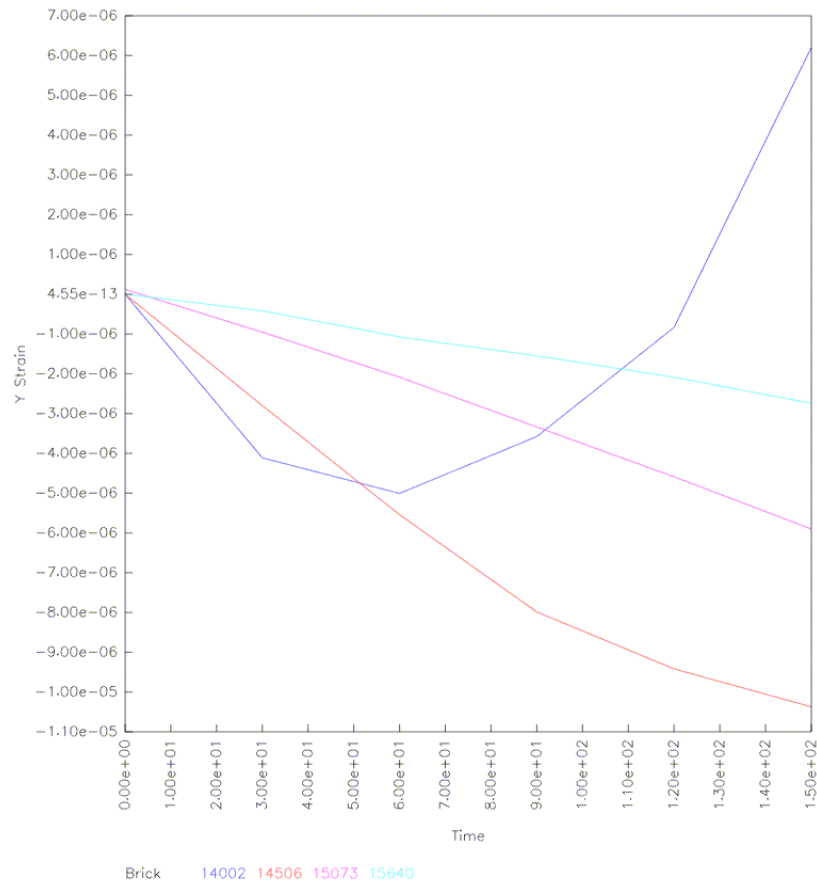


**Figure 6.30 Composite concrete strains, #8 deformed bar, 10-inch diameter sample, quasi-static loading**

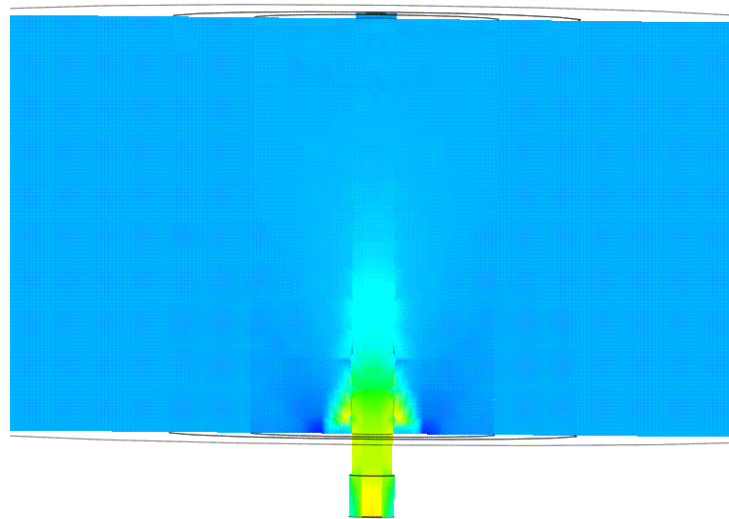


**Figure 6.31 Failure due to excessive deformation of the concrete elements**

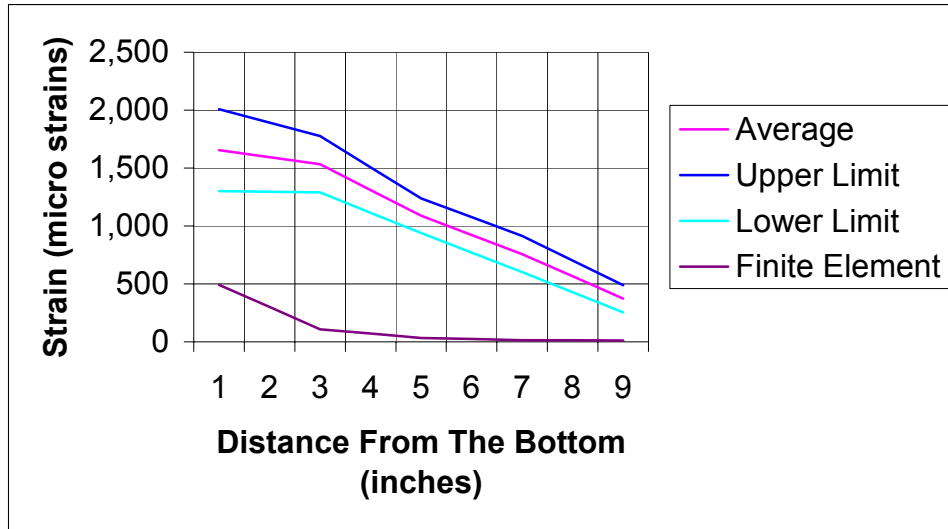


**Figure 6.32 Comparison of empirical and numerical steel strains, #8 deformed bar, 10-inch diameter sample, quasi-static loading**

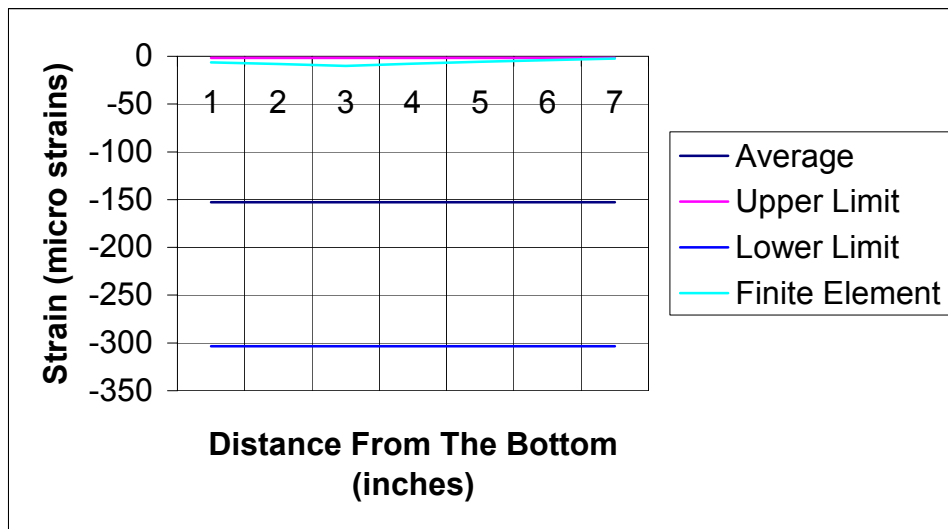


**Figure 6.33 Comparison of empirical and numerical concrete strains, #8 deformed bar, 10-inch diameter sample, quasi-static loading**

#### 6.4.2 Dynamic Loading

This input file was the same as the one in Section 6.3.2 except that the outer ring of concrete was removed to yield a 10-inch diameter model. The steel strains increased as the load was applied until at time  $t=70$  msec, the steel strains varied from a maximum of

6,480 micro strains at 1-inch from the bottom to 43 micro strains 1-inch from the top, as shown in Figure 6.34. At approximately the same time, the concrete strains all went plastic, Figure 6.35. The run finally failed at time  $t=80$  msec due to excessive deformation of the concrete elements. As with the 20-inch diameter specimen, this seems to be an almost balanced failure with both the concrete and steel strains becoming plastic at the same time.

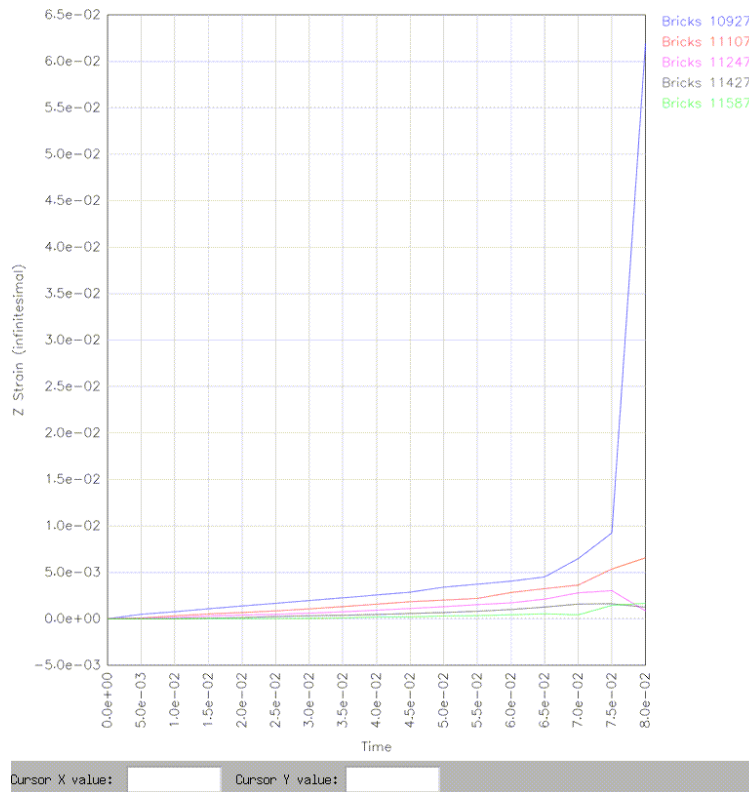


**Figure 6.34 Composite steel strains, #8 deformed bar, 10-inch diameter sample, dynamic loading**

When we compare the numerical and empirical data, we find that the numerical steel strains are larger than the empirical strains at the bottom of the specimen, but come in agreement at the top, Figure 6.36. The numerical concrete strains are larger than the average empirical strains, but within the 95% confidence interval, Figure 6.37.

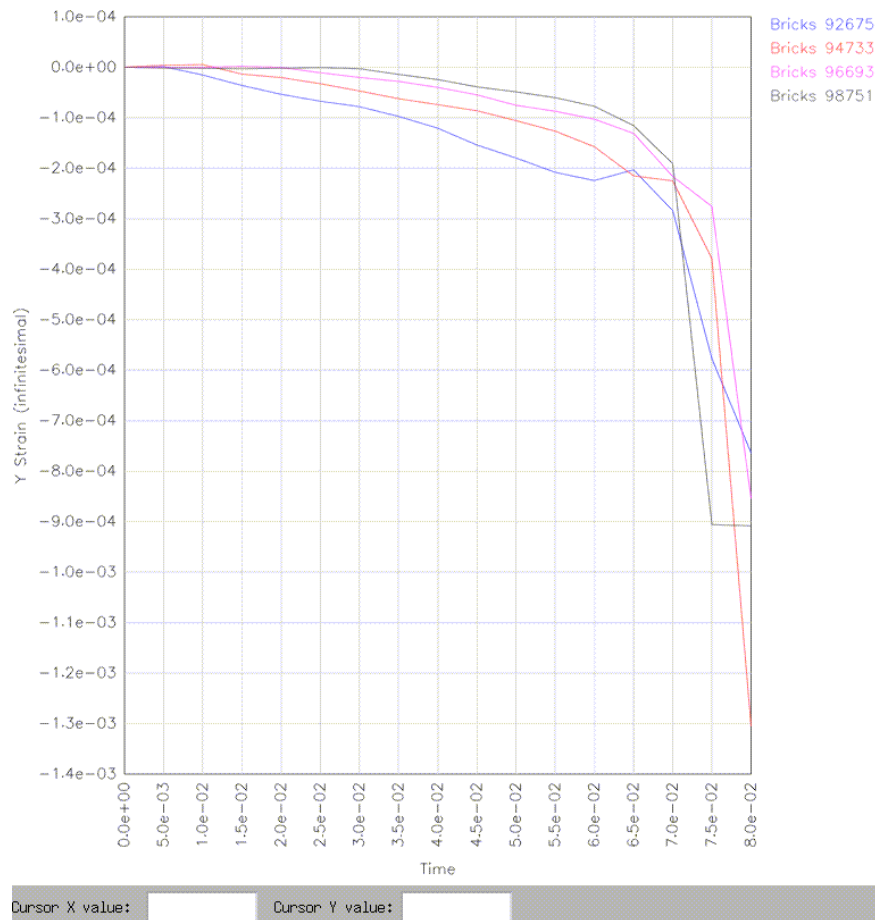


**Figure 6.35 Composite concrete strains, #8 deformed bar, 10-inch diameter sample, dynamic loading**

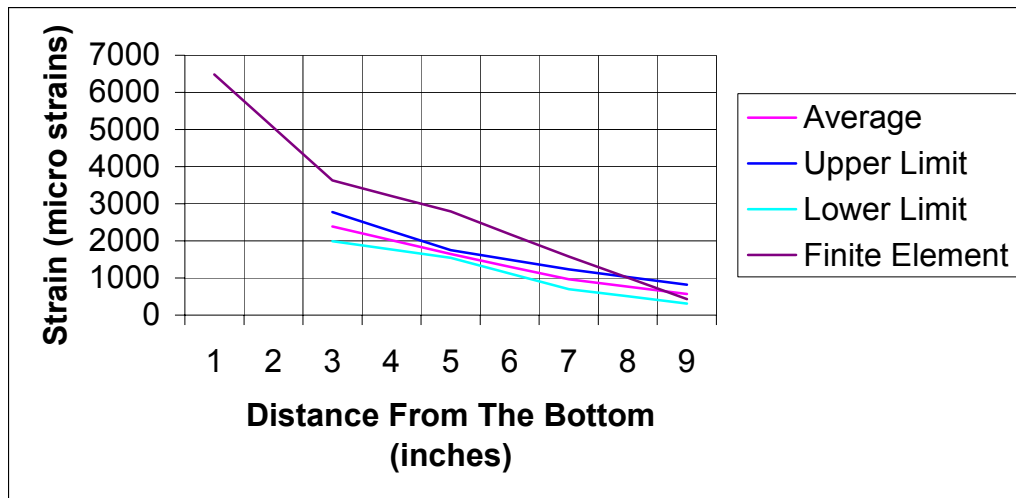


**Figure 6.36 Comparison of empirical and numerical steel strains, #8 deformed bar, 10-inch diameter sample, dynamic loading**



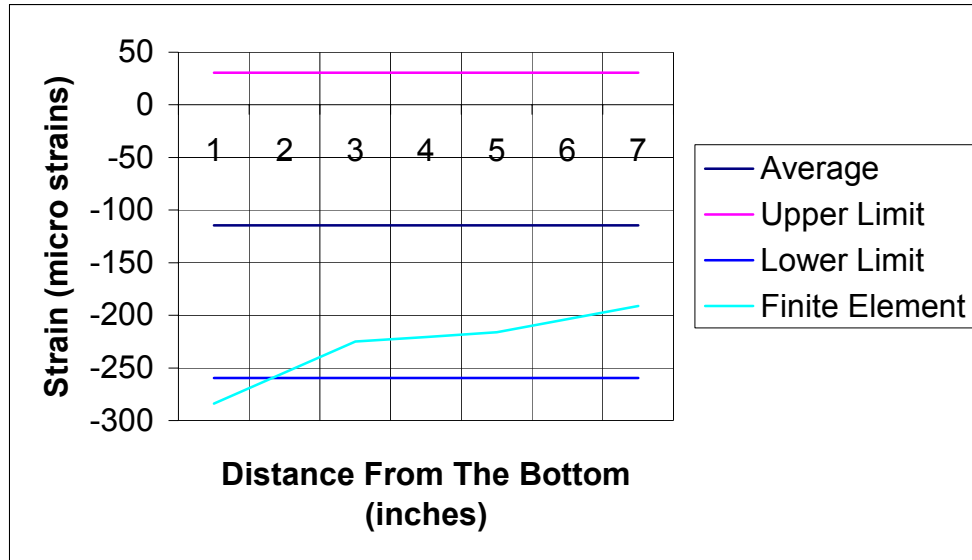


**Figure 6.37 Comparison of empirical and numerical steel concrete, #8 deformed bar, 10-inch diameter sample, dynamic loading**

#### 6.4.3 Impact Loading

This run was a repeat of the one in section 6.3.3, with once again, the outer ring of concrete removed. The steel strains increased until time  $t=5$  msec at which time there was failure of the concrete elements which caused the break slide line to fail, giving the clean failure mode. The steel strain prior to failure varied from a minimum of 6,121 micro strains at the bottom to a minimum of 41 micro strains at the top, as shown in Figure 6.38. All of the concrete strains were in compression with the maximum value occurring at time  $t=4.75$  msec or .25 msec prior to the peak steel strains. The maximum concrete strains (-341 micro strains) occurred at the bottom and decreased to the minimum value of -87 micro strains at the top, Figure 6.39. The model failed due to deformation in the concrete elements indicating failure due to radial cracking.

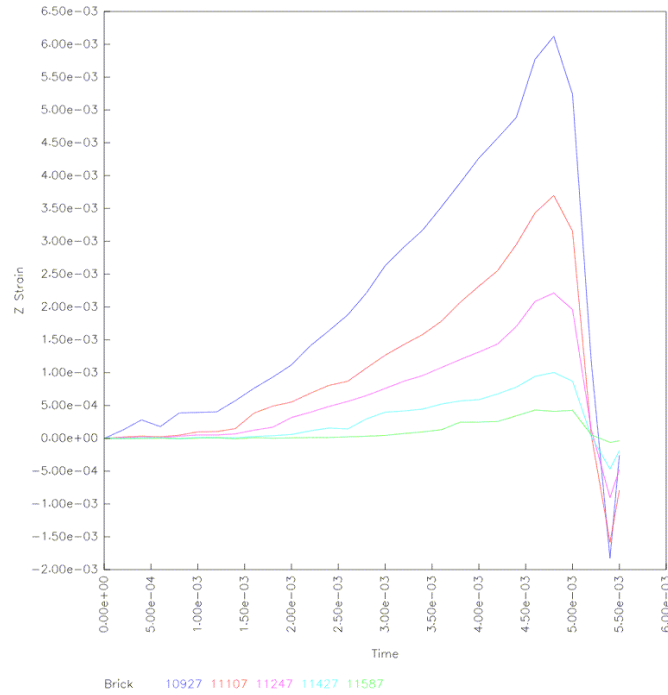


**Figure 6.38 Composite steel strains, #8 deformed bar, 10-inch diameter sample, impact loading**

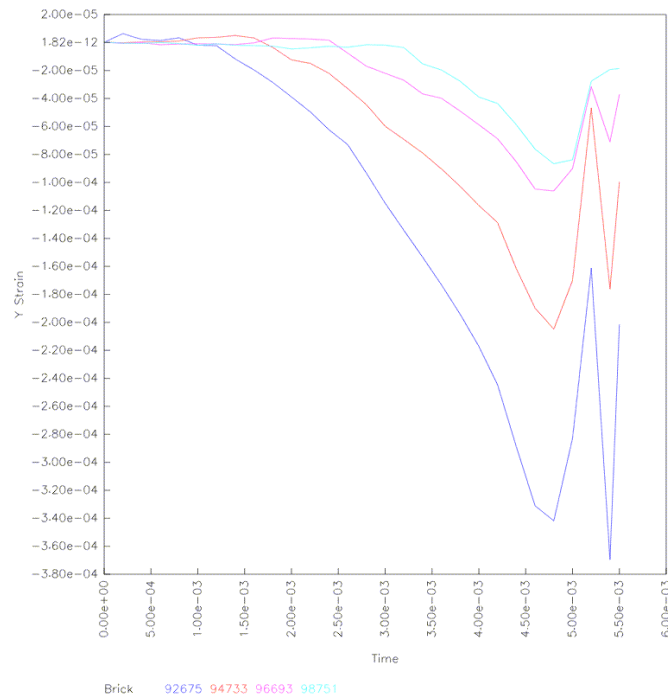


**Figure 6.39 Composite concrete strains, #8 deformed bar, 10-inch diameter sample, impact loading**

As with the dynamic loading, the numerical steel strains were larger than the empirical strains at the bottom of the specimen, but came within the 95% confidence interval at the top of the specimen, Figure 6.40. Likewise, the numerical concrete strains were larger than the empirical strains at the bottom, but fell within the 95% confidence interval at the top of the specimen, Figure 6.41.

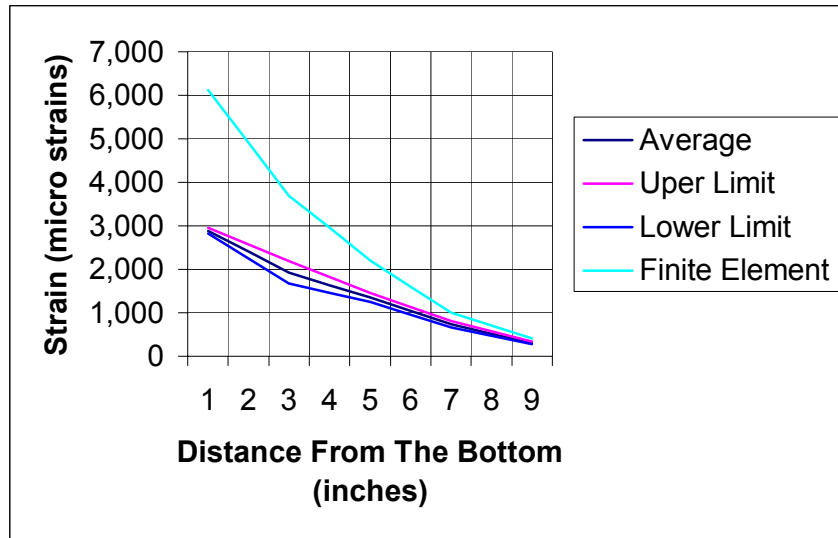


**Figure 6.40 Comparison of empirical and numerical steel strains, #8 deformed bar, 10-inch diameter sample, impact loading**

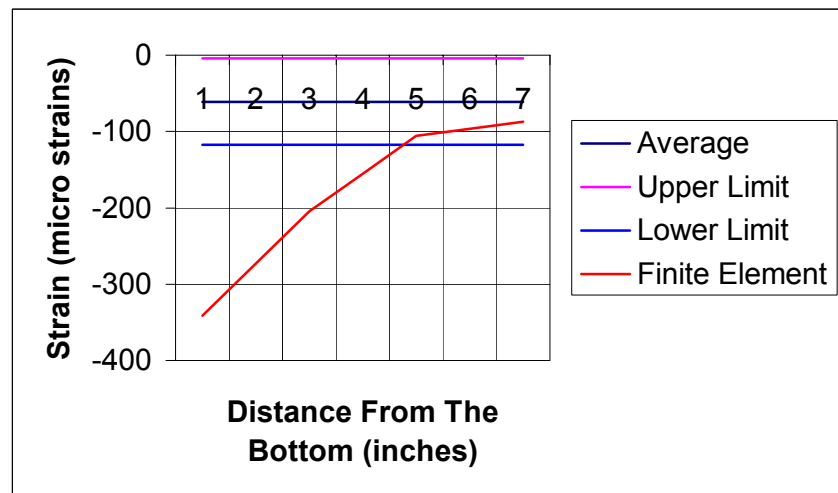


**Figure 6.41 Comparison of empirical and numerical concrete strains, #8 deformed bar, 10-inch diameter sample, impact loading**

## **CHAPTER 7 SUMMARY, CONCLUSIONS AND RECOMMENDATIONS**

### **7.1 Summary**

An experimental and analytical study was conducted to determine for static and dynamic loading conditions; a) the chemical adhesion between the smooth steel bars and concrete, b) the increase in pullout resistance of smooth and deformed bars, c) the influence of concrete confinement and bar diameter on pullout resistance. Finite Element Method of analysis was utilized to conduct the analytical study.

The experimental study involved the testing of 33 pullout specimens representing a range of bar sizes, types and confinements. All the test specimens failed in one of three modes: pullout of the steel bar, radial cracking of the concrete, and yielding of the steel bar. Failure due to pullout of steel occurred only in test specimens with smooth bars, and the failure mode was independent of the loading rate. The only resistance to the pullout of the smooth bars was the static friction and chemical adhesion of the cement paste to the steel bar, and the dynamic friction once this bond was broken. It was determined that the strength of the chemical adhesion and static friction increased with increasing loading rates. The combined static friction and chemical adhesion was 960psi for the quasi-static loading, 2,600psi for the dynamic loading and 3,200 psi for the impact loading. The static friction and chemical adhesion values obtained for the quasi-static loadings compared well with the values estimated based on Menzel's study, namely 900 psi. This difference is due to the higher strength of the concrete (5,000 psi vs. 3,000 psi) used in this investigation.

Failure due to radial cracking of concrete occurred in all of the 10-inch diameter specimens, which had #8 deformed bars, and all 20-inch diameter specimens with #10

deformed bars, regardless of the loading rates. It is pertinent to point out that the deformations in the #8 rebars contributed to a 70% to 77% increase in pullout strength as compared to the smooth bars and this increase was independent of loading rate.

Failure due to yielding of steel occurred in all the 20-inch diameter specimens with #8 deformed bars with the exception of the specimens subjected to quasi-static loading with failure due to radial cracking.

The total load applied before failure increased as the loading rate increased for all test specimens. The impact failure load increased between 70% to 100% over the quasi-static failure load. It is very important to note that as long as the failure mode did not change, the maximum loads applied to the specimens nearly doubled as the loading rates were increased from quasi-static to impact loading. This doubling is in agreement with the dynamic load factor of 2.0 used to increase the design strength of materials subject to impact loading (Biggs 1964).

The steel strains increased as the loading rate went from quasi-static to dynamic, then decreased as the loading rate went from dynamic to impact, due to the nature of the test set up. As was stated in Chapter 5, this was slightly misleading, and the actual strains in the bar were larger in the impact loading than in the dynamic loading. Even though there were large variations in the concrete strains, they tended to increase as the loading rate increased.

Increased concrete confinement increased the strength of the system for all loading rates. This was especially true for specimens tested under quasi-static loadings that failed due to radial cracking of the concrete. For this loading case, doubling the concrete confinement increased the failure load by 58%. The increase was less (20%) for the

dynamic and impact loadings, but this was partly due to the failure mode shifting from concrete cracking to steel yielding.

Since both the concrete and steel materials are rate dependent and exhibit increased strength with increased loading rate, it was not surprising that the test specimens all showed an increase in strength with an increase in loading rate. The average bond stress for the quasi-static loaded deformed bars was 1,310 psi for the 10-inch diameter specimens, 2,080 psi for the 20-inch diameter specimens containing the #8 deformed bars and 1,820 psi for the specimens containing the #10 deformed bars. This was in agreement with the findings of ACI committee 408 which found that the average bond stress for deformed bars ranged from 1,500 psi to 3,000 psi, but was often less due to reduced concrete cover. It is also in agreement with Menzel's work that found the bond stress for a #8 deformed bar to be 838 psi for 3,000 psi concrete. Menzel also stated that the bond stress was dependent on  $\sqrt{f'_c}$ . If we adjust Menzel's values for the increased concrete strength, we get a bond stress of 1,200 psi.

DYNA3D was very effective in modeling the behavior of the test specimens subjected to the dynamic and impact loadings, particularly where the failure was controlled by pullout or yielding of the steel bar. The analysis results showed very good agreement with the experimental data. The material type 10 (Isotropic-Elastic-Plastic-Hydrodynamic) used to model the concrete, did a very good job in the elastic range, but was not as good in the plastic range. The breaking slide line was very successful at modeling the chemical adhesion of the cement paste to the smooth steel bars.

NIKE3D was not very successful at modeling the quasi-static loading cases. The lack of a breaking slide line and a suitable material model for the concrete (material type 3

Elastic-Plastic) caused the computer runs to fail prematurely and greatly underestimate the strains in both the steel and the concrete. However, both programs were able to determine the failure modes that occurred for each specimen and loading combination.

By extending the linear regression for the steel strains, the embedment length required to develop the full yield strength of the steel bars (2000 micro strains) can be calculated. Generally, the development lengths for the quasi-static loading was less than half that required by the ACI code. This would be expected since under normal circumstances, confinement would be much less, and the codes must contain a safety factor. The development length also decreased as the loading rate was increased to dynamic then increased slightly for the impact loading. As has been pointed out before, this is slightly misleading, and is a result of the test setup. Increased confinement resulted in a decrease in the development length, where as increased bar diameter resulted in increased development lengths. Bar deformations were paramount in reducing the development length for all loading rates. The deformations reduced the development lengths by 71% to 78%.

This study has led to a greater understanding of the behavior of steel reinforcement and concrete subjected to dynamic and impact loadings. In particular, the quantifying of the chemical adhesion and the contribution of the steel deformations under dynamic and impact loadings will allow researcher to develop more realistic models for predicting the response and failure of reinforced concrete structures. Finally, these data could be used to develop a concrete/steel reinforcement slide line capable of modeling the concrete/reinforcement interaction under varying load conditions. This would allow

designers the ability to do detailed models of concrete reinforcement systems without the need to model each individual deformation on the reinforcement.

## **7.2 Conclusions**

The study has led to the following conclusions:

- The bond stress, due to static friction and chemical adhesion, is 960 psi for quasi-static loading, 2,600 psi for dynamic loading and 3,200 psi for impact loading for the concrete and steel used in the test program. The values for quasi-static loading compare well with results reported in earlier studies.
- The deformations on the steel bars account for 70% to 77% of the total resistance to pullout regardless of loading rate.
- Increased concrete confinement increased the pullout resistance regardless of loading rate. However, this increase in resistance dropped significantly with increase in loading rate.
- As long as the mode of failure remained constant, the impact-loaded specimens had nearly twice the pullout resistance of the quasi-statically loaded specimens.
- Bond stresses for both the smooth and deformed bars were in good agreement with previous quasi-static work.
- The development length decreased as loading rates increased.
- Development length decreased as confinement increased.
- DYNA3D was capable of modeling the complex bond slip behavior between the steel and concrete. The breaking slide line was very effective in modeling the chemical adhesion of the cement paste to the smooth bars.



### 7.3 Recommendations

This study has led to the following recommendations:

- Testing a larger number of specimens would yield a better statistical analysis of the data.
- Measuring the circumferential concrete strains would probably yield better results. Since the circumferential strain at any radius is constant, the commercially available concrete embedment strain gages could be used. This would have produced more consistent concrete strain data than the methods used in this investigation.
- Another finite element program capable of handling the quasi-static loadings could be identified, and these runs redone.
- The DYNA3D experimental material type 45 (DTRA Concrete/Geological Material) could be modified to handle direct shear. This modified material model might be able to handle the brittle failure of the concrete better.

## BIBLIOGRAPHY

Papados, P. P., "DYNA3D-LLNL: Material Fitting for the Concrete/Geological Model 16, Versions 11, 17, and 1.02," Technical Report SL-97-\_(in preparation), U.S. Army Engineer Waterways Experiment Station, Vicksburg, MS 1997.

Prinaris, A. A., and Papados, P. P., "Reinforced Concrete Bond Modeling in Explicit Computations Using DYNA3D-LLNL," Technical Report SL-96-\_(in preparation), U.S. Army Engineer Waterways Experiment Station, Vicksburg, MS 1996.

Malvar, L. J., and Simons, D. "Concrete Material Modeling in Explicit Computations," Recent Advances in Computational Structural Dynamics and High-Performance Computing, Workshop organized at the U.S. Army Engineer Waterways Experiment Station, Vicksburg, MS 1996.

Papados, P. P., Baylot, J. T., and Hall, R. L., "Analysis of Large Test Structure Task DIPOLE East 51," Proceedings of the "Closed Session" 7th International Symposium on the Interaction of the Effects of Conventional Weapons with Structures, 1995, pp 131-138.

Prinaris, A. A., Papados, P. P., Hall R. L., and Baylot, J. T., "Bond Behavior on One-Way RC Slabs Under Dynamic Loadings," Proceedings of the 65th Shock and Vibration Symposium, Volume III, Shock and Vibration Information Analysis Center, Booz, Allen, and Hamilton, Inc., Arlington, VA, pp 93-102. Presented at the 65th Shock and Vibration Symposium, San Diego, CA, 31 October - 3 November 1994.

Bentur, A., Mindess, S., and Banthia, N.P., "The Fracture of Reinforced Concrete Under Impact Loading," Mindess, S., and Shah, S.P. (eds), Cement-Based Composites: Strain-Rate Effects on Fracture, Vol. 64, 1986, pp 225-234.

Bentur, A., Mindess, S., and Banthia, N.P., "The Behavior of Concrete Under Impact Loading: Experimental Procedures and Methods of Analysis," Materiaux et Constructions, Vol. 19, No. 113, 1986, pp 371-378.

Banthia, N.P., Mindess, S., Bentur, A., and Pigeon, M., "Impact Testing of Concrete Using a Drop Weight Impact Machine," Experimental Mechanics, Vol. 29, No. 2, 1988, pp 63-69.

Goto, Y., "Crack Formed in Concrete Around Deformed Tension Bars," American Concrete Institute Journal, Proceedings, Vol. 68, No. 4, 1971, pp 244-251.

Tepfers, R., "Cracking of Concrete Cover Along Anchored Deformed Reinforcing Bars," Magazine of Concrete Research, Vol. 31, 1979, pp 3-12.

Vervuurt, A., Schlangen, E., and Van Mier, J.G.M., "Analysis of Anchor Pull-Out in Concrete," Accepted for publication in Materials and Structures (RILEM), 1993.

Vervuurt, A., and Van Mier, J.G.M., "A Lattice Approach for Analyzing Steel-Concrete Bond-Slip-Layer Fracture," American Concrete Institute Special Publication SP-156 Interface Fracture and Bond, pp 85-106.

Yan, C., and Mindess, S., "Effect of Fibers on Bond Behavior Under Impact Loading," Mindess, S., and Skalny, J. (eds.), Fibre-Reinforced Cementitious Materials," Materials Research Society, Pittsburgh, PA, Vol. 211, 1991, pp 139-148.

Yan, C., and Mindess, S., "Bond Between Concrete and Steel Reinforcing Bars Under Impact Loading," Brandt, A.H., and Marshall, I.H. (eds.), Brittle Matrix Composites 3, Elsevier Applied Science, 1991, pp 184-192.

Yan, C., "Bond Between Reinforcing Bars and Concrete Under Impact Loading," Ph.D. Thesis, Department of Civil Engineering, University of British Columbia, 1992, p 369.

Vos, I.E., and Reinhardt, H.W., "Influence of Loading Rate on Bond Behavior of Reinforcing Steel and Prestressing Strands," Materiaux et Constructions, Vol. 15, No. 85, 1982, pp 3-10.

Vos, I.E., "Influence of Loading Rate and Radial Pressure on Bond in Reinforced Concrete. A Numerical and Experimental Approach," Ph.D. Thesis, Delft University of Technology, 1983, p 234.

Lin, J.I., "DYNA3D A Nonlinear, Implicit, Three-Dimensional Finite Element Code for Solid and Structural Mechanics User's Manual," Technical Report UCRL-MA-105268, Laurence Livermore National Laboratory, CA, 1999.

Puso, M.A., "NIKE3D A Nonlinear, Implicit, Three-Dimensional Finite Element Code for Solid and Structural Mechanics User's Manual," Technical Report UCRL-MA-105268, Laurence Livermore National Laboratory, CA, 2001.

Christon, M.A., and Dovey, D., "INGRID A 3-D Mesh generator for Modeling Nonlinear Systems User's Manual," Technical Report UCRL-MA-105268, Laurence Livermore National Laboratory, CA, 1992.

Speck, D.E., and Dovey, D.J., "GRIZ Finite Element Analysis Results Visualization for Unstructured Grids User Manual," Technical Report UCRL-MA-105268, Laurence Livermore National Laboratory, CA, 1996.

Bakis, C.E., Uppuluri, V.S., Nanni, A. and Boothby, T.E. "Analysis of Bonding Mechanisms of Smooth and Lugged RFP Rods Embedded in Concrete," Composites Science and Technology, Vol. 58, August 1998, pp1307-1319.

Furguson, P.M. and Thompson, J.N., “Development Length of High Strength Reinforcing Bars in Bond,” Journal of the American Concrete Institute, July, 1962, pp 887-921.

McDermott, J.F., “Effect of Steel Strength and of Reinforcement Ratio on the Mode of Failure and Strain Energy Capacity of Reinforced Concrete Beams,” Report by ACI Committee 439, American Concrete Institute Journal, March 1969, pp 165-172.

Filippou, F.C. and Taucer, F.F., “Fibre Beam–Column Model for Non-Linear analysis of R/C Frames: Part 1 Formulation,” Earthquake Engineering and Structural Dynamics, Vol. 25, 1996, pp 711-725.

Menzel, C.A., “Some Factors Influencing Results of Pull-Out Bond Tests,” Journal of the American Concrete Institute, Vol.35, June 1939, pp 516-543.

Mitchell, D. et al., “State-of-the-Art Report on Bond Under Cyclic Loads,” Reported by ACI Committee 408, ACI 408.2R-92, 1992, pp 1-31.

Ferguson, P.M., and Thompson, J.N., “Development Length for Large High Strength Reinforcing Bars,” Journal of the American Concrete Institute, January 1965, pp 71-91.

Popov, E.P., “Mechanics of Materials,” Prentice-Hall, Inc. Englewood Cliffs, New Jersey, 1976, pp 275-336.

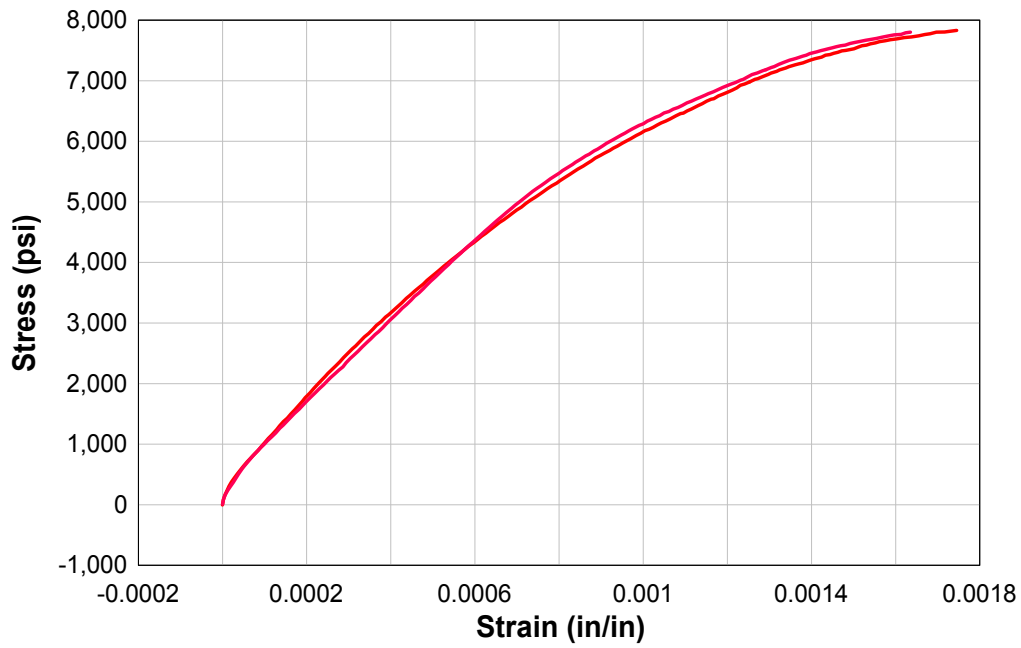
Biggs, J.M., “Introduction to Structural Dynamics,” McGraw-Hill Book Company, New York, 1964, pp 199-233.

## **APPENDIX A: STRESS-STRAIN CURVES FOR STEEL AND CONCRETE**

# Stress Strain Curve

Concrete Speciman 2  
Static Loading

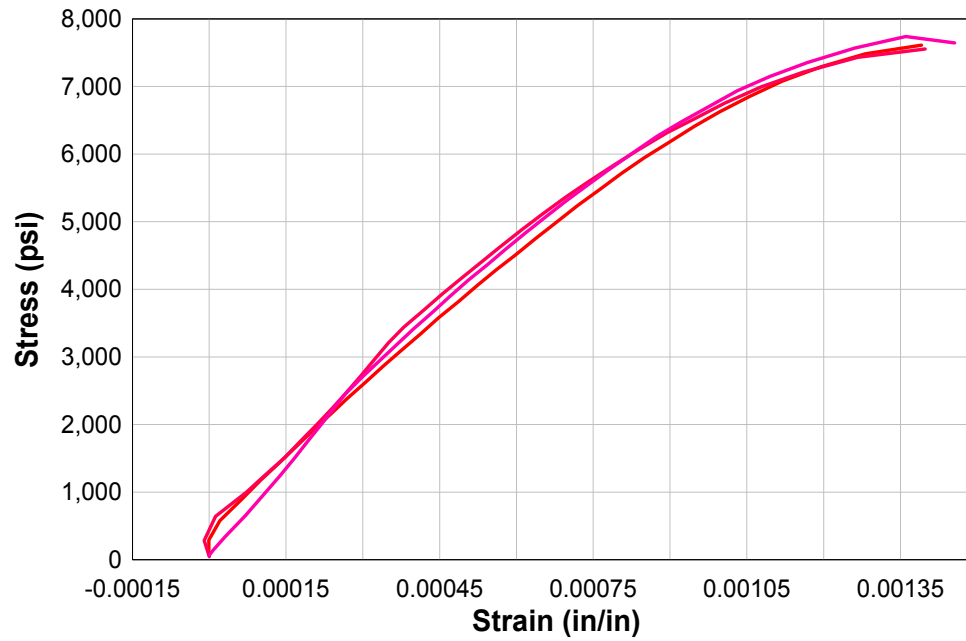
9/19/2002



# Stress Strain Curve

Concrete Speciman 05  
200 msec Loading Rate

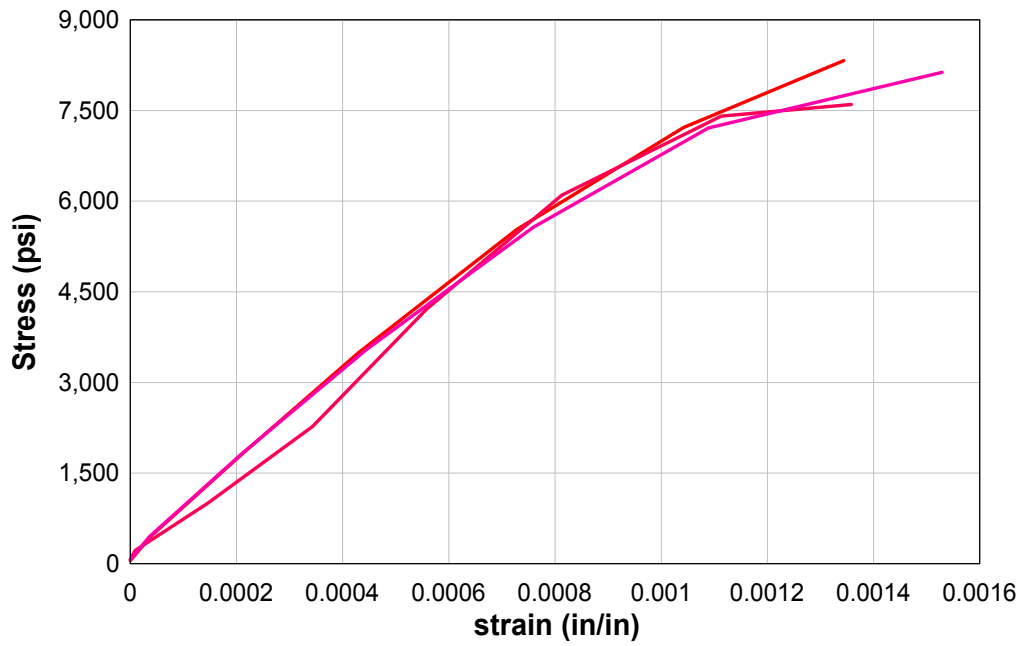
9/19/2002



# Stress Strain Curve

Concrete Speciman 10  
5 msec Loading Rate

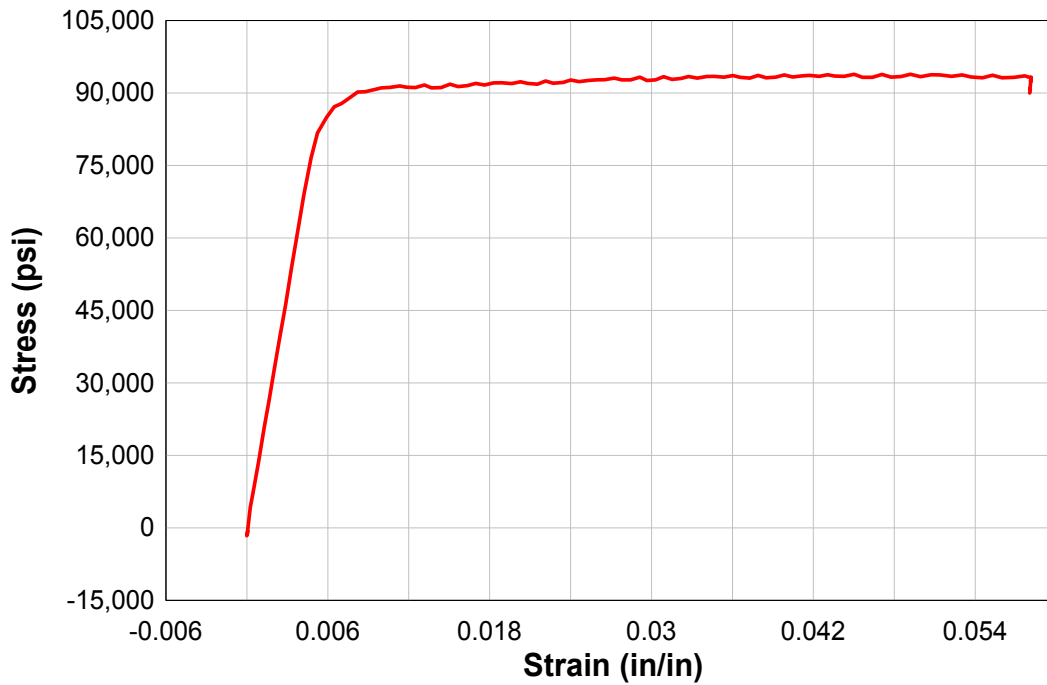
9/19/2002



# Stress Strain Curve

1-inch smooth Bar  
Static Loading (sm-3)

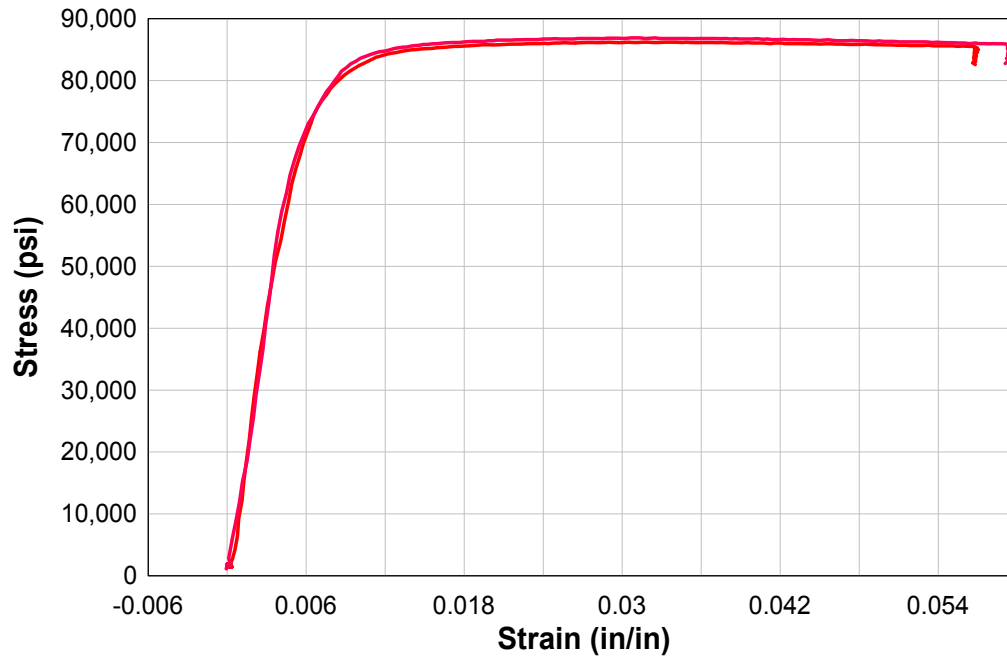
9/19/2002



9/19/2002

## Stress Strain Curve

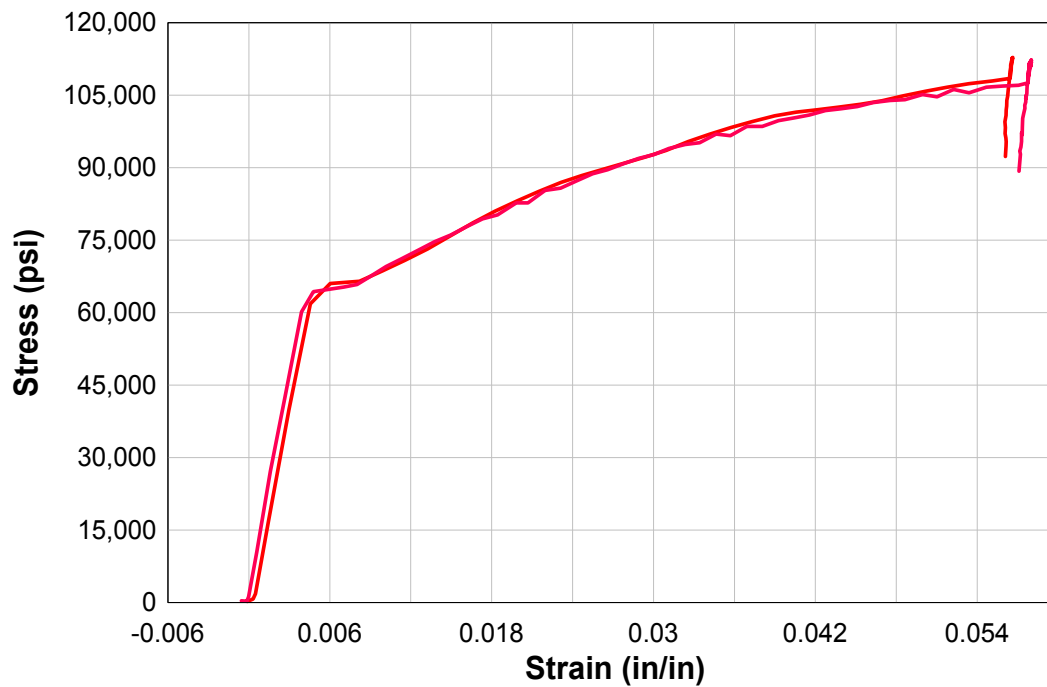
1-inch Smooth Bar  
523 msec Loading (sm-1)



9/19/2002

## Stress Strain Curve

#8 Deformed Bar  
Static Loading (08-01)

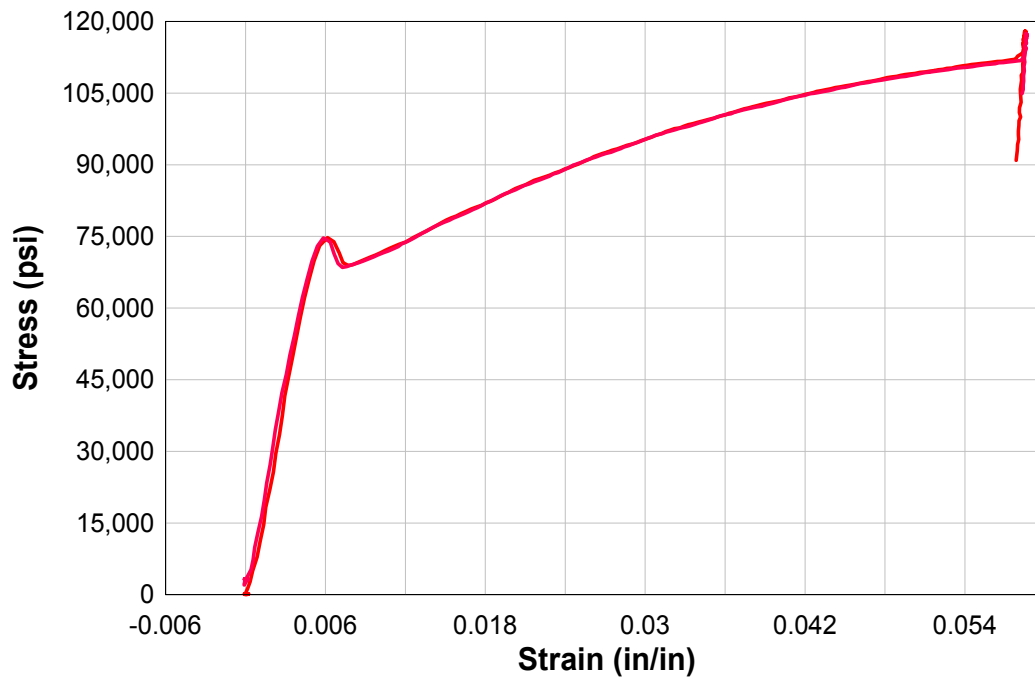




## Stress Strain Curve

9/19/2002

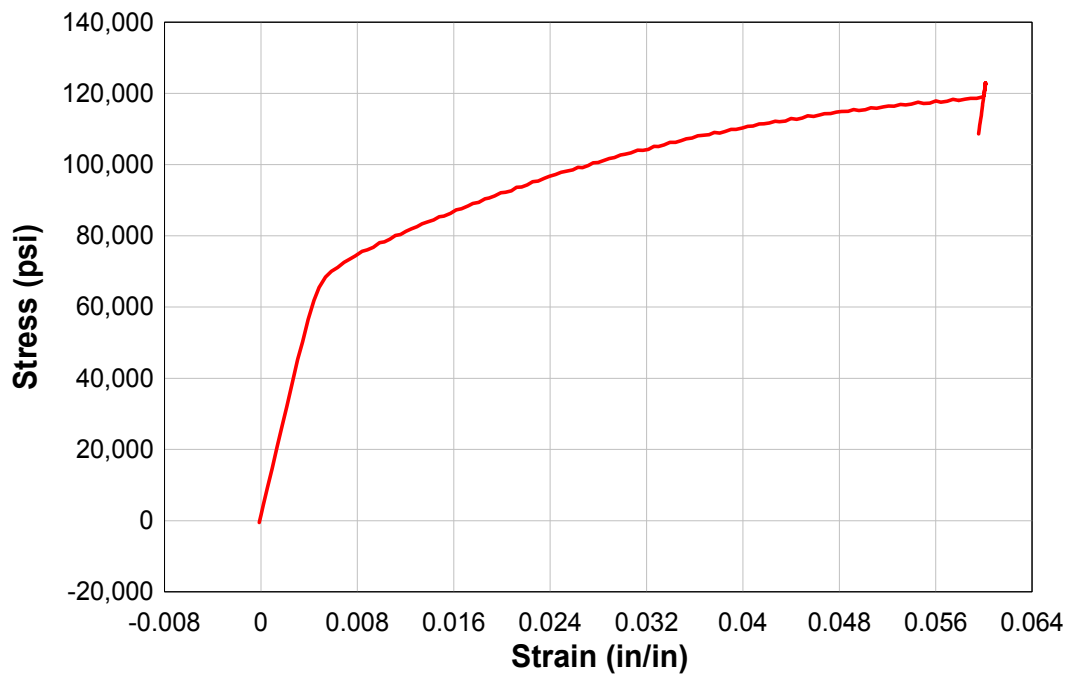
#8 Deformed Bar  
581 msec Loading (08-03)



## Stress Strain Curve

9/19/2002

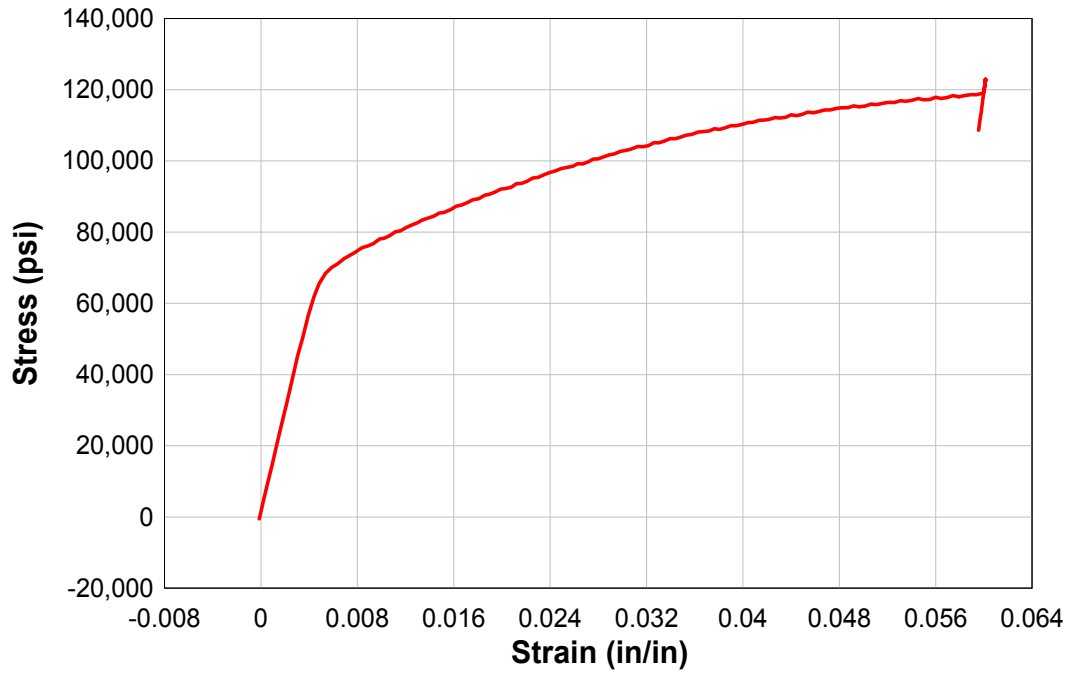
#10 Deformed Bar  
Static Loading (10-03)



## Stress Strain Curve

9/19/2002

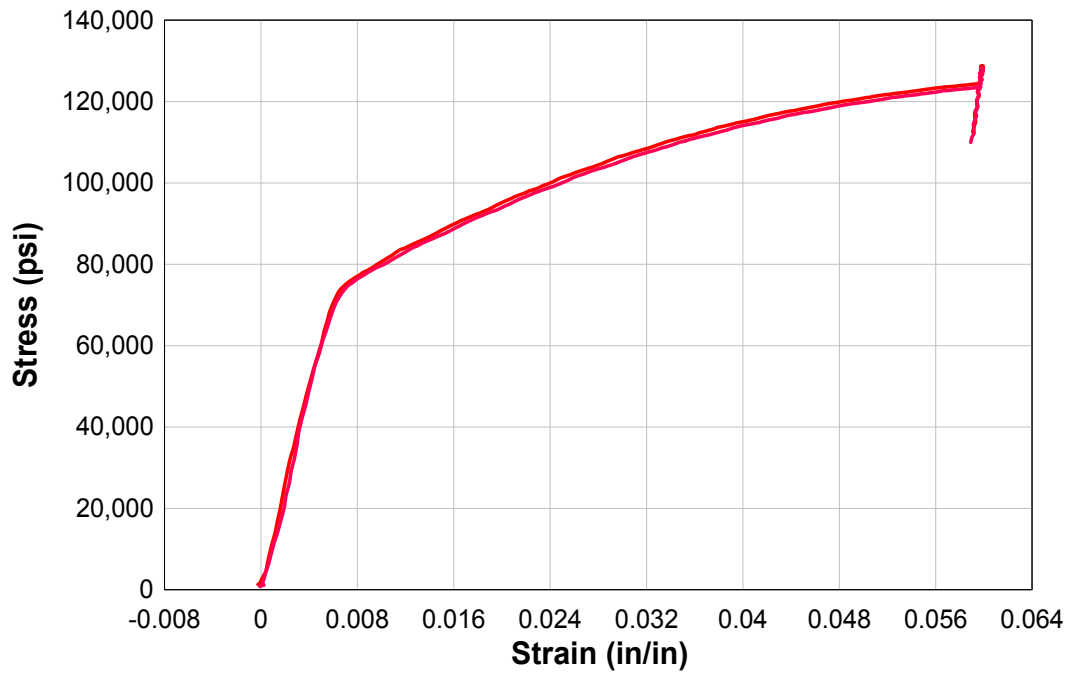
#10 Deformed Bar  
Static Loading (10-03)



## Stress Strain Curve

9/19/2002

#10 Deformed Bar  
565 msec Loading (10-01)



## **APPENDIX B: SUMMARY OF TEST DATA**

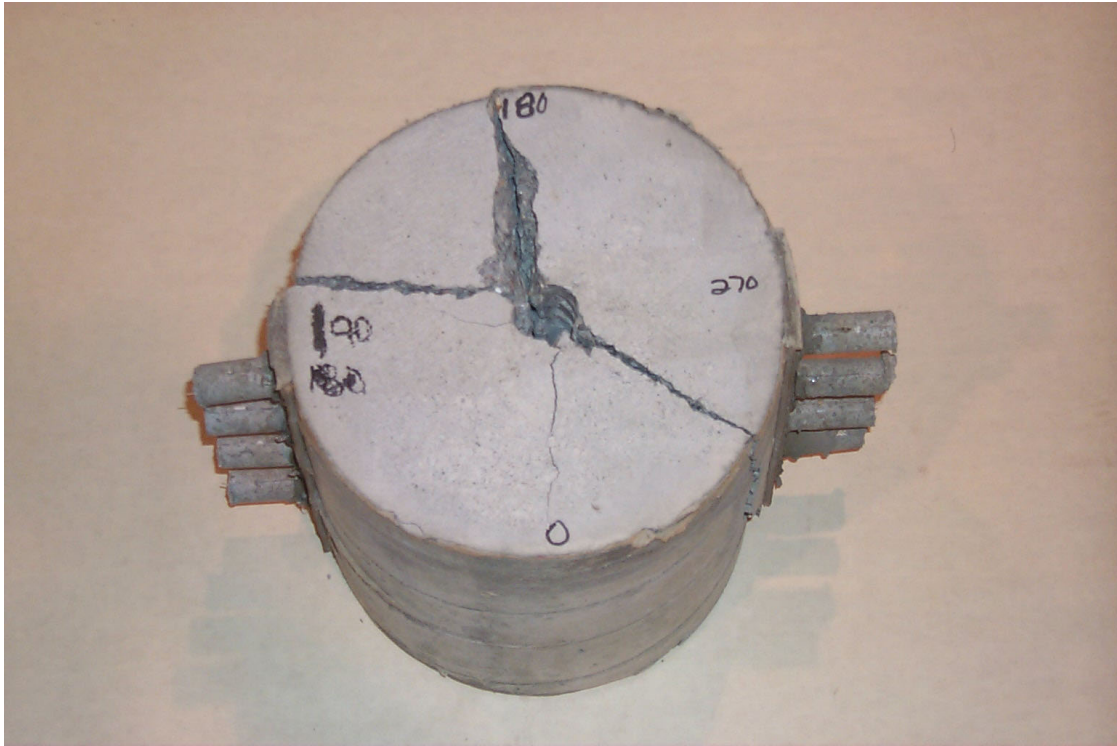


**Figure B-1 Test 1 Post Test**



**Figure B-2 Test 1 Post Test**

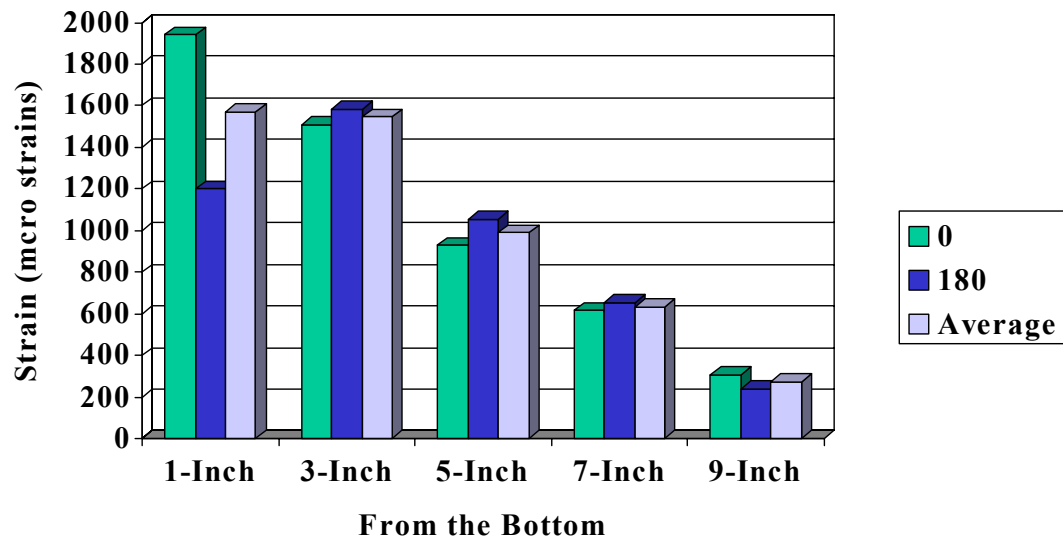


Figure B-3 Adjusted Steel Strains, Test 1

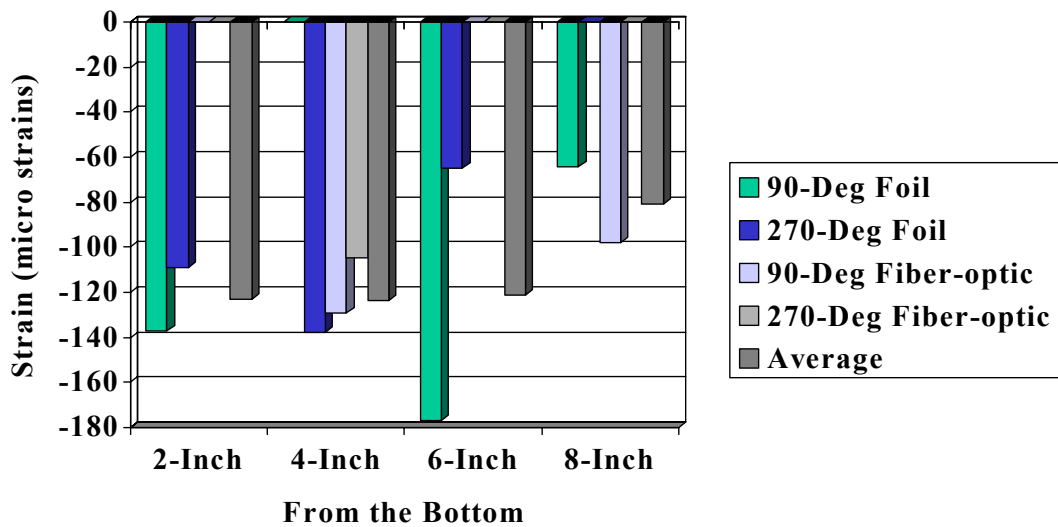
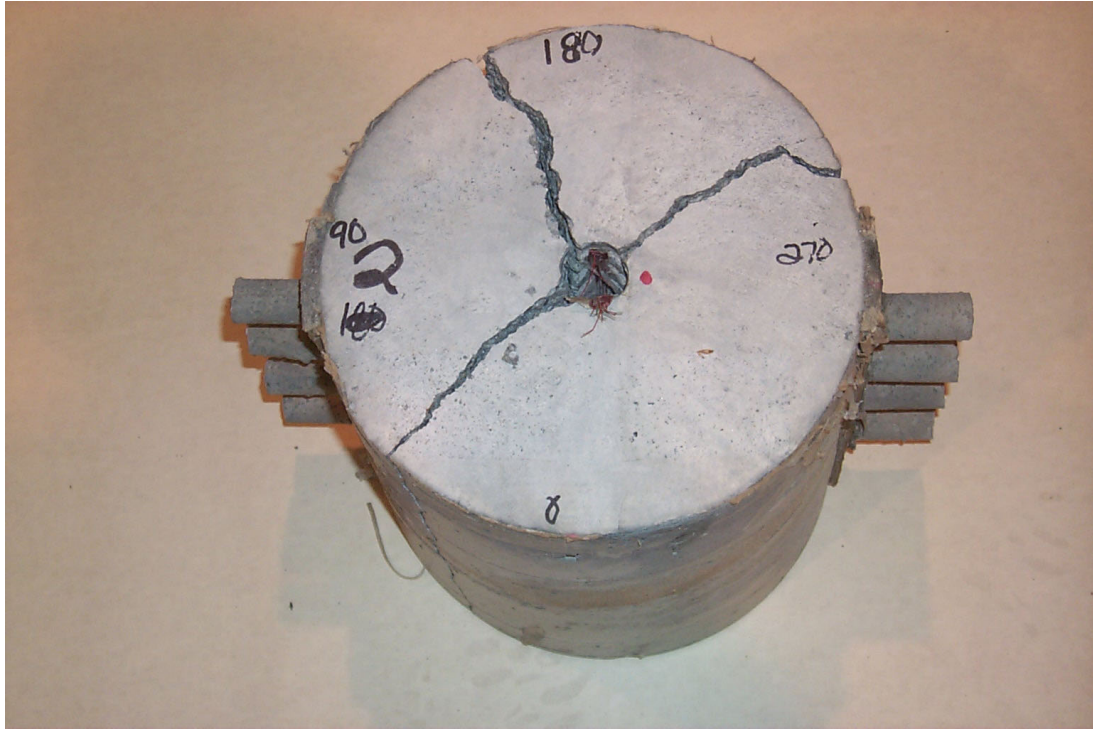


Figure B-4 Adjusted Concrete Strains, Test 1





**Figure B-5 Test 2 Post Test**



**Figure B-6 Test Specimen 2 Post Test**

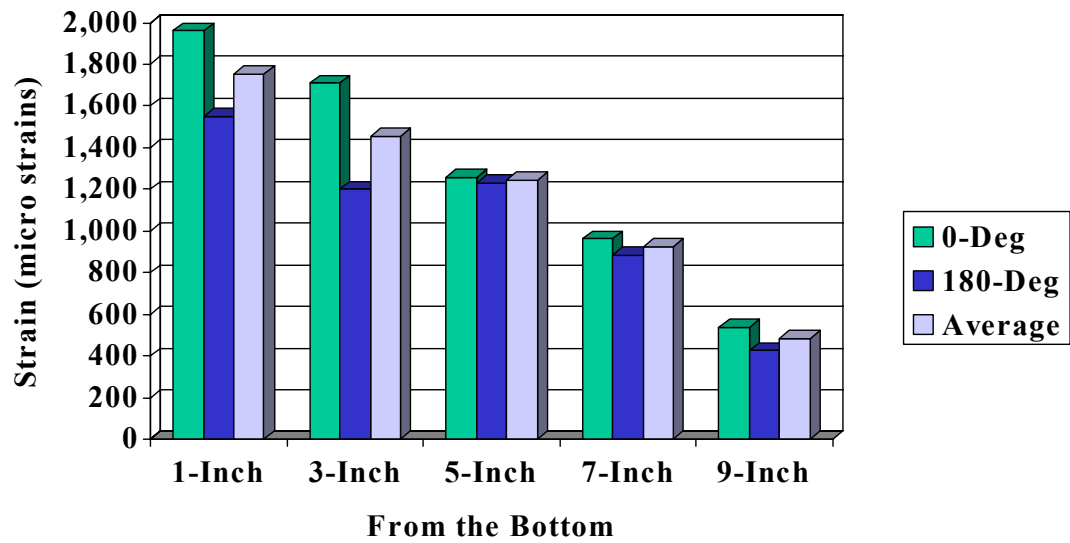


Figure B-7 Steel Strains, Test 2

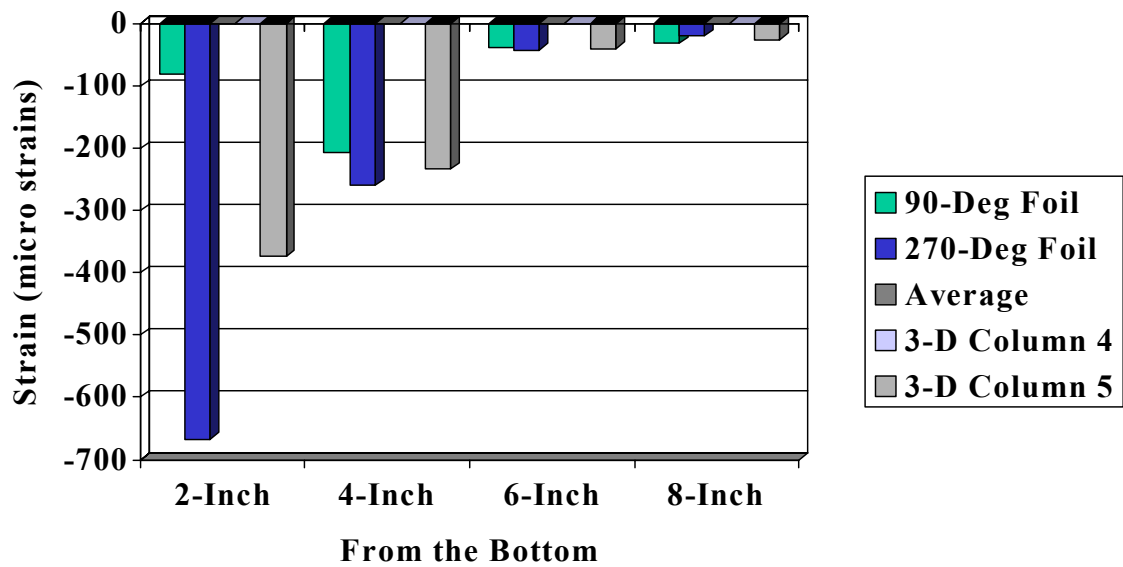
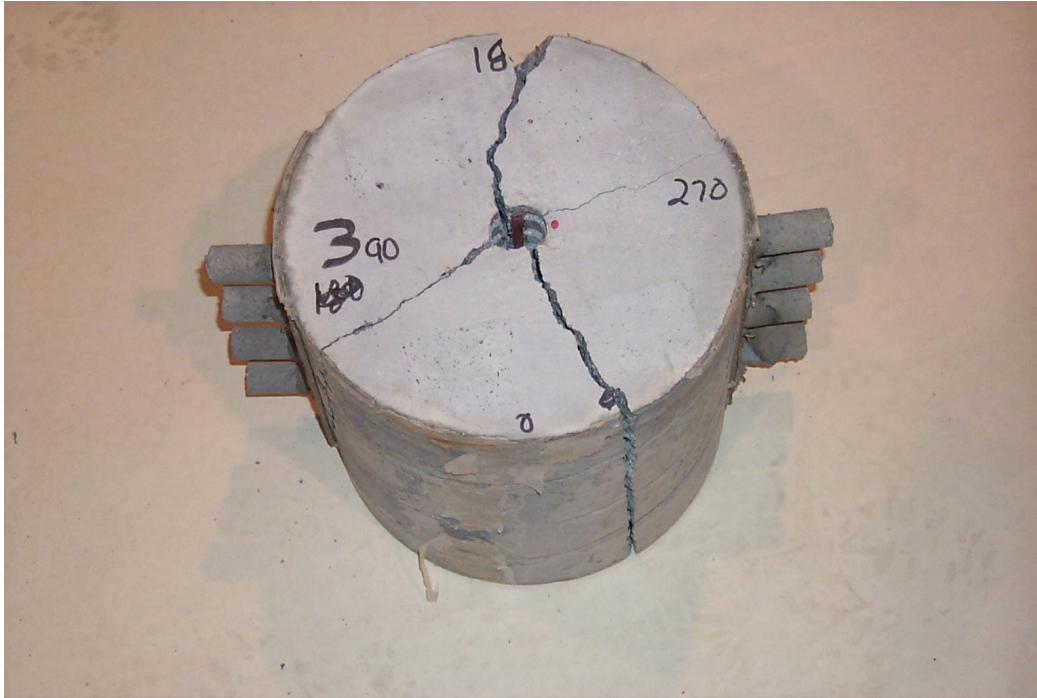


Figure B-8 Concrete Strains, Test 2





**Figure B-9 Test Specimen 3 Post Test**



**Figure B-10 Test Specimen 3 Post Test**



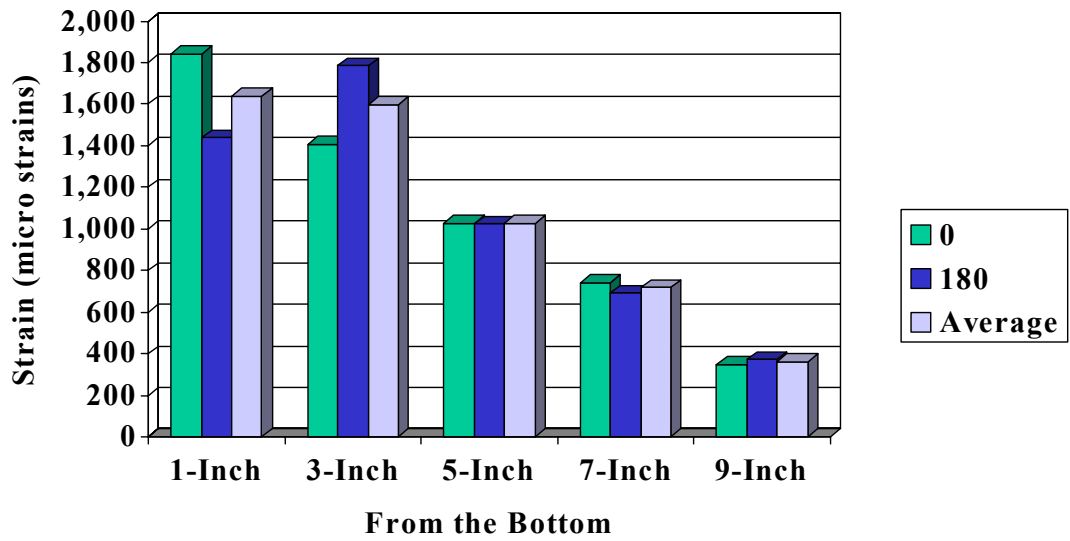


Figure B-11 Adjusted Steel Strains Test 3

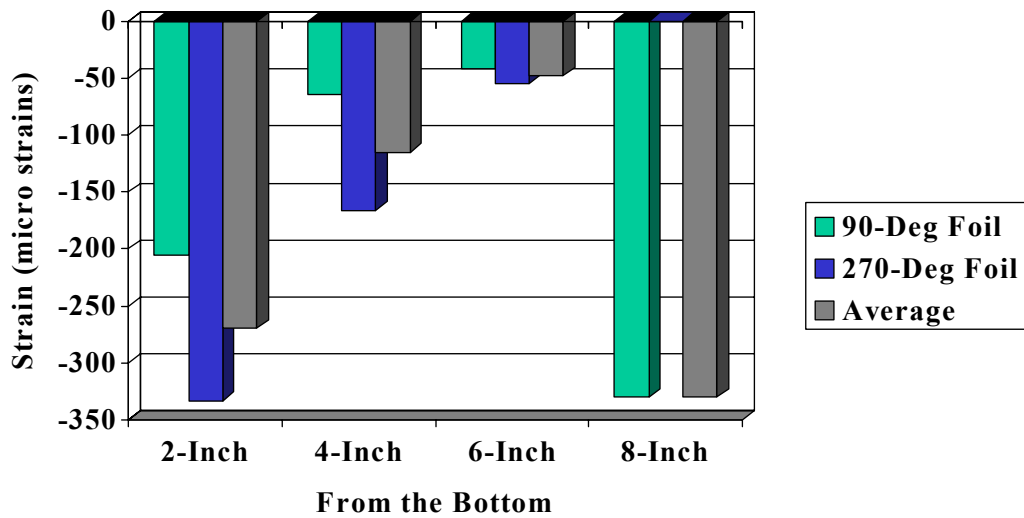


Figure B-12 Adjusted Concrete Strains Test 3  
Table B.0.1 Statistical Analysis of Steel Strains from Tests 1, 2 and 3

**Table B.1 Statistical analysis of steel strains for tests 1, 2 and 3**

Test 01 Adjusted Steel Strains						
Position		1-Inch	3-Inch	5-Inch	7-Inch	9-Inch
0-Deg	Gage	SS-01	SS-03	SS-05	SS-07	SS-09
	Value	1941	1509	928	616	309
180-Deg	Gage	SS-02	SS-04	SS-06	SS-08	SS-10
	Value	1,199	1,584	1,054	653	241
Average		1,570	1,547	991	635	275

Test 02 Adjusted Steel Strains						
Position		1-Inch	3-Inch	5-Inch	7-Inch	9-Inch
0-Deg	Gage	SS-01	SS-03	SS-05	SS-07	SS-09
	Value	1,960	1,710	1,260	963	539
180-Deg	Gage	SS-02	SS-04	SS-06	SS-08	SS-10
	Value	1,550	1,200	1,230	884	425
Average		1,755	1,455	1,245	924	482

Test 03 Adjusted Steel Strains						
Position		1-Inch	3-Inch	5-Inch	7-Inch	9-Inch
0-Deg	Gage	SS-01	SS-03	SS-05	SS-07	SS-09
	Value	1,842	1,408	1,029	742	348
180-Deg	Gage	SS-02	SS-04	SS-06	SS-08	SS-10
	Value	1,438	1,785	1,024	692	371
Average		1,640	1,597	1,027	717	360

Average Adjusted Steel Strains for Tests 01, 02 AND 03						
Position		1-Inch	3-Inch	5-Inch	7-Inch	9-Inch
Test 01		1,570	1,547	991	635	275
Test 02		1,755	1,455	1,245	924	482
Test 03		1,640	1,597	1,027	717	360
n		6	6	6	6	6
High		1,960	1,710	1,260	963	539
Low		1,199	1,200	928	616	241
Extreme Spread		761	510	332	347	298
Average		1,655	1,533	1,088	758	372
Variance		95,168	44,905	16,816	18,740	10,481
Standard Deviation		308	212	130	137	102
Coefficient of Variation		19	14	12	18	28

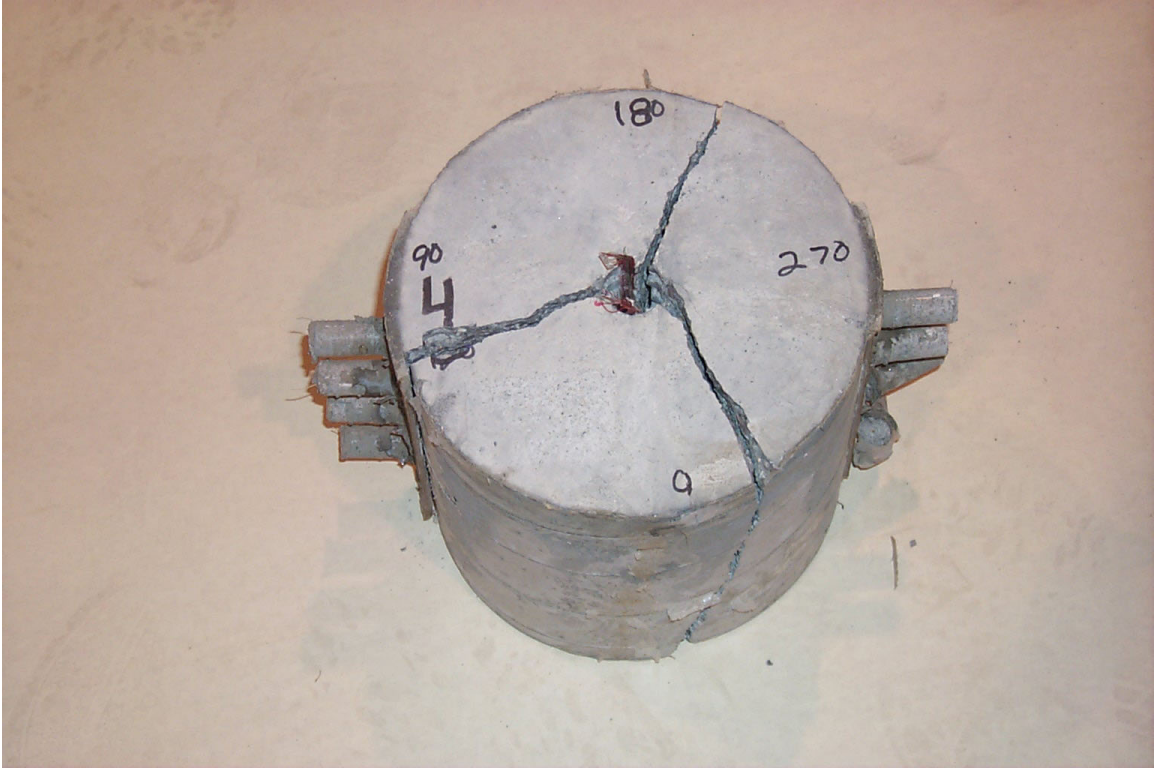


**Figure B-13 Test Specimen 4 Post Test**

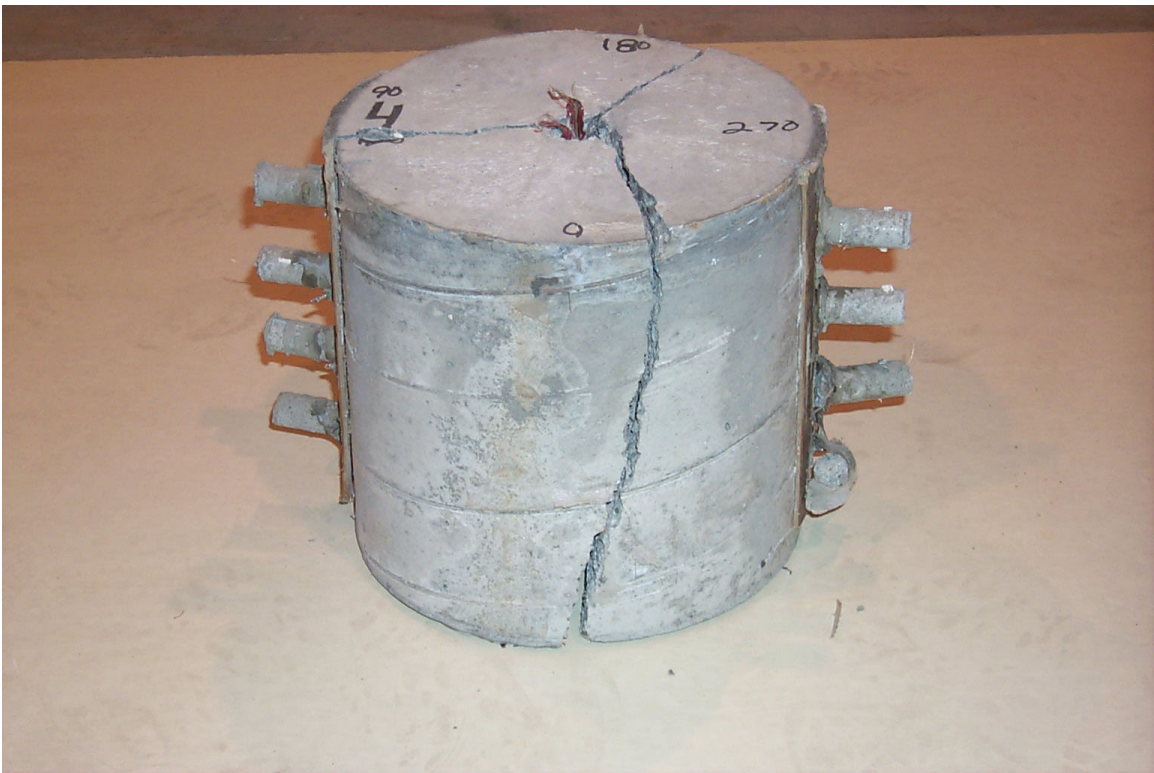


**Figure B-14 Test Specimen 4 Post Test**

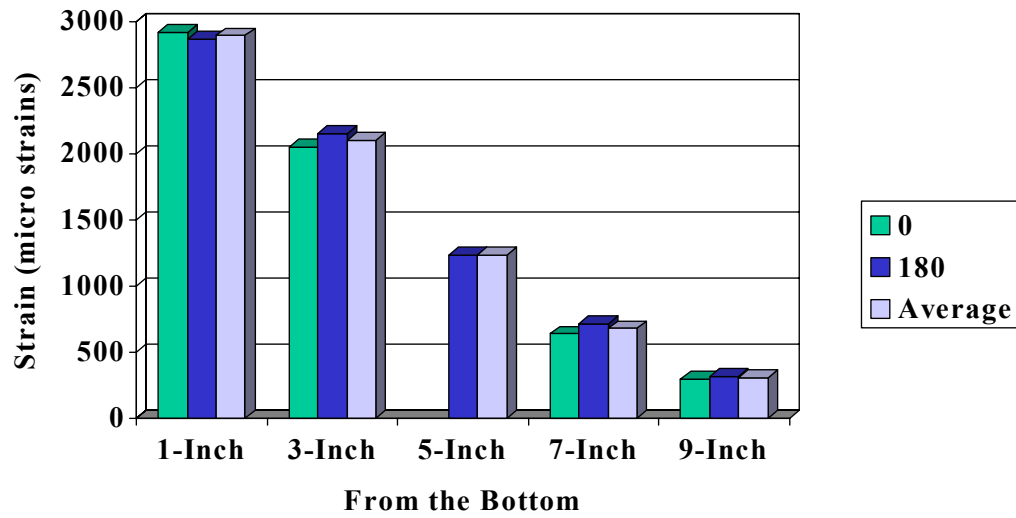


**Figure B-15 Adjusted Steel Strains, Test 4**

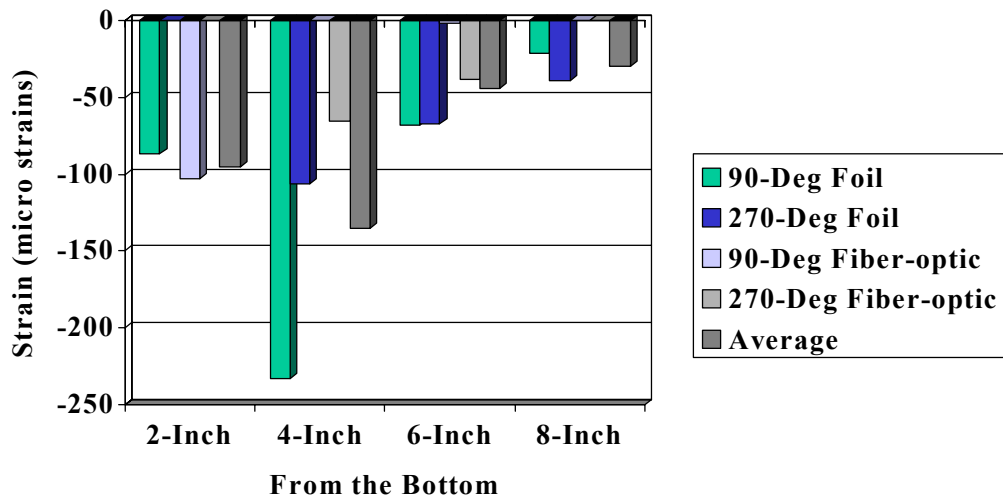


**Figure B-16 Adjusted Concrete Strains, Test 4**



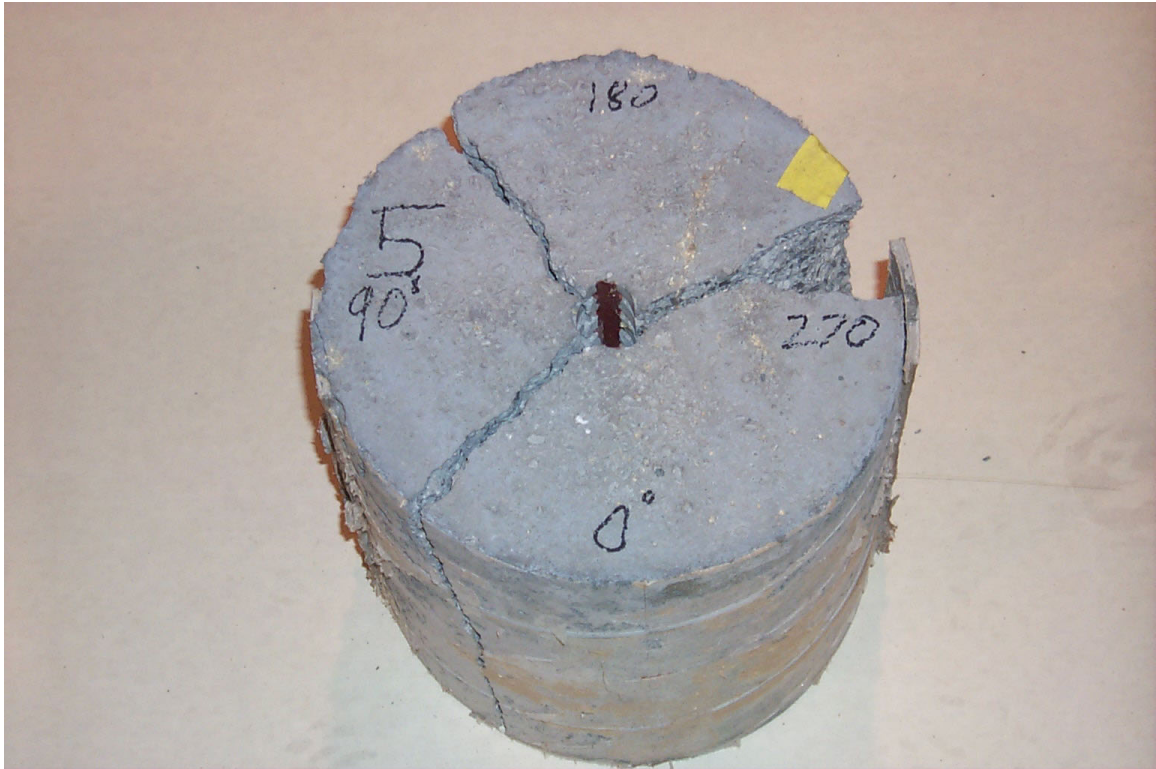


**Figure B-17 Test Specimen 5 Post Test**



**Figure B-18 Test Specimen 5 Post Test**

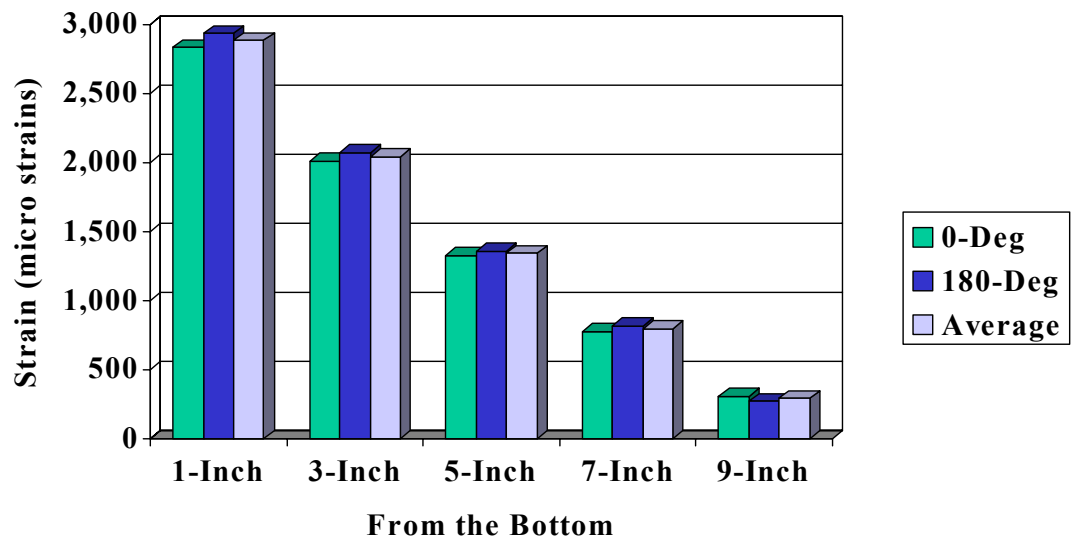


**Figure B-19 Steel Strains Test 5**



**Figure B-20 Test Specimen 6 Post Test**

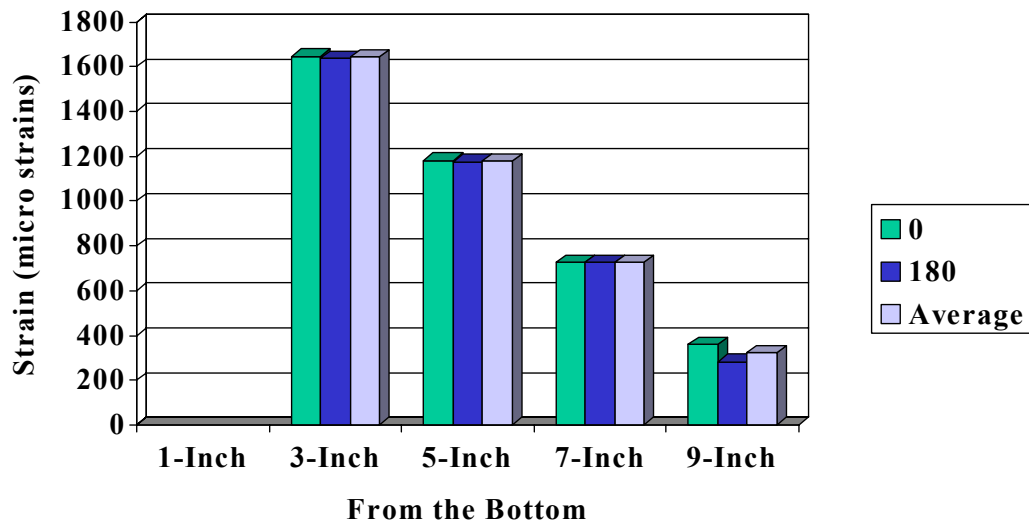


Figure B-21 Adjusted Steel Strains, Test 6

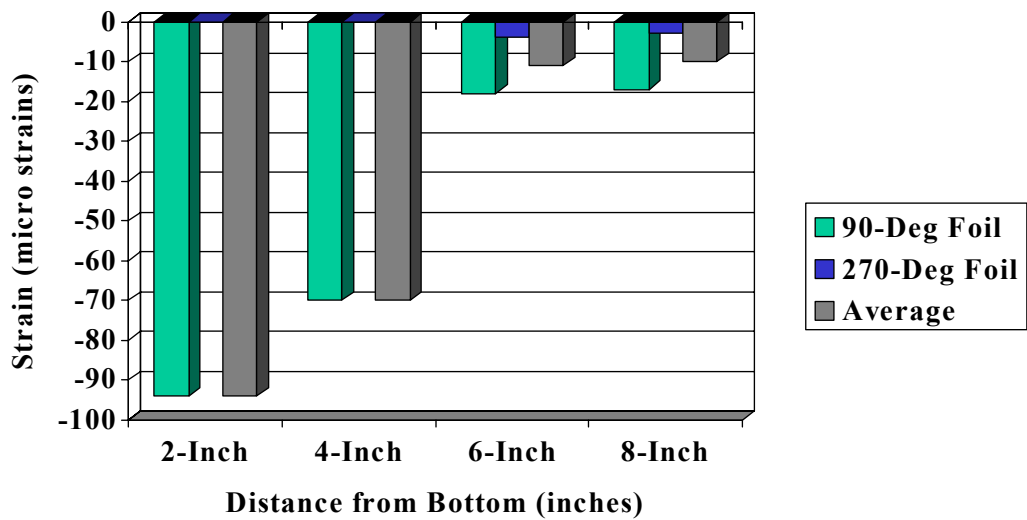


Figure B-22 Adjusted Concrete Strains, Test 6  
Table B.0.2 Statistical Analysis of Steel Strains from Tests 4, 5 and 6

**Table B.2 Statistical Analysis of Steel Strains for Tests 4, 5 and 6**

Test 04 Adjusted Steel Strains						
Position		1-Inch	3-Inch	5-Inch	7-Inch	9-Inch
0-Deg	Gage	SS-01	SS-03	SS-05	SS-07	SS-09
	Value	2919	2048	NA	639	299
180-Deg	Gage	SS-02	SS-04	SS-06	SS-08	SS-10
	Value	2,863	2,150	1,234	716	320
Average		2,891	2,099	1,234	678	310

Test 05 Adjusted Steel Strains						
Position		1-Inch	3-Inch	5-Inch	7-Inch	9-Inch
0-Deg	Gage	SS-01	SS-03	SS-05	SS-07	SS-09
	Value	2,830	2,012	1,325	778	309
180-Deg	Gage	SS-02	SS-04	SS-06	SS-08	SS-10
	Value	2,930	2,070	1,360	820	273
Average		2,880	2,041	1,343	799	291

Test 06 Adjusted Steel Strains						
Position		1-Inch	3-Inch	5-Inch	7-Inch	9-Inch
0-Deg	Gage	SS-01	SS-03	SS-05	SS-07	SS-09
	Value	NA	1,647	1,182	726	358
180-Deg	Gage	SS-02	SS-04	SS-06	SS-08	SS-10
	Value	NA	1,638	1,175	726	283
Average		NA	1,643	1,179	726	321

Average Adjusted Steel Strains for Tests 04, 05 and 06						
Position		1-Inch	3-Inch	5-Inch	7-Inch	9-Inch
Test 04		2,891	2,099	1,530	678	310
Test 05		2,880	2,041	1,343	799	291
Test 06		N/A	1,643	1,179	726	321
n		4	6	5	6	6
High		2,930	2,150	1,360	820	358
Low		2,830	1,638	1,175	639	273
Extreme Spread		100	512	185	181	85
Average		2,886	1,928	1,350	734	307
Variance		2,230	50,793	7,024	3,762	914
Standard Deviation		47	225	84	61	30
Coefficient of Variation		2	12	6	8	10



**Table B.3 Statistical Analysis of Concrete Strains from Tests 4, 5 and 6**

Test 04 Adjusted Concrete Strains					
Position		2-Inch	4-Inch	6-Inch	8-Inch
90-Deg	Gage	CS-01	CS-03	CS-05	CS-07
	Value	-87	-233	-68	-21
	Gage	FO-01	FO-03	FO-05	FO-07
	Value	-102.7		-2.0	
270-Deg	Gage	CS-02	CS-04	CS-06	CS-08
	Value		-106	-67	-39
	Gage	FO-02	FO-04	FO-06	FO-08
	Value		-65.4	-38.7	
Average		-94.9	-134.8	-43.9	-30.0
Test 05 Adjusted Concrete Strains (no data)					
Position		2-Inch	4-Inch	6-Inch	8-Inch
90-Deg	Gage				
	Value				
	Gage				
	Value				
270-Deg	Gage				
	Value				
	Gage				
	Value				
Average					
Test 06 Adjusted Concrete Strains					
Position		2-Inch	4-Inch	6-Inch	8-Inch
90-Deg	Gage	CS-01	CS-03	CS-05	CS-07
	Value	-94	-70	-18	-17
	Gage				
	Value				
270-Deg	Gage	CS-02	CS-04	CS-06	CS-08
	Value			-4	-3
	Gage				
	Value				
Average		-94.0	-70.0	-11.0	-10.0
Average Fiber-Optic and Foil Concrete Strains for Tests 04, 05 and 06					
Position		2-Inch	4-Inch	6-Inch	8-Inch
Test 04		-94.9	-134.8	-43.9	-30.0
Test 05					
Test 06		-94.0	-70.0	-11.0	-10.0
Average		-94.6	-118.6	-33.0	-20.0
n		3	4	6	4
High		-87.0	-65.4	-2.0	-3.0
Low		-102.7	-233.0	-68.0	-39.0
Extreme Spread		15.7	167.6	66.0	36.0
Variance		62.2	6145.6	887.6	220.0
Standard Deviation		7.9	78.4	29.8	14.8
Coefficient of Variation		-8.3	-66.1	-90.4	-74.2

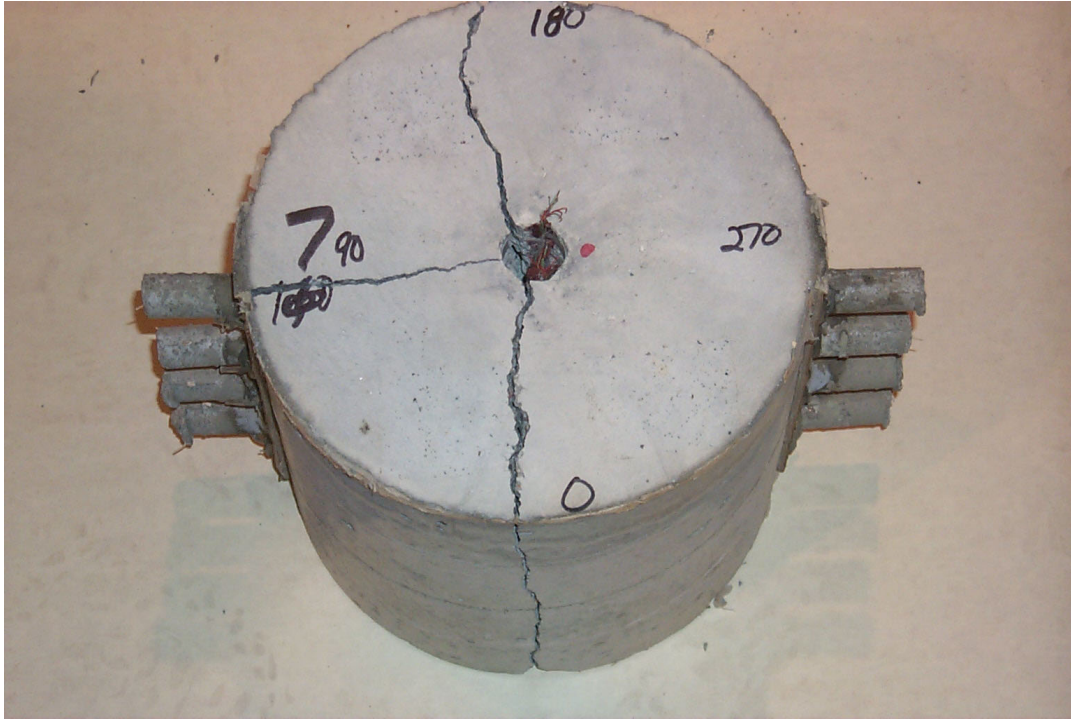


**Figure B-23 Test Specimen 7 Post Test**



**Figure B-24 Test Specimen 7 Post Test**

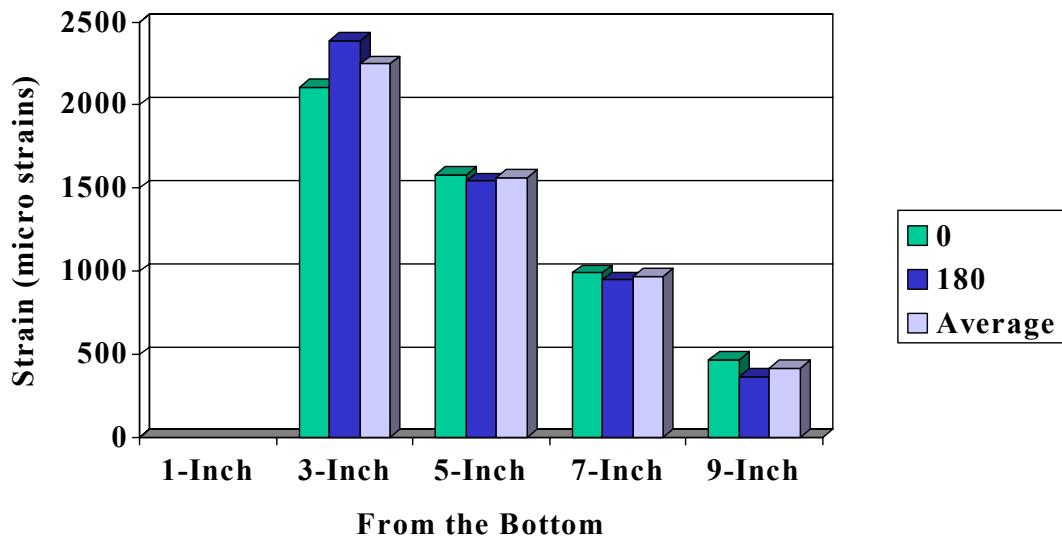


Figure B-25 Adjusted Steel Strains, Test 7

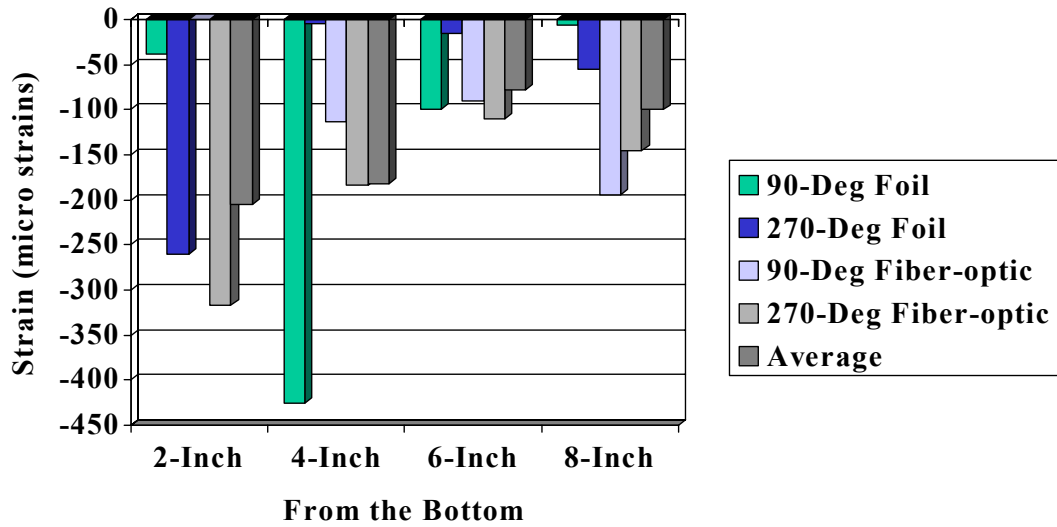
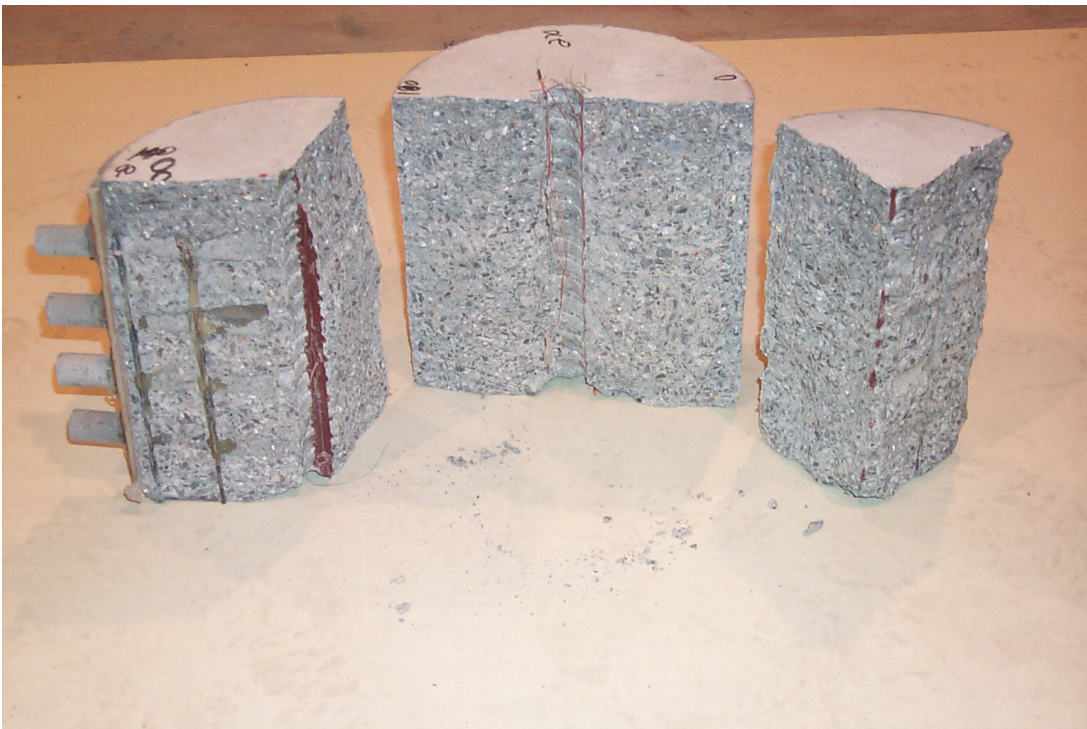


Figure B-26 Adjusted Concrete Strains, Test 7





**Figure B-27 Test Specimen 8, Post Test**



**Figure B-28 Test Specimen 8, Post Test**

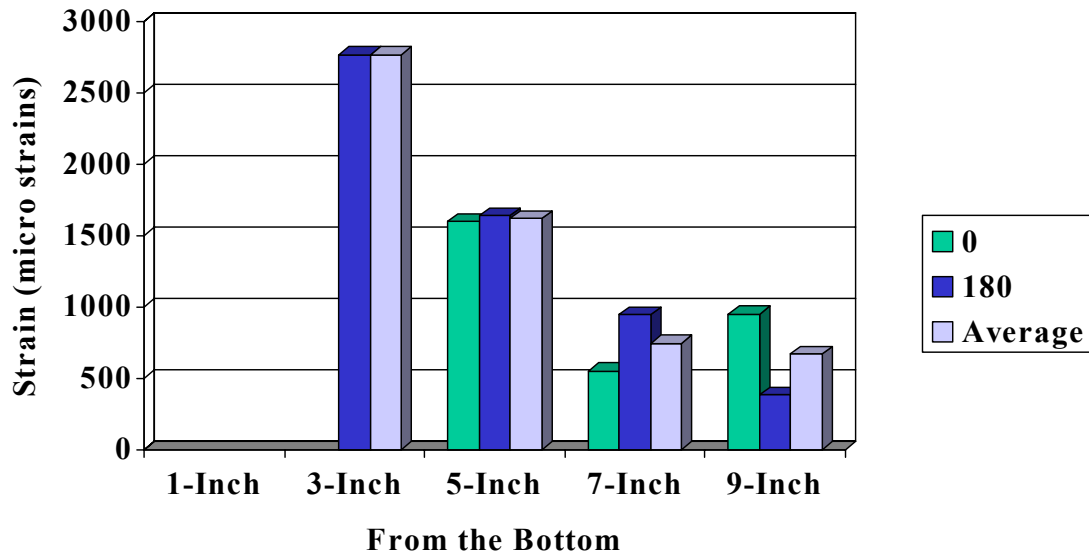


Figure B-29 Adjusted Steel Strains, Test 8

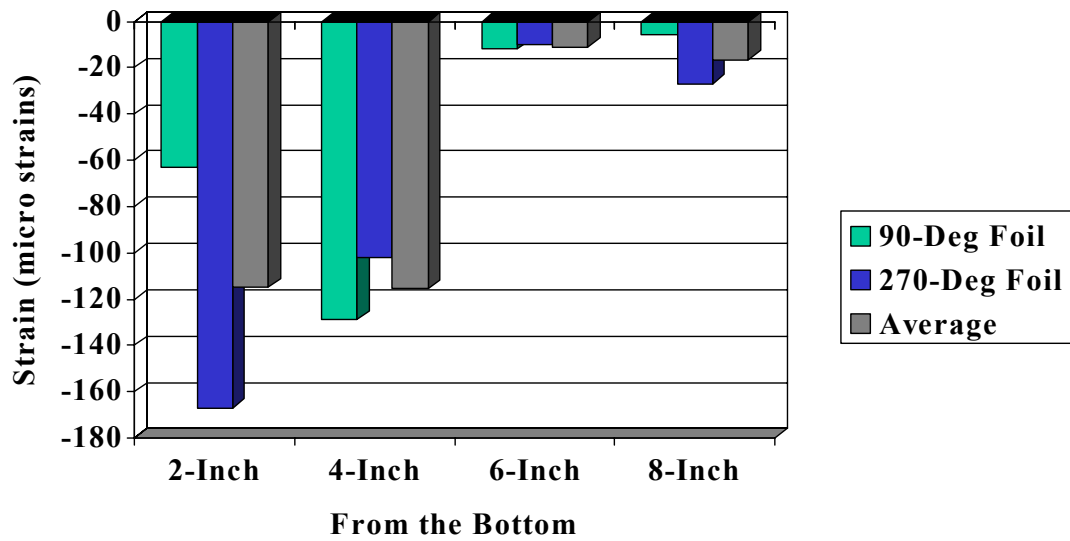
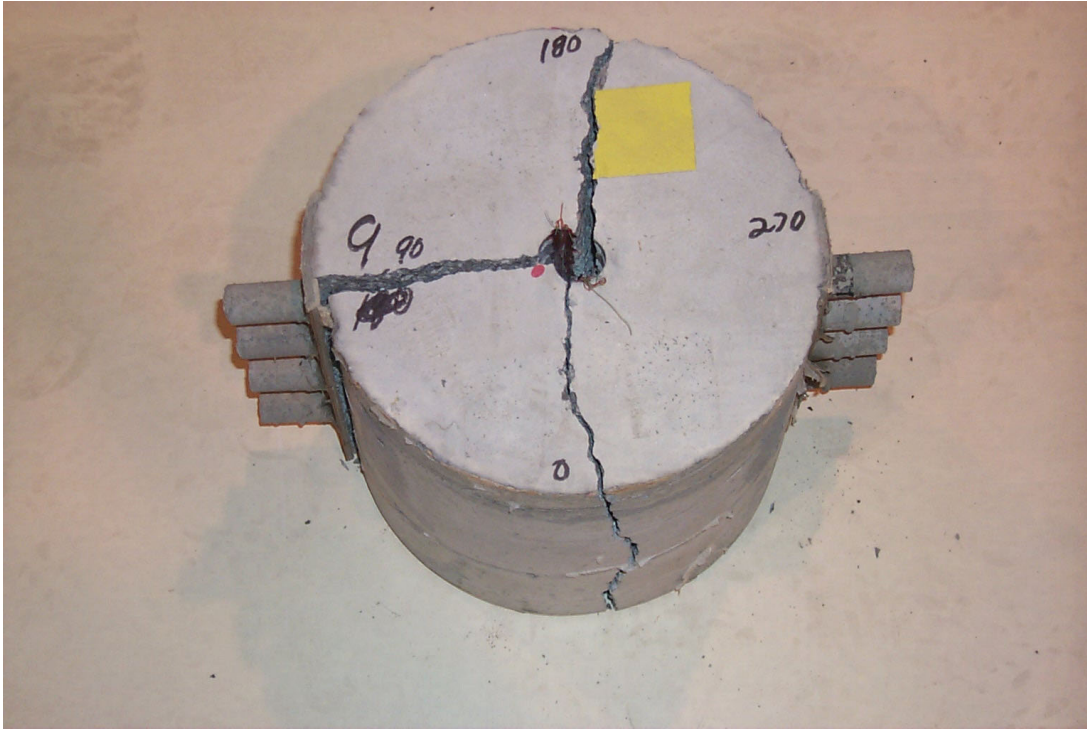
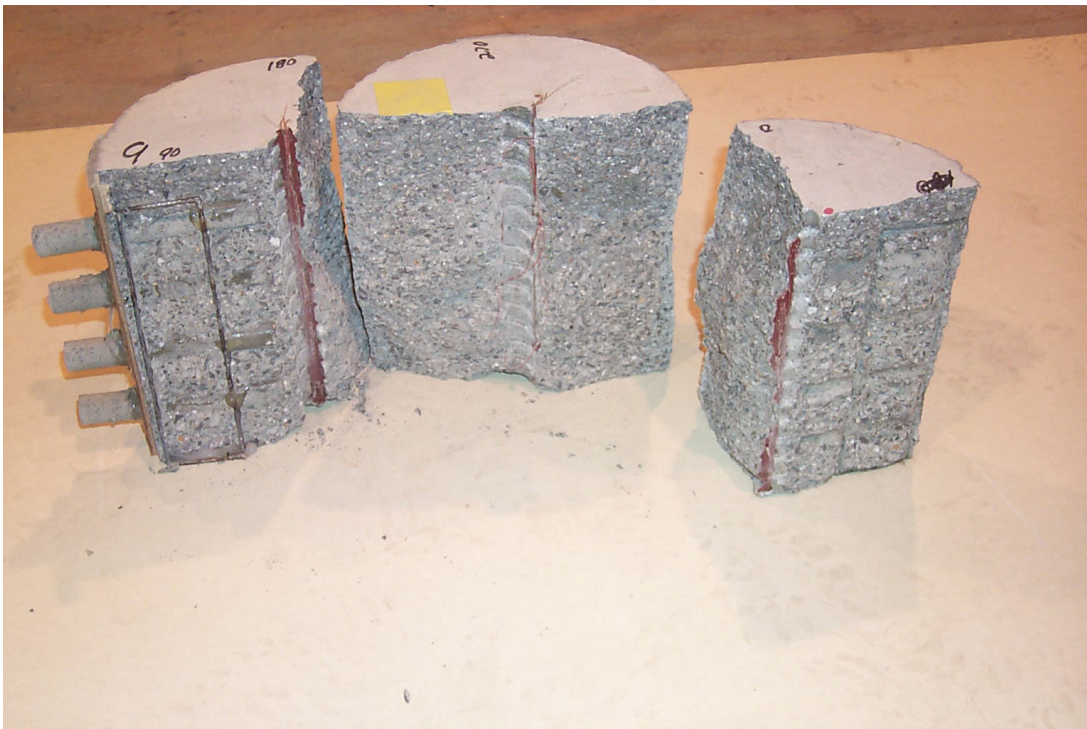


Figure B-30 Adjusted Concrete Strains, Test 8



**Figure B-31 Test Specimen 9, Post Test**



**Figure B-32 Test Specimen 9, Post Test**



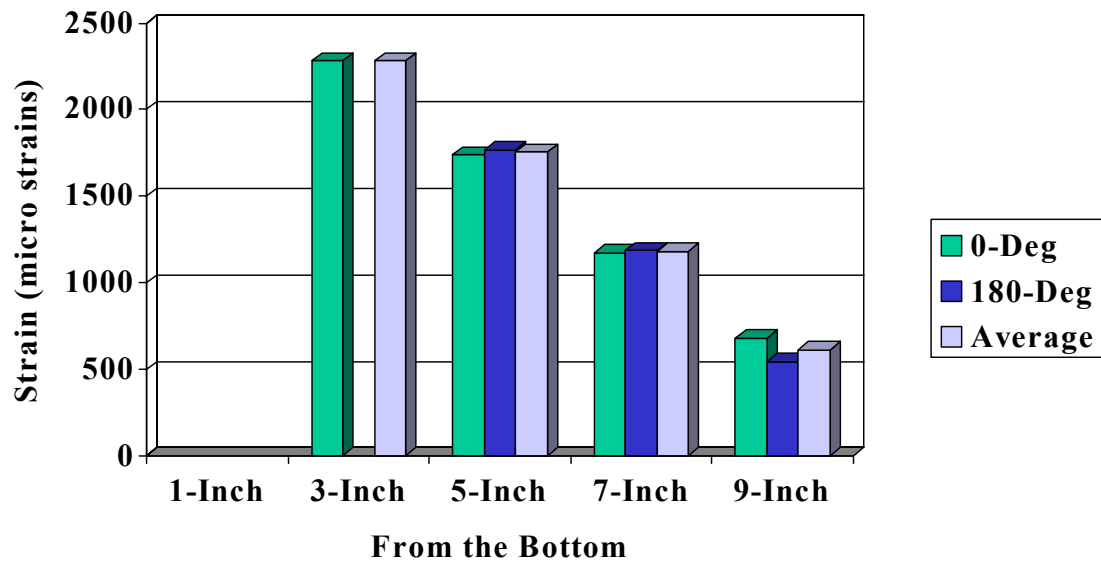


Figure B-33 Steel Strains, Test 9

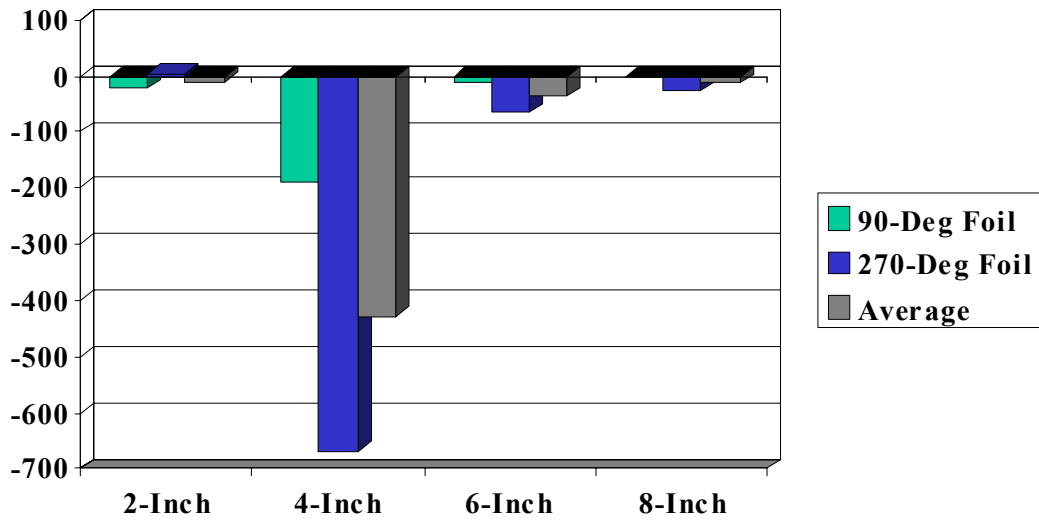


Figure B-34 Adjusted Concrete Strains, Test 9

**Table B.4 Statistical Analysis of Steel Strains for Tests 7, 8 and 9**

Test 07 Adjusted Steel Strains						
Position		1-Inch	3-Inch	5-Inch	7-Inch	9-Inch
0-Deg	Gage	SS-01	SS-03	SS-05	SS-07	SS-09
	Value	N/A	2,108	1,581	990	470
180-Deg	Gage	SS-02	SS-04	SS-06	SS-08	SS-10
	Value	NA	2,386	1,544	950	367
Average		N/A	2,247	1,563	970	419

Test 08 Adjusted Steel Strains						
Position		1-Inch	3-Inch	5-Inch	7-Inch	9-Inch
0-Deg	Gage	SS-01	SS-03	SS-05	SS-07	SS-09
	Value	N/A	N/A	1,599	550	950
180-Deg	Gage	SS-02	SS-04	SS-06	SS-08	SS-10
	Value	N/A	2,762	1,637	946	386
Average		N/A	2,762	1,618	748	668

Test 09 Adjusted Steel Strains						
Position		1-Inch	3-Inch	5-Inch	7-Inch	9-Inch
0-Deg	Gage	SS-01	SS-03	SS-05	SS-07	SS-09
	Value	N/A	2,280	1,740	1,175	680
180-Deg	Gage	SS-02	SS-04	SS-06	SS-08	SS-10
	Value	N/A	N/A	1,770	1,185	545
Average		N/A	2,280	1,755	1,180	613

Average Adjusted Steel Strains for Tests 07, 08 AND 09						
Position		1-Inch	3-Inch	5-Inch	7-Inch	9-Inch
Test 07		N/A	2,247	1,563	970	419
Test 08		N/A	2,762	1,618	748	668
Test 09		N/A	2,280	1,755	1,180	613
n		0	4	6	6	6
High		N/A	2,762	1,770	1,185	950
Low		N/A	2,108	1,544	550	367
Extreme Spread		N/A	654	226	635	583
Average		N/A	2,384	1,645	966	566
Variance		N/A	76,627	8,225	53,186	48,422
Standard Deviation		N/A	277	91	231	220
Coefficient of Variation		N/A	12	6	24	39



**Table B.5 Statistical Analysis of Concrete Strains for Tests 7, 8 and 9**

Test 07 Adjusted Concrete Strains					
Position		2-Inch	4-Inch	6-Inch	8-Inch
90-Deg	Gage	CS-01	CS-03	CS-05	CS-07
	Value	-39	-425	-99	-6
	Gage	FO-01	FO-03	FO-05	FO-07
	Value		-113.2	-89.8	-194.6
270-Deg	Gage	CS-02	CS-04	CS-06	CS-08
	Value	-260	-5	-16	-55
	Gage	FO-02	FO-04	FO-06	FO-08
	Value	-316.9	-183.6	-109.905	-145.4
Average		-205.3	-181.7	-78.7	-100.3
Test 08 Adjusted Concrete Strains					
Position		2-Inch	4-Inch	6-Inch	8-Inch
90-Deg	Gage	CS-01	CS-03	CS-05	CS-07
	Value	-63	-129	-12	-6
	Gage				
	Value				
270-Deg	Gage	CS-02	CS-04	CS-06	CS-08
	Value	-167	-102	-10	-27
	Gage				
	Value				
Average		-115.0	-115.5	-11.0	-16.5
Test 09 Adjusted Concrete Strains					
Position		2-Inch	4-Inch	6-Inch	8-Inch
90-Deg	Gage	CS-01	CS-03	CS-05	CS-07
	Value	-22	-189	-8	-0.7
	Gage				
	Value				
270-Deg	Gage	CS-02	CS-04	CS-06	CS-08
	Value	5	-669	-67	-26
	Gage				
	Value				
Average		-8.5	-429.0	-37.5	-13.4
Average Fiber-Optic and Foil Concrete Strains for Tests 07, 08 and 09					
Position		2-Inch	4-Inch	6-Inch	8-Inch
Test 07		-205.3	-181.7	-78.7	-100.3
Test 08		-115.0	-115.5	-11.0	-16.5
Test 09		-8.5	-429.0	-37.5	-13.4
Average		-123.3	-227.0	-51.5	-57.6
n		7	8	8	8
High		5.0	-5.0	-8.0	-0.7
Low		-316.9	-669.0	-109.9	-194.6
Extreme Spread		321.9	664.0	101.9	193.9
Variance		15923.8	46480.4	1972.3	5284.3
Standard Deviation		126.2	215.6	44.4	72.7
Coefficient of Variation		-102.4	-95.0	-86.3	-126.2

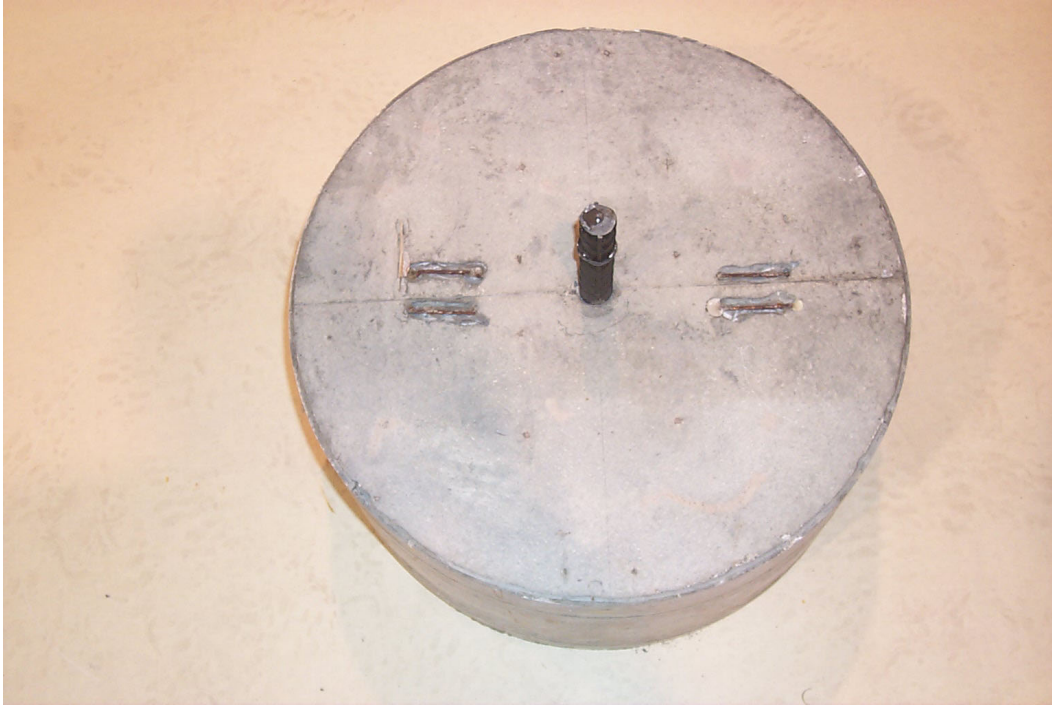


**Figure B-35 Test Specimen 10 Post Test**



**Figure B-36 Test Specimen 10, Post Test**

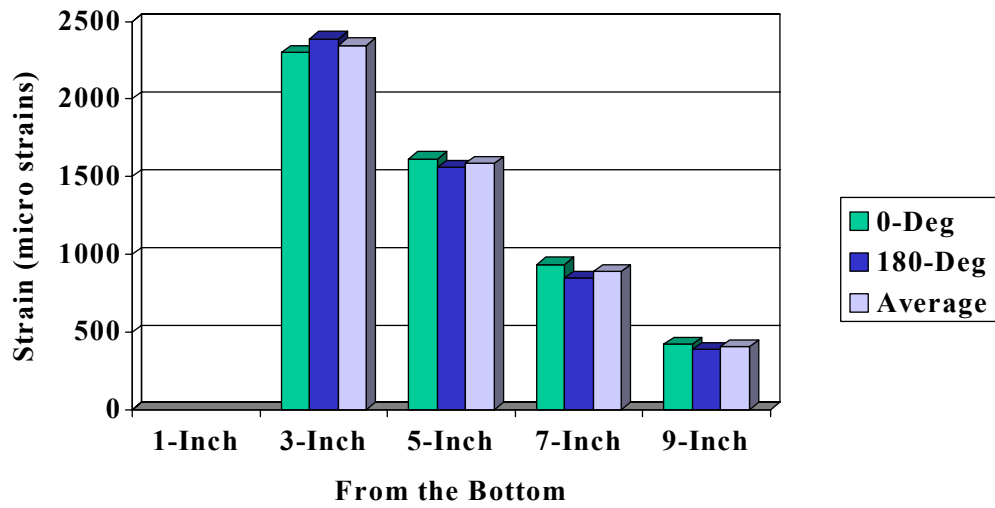


Figure B-37 Steel Strains, Test 10

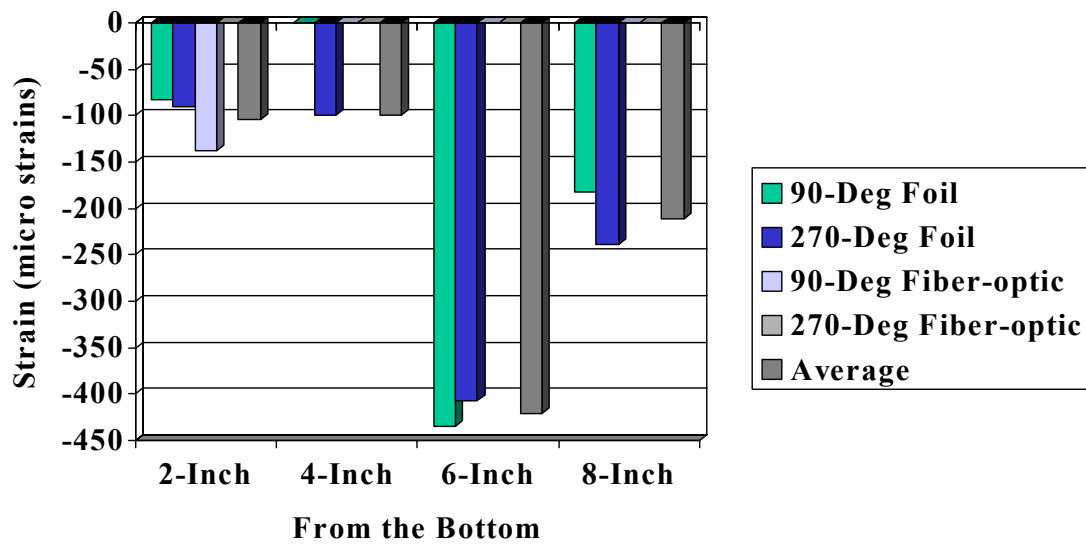


Figure B-38 Concrete Strains, Test 10



**Figure B-39 Test Specimen 11, Post Test**



**Figure B-40 Test Specimen 11, Post Test**

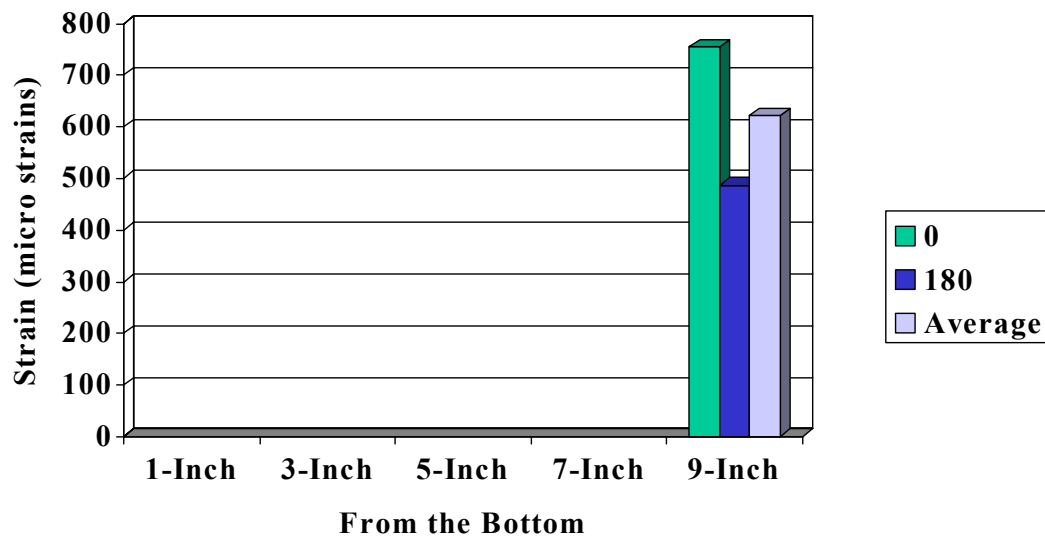


Figure B-41 Adjusted Steel Strains, Test 11

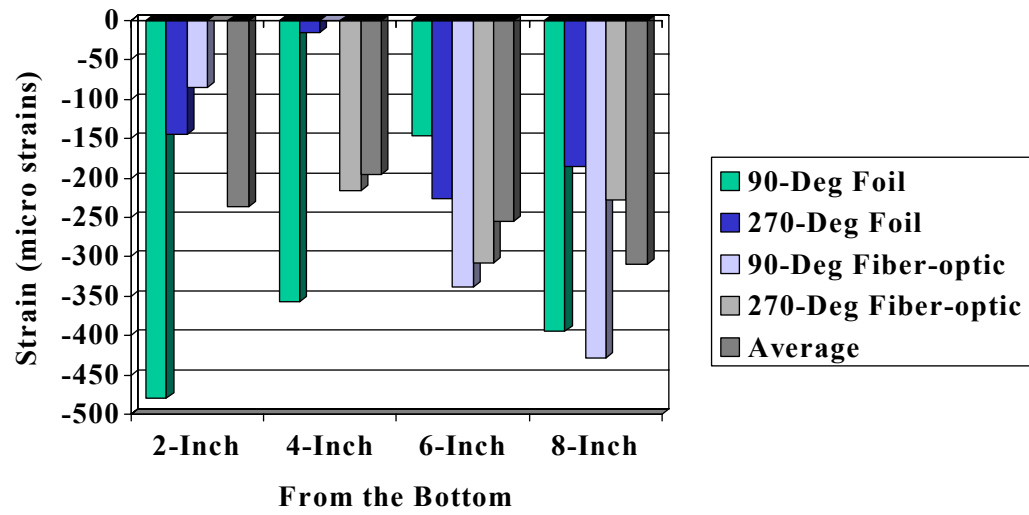
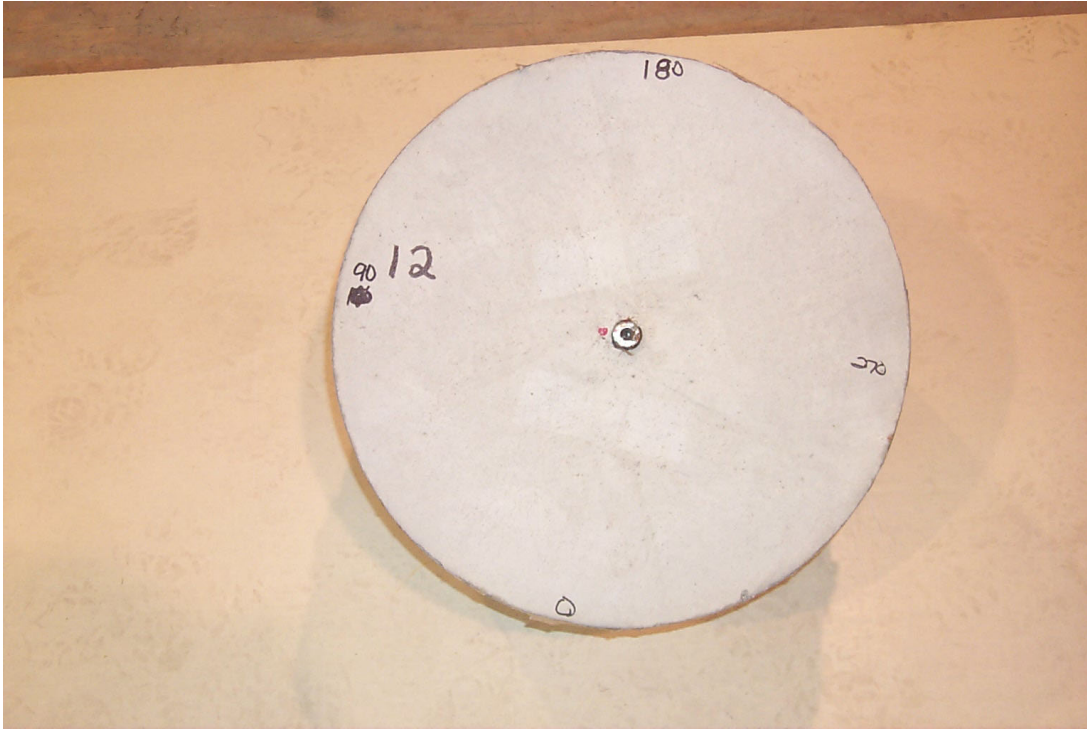


Figure B-42 Adjusted Concrete Strains, Test 11





**Figure B-43 Test Specimen 12, Post Test**



**Figure B-44 Test Specimen 12, Post Test**

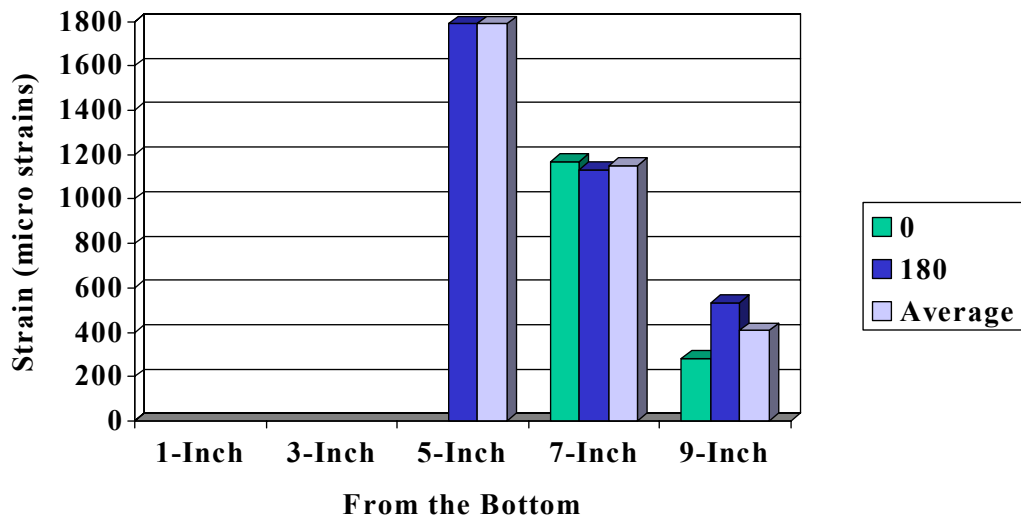


**Figure B-45 Adjusted Steel Strains, Test 12**

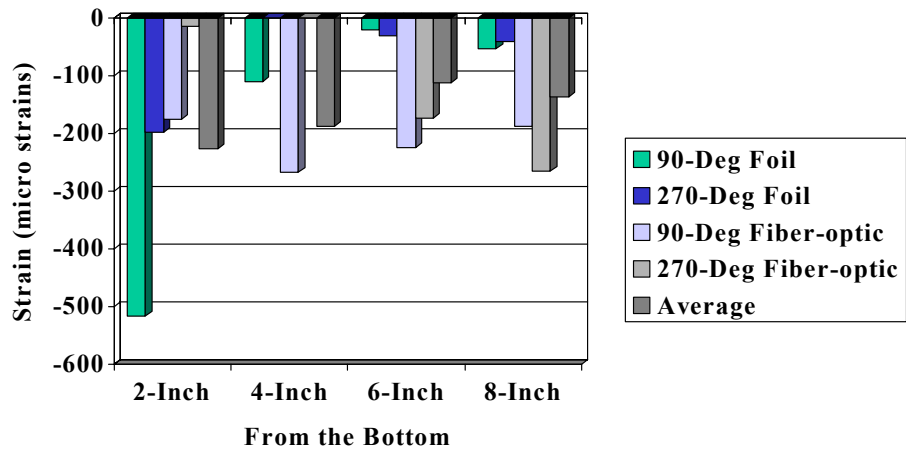


**Figure B-46 Adjusted Concrete Strains, Test 12**

**Table B.6 Statistical Analysis of Steel Strains for Tests 10, 11 and 12**

Test 10 Adjusted Steel Strains						
Position		1-Inch	3-Inch	5-Inch	7-Inch	9-Inch
0-Deg	Gage	SS-01	SS-03	SS-05	SS-07	SS-09
	Value	N/A	2,300	1,614	935	421
180-Deg	Gage	SS-02	SS-04	SS-06	SS-08	SS-10
	Value	N/A	2,390	1,560	845	390
Average		N/A	2,345	1,587	890	406

Test 11 Adjusted Steel Strains						
Position		1-Inch	3-Inch	5-Inch	7-Inch	9-Inch
0-Deg	Gage	SS-01	SS-03	SS-05	SS-07	SS-09
	Value	N/A	N/A	N/A	N/A	754
180-Deg	Gage	SS-02	SS-04	SS-06	SS-08	SS-10
	Value	N/A	N/A	N/A	N/A	487
Average		N/A	N/A	N/A	N/A	621

Test 12 Adjusted Steel Strains						
Position		1-Inch	3-Inch	5-Inch	7-Inch	9-Inch
0-Deg	Gage	SS-01	SS-03	SS-05	SS-07	SS-09
	Value	N/A	N/A	N/A	1,168	282
180-Deg	Gage	SS-02	SS-04	SS-06	SS-08	SS-10
	Value	N/A	N/A	1,790	1,132	534
Average		N/A	N/A	1,790	1,150	408

Average Adjusted Steel Strains for Tests 10, 11 and 12						
Position		1-Inch	3-Inch	5-Inch	7-Inch	9-Inch
Test 10		N/A	2,345	1,587	890	406
Test 11		N/A	N/A	N/A	N/A	621
Test 12		N/A	N/A	1,790	1,150	408
n		0	2	3	4	6
High		N/A	2,390	1,790	1,168	754
Low		N/A	2,300	1,560	845	282
Extreme Spread		N/A	90	230	323	472
Average		N/A	2,345	1,655	1,020	478
Variance		N/A	N/A	14,465	24,099	25,760
Standard Deviation		N/A	N/A	120	155	161
Coefficient of Variation		N/A	N/A	7	15	34



**Table B.7 Statistical Analysis of Concrete Strains for Tests 10, 11 and 12**

Test 10 Adjusted Concrete Strains					
Position		2-Inch	4-Inch	6-Inch	8-Inch
90-Deg	Gage	CS-01	CS-03	CS-05	CS-07
	Value	-82		-435	-182
	Gage	FO-01	FO-03	FO-05	FO-07
	Value	-137.7			
270-Deg	Gage	CS-02	CS-04	CS-06	CS-08
	Value	-91	-100	-407	-239
	Gage	FO-02	FO-04	FO-06	FO-08
	Value				
Average		-103.6	-100.0	-421.0	-210.5
Test 11 Adjusted Concrete Strains					
Position		2-Inch	4-Inch	6-Inch	8-Inch
90-Deg	Gage	CS-01	CS-03	CS-05	CS-07
	Value	-479	-357	-147	-394
	Gage	FO-01	FO-03	FO-05	FO-07
	Value	-84.7		-339.1	-429.1
270-Deg	Gage	CS-02	CS-04	CS-06	CS-08
	Value	-145	-16	-226	-186
	Gage	FO-02	FO-04	FO-06	FO-08
	Value		-215.9	-307.7	-228.6
Average		-236.2	-196.3	-255.0	-309.4
Test 12 Adjusted Concrete Strains					
Position		2-Inch	4-Inch	6-Inch	8-Inch
90-Deg	Gage	CS-01	CS-03	CS-05	CS-07
	Value	-517	-110	-20	-53
	Gage	FO-01	FO-03	FO-05	FO-07
	Value	-174.6	-266.6	-224.2	-188.3
270-Deg	Gage	CS-02	CS-04	CS-06	CS-08
	Value	-198		-30	-41
	Gage	FO-02	FO-04	FO-06	FO-08
	Value	-13.6		-172.8	-264.9
Average		-225.8	-188.3	-111.7	-136.8
Average Fiber-Optic and Foil Concrete Strains for Tests 10, 11 and 12					
Position		2-Inch	4-Inch	6-Inch	8-Inch
Test 10		-103.6	-100.0	-421.0	-210.5
Test 11		-236.2	-196.3	-255.0	-309.4
Test 12		-225.8	-188.3	-111.7	-136.8
Average		-192.3	-177.6	-230.9	-220.6
n		10	6	10	10
High		-13.6	-16.0	-20.0	-41.0
Low		-517.0	-357.0	-435.0	-429.1
Extreme Spread		503.4	341.0	415.0	388.1
Variance		28791.4	15655.2	20624.0	15555.5
Standard Deviation		169.7	125.1	143.6	124.7
Coefficient of Variation		-88.3	-70.5	-62.2	-56.5

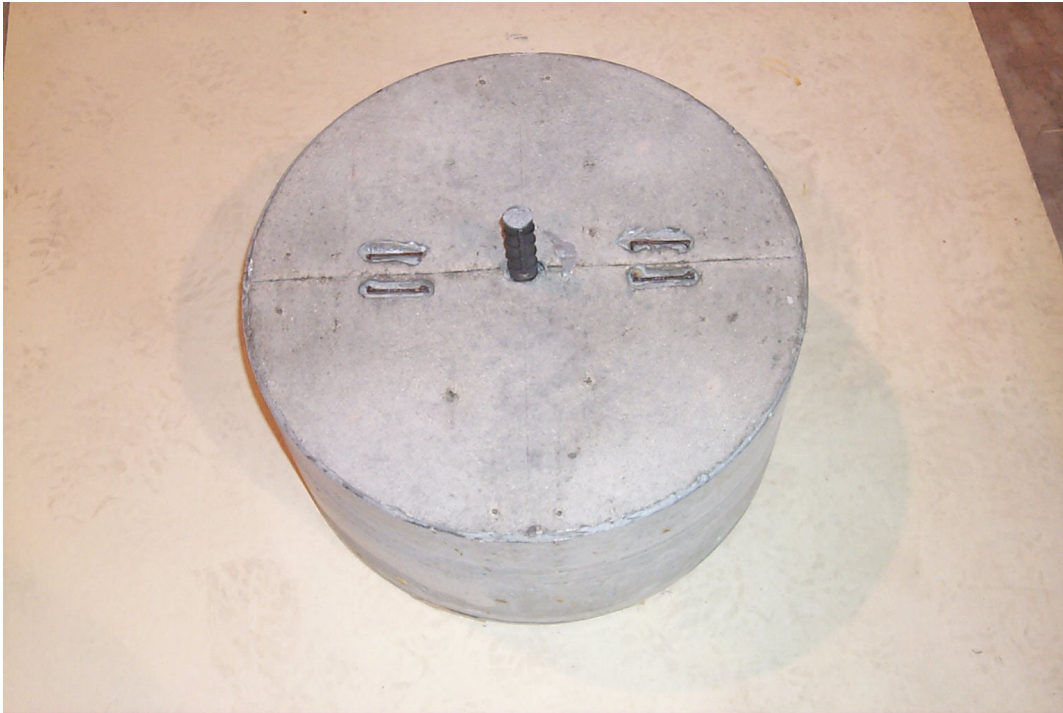


**Figure B-47 Test Specimen 13, Post Test**



**Figure B-48 Test Specimen 13, Post Test**

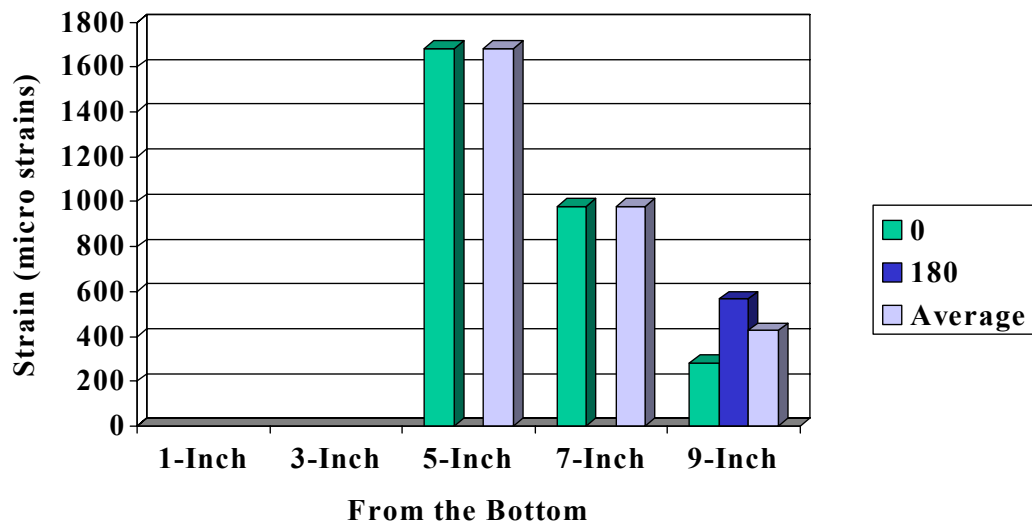


Figure B-49 Adjusted Steel Strains, Test 13

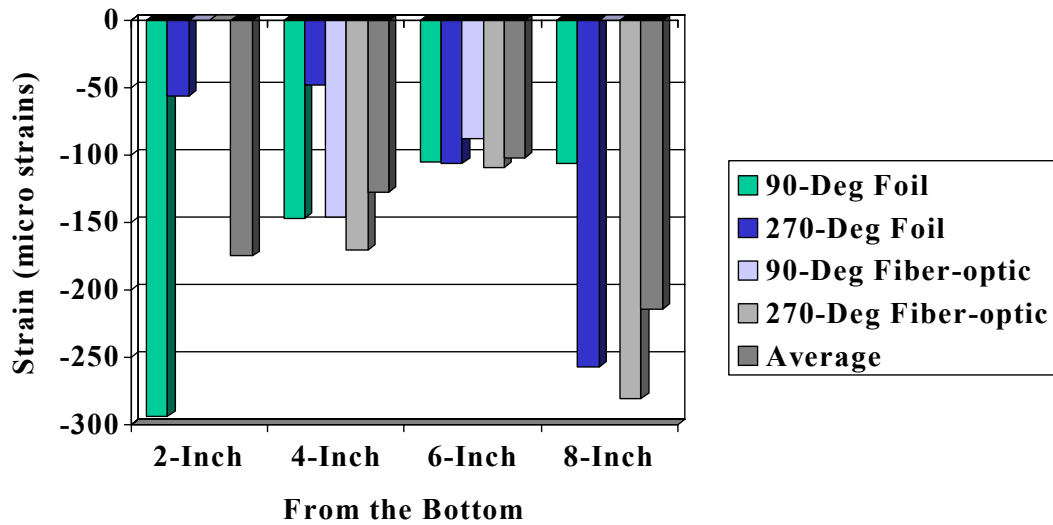
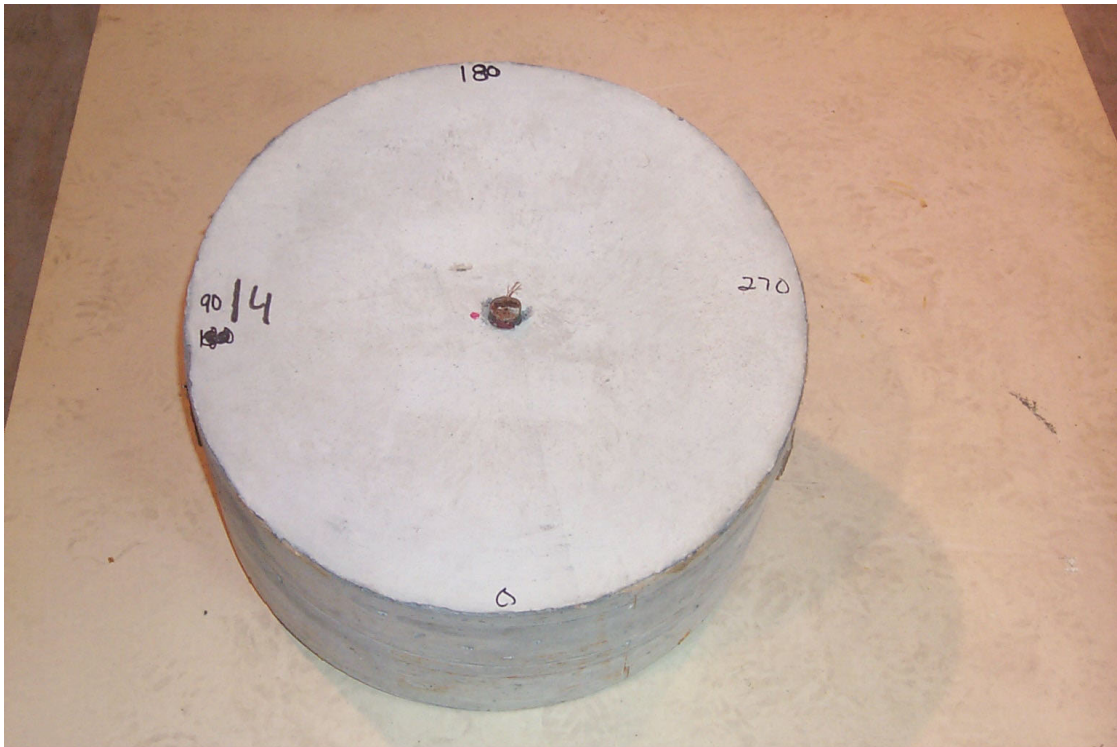


Figure B-50 Adjusted Concrete Strains, Test 13



**Figure B-51 Test Specimen 14, Post Test**



**Figure B-52 Test Specimen 14, Post Test**



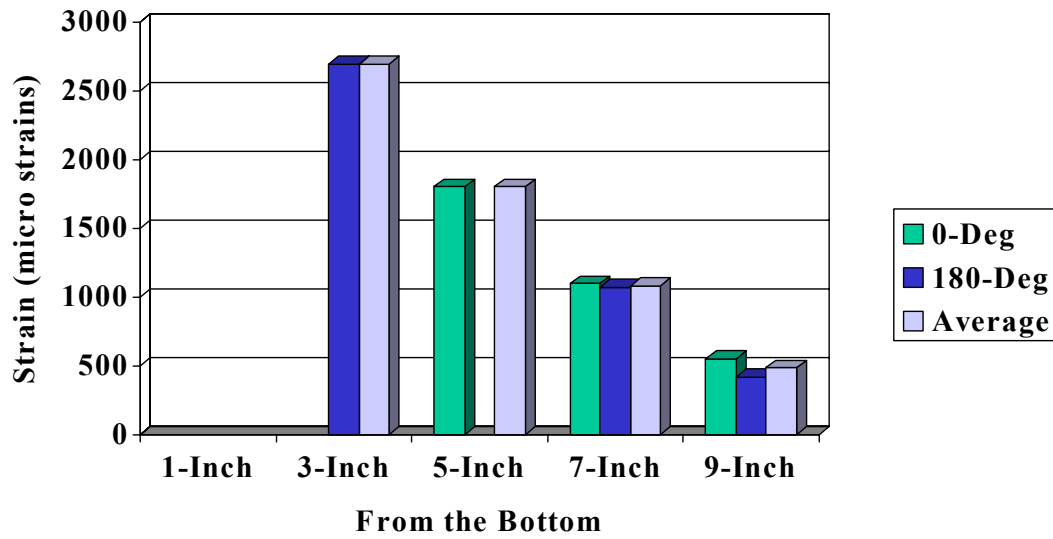


Figure B-53 Adjusted Steel Strains, Test 14

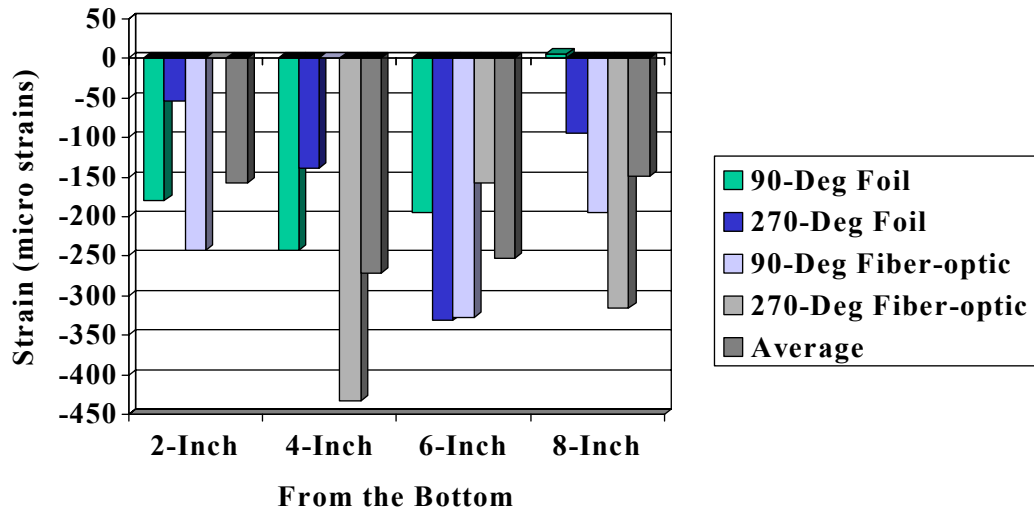
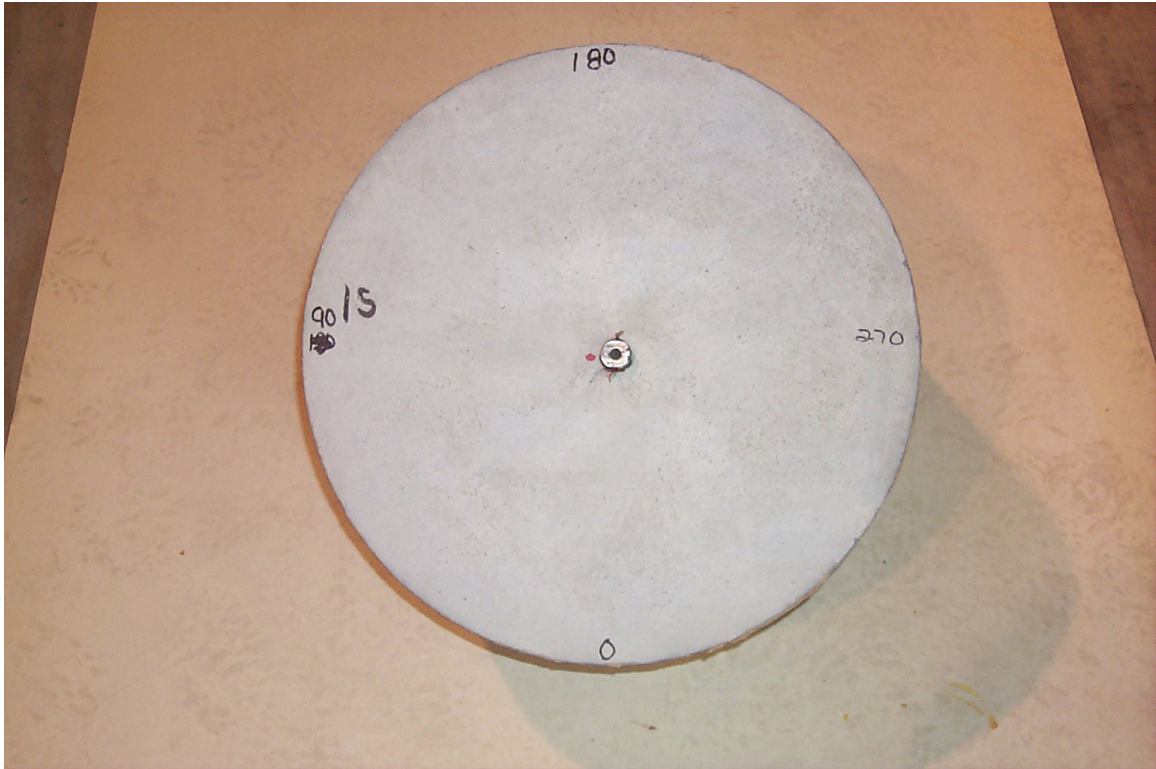
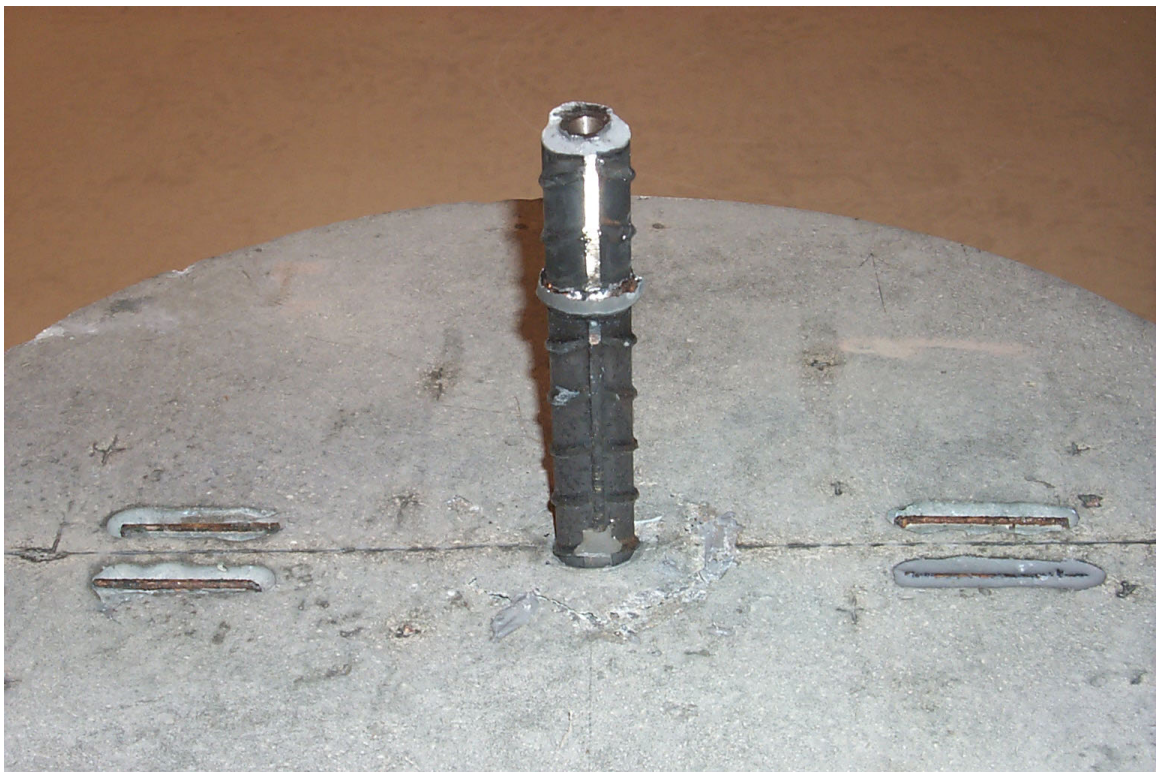


Figure B-54 Adjusted Concrete Strains, Test 14



**Figure B-55 Test Specimen 15, Post Test**



**Figure B-56 Test Specimen 15 Post Test**

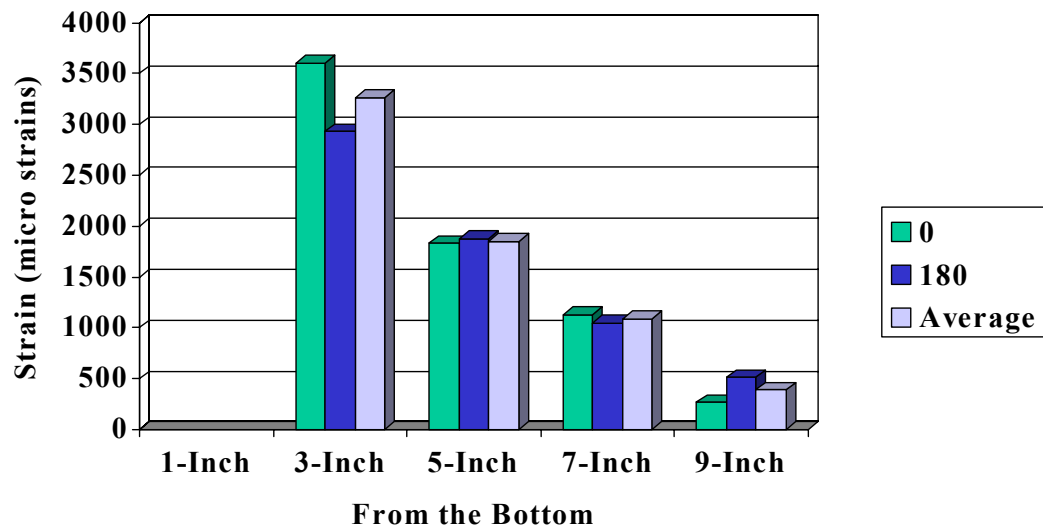


Figure B-57 Adjusted Steel Strains, Test 15

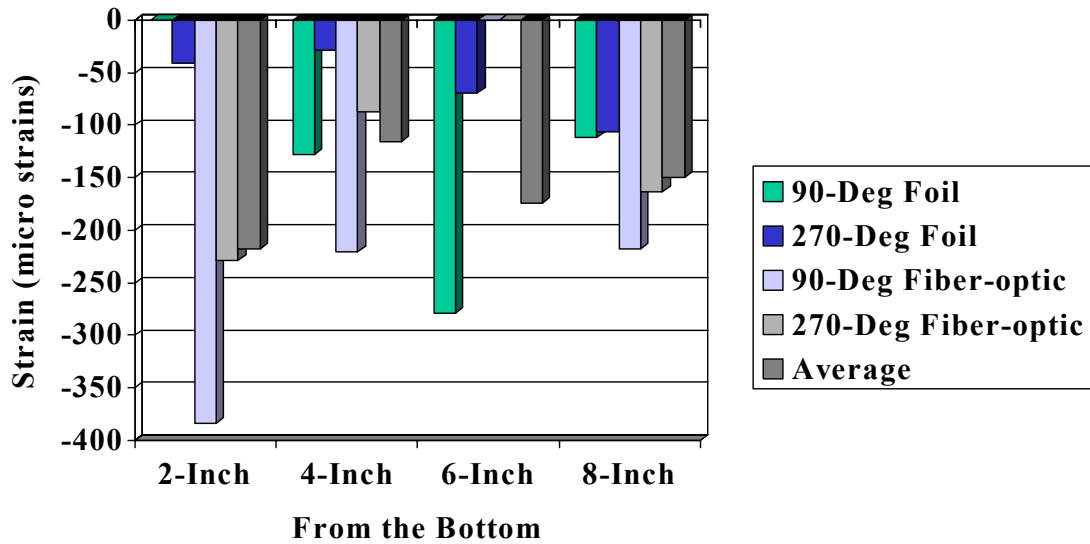


Figure B-58 Adjusted Concrete Strains, Test 15

**Table B.8 Statistical Analysis of Steel Strains for Tests 13, 14 and 15**

Test 13 Adjusted Steel Strains						
Position		1-Inch	3-Inch	5-Inch	7-Inch	9-Inch
0-Deg	Gage	SS-01	SS-03	SS-05	SS-07	SS-09
	Value	N/A	N/A	1,682	980	282
180-Deg	Gage	SS-02	SS-04	SS-06	SS-08	SS-10
	Value	N/A	N/A	N/A	N/A	567
Average		N/A	N/A	1,682	980	425

Test 14 Adjusted Steel Strains						
Position		1-Inch	3-Inch	5-Inch	7-Inch	9-Inch
0-Deg	Gage	SS-01	SS-03	SS-05	SS-07	SS-09
	Value	N/A	N/A	1,800	1,098	551
180-Deg	Gage	SS-02	SS-04	SS-06	SS-08	SS-10
	Value	N/A	2,690	N/A	1,070	420
Average		N/A	2,690	1,800	1,084	486

Test 15 Adjusted Steel Strains						
Position		1-Inch	3-Inch	5-Inch	7-Inch	9-Inch
0-Deg	Gage	SS-01	SS-03	SS-05	SS-07	SS-09
	Value	N/A	3,602	1,828	1,130	270
180-Deg	Gage	SS-02	SS-04	SS-06	SS-08	SS-10
	Value	N/A	2,930	1,880	1,052	514
Average		N/A	3,266	1,854	1,091	392

Average Adjusted Steel Strains for Tests 13, 14 and 15						
Position		1-Inch	3-Inch	5-Inch	7-Inch	9-Inch
Test 13		N/A	N/A	1,682	980	425
Test 14		N/A	2,690	1,800	1,084	486
Test 15		N/A	3,266	1,854	1,091	392
n		0	3	4	5	6
High		N/A	3,602	1,880	1,130	567
Low		N/A	2,690	1,682	980	270
Extreme Spread		N/A	912	198	150	297
Average		N/A	3,074	1,798	1,066	434
Variance		N/A	223,488	7,028	3,182	17,595
Standard Deviation		N/A	473	84	56	133
Coefficient of Variation		N/A	15	5	5	31



**Table B.9 Statistical Analysis of Concrete Strains for Tests 13, 14 and 15**

Test 13 Adjusted Concrete Strains					
Position		2-Inch	4-Inch	6-Inch	8-Inch
90-Deg	Gage	CS-01	CS-03	CS-05	CS-07
	Value	-294	-147	-105	-106
	Gage	FO-01	FO-03	FO-05	FO-07
	Value		-146.3	-87.7	
270-Deg	Gage	CS-02	CS-04	CS-06	CS-08
	Value	-56	-48	-106	-257
	Gage	FO-02	FO-04	FO-06	FO-08
	Value		-170.0	-108.9	-280.2
Average		-175.0	-127.8	-101.9	-214.4
Test 14 Adjusted Concrete Strains					
Position		2-Inch	4-Inch	6-Inch	8-Inch
90-Deg	Gage	CS-01	CS-03	CS-05	CS-07
	Value	-179	-243	-195	5
	Gage	FO-01	FO-03	FO-05	FO-07
	Value	-242.1		-327.7	-194.2
270-Deg	Gage	CS-02	CS-04	CS-06	CS-08
	Value	-53	-138	-331	-94
	Gage	FO-02	FO-04	FO-06	FO-08
	Value		-433.7	-157.9	-315.7
Average		-158.0	-271.6	-252.9	-149.7
Test 15 Adjusted Concrete Strains					
Position		2-Inch	4-Inch	6-Inch	8-Inch
90-Deg	Gage	CS-01	CS-03	CS-05	CS-07
	Value		-128	-279	-112
	Gage	FO-01	FO-03	FO-05	FO-07
	Value	-383.5	-219.8		-218.2
270-Deg	Gage	CS-02	CS-04	CS-06	CS-08
	Value	-41	-29	-69	-106
	Gage	FO-02	FO-04	FO-06	FO-08
	Value	-228.2	-86.7		-163.5
Average		-217.6	-115.9	-174.0	-149.9
Average Fiber-Optic and Foil Concrete Strains for Tests 13, 14 and 15					
Position		2-Inch	4-Inch	6-Inch	8-Inch
Test 13		-175.0	-127.8	-101.9	-214.4
Test 14		-158.0	-271.6	-252.9	-149.7
Test 15		-217.6	-115.9	-174.0	-149.9
Average		-184.6	-162.7	-176.7	-167.4
n		8	11	10	11
High		-41.0	-29.0	-69.0	5.0
Low		-383.5	-433.7	-331.0	-315.7
Extreme Spread		342.5	404.7	262.0	320.7
Variance		15894.0	12234.1	10226.6	9177.9
Standard Deviation		126.1	110.6	101.1	95.8
Coefficient of Variation		-68.3	-68.0	-57.2	-57.2



**Figure B-59 Test Specimen 16, Post Test**



**Figure B-60 Test Specimen 16, Post Test**

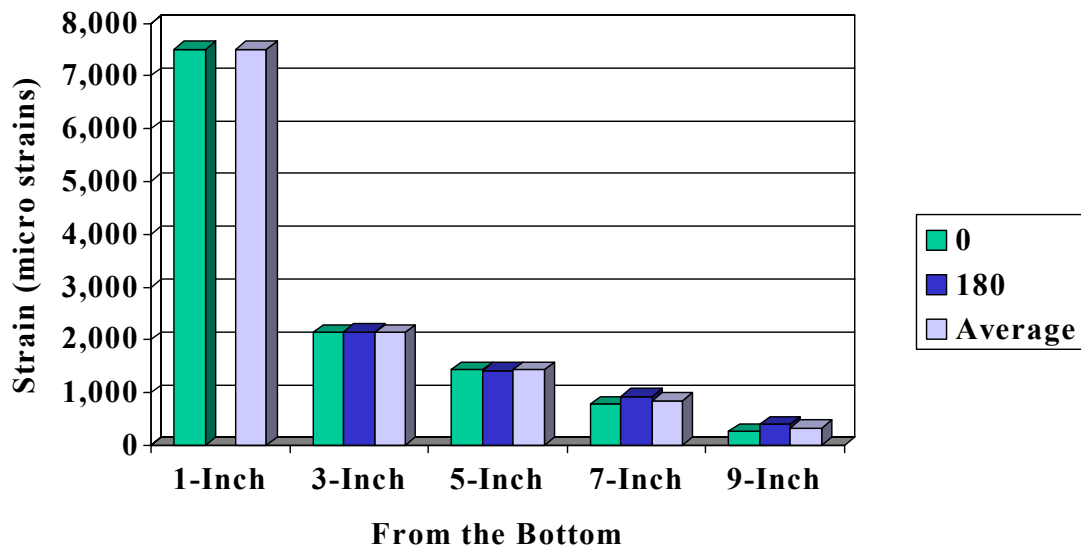


Figure B-61 Adjusted Steel Strains, Test 16

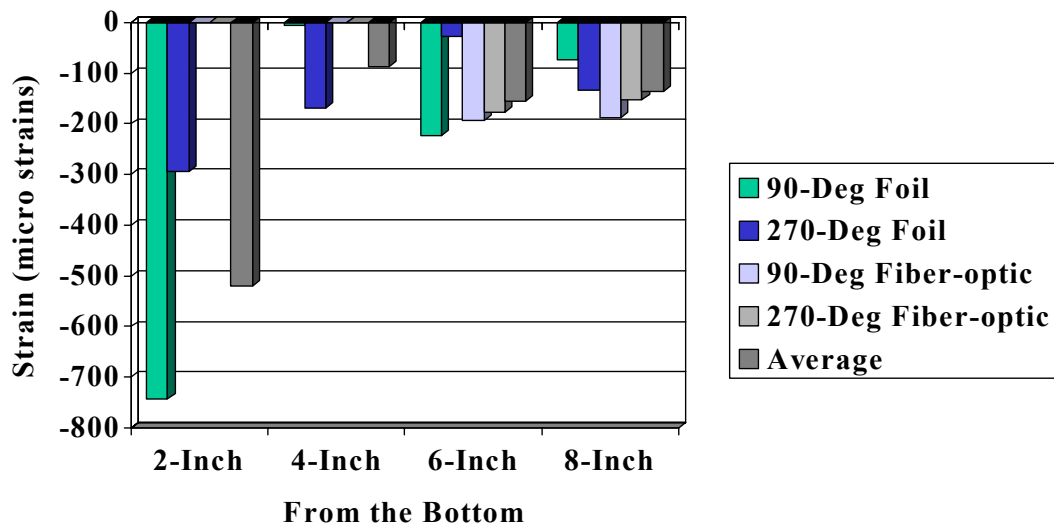
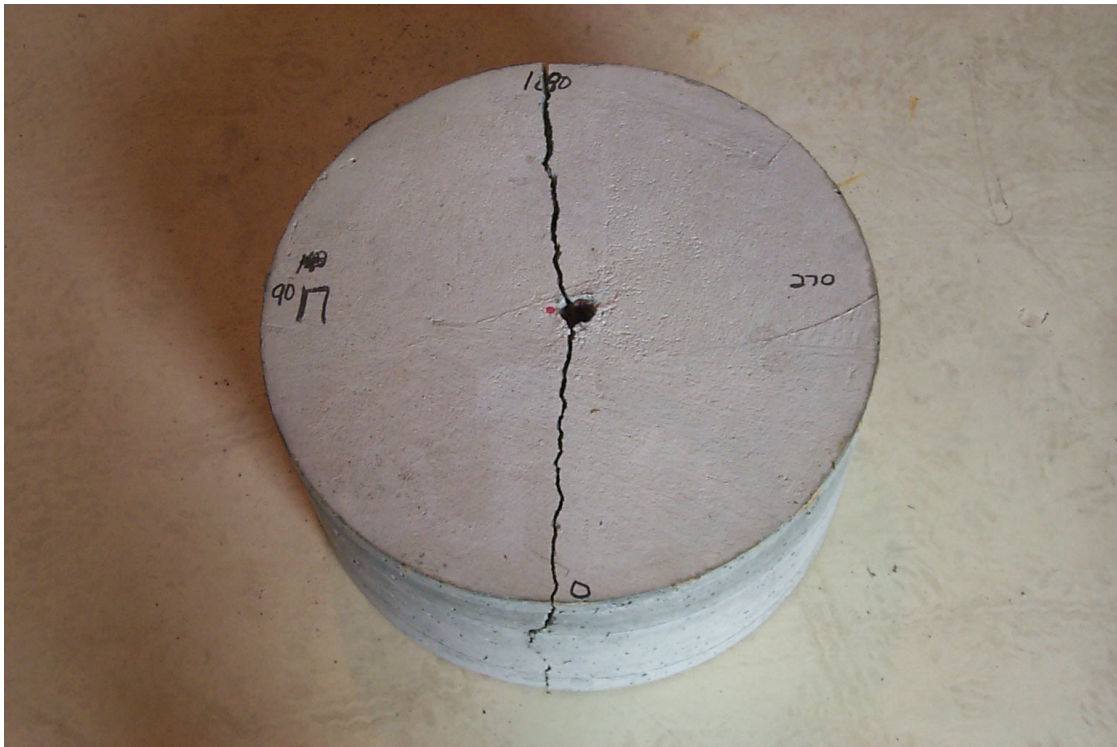


Figure B-62 Adjusted Concrete Strains, Test 16





**Figure B-63 Test Specimen 17, Post Test**



**Figure B-64 Test Specimen 17, Post Test**

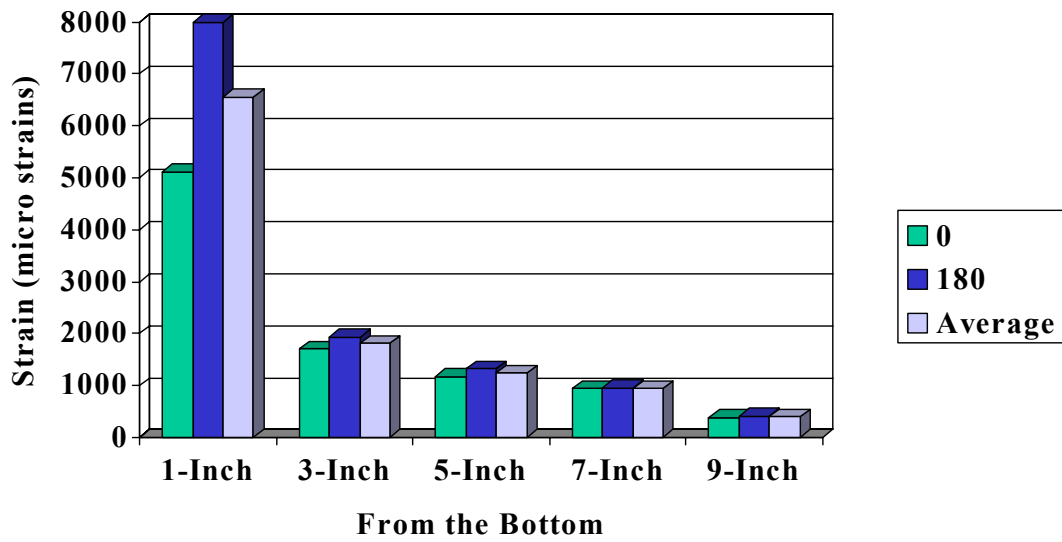


Figure B-65 Adjusted Steel Strains, Test 17

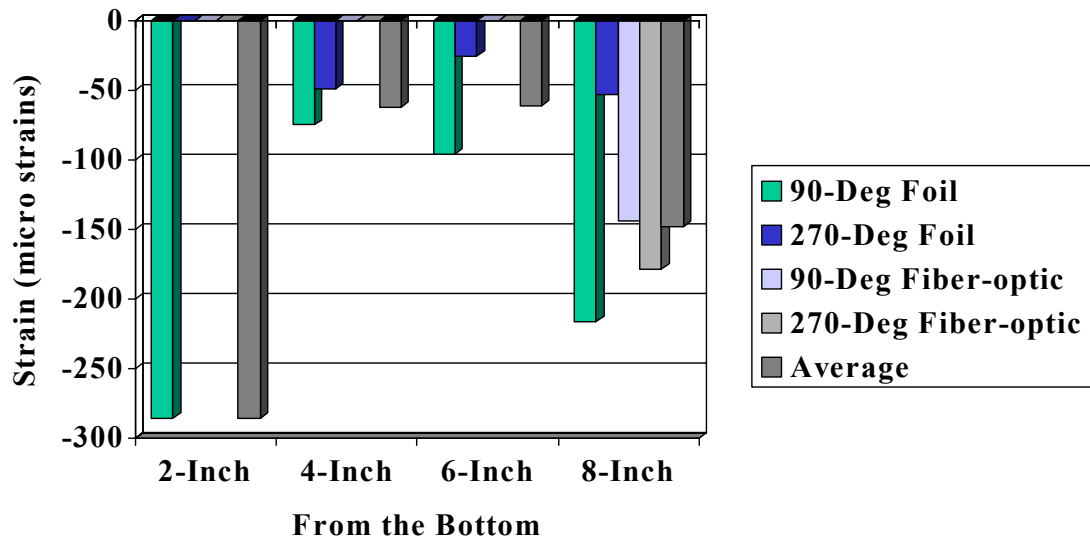
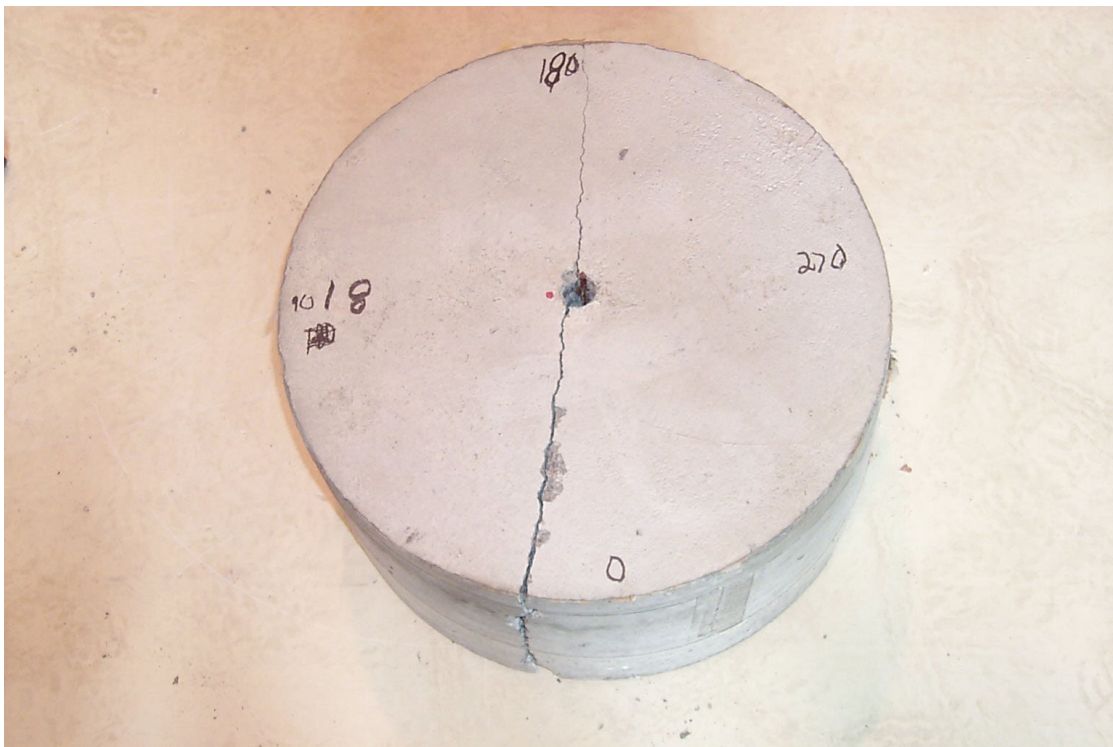


Figure B-66 Adjusted Concrete Strains, Test 17



**Figure B-67 Test Specimen 18, Post Test**



**Figure B-68 Test Specimen 18, Post Test**

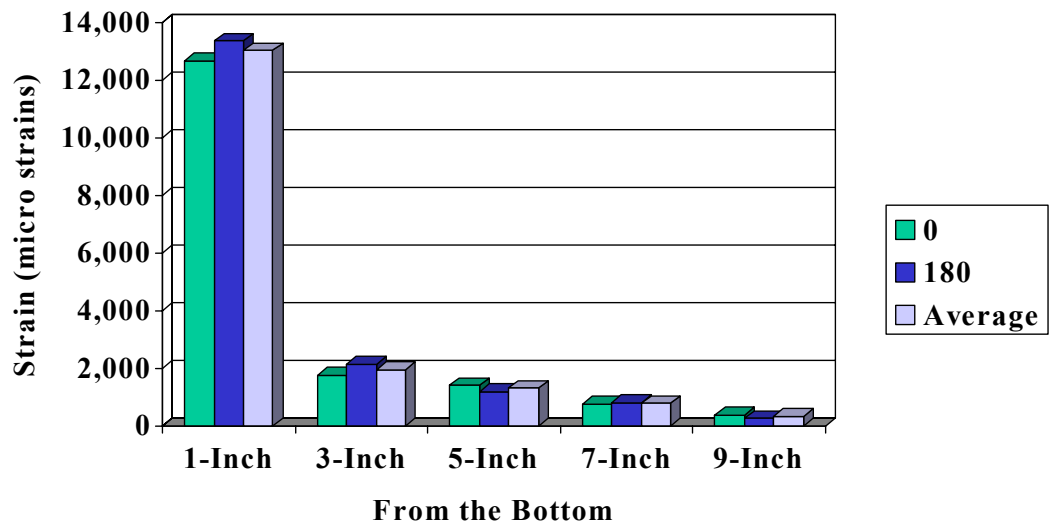


Figure B-69 Adjusted Steel Strains, Test 18

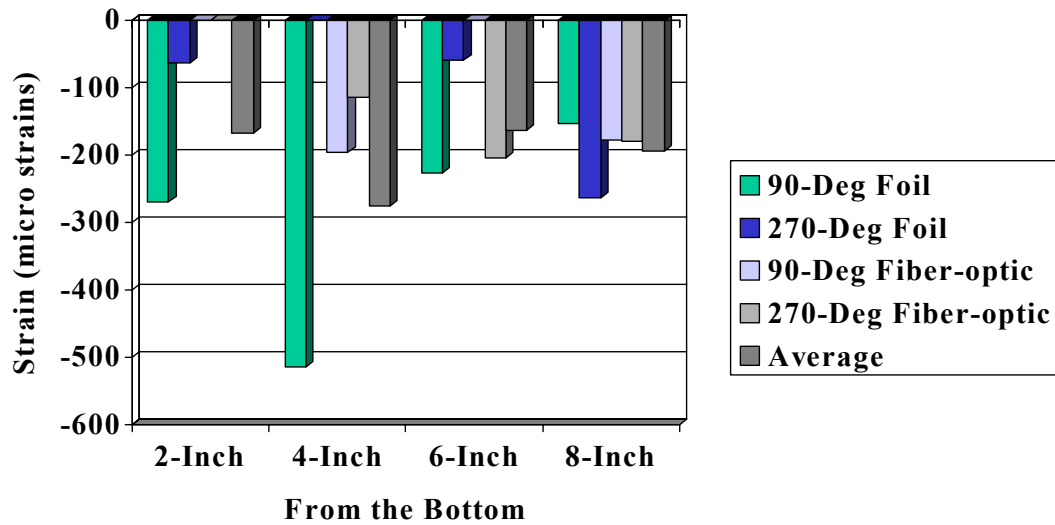


Figure B-70 Adjusted Concrete Strains, Test 18



**Table B.10 Statistical Analysis of Steel Strains for Tests 16, 17 and 18**

Test 16 Adjusted Steel Strains						
Position		1-Inch	3-Inch	5-Inch	7-Inch	9-Inch
0-Deg	Gage	SS-01	SS-03	SS-05	SS-07	SS-09
	Value	7,500	2136	1438	778	268
180-Deg	Gage	SS-02	SS-04	SS-06	SS-08	SS-10
	Value	Broke	2147	1420	925	399
Average		7,500	2,142	1,429	852	334

Test 17 Adjusted Steel Strains						
Position		1-Inch	3-Inch	5-Inch	7-Inch	9-Inch
0-Deg	Gage	SS-01	SS-03	SS-05	SS-07	SS-09
	Value	5,120	1,700	1,170	940	388
180-Deg	Gage	SS-02	SS-04	SS-06	SS-08	SS-10
	Value	8,000	1,930	1,320	950	420
Average		6,560	1,815	1,245	945	404

Test 18 Adjusted Steel Strains						
Position		1-Inch	3-Inch	5-Inch	7-Inch	9-Inch
0-Deg	Gage	SS-01	SS-03	SS-05	SS-07	SS-09
	Value	12,671	1,770	1,405	783	386
180-Deg	Gage	SS-02	SS-04	SS-06	SS-08	SS-10
	Value	13,340	2,163	1,211	818	275
Average		13,006	1,967	1,308	801	331

Adjusted Average Steel Strains for Tests 16, 17 and 18						
Position		1-Inch	3-Inch	5-Inch	7-Inch	9-Inch
Test 16		7,500	1,815	1,429	852	334
Test 17		6,560	1,815	1,245	945	404
Test 18		13,006	1,967	1,308	801	331
n		5	6	6	6	6
High		13,340	2,163	1438	950	420
Low		5,120	1,700	1,170	778	268
Extreme Spread		8,220	463	268	172	152
Average		9,022	1,866	1,327	866	356
Variance		12,521,052	42,104	13,041	6,590	4,435
Standard Deviation		3,539	205	114	81	67
Coefficient of Variation		39	11	9	9	19



**Table B.11 Statistical Analysis of Concrete Strains for Tests, 16, 17 and 18**

Test 16 Adjusted Concrete Strains					
Position		2-Inch	4-Inch	6-Inch	8-Inch
90-Deg	Gage	CS-01	CS-03	CS-05	CS-07
	Value	-744	-6	-224	-74
	Gage	FO-01	FO-03	FO-05	FO-07
	Value			-193.3	-186.7
270-Deg	Gage	CS-02	CS-04	CS-06	CS-08
	Value	-295	-170	-28	-134
	Gage	FO-02	FO-04	FO-06	FO-08
	Value			-176.8	-152.1
Average		-519.5	-88.0	-155.5	-136.7
Test 17 Adjusted Concrete Strains					
Position		2-Inch	4-Inch	6-Inch	8-Inch
90-Deg	Gage	CS-01	CS-03	CS-05	CS-07
	Value	-286	-75	-96	-216
	Gage	FO-01	FO-03	FO-05	FO-07
	Value				-144.2
270-Deg	Gage	CS-02	CS-04	CS-06	CS-08
	Value		-49	-26	-53
	Gage	FO-02	FO-04	FO-06	FO-08
	Value				-178.4
Average		-286.0	-62.0	-61.0	-147.9
Test 18 Adjusted Concrete Strains					
Position		2-Inch	4-Inch	6-Inch	8-Inch
90-Deg	Gage	CS-01	CS-03	CS-05	CS-07
	Value	-270	-515	-226	-154
	Gage	FO-01	FO-03	FO-05	FO-07
	Value		-195.4		-178.2
270-Deg	Gage	CS-02	CS-04	CS-06	CS-08
	Value	-64		-59	-263
	Gage	FO-02	FO-04	FO-06	FO-08
	Value		-114.8	-203.3	-180.5
Average		-167.0	-275.1	-162.8	-193.9
Average Fiber-Optic and Foil Concrete Strains for Tests 16, 17 and 18					
Position		2-Inch	4-Inch	6-Inch	8-Inch
Test 16		-519.5	-88.0	-155.5	-136.7
Test 17		-286.0	-62.0	-61.0	-147.9
Test 18		-167.0	-275.1	-162.8	-193.9
Average		-331.8	-160.7	-136.9	-159.5
n		5	7	9	12
High		-64.0	-6.0	-26.0	-53.0
Low		-744.0	-515.0	-226.0	-263.0
Extreme Spread		680.0	509.0	200.0	210.0
Variance		62224.2	28780.2	7075.7	3219.4
Standard Deviation		249.4	169.6	84.1	56.7
Coefficient of Variation		-75.2	-105.5	-61.4	-35.6

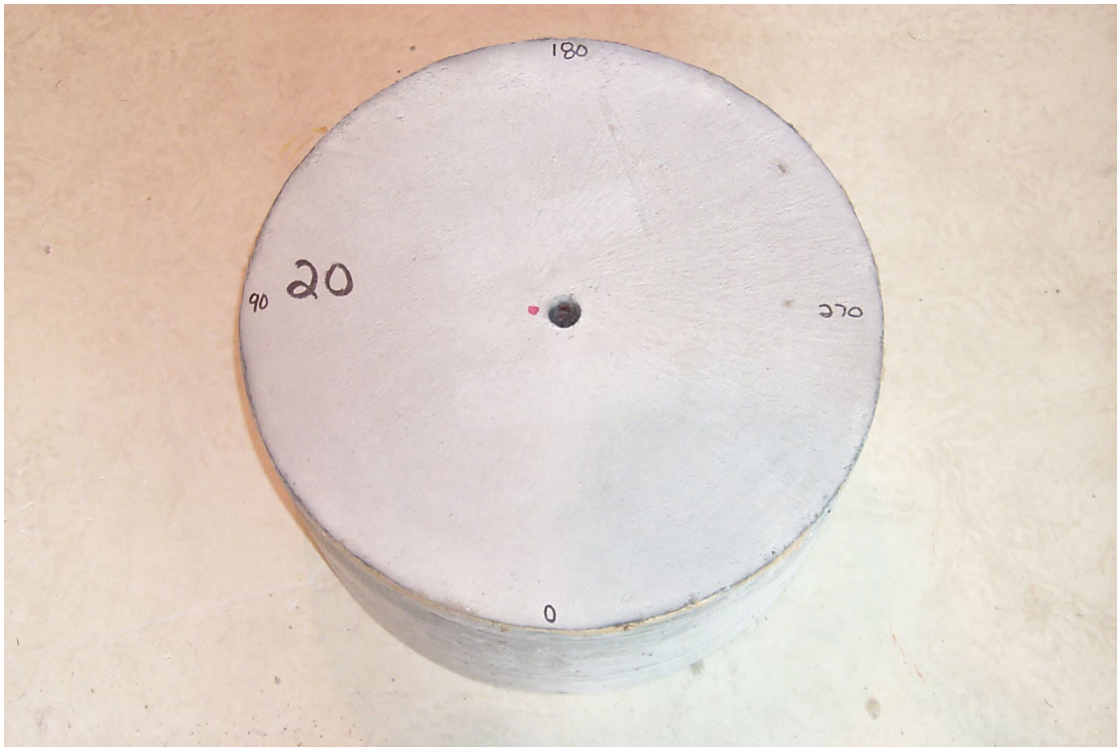


**Figure B-71 Test Specimen 20, Post Test**

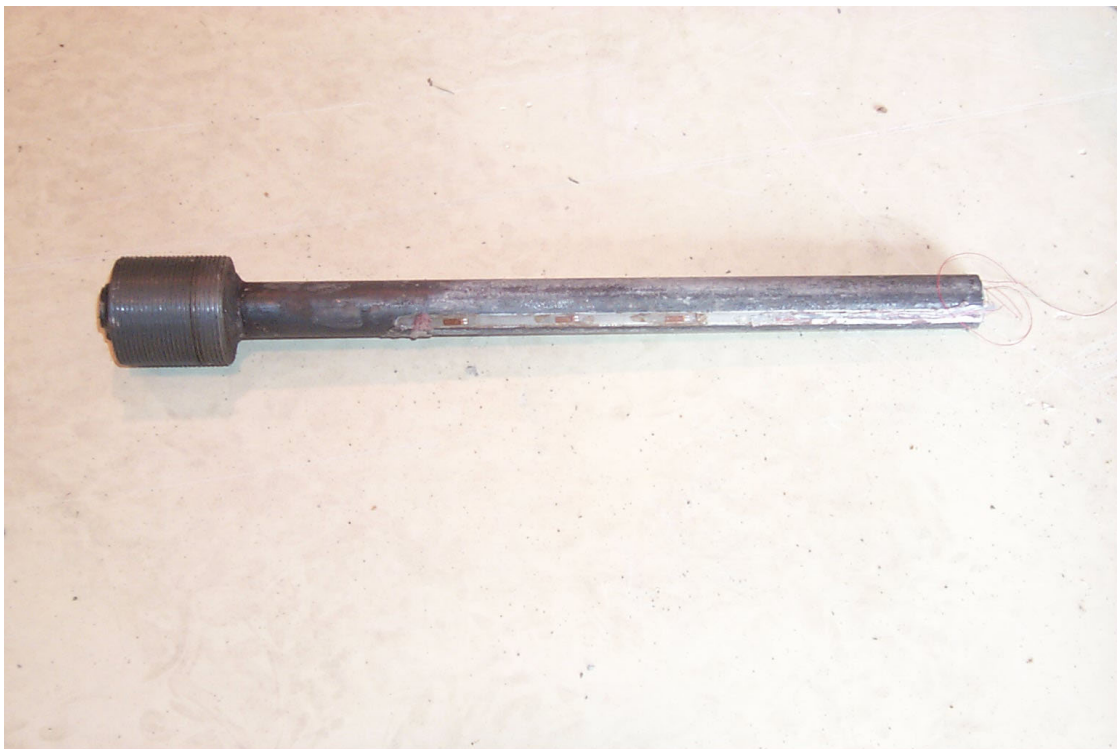


**Figure B-72 Test Specimen 20, Post Test**

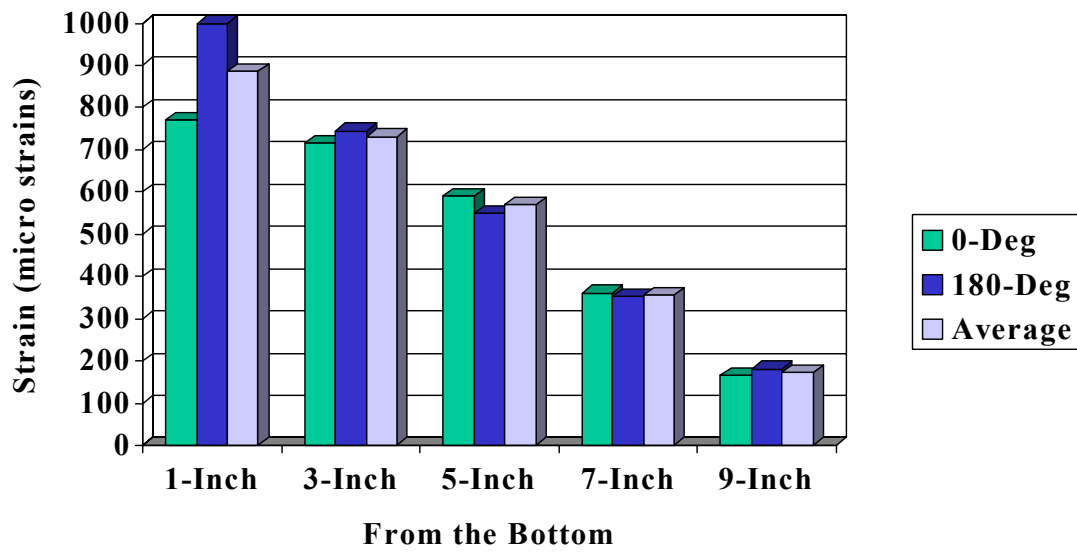


Figure B-73 Adjusted Steel Strains, Test 20

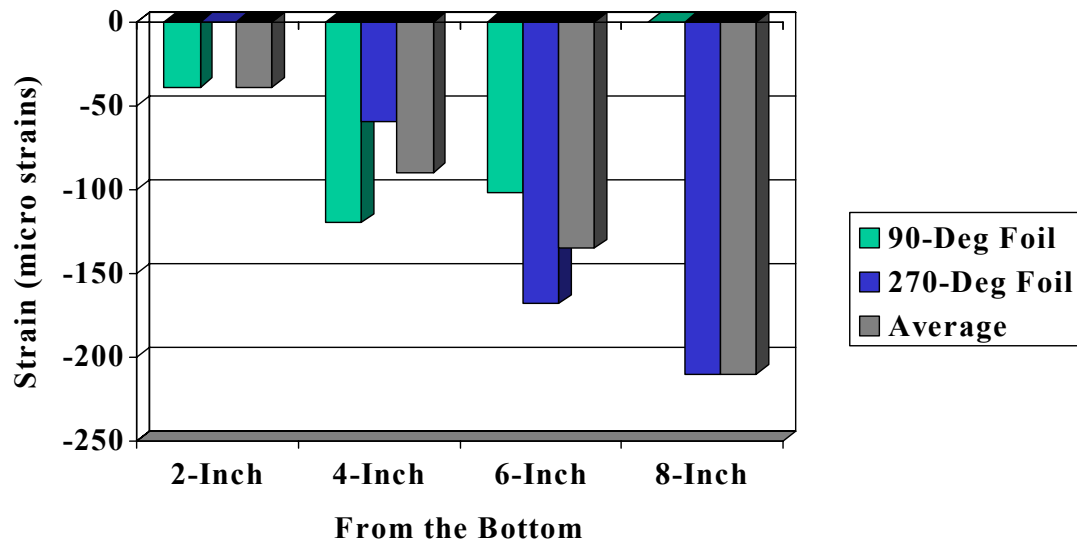


Figure B-74 Adjusted Concrete Strains, Test 20

**Table B.12 Statistical Analysis of Steel Strains for Test 20**

Test 19 Steel Strains (NO DATA)						
Position		1-Inch	3-Inch	5-Inch	7-Inch	9-Inch
0-Deg	Gage	SS-01	SS-03	SS-05	SS-07	SS-09
	Value	N/A	N/A	N/A	N/A	N/A
180-Deg	Gage	SS-02	SS-04	SS-06	SS-08	SS-10
	Value	N/A	N/A	N/A	N/A	N/A
Average		N/A	N/A	N/A	N/A	N/A

Test 20 Steel Strains						
Position		1-Inch	3-Inch	5-Inch	7-Inch	9-Inch
0-Deg	Gage	SS-01	SS-03	SS-05	SS-07	SS-09
	Value	770	716	590	360	165
180-Deg	Gage	SS-02	SS-04	SS-06	SS-08	SS-10
	Value	1,000	745	550	352	180
Average		885	731	570	356	173

Average Steel Strains for Tests 19 and 20						
Position		1-Inch	3-Inch	5-Inch	7-Inch	9-Inch
Test 19		N/A	N/A	N/A	N/A	N/A
Test 20		885	731	570	356	173
n		2	2	2	2	2
High		1,000	745	590	360	180
Low		770	716	550	352	165
Extreme Spread		230	29	40	8	15
Average		N/A	N/A	N/A	N/A	N/A
Variance		N/A	N/A	N/A	N/A	N/A
Standard Deviation		N/A	N/A	N/A	N/A	N/A
Coefficient of Variation		N/A	N/A	N/A	N/A	N/A

**Table B.13 Statistical Analysis of Concrete Strains for Test 20**

Test 19 Adjusted Concrete Strains (no data)					
Position		2-Inch	4-Inch	6-Inch	8-Inch
90-Deg	Gage	CS-01	CS-03	CS-05	CS-07
	Value				
	Gage	FO-01	FO-03	FO-05	FO-07
	Value				
270-Deg	Gage	CS-02	CS-04	CS-06	CS-08
	Value				
	Gage	FO-02	FO-04	FO-06	FO-08
	Value				
Average					

Test 20 Adjusted Concrete Strains					
Position		2-Inch	4-Inch	6-Inch	8-Inch
90-Deg	Gage	CS-01	CS-03	CS-05	CS-07
	Value	-39	-120	-102	
	Gage				
	Value				
270-Deg	Gage	CS-02	CS-04	CS-06	CS-08
	Value		-60	-168	-210
	Gage				
	Value				
Average		-39.0	-90.0	-135.0	-210.0

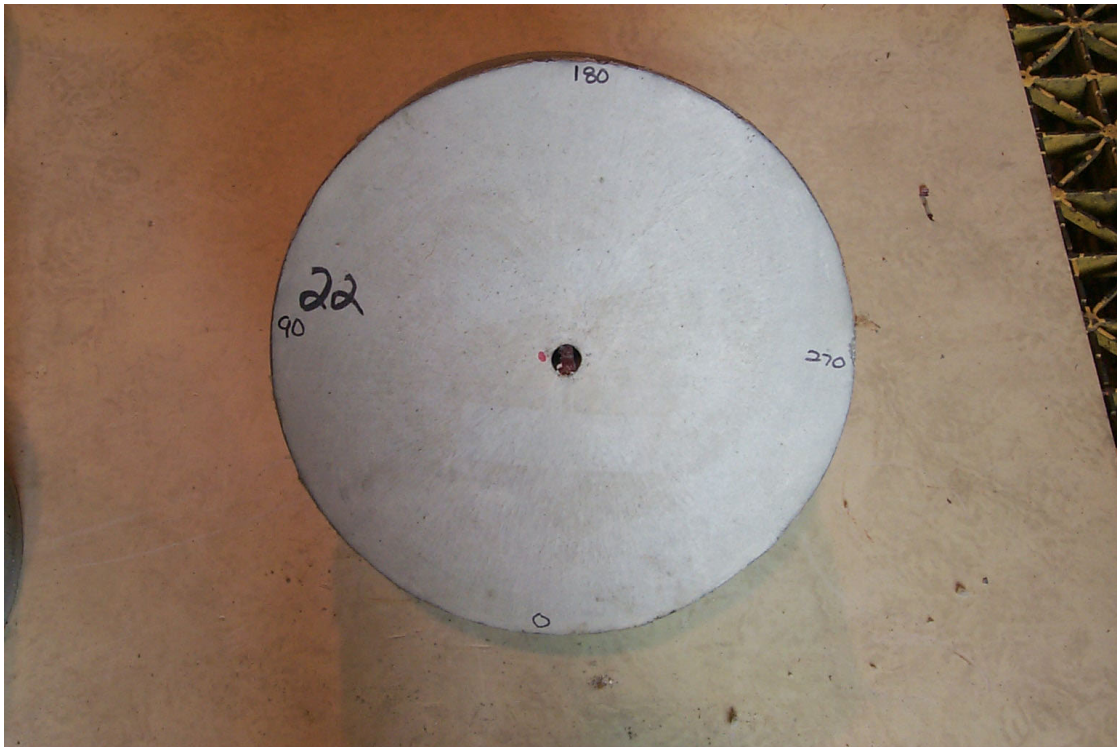


**Figure B-75 Test Specimen 22, Post Test**



**Figure B-76 Test Specimen 22, Post Test**



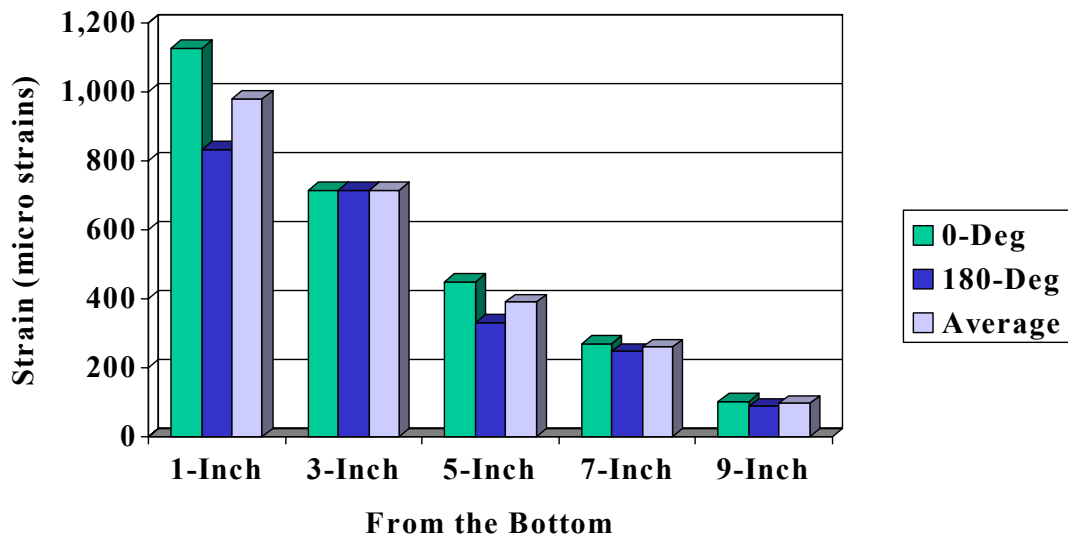


Figure B-77 Adjusted Steel Strains, Test 22

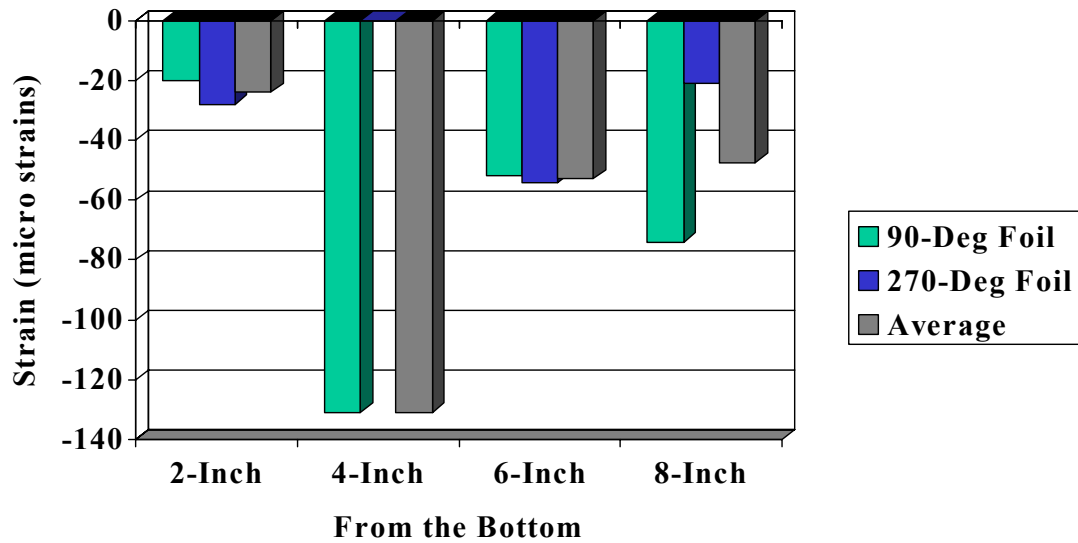


Figure B-78 Adjusted Concrete Strains, Test 22

**Table B.14 Statistical Analysis of Steel Strains for Test 22**

Test 21 Steel Strains (Bond broke before test)						
Position		1-Inch	3-Inch	5-Inch	7-Inch	9-Inch
0-Deg	Gage	SS-01	SS-03	SS-05	SS-07	SS-09
	Value	N/A	N/A	N/A	N/A	N/A
180-Deg	Gage	SS-02	SS-04	SS-06	SS-08	SS-10
	Value	40	125	153	290	412
Average		N/A	N/A	N/A	N/A	N/A

Test 22 Steel Strains						
Position		1-Inch	3-Inch	5-Inch	7-Inch	9-Inch
0-Deg	Gage	SS-01	SS-03	SS-05	SS-07	SS-09
	Value	1,126	714	450	269	103
180-Deg	Gage	SS-02	SS-04	SS-06	SS-08	SS-10
	Value	833	715	331	248	89
Average		980	715	391	259	96

Average Steel Strains for Tests 21 and 22						
Position		1-Inch	3-Inch	5-Inch	7-Inch	9-Inch
Test 21		N/A	N/A	N/A	N/A	N/A
Test 22		980	715	391	259	96
Test		0	0	0	0	0
n		2	2	2	2	2
High		1,126	7,500	2,060	1,420	560
Low		833	715	450	269	103
Extreme Spread		293	714	331	248	89
Average		980	715	391	259	96
Variance		N/A	N/A	N/A	N/A	N/A
Standard Deviation		N/A	N/A	N/A	N/A	N/A
Coefficient of Variation		N/A	N/A	N/A	N/A	N/A



**Table B.14 Statistical Analysis of Concrete Strains for Test 22**

Test 21 Adjusted Concrete Strains					
Position		2-Inch	4-Inch	6-Inch	8-Inch
90-Deg	Gage	CS-01	CS-03	CS-05	CS-07
	Value				
	Gage				
	Value				
270-Deg	Gage	CS-02	CS-04	CS-06	CS-08
	Value				
	Gage				
	Value				
Average					

Test 22 Adjusted Concrete Strains					
Position		2-Inch	4-Inch	6-Inch	8-Inch
90-Deg	Gage	CS-01	CS-03	CS-05	CS-07
	Value	-20	-131	-52	-74
	Gage				
	Value				
270-Deg	Gage	CS-02	CS-04	CS-06	CS-08
	Value	-28		-54	-21
	Gage				
	Value				
Average		-24.0	-131.0	-53.0	-47.5

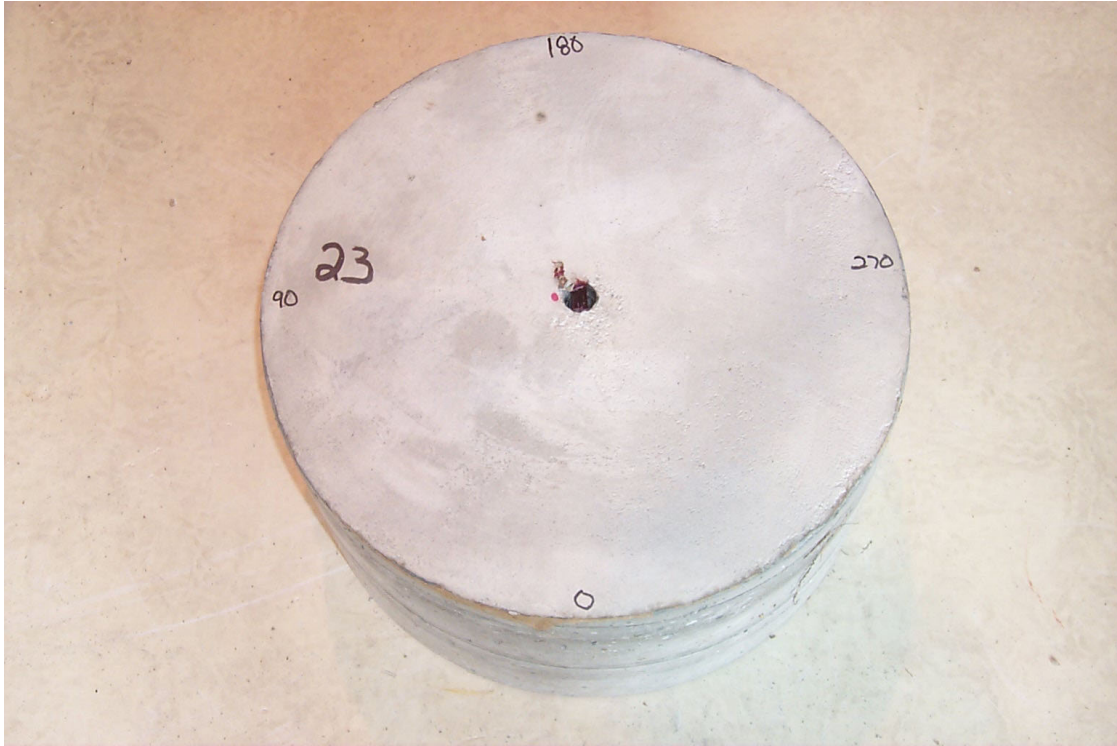


**Figure B-79 Test Specimen 23, Post Test**

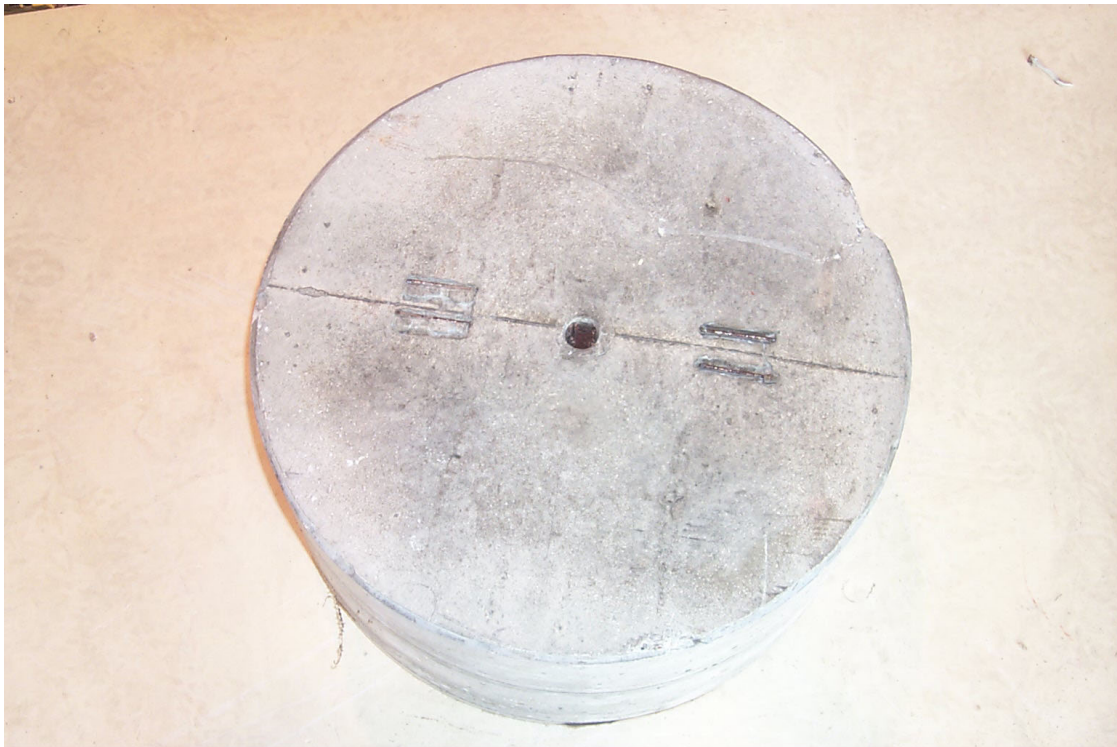


**Figure B-80 Test Specimen 23, Post Test**

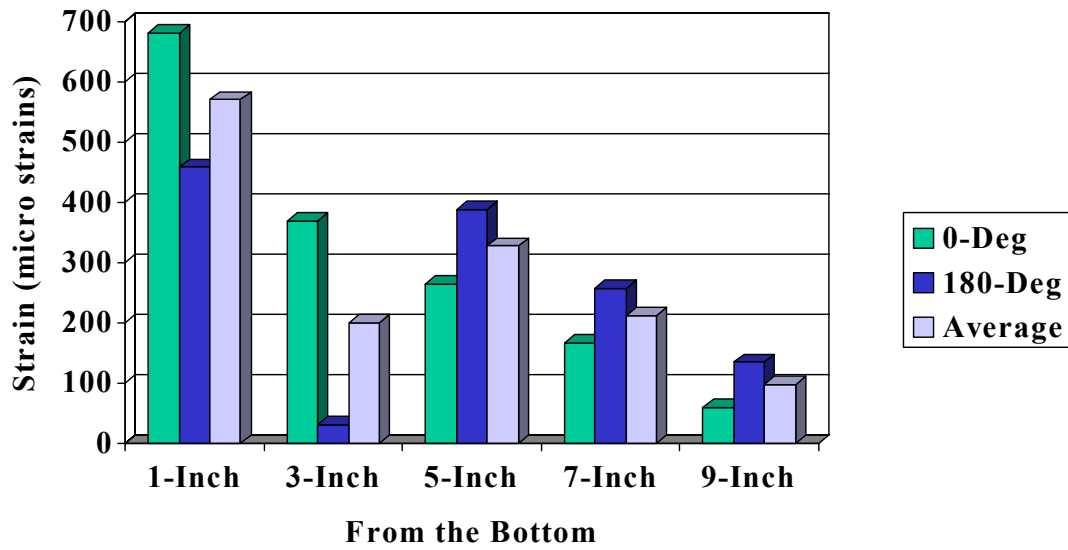


Figure B-81 Adjusted Steel Strains, Test 23

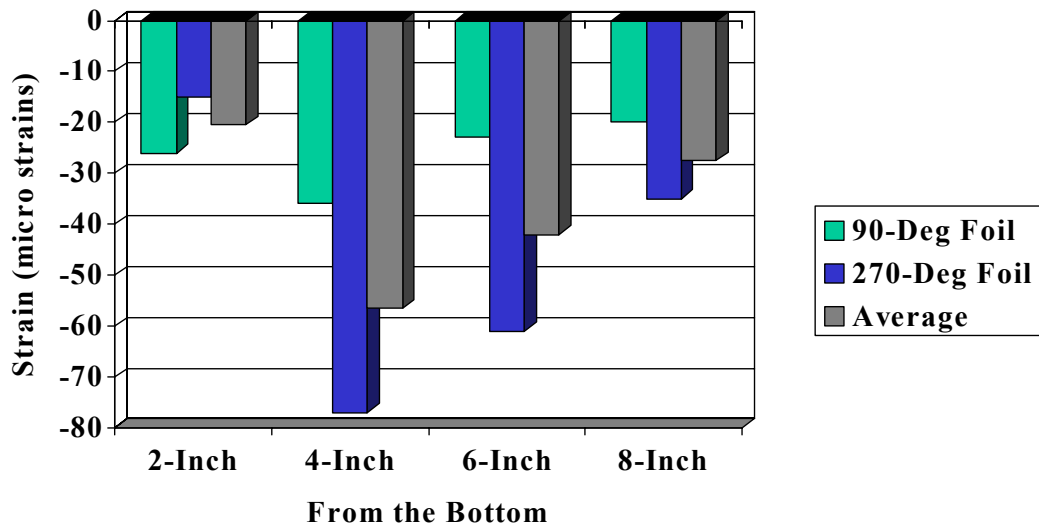
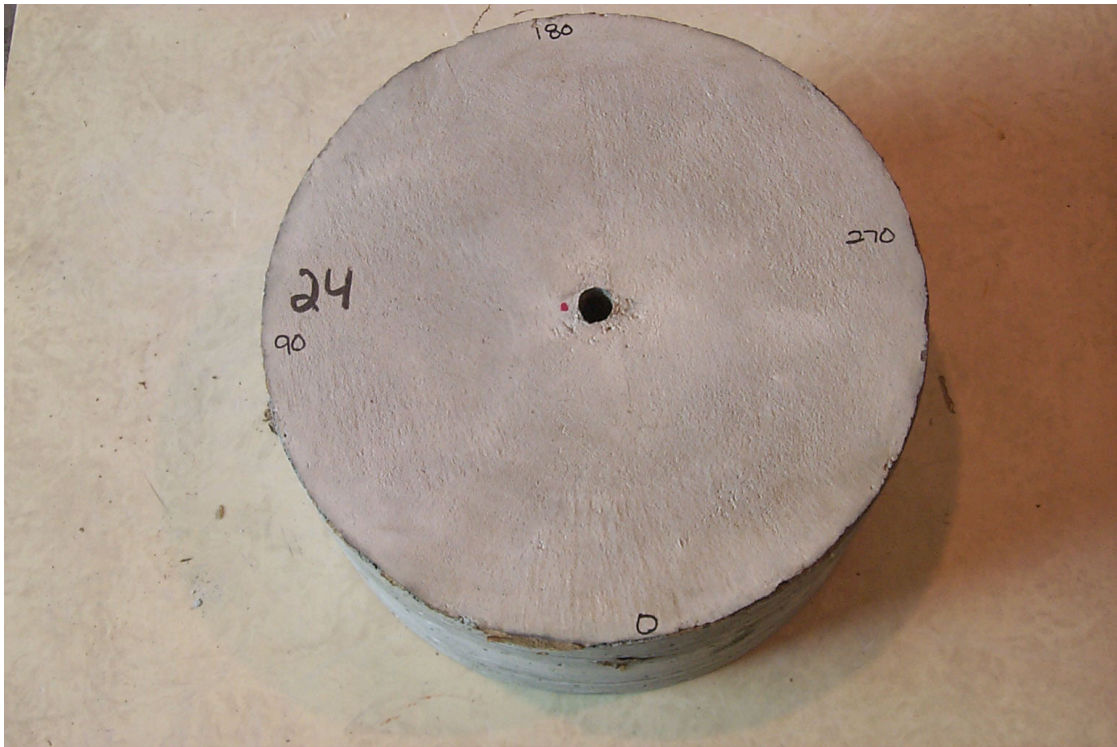


Figure B-82 Adjusted Concrete Strains, Test 23



**Figure B-83 Test Specimen 24, Post Test**



**Figure B-84 Test Specimen 24, Post Test**

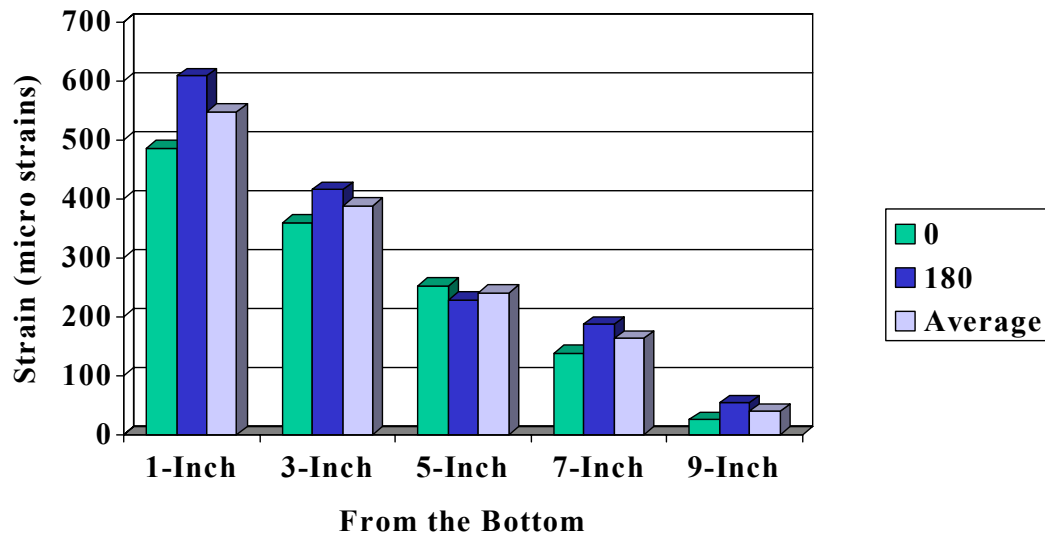


Figure B-85 Adjusted Steel Strains, Test 24

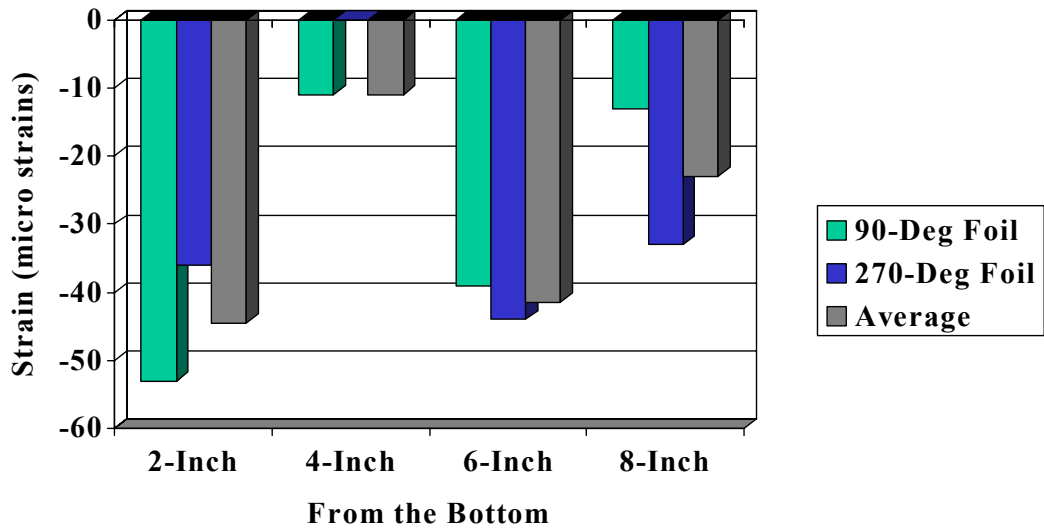


Figure B-86 Adjusted Concrete Strains, Test 24

**Table B.15 Statistical Analysis of Steel Strains for Tests 23 and 24**

Test 23 Adjusted Steel Strains						
Position		1-Inch	3-Inch	5-Inch	7-Inch	9-Inch
0-Deg	Gage	SS-01	SS-03	SS-05	SS-07	SS-09
	Value	681	369	265	167	60
180-Deg	Gage	SS-02	SS-04	SS-06	SS-08	SS-10
	Value	458	N/A	388	257	135
Average		570	369	327	212	98

Test 24 Adjusted Steel Strains						
Position		1-Inch	3-Inch	5-Inch	7-Inch	9-Inch
0-Deg	Gage	SS-01	SS-03	SS-05	SS-07	SS-09
	Value	485	360	252	138	25
180-Deg	Gage	SS-02	SS-04	SS-06	SS-08	SS-10
	Value	608	415	229	187	54
Average		547	388	241	163	40

Average Adjusted Steel Strains for Tests 23 and 24						
Position		1-Inch	3-Inch	5-Inch	7-Inch	9-Inch
Test 23		570	369	327	212	98
Test 24		547	388	241	163	40
n		4	3	4	4	4
High		681	415	388	257	135
Low		458	360	229	138	25
Extreme Spread		223	55	159	119	110
Average		558	381	284	187	69
Variance		10,986	870	5,075	2,567	2,199
Standard Deviation		105	30	71	51	47
Coefficient of Variation		19	8	25	27	68

**Table B.16 Statistical Analysis of Concrete Strains for Tests 23 and 24**

Test 23 Adjusted Concrete Strains					
Position		2-Inch	4-Inch	6-Inch	8-Inch
90-Deg	Gage	CS-01	CS-03	CS-05	CS-07
	Value	-26	-36	-23	-20
	Gage				
	Value				
270-Deg	Gage	CS-02	CS-04	CS-06	CS-08
	Value	-15	-77	-61	-35
	Gage				
	Value				
Average		-20.5	-56.5	-42.0	-27.5
Test 24 Adjusted Concrete Strains					
Position		2-Inch	4-Inch	6-Inch	8-Inch
90-Deg	Gage	CS-01	CS-03	CS-05	CS-07
	Value	-53	-11	-39	-13
	Gage				
	Value				
270-Deg	Gage	CS-02	CS-04	CS-06	CS-08
	Value	-36		-44	-33
	Gage				
	Value				
Average		-44.5	-11.0	-41.5	-23.0

Average Fiber-Optic and Foil Concrete Strains for Tests 23 and 24				
Position	2-Inch	4-Inch	6-Inch	8-Inch
Test 23	-20.5	-56.5	-42.0	-27.5
Test 24	-44.5	-11.0	-41.5	-23.0
Average	-32.5	-41.3	-41.8	-25.3
n	4	3	4	4
High	-15.0	-11.0	-23.0	-13.0
Low	-53.0	-77.0	-61.0	-35.0
Extreme Spread	38.0	66.0	38.0	22.0
Variance	260.3	1110.3	244.9	110.9
Standard Deviation	16.1	33.3	15.6	10.5
Coefficient of Variation	-49.6	-80.6	-37.5	-41.7





**Figure B-87 Test Specimen 25, Post Test**



**Figure B-88 Test Specimen 25, Post Test**



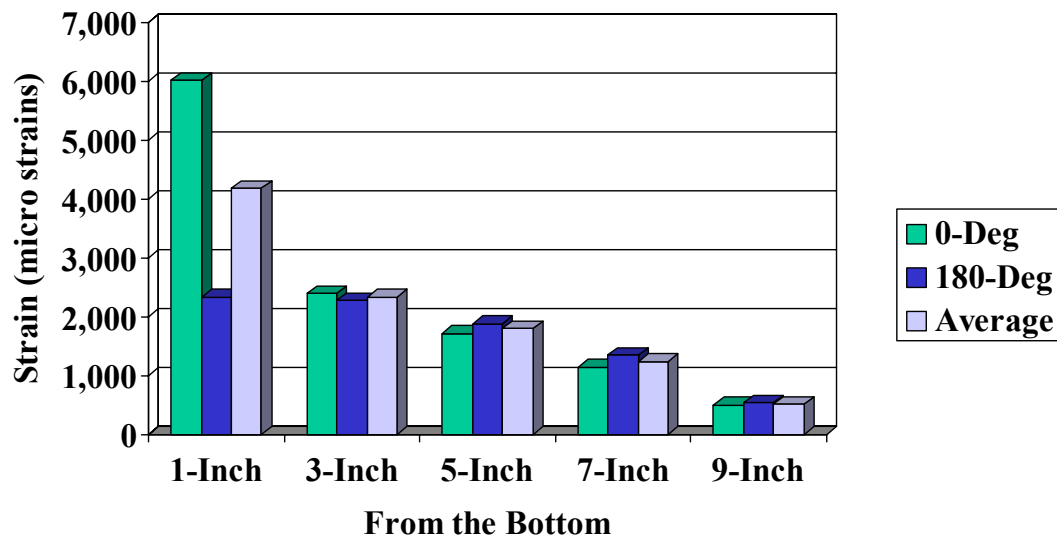


Figure B-89 Adjusted Steel Strains, Test 25

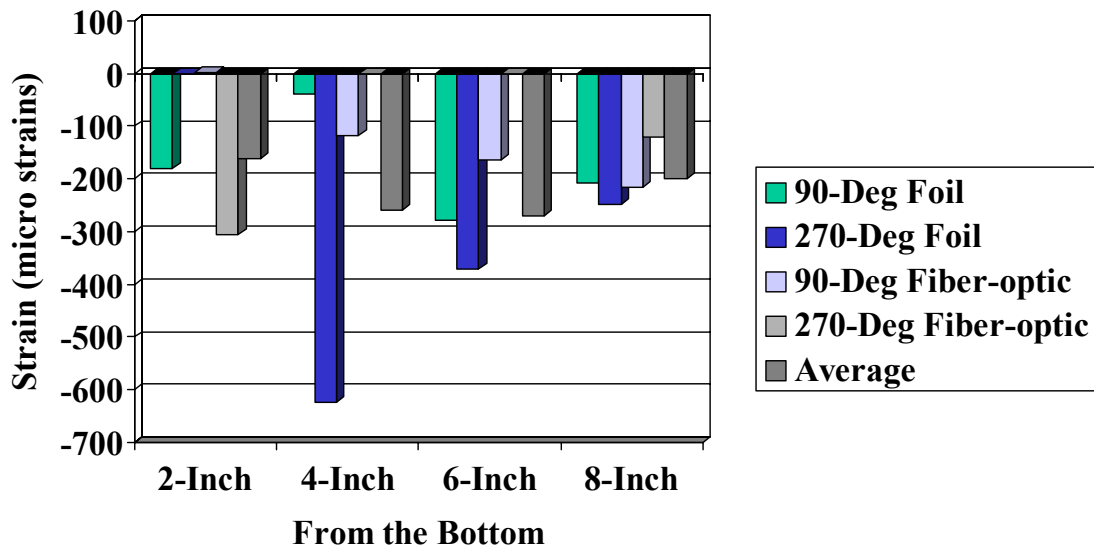
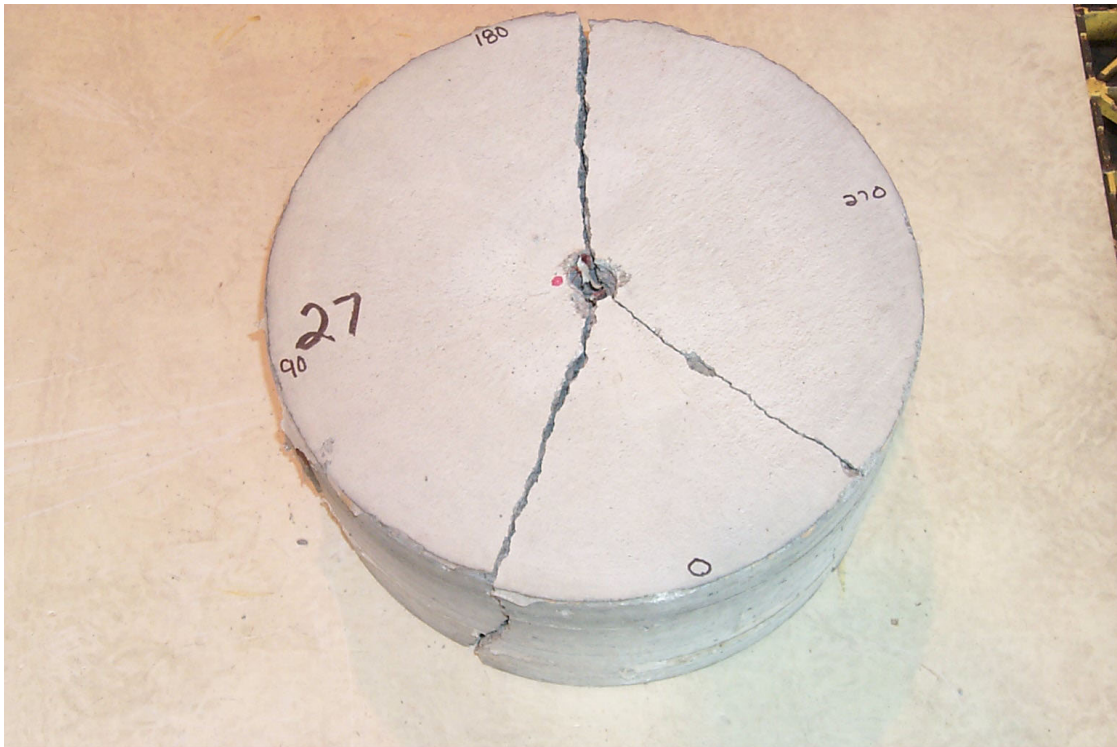


Figure B-90 Adjusted Concrete Strains, Test 25



**Figure B-91 Test Specimen 27 Post Test**



**Figure B-92 Test Specimen 27, Post Test**

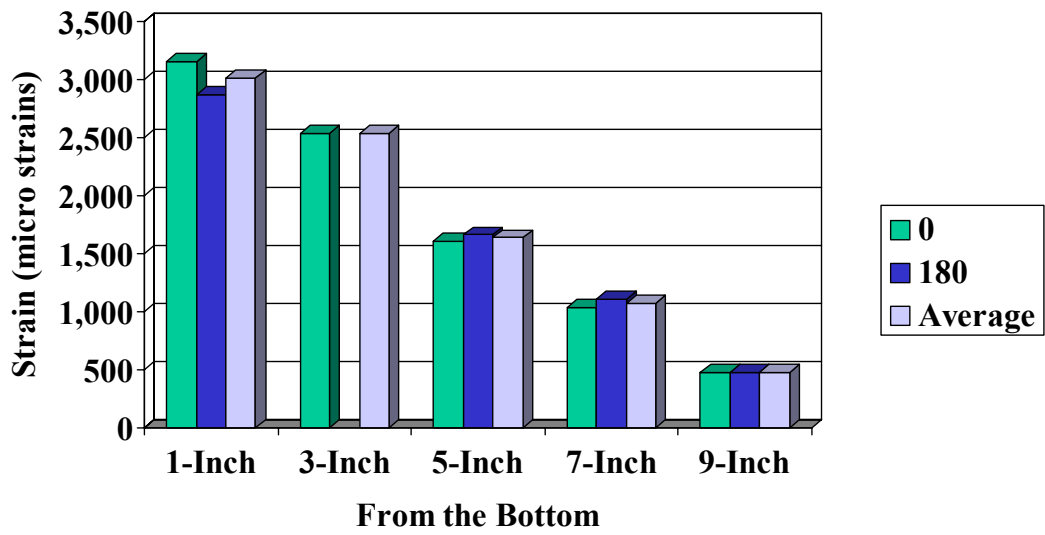


Figure B-93 Adjusted Steel Strains, Test 27

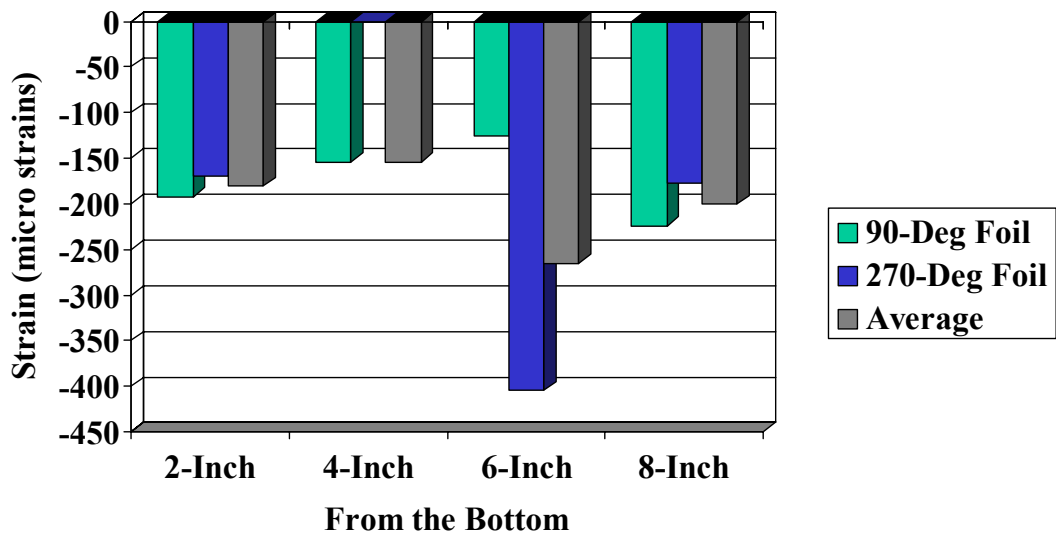


Figure B-94 Adjusted Concrete Strains, Test 27

**Table B.17 Statistical Analysis of Steel Strains for Tests 25 and 27**

Test 25 Adjusted Steel Strains						
Position		1-Inch	3-Inch	5-Inch	7-Inch	9-Inch
0-Deg	Gage	SS-01	SS-03	SS-05	SS-07	SS-09
	Value	6,010	2,396	1,714	1,144	505
180-Deg	Gage	SS-02	SS-04	SS-06	SS-08	SS-10
	Value	2,340	2,275	1,890	1,345	535
Average		4,175	2,336	1,802	1,245	520

Test 26 Steel Strains (NO DATA)						
Position		1-Inch	3-Inch	5-Inch	7-Inch	9-Inch
0-Deg	Gage	SS-01	SS-03	SS-05	SS-07	SS-09
	Value					
180-Deg	Gage	SS-02	SS-04	SS-06	SS-08	SS-10
	Value					
Average		0	0	0	0	0

Test 27 Adjusted Steel Strains						
Position		1-Inch	3-Inch	5-Inch	7-Inch	9-Inch
0-Deg	Gage	SS-01	SS-03	SS-05	SS-07	SS-09
	Value	3,151	2,537	1,609	1,034	477
180-Deg	Gage	SS-02	SS-04	SS-06	SS-08	SS-10
	Value	2,867	N/A	1,661	1,105	475
Average		3,009	2,537	1,635	1,070	476

Average Steel Strains for Tests 25, 26 and 27						
Position		1-Inch	3-Inch	5-Inch	7-Inch	9-Inch
Test 25		4,175	2,336	1,802	1,245	520
Test 26		0	0	0	0	0
Test 27		3,009	2,537	1,635	1,070	476
n		4	3	4	4	4
High		6,010	2,640	1,910	1,345	682
Low		2,340	2,275	1,714	1,144	505
Extreme Spread		3,670	365	196	201	177
Average		3,592	2,403	1,719	1,157	498
Variance		2,711,445	17,194	14,910	17,782	796
Standard Deviation		1,647	131	122	133	28
Coefficient of Variation		46	5	7	12	6

**Table B.18 Statistical Analysis of Concrete Strains for Tests 25 and 27**

Test 25 Adjusted Concrete Strains					
Position		2-Inch	4-Inch	6-Inch	8-Inch
90-Deg	Gage	CS-01	CS-03	CS-05	CS-07
	Value	-180	-38	-278	-207
	Gage	FO-01	FO-03	FO-05	FO-07
	Value	2.3	-118.4	-164.8	-215.8
270-Deg	Gage	CS-02	CS-04	CS-06	CS-08
	Value		-624	-370	-249
	Gage	FO-02	FO-04	FO-06	FO-08
	Value	-304.7			-121.5
Average		-160.8	-260.1	-270.9	-198.3
Test 26 Adjusted Concrete Strains (no data)					
Position		2-Inch	4-Inch	6-Inch	8-Inch
90-Deg	Gage	CS-01	CS-03	CS-05	CS-07
	Value				
	Gage	FO-01	FO-03	FO-05	FO-07
	Value				
270-Deg	Gage	CS-02	CS-04	CS-06	CS-08
	Value				
	Gage	FO-02	FO-04	FO-06	FO-08
	Value				
Average					
Test 27 Adjusted Concrete Strains					
Position		2-Inch	4-Inch	6-Inch	8-Inch
90-Deg	Gage	CS-01	CS-03	CS-05	CS-07
	Value	-192	-154	-125	-224
	Gage				
	Value				
270-Deg	Gage	CS-02	CS-04	CS-06	CS-08
	Value	-170		-405	-177
	Gage				
	Value				
Average		-181.0	-154.0	-265.0	-200.5
Average Fiber-Optic and Foil Concrete Strains for Tests 25, 26 and 27					
Position		2-Inch	4-Inch	6-Inch	8-Inch
Test 25		-160.8	-260.1	-270.9	-198.3
Test 26					
Test 27		-181.0	-154.0	-265.0	-200.5
Average		-168.9	-233.6	-268.6	-199.0
n		5	4	5	6
High		2.3	-38.0	-125.0	-121.5
Low		-304.7	-624.0	-405.0	-249.0
Extreme Spread		307.0	586.0	280.0	127.5
Variance		12101.7	70094.2	15092.5	1993.5
Standard Deviation		110.0	264.8	122.9	44.6
Coefficient of Variation		-65.1	-113.3	-45.7	-22.4



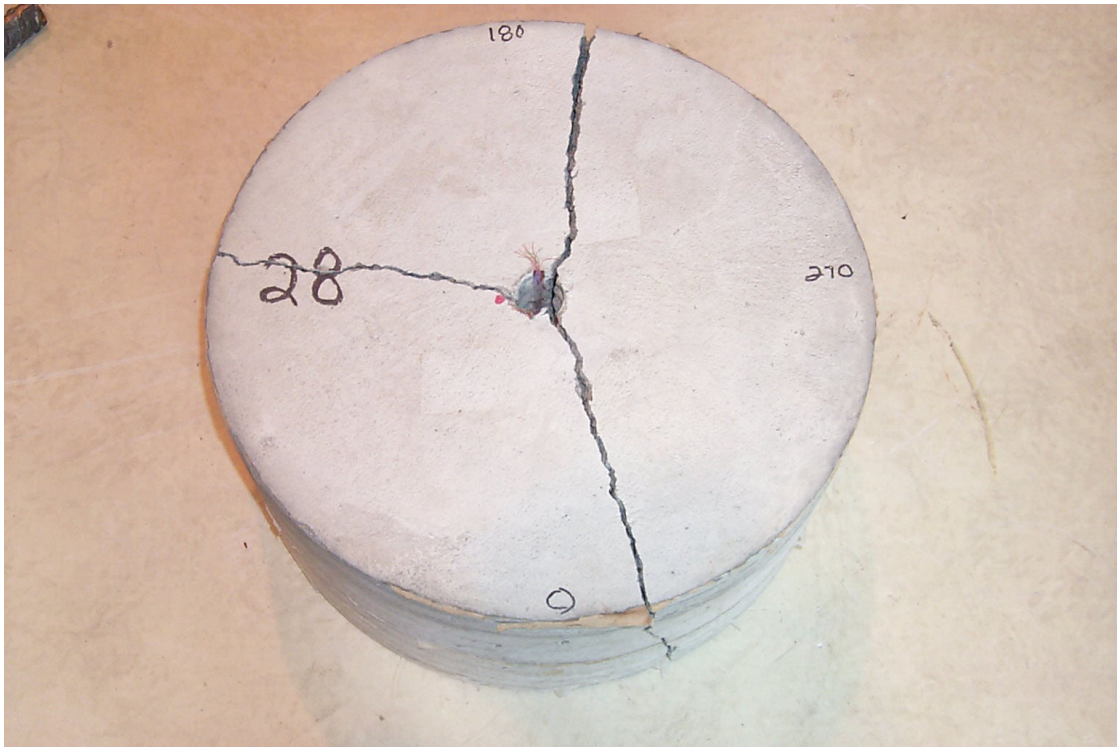


**Figure B-95 Test Specimen 28, Post Test**

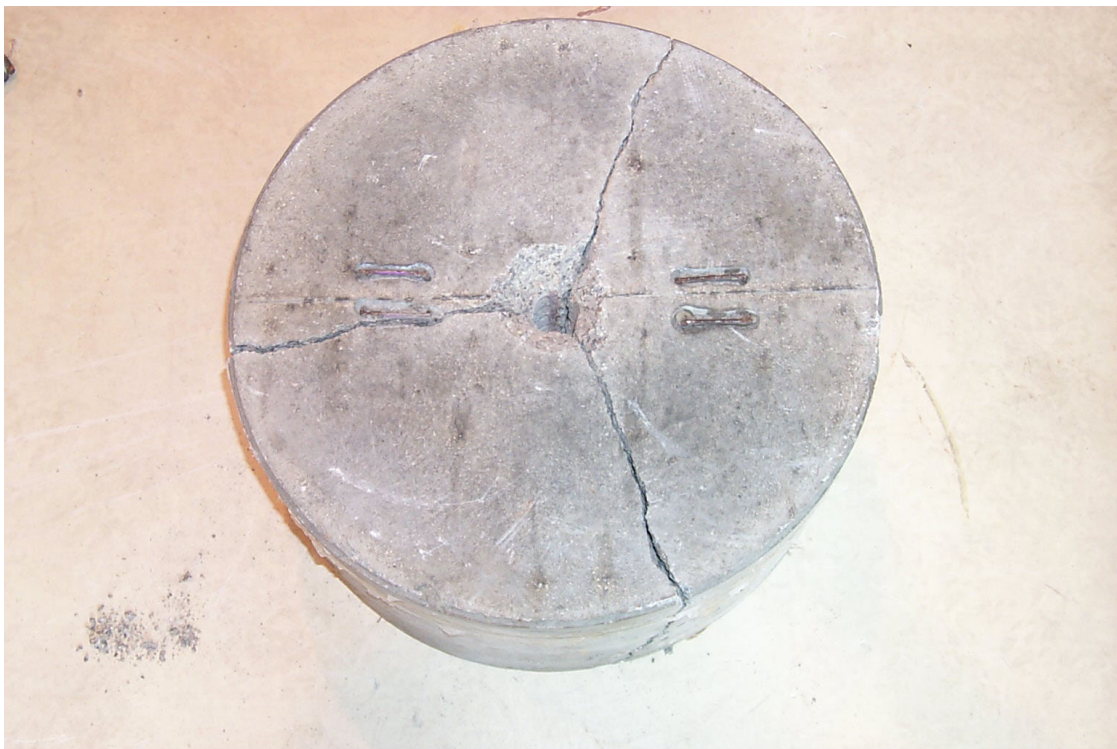


**Figure B-96 Test Specimen 28, Post Test**

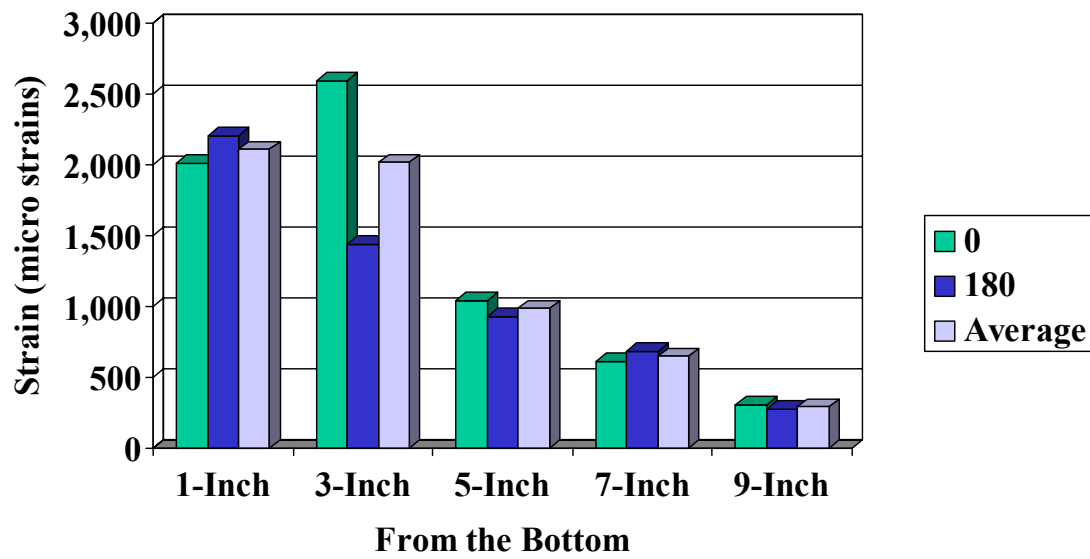


Figure B-97 Adjusted Steel Strains, Test 28

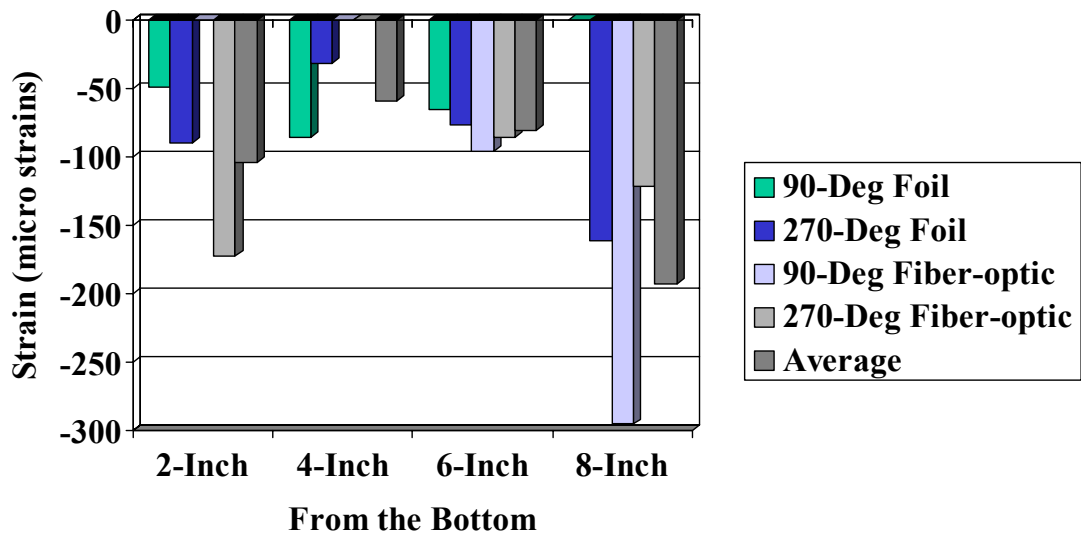
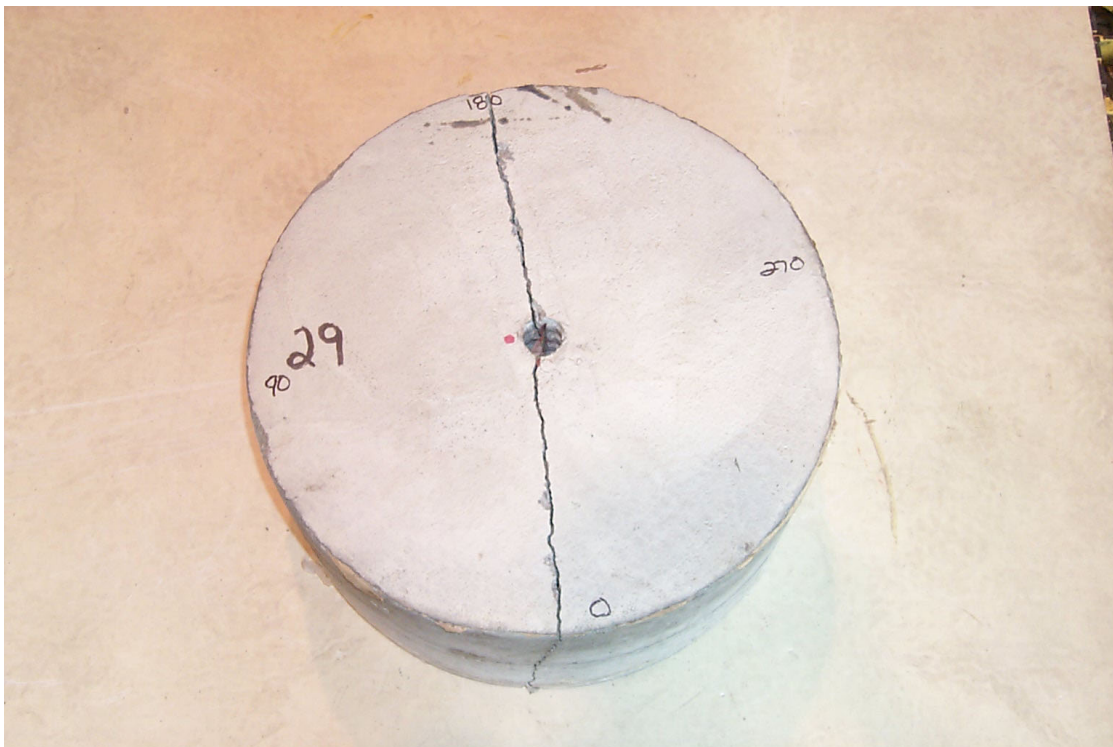


Figure B-98 Adjusted Concrete Strains, Test 28



**Figure B-99 Test Specimen 29, Post Test**



**Figure B-100 Test Specimen 29, Post Test**



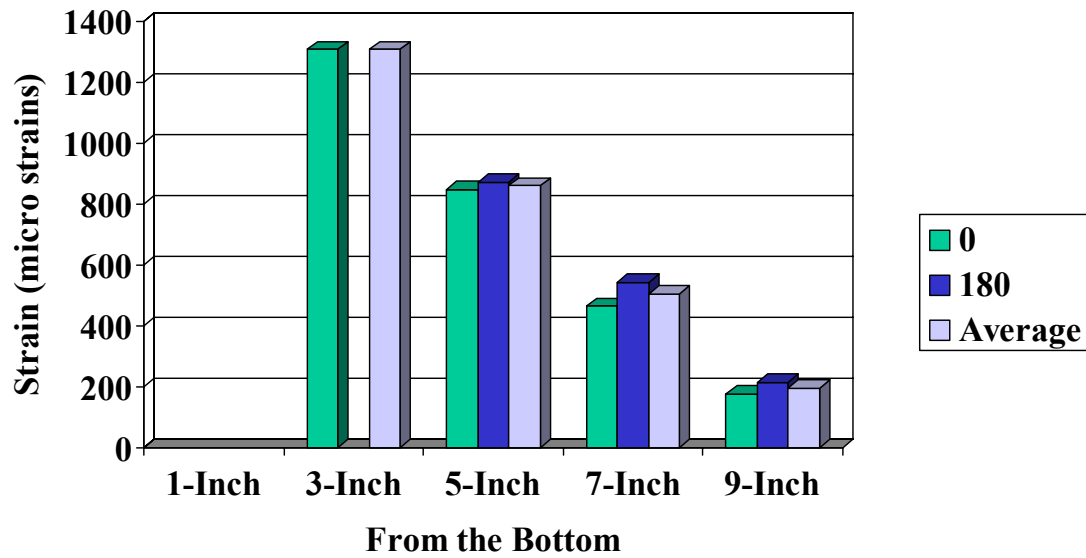


Figure B-101 Adjusted Steel Strains, Test 29

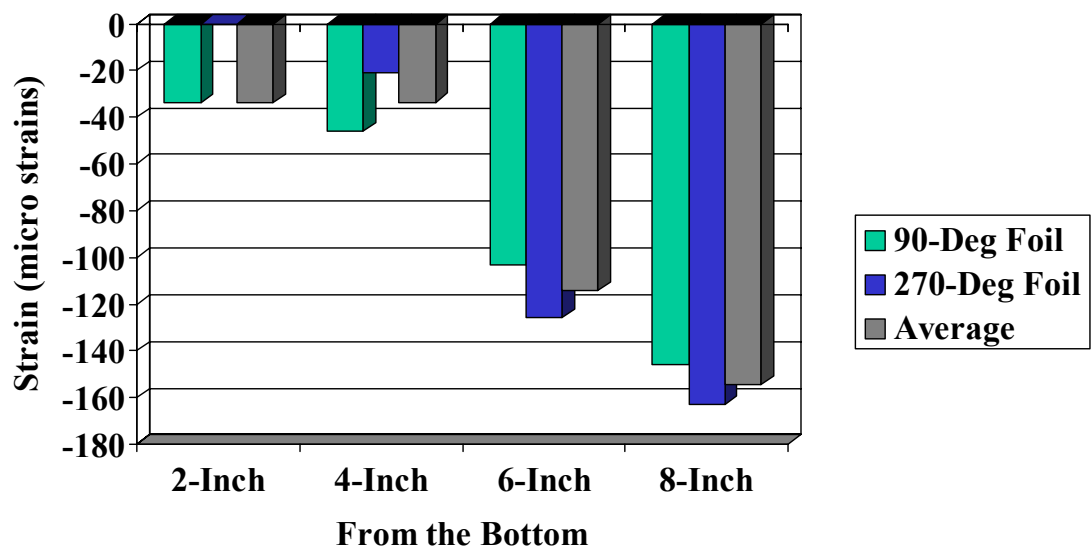
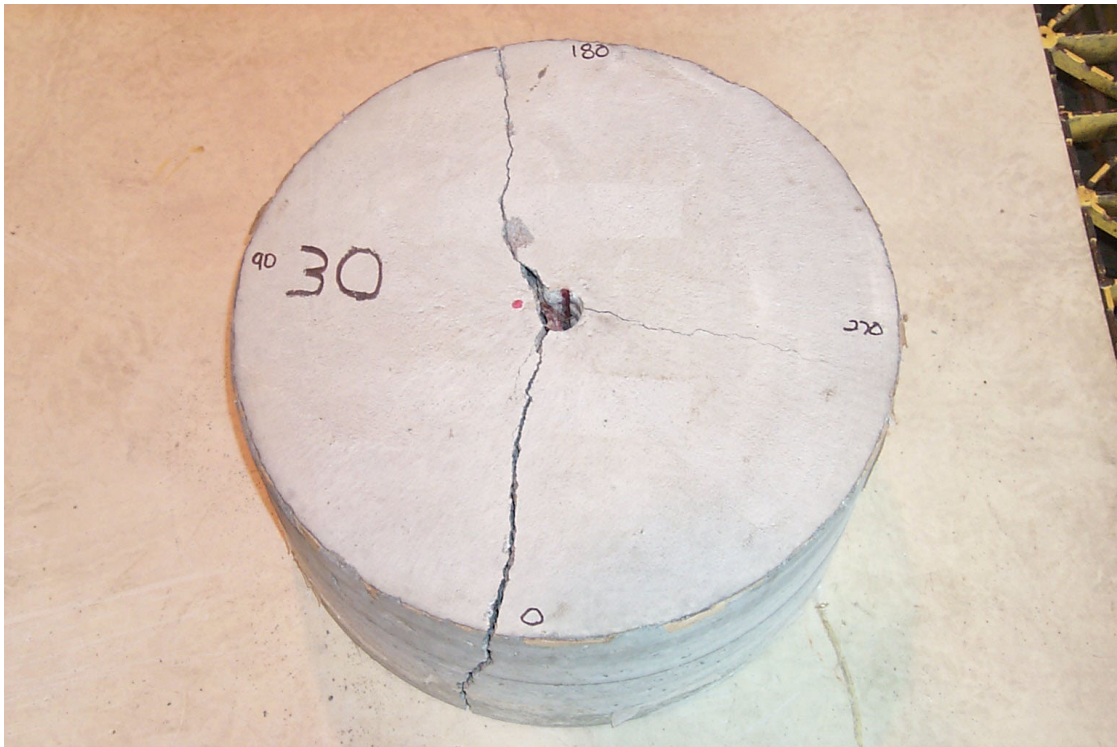
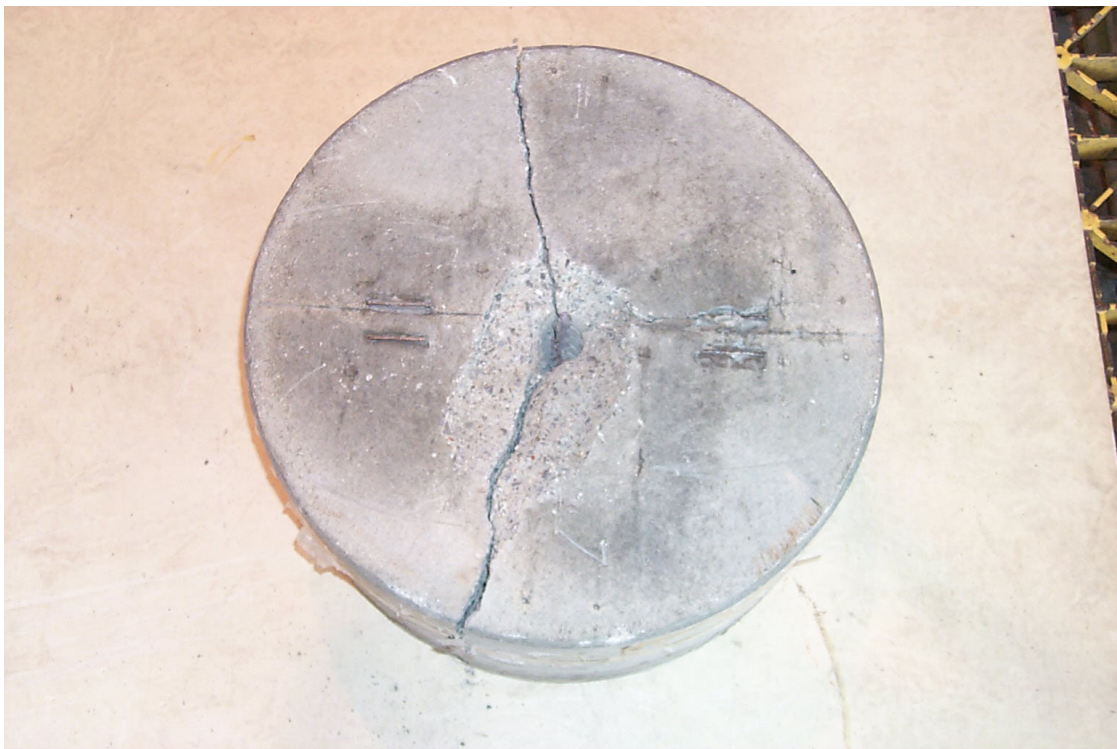


Figure B-102 Adjusted Concrete Strains, Test 29



**Figure B-103 Test Specimen 30, Post Test**



**Figure B-104 Test Specimen 30, Post Test**

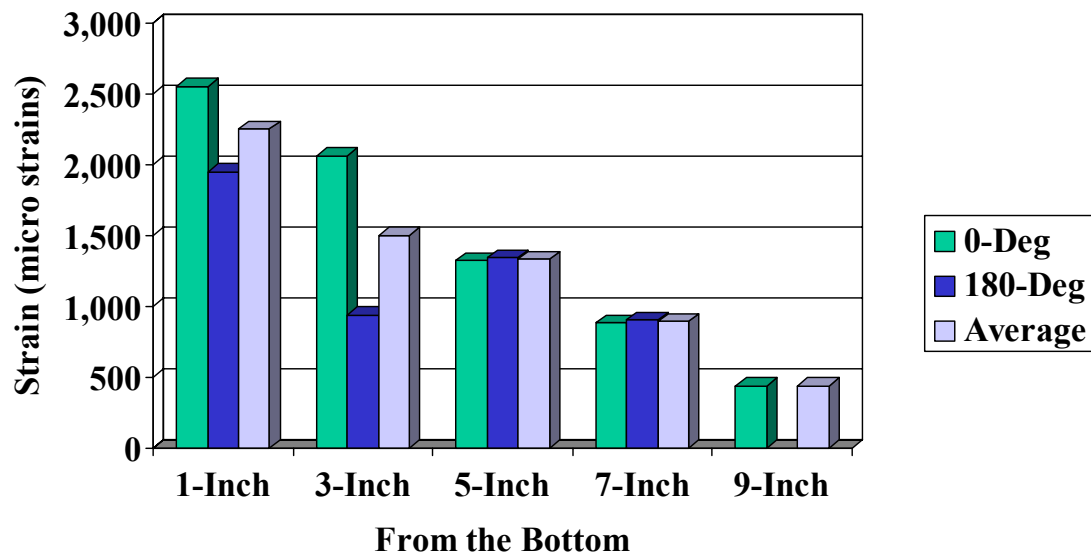


Figure B-105 Adjusted Steel Strains, Test 30

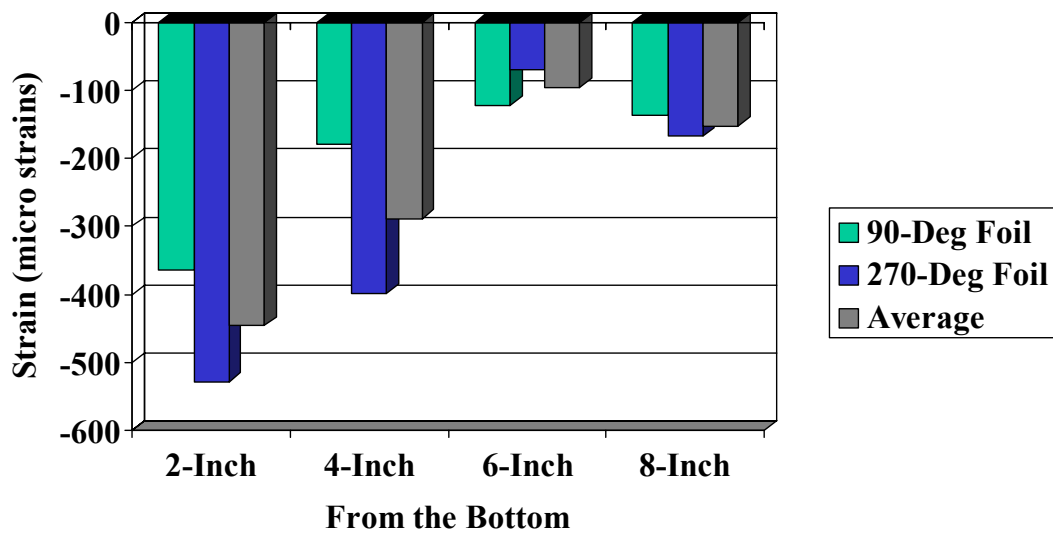


Figure B-106 Adjusted Concrete Strains, Test 30

**Table B.19 Statistical Analysis of Steel Strains for Tests 28, 29 and 30**

Test 28 Adjusted Steel Strains						
Position		1-Inch	3-Inch	5-Inch	7-Inch	9-Inch
0-Deg	Gage	SS-01	SS-03	SS-05	SS-07	SS-09
	Value	2,009	2,590	1,043	614	309
180-Deg	Gage	SS-02	SS-04	SS-06	SS-08	SS-10
	Value	2,202	1,439	929	686	278
Average		2,106	2,015	986	650	294

Test 29 Adjusted Steel Strains						
Position		1-Inch	3-Inch	5-Inch	7-Inch	9-Inch
0-Deg	Gage	SS-01	SS-03	SS-05	SS-07	SS-09
	Value	N/A	1,307	848	465	177
180-Deg	Gage	SS-02	SS-04	SS-06	SS-08	SS-10
	Value	N/A	N/A	872	543	216
Average		N/A	1,307	860	504	197

Test 30 Adjusted Steel Strains						
Position		1-Inch	3-Inch	5-Inch	7-Inch	9-Inch
0-Deg	Gage	SS-01	SS-03	SS-05	SS-07	SS-09
	Value	2,550	2,060	1,320	885	443
180-Deg	Gage	SS-02	SS-04	SS-06	SS-08	SS-10
	Value	1,950	937	1,340	902	N/A
Average		2,250	1,499	1,330	894	443

Average Adjusted Steel Strains for Tests 28, 29 and 30						
Position		1-Inch	3-Inch	5-Inch	7-Inch	9-Inch
Test 28		2,106	2,015	986	650	294
Test 29		N/A	1,307	860	504	197
Test 30		2,250	1,499	1,330	894	443
n		4	5	6	6	5
High		2,550	2,590	1,340	902	443
Low		1,950	937	848	465	177
Extreme Spread		600	1,653	492	437	266
Average		2,178	1,667	1,059	683	285
Variance		73,168	430,215	48,745	32,132	10,503
Standard Deviation		270	656	221	179	102
Coefficient of Variation		12	39	21	26	36

**Table B.20 Statistical Analysis of Concrete Strains for Tests 28, 29 and 30**

Test 28 Adjusted Concrete Strains					
Position		2-Inch	4-Inch	6-Inch	8-Inch
90-Deg	Gage	CS-01	CS-03	CS-05	CS-07
	Value	-49	-86	-65	
	Gage	FO-01	FO-03	FO-05	FO-07
	Value			-96.1	-295.4
270-Deg	Gage	CS-02	CS-04	CS-06	CS-08
	Value	-90	-32	-77	-161
	Gage	FO-02	FO-04	FO-06	FO-08
	Value	-172.8		-86.1	-121.4
Average		-103.9	-59.0	-81.1	-192.6
Test 29 Adjusted Concrete Strains					
Position		2-Inch	4-Inch	6-Inch	8-Inch
90-Deg	Gage	CS-01	CS-03	CS-05	CS-07
	Value	-34	-46	-103	-146
	Gage				
	Value				
270-Deg	Gage	CS-02	CS-04	CS-06	CS-08
	Value		-21	-126	-163
	Gage				
	Value				
Average		-34.0	-33.5	-114.5	-154.5
Test 30 Adjusted Concrete Strains					
Position		2-Inch	4-Inch	6-Inch	8-Inch
90-Deg	Gage	CS-01	CS-03	CS-05	CS-07
	Value	-364	-180	-122	-137
	Gage				
	Value				
270-Deg	Gage	CS-02	CS-04	CS-06	CS-08
	Value	-528	-398	-69	-168
	Gage				
	Value				
Average		-446.0	-289.0	-95.5	-152.5
Average Fiber-Optic and Foil Concrete Strains for Tests 28, 29 and 30					
Position		2-Inch	4-Inch	6-Inch	8-Inch
Test 28		-103.9	-59.0	-81.1	-192.6
Test 29		-34.0	-33.5	-114.5	-154.5
Test 30		-446.0	-289.0	-95.5	-152.5
Average		-206.3	-127.2	-93.0	-170.2
n		6	6	8	7
High		-34.0	-21.0	-65.0	-121.4
Low		-528.0	-398.0	-126.0	-295.4
Extreme Spread		494.0	377.0	61.0	174.0
Variance		39487.8	20950.6	529.1	3313.6
Standard Deviation		198.7	144.7	23.0	57.6
Coefficient of Variation		-96.3	-113.8	-24.7	-33.8



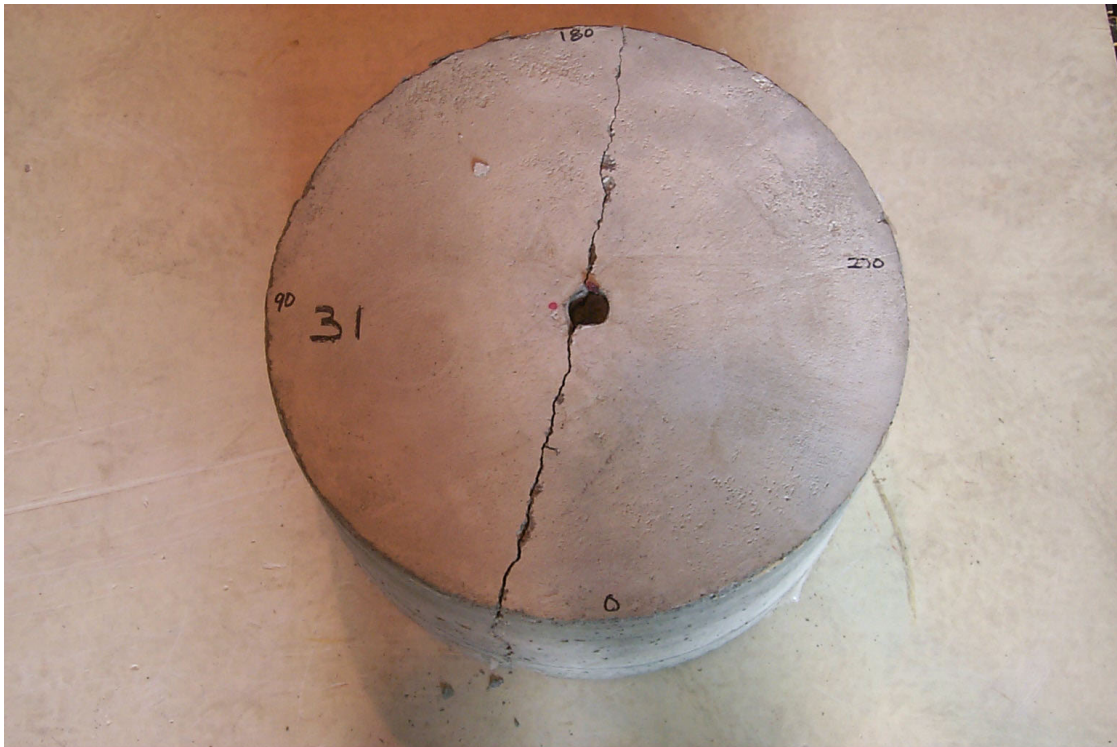


**Figure B-107 Test Specimen 31, Post Test**



**Figure B-108 Test Specimen 31 Post Test**

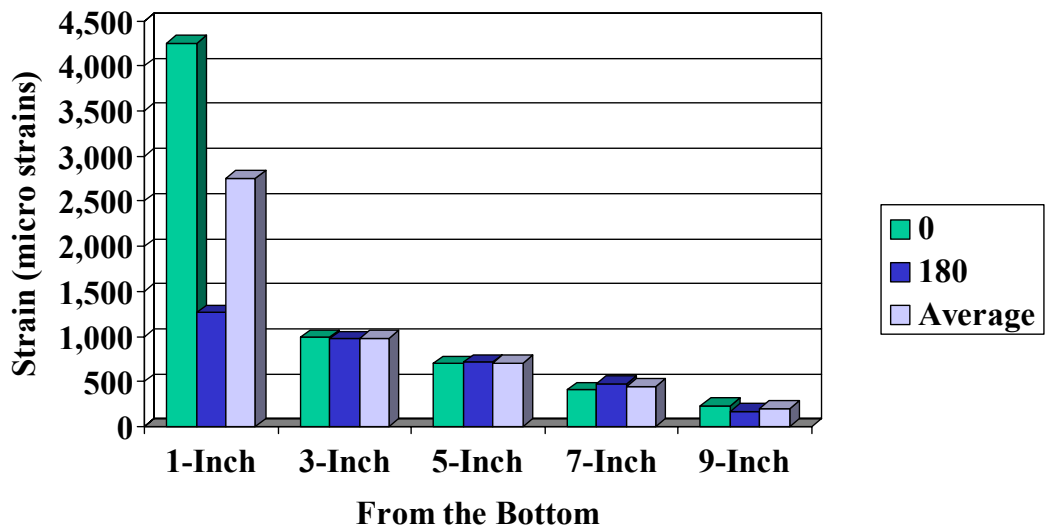


Figure B-109 Adjusted Steel Strains, Test 31

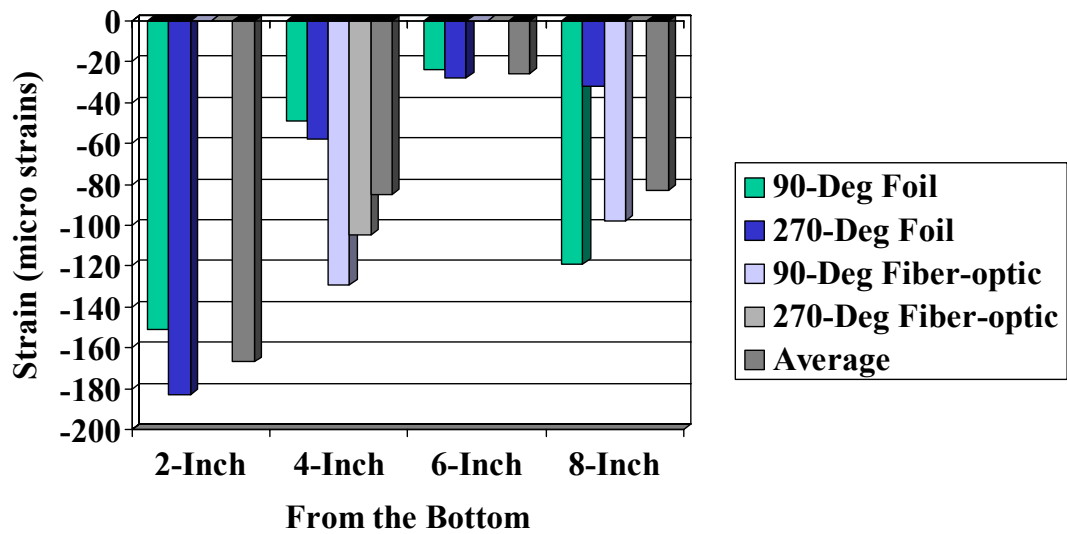


Figure B-110 Adjusted Concrete Strains, Test 31





**Figure B-111 Test Specimen 32, Post Test**



**Figure B-112 Test Specimen 32, Post Test**



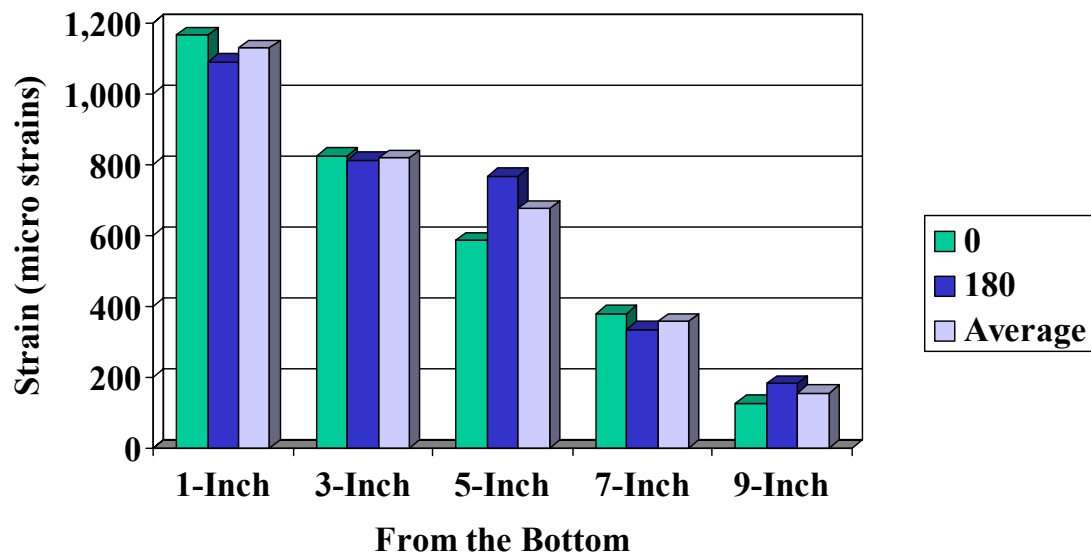


Figure B-113 Adjusted Steel Strains, Test 32

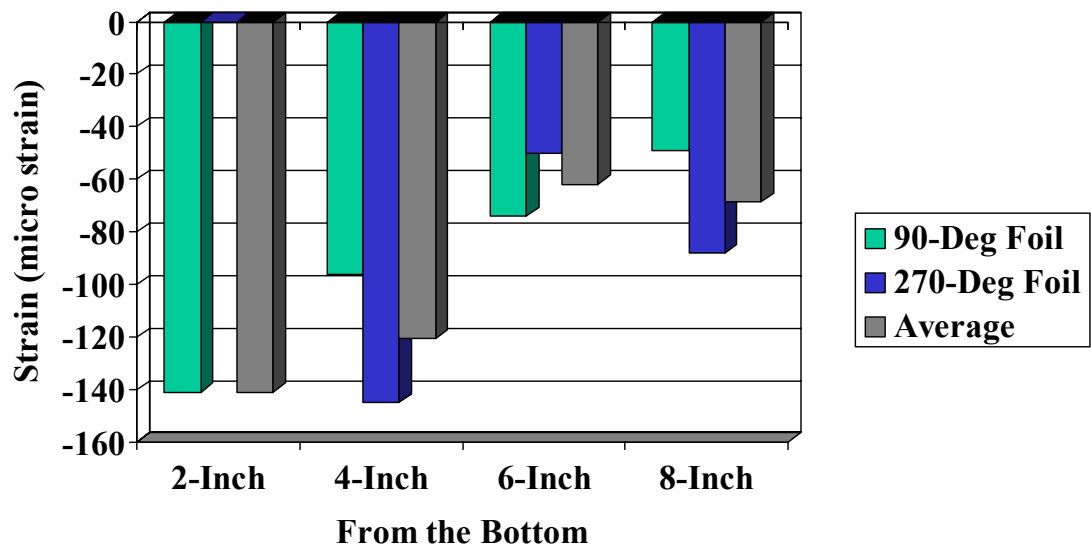
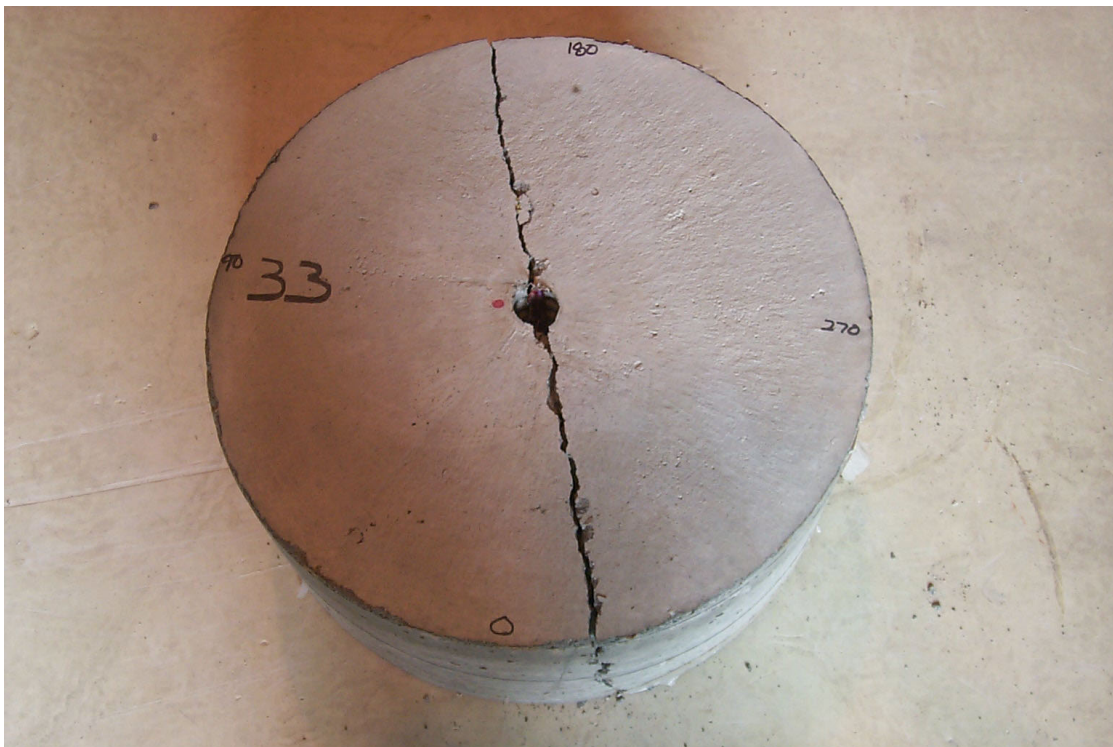


Figure B-114 Adjusted Concrete Strains, Test 32



**Figure B-115 Test Specimen 33, Post Test**



**Figure B-116 Test Specimen 33, Post Test**

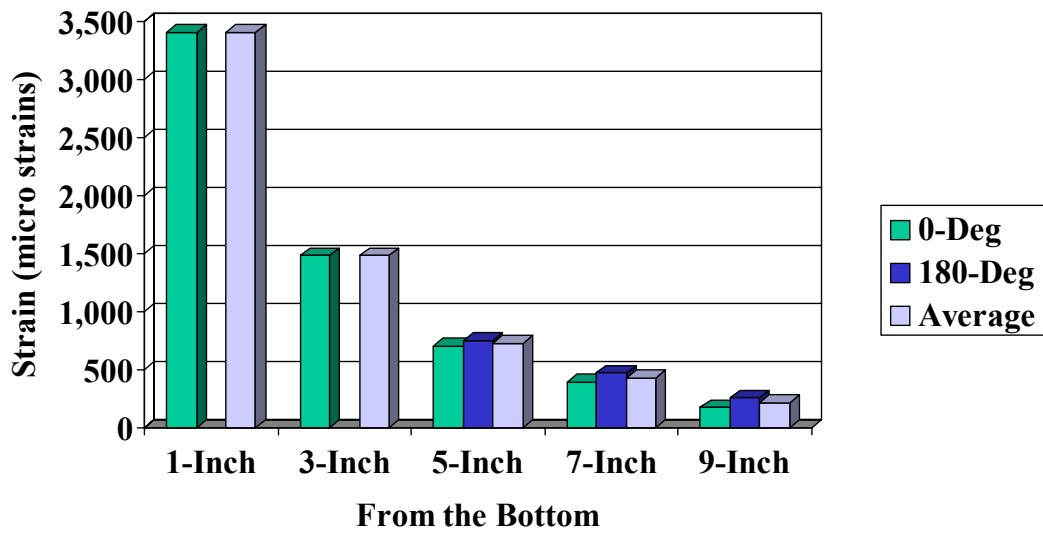


Figure B-117 Adjusted Steel Strains, Test 33

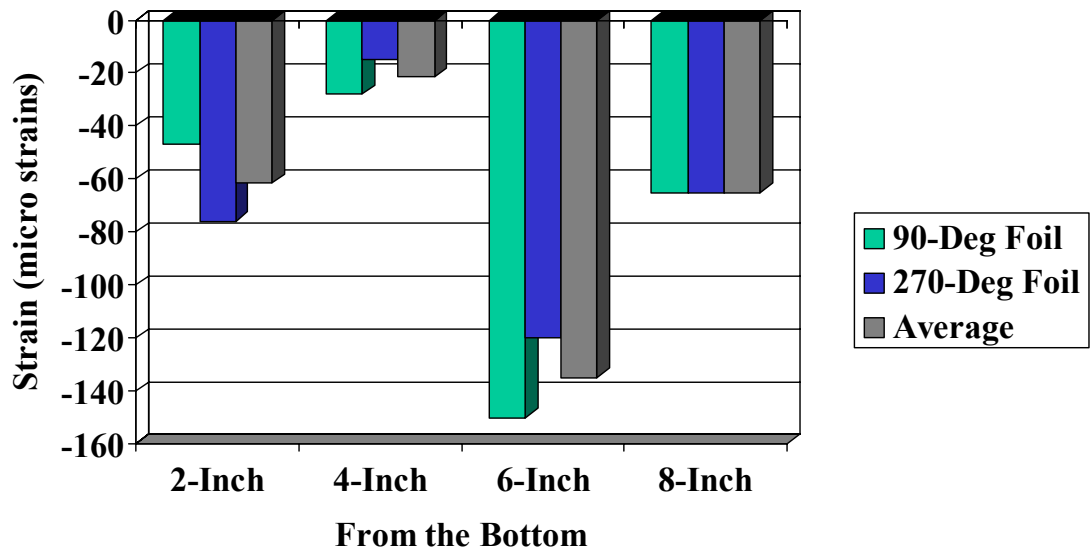


Figure B-118 Adjusted Concrete Strains, Test 33

**Table B.21 Statistical Analysis of Steel Strains for Tests 31, 32 and 33**

Test 31 Adjusted Steel Strains						
Position		1-Inch	3-Inch	5-Inch	7-Inch	9-Inch
0-Deg	Gage	SS-01	SS-03	SS-05	SS-07	SS-09
	Value	4,248	986	699	411	232
180-Deg	Gage	SS-02	SS-04	SS-06	SS-08	SS-10
	Value	1,262	971	712	481	171
Average		2,755	979	706	446	202

Test 32 Adjusted Steel Strains						
Position		1-Inch	3-Inch	5-Inch	7-Inch	9-Inch
0-Deg	Gage	SS-01	SS-03	SS-05	SS-07	SS-09
	Value	1,164	824	585	381	128
180-Deg	Gage	SS-02	SS-04	SS-06	SS-08	SS-10
	Value	1,090	811	767	335	183
Average		1,127	818	676	358	156

Test 33 Adjusted Steel Strains						
Position		1-Inch	3-Inch	5-Inch	7-Inch	9-Inch
0-Deg	Gage	SS-01	SS-03	SS-05	SS-07	SS-09
	Value	3,400	1,480	707	392	175
180-Deg	Gage	SS-02	SS-04	SS-06	SS-08	SS-10
	Value	N/A	N/A	750	470	258
Average		3,400	1,480	729	431	217

Average Adjusted Steel Strains for Tests 31, 32 and 33						
Position		1-Inch	3-Inch	5-Inch	7-Inch	9-Inch
Test 31		2,755	979	706	446	202
Test 32		1,127	818	676	358	156
Test 33		3,400	1,480	729	431	217
n		5	5	6	6	6
High		4,248	1,480	750	470	258
Low		1,090	811	585	335	128
Extreme Spread		3,158	669	165	135	130
Average		2,233	1,014	703	412	191
Variance		2,203,541	74,274	4,068	3,083	2,172
Standard Deviation		1,484	273	64	56	47
Coefficient of Variation		66	27	9	13	24

**Table B.22 Statistical Analysis of Concrete Strains for Tests 31, 32 and 33**

Test 31 Adjusted Concrete Strains					
Position		2-Inch	4-Inch	6-Inch	8-Inch
90-Deg	Gage	CS-01	CS-03	CS-05	CS-07
	Value	-151	-49	-24	-119
	Gage	FO-01	FO-03	FO-05	FO-07
	Value		-129.0		-97.8
270-Deg	Gage	CS-02	CS-04	CS-06	CS-08
	Value	-183	-58	-28	-32
	Gage	FO-02	FO-04	FO-06	FO-08
	Value		-104.8		
Average		-167.0	-85.2	-26.0	-82.9
Test 32 Adjusted Concrete Strains					
Position		2-Inch	4-Inch	6-Inch	8-Inch
90-Deg	Gage	CS-01	CS-03	CS-05	CS-07
	Value	-141	-96	-74	-49
	Gage				
	Value				
270-Deg	Gage	CS-02	CS-04	CS-06	CS-08
	Value		-145	-50	-88
	Gage				
	Value				
Average		-141.0	-120.5	-62.0	-68.5
Test 33 Adjusted Concrete Strains					
Position		2-Inch	4-Inch	6-Inch	8-Inch
90-Deg	Gage	CS-01	CS-03	CS-05	CS-07
	Value	-47	-28	-150	-65
	Gage				
	Value				
270-Deg	Gage	CS-02	CS-04	CS-06	CS-08
	Value	-76	-15	-120	-65
	Gage				
	Value				
Average		-61.5	-21.5	-135.0	-65.0
Average Fiber-Optic and Foil Concrete Strains for Tests 31, 32 and 33					
Position		2-Inch	4-Inch	6-Inch	8-Inch
Test 31		-167.0	-85.2	-26.0	-82.9
Test 32		-141.0	-120.5	-62.0	-68.5
Test 33		-61.5	-21.5	-135.0	-65.0
Average		-119.6	-78.1	-74.3	-73.7
n		5	8	6	7
High		-47.0	-15.0	-24.0	-32.0
Low		-183.0	-145.0	-150.0	-119.0
Extreme Spread		136.0	130.0	126.0	87.0
Variance		3158.8	2263.2	2616.7	889.2
Standard Deviation		56.2	47.6	51.2	29.8
Coefficient of Variation		-47.0	-60.9	-68.8	-40.5

## **VITA**

John Henry Weathersby was born on April 5<sup>th</sup>, 1960 in Coahoma, Mississippi. He attended high school at Lee Academy in Clarksdale, Mississippi. He received his Bachelor of Science in Civil Engineering in 1983 and his Master of Engineering in Structural Engineering in 1989 from Mississippi State University. John began working as a Research Engineer for the U. S. Army Corps of Engineers, Waterways Experiment Station in 1983. He transferred to the European Division in 1989, where he served as a structural design engineer. During this time he met his wife, Anne Halpenny-Weathersby. Mr. Weathersby now works as a Senior Research Engineer for the U.S. Army Engineer Research and Development Center in Vicksburg, Mississippi.

REPORT DOCUMENTATION PAGE				Form Approved OMB No. 0704-0188	
Public reporting burden for this collection of information is estimated to average 1 hour per response, including the time for reviewing instructions, searching existing data sources, gathering and maintaining the data needed, and completing and reviewing this collection of information. Send comments regarding this burden estimate or any other aspect of this collection of information, including suggestions for reducing this burden to Department of Defense, Washington Headquarters Services, Directorate for Information Operations and Reports (0704-0188), 1215 Jefferson Davis Highway, Suite 1204, Arlington, VA 22202-4302. Respondents should be aware that notwithstanding any other provision of law, no person shall be subject to any penalty for failing to comply with a collection of information if it does not display a currently valid OMB control number. PLEASE DO NOT RETURN YOUR FORM TO THE ABOVE ADDRESS.					
1. REPORT DATE (DD-MM-YYYY) August 2003		2. REPORT TYPE Final report		3. DATES COVERED (From - To)	
4. TITLE AND SUBTITLE  Investigation of Bond Slip Between Concrete and Steel Reinforcement Under Dynamic Loading Conditions				5a. CONTRACT NUMBER	
				5b. GRANT NUMBER	
				5c. PROGRAM ELEMENT NUMBER	
6. AUTHOR(S)  John H. Weathersby				5d. PROJECT NUMBER	
				5e. TASK NUMBER	
				5f. WORK UNIT NUMBER	
7. PERFORMING ORGANIZATION NAME(S) AND ADDRESS(ES)  U.S. Army Engineer Research and Development Center Geotechnical and Structures Laboratory 3909 Halls Ferry Road Vicksburg, MS 39180-6199				8. PERFORMING ORGANIZATION REPORT NUMBER  ERDC/GSL TR-03-9	
9. SPONSORING / MONITORING AGENCY NAME(S) AND ADDRESS(ES)  U.S. Army Engineer Research and Development Center Laboratory Discretionary Research and Development Program 3909 Halls Ferry Road Vicksburg, MS 39180-6199				10. SPONSOR/MONITOR'S ACRONYM(S)	
				11. SPONSOR/MONITOR'S REPORT NUMBER(S)	
12. DISTRIBUTION / AVAILABILITY STATEMENT  Approved for public release; distribution is unlimited.					
13. SUPPLEMENTARY NOTES					
14. ABSTRACT  Structural failures during recent earthquakes and terrorist attacks have demonstrated shortcomings in the design procedures for reinforced concrete structures. Earlier research has demonstrated that a major limitation of the Finite Element (FE) modeling of the response of reinforced concrete is the accurate modeling of the interaction of the concrete with the steel reinforcement. Presently, there are insufficient data on the dynamic nonlinear interaction between the concrete material and the steel reinforcement to develop a numerical model of this interaction.  The primary objective of this study was to experimentally investigate the dynamic interaction (bond slip) of reinforcement with concrete and gain a better understanding of the parameters that control this interaction. Specifically, the effects of concrete confinement, bar deformation and bar diameter on the bond slip, and the influence of loading rates - static to impact – on these effects were investigated. Additionally, the variation of the strain along the length of the steel bar and strain transfer to the concrete were investigated. Finite Element analyses were performed using the experimental parameters to determine the value of the chemical adhesion and to compare the experimental results with the analytical values.  (Continued)					
15. SUBJECT TERMS Bond slip                                      Concrete reinforcement                                      Dynamically loaded concrete					
16. SECURITY CLASSIFICATION OF:			17. LIMITATION OF ABSTRACT	18. NUMBER OF PAGES  283	19a. NAME OF RESPONSIBLE PERSON
a. REPORT UNCLASSIFIED	b. ABSTRACT UNCLASSIFIED	c. THIS PAGE UNCLASSIFIED			19b. TELEPHONE NUMBER (include area code)

#### **14. ABSTRACT (Concluded)**

To accomplish the research objectives, 33 pullout tests were performed. The test specimens were subjected to quasi-static, dynamic, and impact loadings to investigate the influence of rebar size and shape, confinement and loading rate on pullout resistance, and failure mode.

The results of the study have shown that, for the concrete and steel used in this investigation, the stress resulting from static friction and chemical adhesion is 960 psi for quasi-static loading, 2,600 psi for dynamic loading, and 3,200 psi for impact loading. The steel bar deformations accounted for 70 to 77 percent of the total resistance to pullout regardless of loading rate. Impact loaded specimens had nearly twice the pullout resistance of the quasi-statically loaded specimens, and the development length decreased as the loading rate or confinement increased. Bond stresses obtained for both smooth and deformed bars were in good agreement with results obtained in earlier studies involving quasi-static tests.